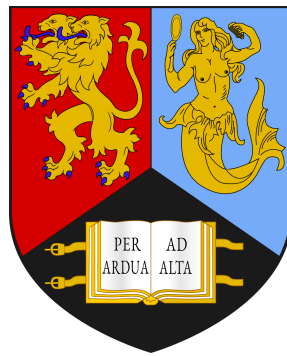# Developing and Evaluating the Driving and Powertrain Systems of Automated and Electrified Vehicles (AEVs) for Sustainable Transport

Yinglong He

This dissertation is submitted for the degree of

Doctor of Philosophy

Department of Mechanical Engineering

School of Engineering

College of Engineering and Physical Science

University of Birmingham

June 2021

UNIVERSITY OF BIRMINGHAM

University of Birmingham Research Archive

e-theses repository

University of Birmingham Research Archive

e-Theses Repository

Abstract

In the transition towards sustainable transport, automated and electrified vehicles (AEVs) play a key role in overcoming challenges such as fuel consumption, emissions, safety, and congestion. The development and assessment of AEVs require bringing together insights from multiple disciplines such as vehicle studies to design and control AEVs and traffic flow studies to describe and evaluate their driving behaviours. This thesis, therefore, addresses the needs of automotive and civil engineers, and investigates three classes of problems: optimizing the driving and powertrain systems of AEVs, modelling their driving behaviours in microscopic traffic simulation, and evaluating their performance in real-world driving conditions.

The first part of this thesis proposes Pareto-based multi-objective optimization (MOO) frameworks for the optimal sizing of powertrain components, e.g., battery and ultracapacitor, and for the integrated calibration of control systems including adaptive cruise control (ACC) and energy management strategy (EMS). We demonstrate that these frameworks can bring collective improvements in energy efficiency, greenhouse gas (GHG) emissions, ride comfort, safety, and cost-effectiveness.

The second part of this thesis develops microscopic free-flow or car-following models for reproducing longitudinal driving behaviours of AEVs in traffic simulation, which can support the needs to predict the impact of AEVs on traffic flow and maximize their benefits to the road network. The proposed models can account for electrified vehicle dynamics, road geometric characteristics, and sensing/perception delay, which have significant effects on driving behaviours of AEVs but are largely ignored in traffic flow studies.

Finally, we systematically evaluate the energy and safety performances of AEVs in real-world driving conditions. A series of vehicle platoon experiments are carried out on public roads and test tracks, to identify the difference in driving behaviours between ACC-equipped vehicles and human-driven vehicles (HDVs) and to examine the impact of ACC time-gap settings on energy consumption.

Acknowledgements

First and foremost, I am very fortunate to have Prof. Hongming Xu as my PhD supervisor and would like to thank him for his continued support, guidance, and encouragements. Throughout our meetings and discussions, his insights and intuitions have shaped my understanding of many topics such as vehicle dynamics and control. He has given me the freedom to explore different research directions, provided opportunities for me to travel, and introduced me to many people. This thesis and my future career would not have been the same without him. I would also like to thank Dr Dawei Wu and Dr Dezong Zhao for being my thesis examiners.

I would like to express my sincere acknowledgement to Dr Biagio Ciuffo at the Joint Research Centre (JRC) of the European Commission (EC), who offered me opportunities to visit his group in February 2018 and February 2019. I would like to thank him for the kind support and advice he provided, and for sharing insightful ideas on microscopic traffic simulation. Many results in Parts II and III of this thesis have been obtained in collaboration with him and his colleagues including Dr Michail Makridis, Dr Konstantinos Mattas, Dr Georgios Fontaras, Dr Alessandro Tansini, Aikaterini Anesaidou, Giovanni Albano, and Dr Riccardo Dona. It is my great pleasure to work with them all and learn from their expertise. I look forward to my next project with them. I am also grateful to Prof. Vincenzo Punzo and Prof. Marcello Montanino at the University of Naples Federico II for their invaluable suggestions and inputs on the calibration of car-following models.

I have met many other wonderful people during my time at the University of Birmingham. I am grateful to Prof. Huw Williams, Dr Quan Zhou, and Dr Chongming Wang for their guidance and advice in my academic research and career development. I would also like to acknowledge Dr Richard Hood and Dr Yueting Sun for their suggestions in my annual progress reviews. Many thanks also to Dr Haoye Liu, Dr Amrit Sahu, Dr Yunfan Zhang, Dr Scott Cash, Dr Ziyang Li, Dr Aawishkar Dharmadhikari, Dr Ji Li, Dr Lewis Parry, Bin Shuai, Mengzhu Zhang, Zeyu Sun, Cetengfei Zhang, and all the other members of the research group for making it such an enjoyable place to work. The work

Most of all, I wish to thank my family for their support and encouragement, especially my parents, Bingzhou He and Fengxiang Ye, and my sisters, Fang He and Qin He. Finally, to Dr Timan Lei, with all of my love, I dedicate this thesis to you.

List of publications

Journal Articles

1) **Yinglong He**, Chongming Wang, Quan Zhou, Ji Li, Michail Makridis, Huw Williams, Guoxiang Lu, and Hongming Xu*. Multiobjective component sizing of a hybrid ethanol-electric vehicle propulsion system. *Applied Energy*. 2020 May 15; 266:114843. (*SCI, IF = 8.426, JCR Q1*) [Link]

2) **Yinglong He**, Quan Zhou, Michail Makridis, Konstantinos Mattas, Ji Li, Huw Williams, and Hongming Xu*. Multiobjective co-optimization of cooperative adaptive cruise control and energy management strategy for PHEVs. *IEEE Transactions on Transportation Electrification*. 2020 Feb 17; 6(1):346-355. (*SCI, IF = 5.444, JCR Q1*) [Link]

3) **Yinglong He**, Michail Makridis, Konstantinos Mattas, Georgios Fontaras, Biagio Ciuffo*, and Hongming Xu. Introducing electrified vehicle dynamics in traffic simulation. *Transportation Research Record*. 2020 Jul 7; 2674(9):776-791 (*SCI, IF = 0.748, JCR Q4*) [Link]

4) **Yinglong He**, Michail Makridis*, Georgios Fontaras, Konstantinos Mattas, Hongming Xu, and Biagio Ciuffo. The energy impact of adaptive cruise control in real-world highway multiple-car-following scenarios. *European Transport Research Review*. 2020 Mar 24; 12(1):1-11. (*SCI, IF = 1.727, JCR Q3*) [Link]

5) **Yinglong He**, Konstantinos Mattas, Riccardo Dona, Giovanni Albano, and Biagio Ciuffo*. Introducing the effects of road geometry into microscopic traffic models for automated vehicles. *IEEE Transactions on Intelligent Transportation Systems*. 2021. (*Under Review*) [Link]

6) **Yinglong He**, Marcello Montanino*, Konstantinos Mattas, Vincenzo Punzo, and Biagio Ciuffo. Physics-augmented models to simulate commercial adaptive cruise control

(ACC) systems. *Transportation Research Part C: Emerging Technologies*. 2021. (*Under Review*) [Link]

7) Biagio Ciuffo, Konstantinos Mattas, Michail Makridis, Giovanni Albano, Aikaterini Anesiadou, **Yinglong He**, Szilard Josvai, Dimitris Komnos, Marton Pataki, Sandor Vass, and Zsolt Szalay*. Requiem on the positive effects of commercial adaptive cruise control on motorway traffic and recommendations for future automated driving systems. *Transportation Research Part C: Emerging Technologies*. 2021 Sep 1; 130:103305. (*SCI, IF = 8.089, JCR Q1*) [Link]

8) Bin Shuai, Quan Zhou*, Ji Li, **Yinglong He**, Ziyang Li, Huw Williams, Hongming Xu, and Shijin Shuai. Heuristic action execution for energy efficient charge-sustaining control of connected hybrid vehicles with model-free double Q-learning. *Applied Energy*. 2020 Jun 1; 267:114900. (*SCI, IF = 8.426, JCR Q1*) [Link]

9) Quan Zhou*, **Yinglong He**, Dezong Zhao, Ji Li, Yanfei Li, Huw Williams, and Hongming Xu*. Modified particle swarm optimization with chaotic attraction strategy for modular design of hybrid powertrains. *IEEE Transactions on Transportation Electrification*. 2020 Aug 7. (*SCI, IF = 5.444, JCR Q1*) [Link]

10) Ji Li, Quan Zhou, **Yinglong He**, Huw Williams, and Hongming Xu*. Driver-identified supervisory control system of hybrid electric vehicles based on spectrum-guided fuzzy feature extraction. *IEEE Transactions on Fuzzy Systems*. 2020 Feb 11; 28(11):2691-2701. (*SCI, IF = 8.759, JCR Q1*) [Link]

11) Quan Zhou, Ji Li, Bin Shuai, Huw Williams, **Yinglong He**, Ziyang Li, Hongming Xu*, and Fuwu Yan. Multi-step reinforcement learning for model-free predictive energy management of an electrified off-highway vehicle. *Applied Energy*. 2019 Dec 1; 255:113755. (*SCI, IF = 8.426, JCR Q1*) [Link]

12) Ji Li, Quan Zhou, **Yinglong He**, Bin Shuai, Ziyang Li, Huw Williams, and Hongming Xu*. Dual-loop online intelligent programming for driver-oriented predict energy management of plug-in hybrid electric vehicles. *Applied Energy*. 2019 Nov 1; 253:113617. (*SCI, IF = 8.426, JCR Q1*) [Link]

Conference Papers

1) **Yinglong He**, Biagio Ciuffo*, Quan Zhou, Michail Makridis, Konstantinos Mattas, Ji Li, Ziyang Li, Fuwu Yan, and Hongming Xu*. Adaptive cruise control strategies implemented on experimental vehicles: A review. *9th IFAC Symposium on Advances in Automotive Control (AAC)*. 23-27 Jun 2019. Orleans, France. [Link]

2) **Yinglong He**, Michail Makridis, Konstantinos Mattas, Georgios Fontaras, Biagio Ciuffo*, and Hongming Xu. Enhanced MFC: Introducing dynamics of electrified vehicles for free flow microsimulation modelling. *Transportation Research Board (TRB) 99th Annual Meeting*. 12-16 Jan 2020. Washington DC, USA. [Link]

3) **Yinglong He**, Michail Makridis*, Georgios Fontaras, Konstantinos Mattas, Hongming Xu, and Biagio Ciuffo. The impact of adaptive cruise control on tractive energy consumption in real-world highway multiple-car-following scenarios. *Proceedings of TRA2020, the 8th Transport Research Arena: Rethinking transport - towards clean and inclusive mobility*. 27–30 Apr 2020. Helsinki, Finland. [Link]

4) Quan Zhou, Ji Li, **Yinglong He**, Bin Shuai, Huw Williams, Hongming Xu*, Yanfei Li, and Fuwu Yan. K-fold fuzzy learning for implementation of dynamic programming results in real-time energy management of the plug-in hybrid vehicle. *Applied Energy Symposium 2020: Low Carbon Cities and Urban Energy Systems*. 10-17 Oct 2020, Tokyo, Japan (Online). [Link]

List of awards

Honors

1) Jan 2020: **Best Simulation Application Paper Award** *(the 1st author)*, 99th Annual Meeting of Transportation Research Board (TRB, *the world's largest transportation research conference*). Washington DC, USA. [Link]

2) Mar 2020: **Front Cover Paper** *(the 1st author)* of IEEE Transactions on Transportation Electrification (*SCI, IF = 5.444, JCR Q1*), Volume 6, Issue 1, 2020. [Link]

3) Apr 2020: **Best Research Paper** *(the 1st author)* of the 8th Transport Research Arena (TRA, *the foremost European transport event*). *"Rethinking transport - towards clean and inclusive mobility"*. Helsinki, Finland. [Link]

4) Jul 2018: Finalist, "Chunhui Cup" Chinese Overseas Students Innovation and Entrepreneurship. Guangzhou, China. [Link]

Scholarships

1) 2017 - 2019: **School Scholarship** (£ 20K per year), School of Engineering, University of Birmingham (UoB). Birmingham, UK.

I would like to dedicate this thesis to my loving parents, who have been my source of inspiration and gave me strength when I thought of giving up, who continually provide their moral, emotional, and financial support. To my sisters, brothers, relatives, supervisor, and friends, who shared their words of advice and encouragement to finish this study . . .

Table of contents

III   To evaluate AEVs in real-world driving conditions   163

8   Comparing energy and safety performances between ACC and human driving behaviours   165

9   Energy impacts of time-gap settings on ACC vehicle platoons on test tracks   181

List of figures

List of tables

Nomenclature

Roman Symbols

a Acceleration (m/s^2)

F Force (N)

g Gravitational acceleration ($\simeq$ 9.81 m/s^2)

I Electrical current (A)

l Length (m)

m Mass (kg)

P Power (W)

R Electrical resistance (Ω)

r Radius (m)

s Spacing (m)

T Torque (Nm)

t Time (s)

U Electrical voltage (V)

v Speed (m/s)

x Position (m)

Greek Symbols

η Efficiency

ω Rotational speed (rad/s)

π Archimedes' constant ($\simeq$ 3.14)

τ	Time constant (s)

Acronyms / Abbreviations

ACC	Adaptive cruise control
ACES	Automation, connectivity, electrification, and sharing
ADAS	Advanced driver assistance systems
AER	All-electric range
AEV	Automated and electrified vehicle
AV	Automated vehicle
BCU	Battery control unit
BEV	Battery electric vehicle
CACC	Cooperative adaptive cruise control
CAGR	Compound annual growth rate
CAV	Connected and automated vehicle
CD–CS	Charge depleting - charge sustaining
DP	Dynamic programming
EA	Evolutionary algorithm
EcoACC	Ecological adaptive cruise control
ECU	Engine control unit
EGU	Engine-generator unit
EM	Electric motor
EMS	Energy management strategy
EV	Electrified vehicle
FCEV	Fuel cell electric vehicle

FC	Fuel cell
FFV	Flex-fuel vehicle
FL	Fuzzy logic
FVDM	Full velocity difference model
GFM	Generalized force model
GHG	Greenhouse gas
GHR	Gazis-Herman-Rothery
GNSS	Global navigation satellite system
GPS	Global positioning system
HDV	Human-driven vehicle
HEV	Hybrid electric vehicle
HMI	Human machine interface
ICE	Internal combustion engine
ICEV	Internal combustion engine vehicle
IDM	Intelligent driver model
IMU	Inertial measurement unit
IQR	Interquartile range
ITS	Intelligent transportation systems
LCA	Life cycle assessment
MaaS	Mobility as a service
MCU	Motor control unit
ML	Machine learning
MOO	Multi-objective optimization

MPC	Model predictive control
MUR	Maximum unambiguous range
NEDC	New European Driving Cycle
NN	Neural network
NSGA	Non-dominated sorting genetic algorithm
OV	Optimal velocity model
PEMS	Portable emission measurement system
PF	Pareto frontier
PGS	Planetary gearset
PHEV	Plug-in hybrid electric vehicle
PID	Proportional, integral, and derivative
PSD	Power-split device
PSO	Particle swarm optimization
RB	Rule-based
RDE	Real driving emissions
RL	Reinforcement learning
RSU	Roadside unit
SoC	State-of-charge
SoH	State-of-health
TCU	Transmission control unit
WLTC	Worldwide Harmonised Light Vehicle Test Cycles
WTW	Well-to-wheel

1 Introduction

Automated and electrified vehicles (AEVs) have attracted significant attention in recent years due to their potential to provide sustainable mobility solutions, including safety, congestion, emissions, and fuel economy. The development and assessment of AEVs require bringing together insights from multiple disciplines. This thesis, therefore, integrates knowledge and techniques from across vehicle control, traffic flow, and related fields to address the most important fundamental and applied questions on AEVs from three aspects, namely, how to optimize the components and controllers of their driving and powertrain systems, how to model the impacts of their driving behaviours on traffic flow dynamics, and how to evaluate their energy and safety performances in real-world driving conditions. In this chapter, we introduce the background, motivations, and objectives of this research, finally followed by the outline of the thesis.

1.1 Background

1.1.1 Challenges and opportunities for road transport

Road transport, connecting and providing access to people, goods, and services in societies, is fundamental to economic and social activities worldwide [1]. In the coming decades, passenger and freight mobility demand is expected to rise significantly because of continuing population growth and urbanization [2].

As shown in Figure 1.1 (a), the International Transport Forum (ITF) has projected the global passenger transport demand to increase over twofold between 2020 and 2050, from 55 trillion to 121 trillion passenger kilometers (pkm). Private vehicles are the preferred mode of travel, which will account for 50-52% over the next 30 years. Public transport ridership will increase at an annual rate of 3.2% through 2020 and 2050, covering 35% road trips by 2050. Two- and three-wheelers were only responsible for 5% of worldwide road passenger transport in 2000, but that proportion is likely to reach 13% in 2050. According to the data in Figure 1.1 (b), the current global freight transport demand of 15 trillion tonne

kilometres (tkm) is expected to increase by 4 trillion tkm (29%) in 2030 and 17 trillion tkm (117%) in 2050, with heavy-duty vehicles maintaining a dominant share (over 75%) of road freight movements.

(a) Global road passenger transport activity
(in trillion passenger kilometres, trillion pkm)

(b) Global road freight transport activity
(in trillion tonne kilometres, trillion tkm)
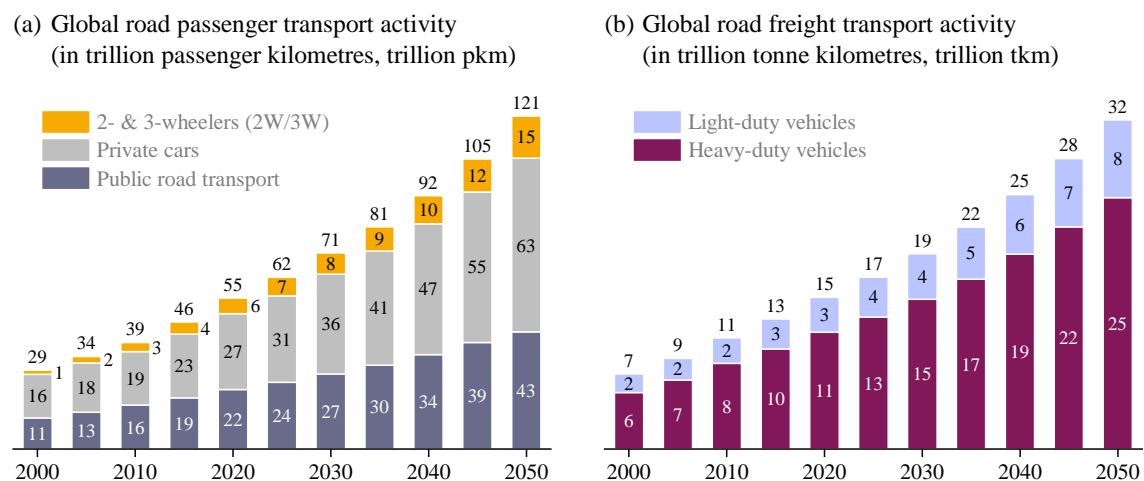
Sources: Adapted from International Council on Clean Transportation (ICCT) - "Global transportation roadmap" [3], International Transport Forum (ITF) - "ITF transport outlook 2019" [4] and Khalili et al. [5].
Note: Figures may not sum, because of rounding.

Figure 1.1 Global road transport activity evolution (2000-2050) for (a) passenger (in trillion passenger kilometres, trillion pkm) and (b) freight (in trillion tonne kilometres, trillion tkm).

The rising demand for road transport poses unprecedented environmental, economic, and social challenges, particularly with the increasing urgency to save energy, reduce carbon emissions and air pollutants, avoid crashes, and relieve congestion [6]. For example, as reported by International Energy Agency (IEA), over 53% of global primary oil consumption in 2010 was used to meet 94% of the total transport energy demand [7]. The Intergovernmental Panel on Climate Change (IPCC) reported that, in 2014, the global transportation sector is responsible for almost one-quarter of greenhouse gas (GHG) emissions, with about 72% thereof from road transport [8, 9]. In the 2018 Global Status Report on Road Safety [10], the World Health Organization (WHO) highlights that the number of annual road traffic fatalities continues to increase steadily since 2000, reaching 1.35 million in 2016. In addition, according to the INRIX Roadway Analytics in 2017, over the next 10 years, across all 25 most-congested cities of the United States (US), e.g., Los Angeles, New York, and San Francisco, traffic jams are estimated to cost the drivers $480 billion due to lost time, wasted fuel, and carbon emitted [11, 12].

Overcoming the above problems, such as carbon emissions, air pollution, nonrenewable energy consumption, deaths, injuries, wasted time, and congestion, requires rethinking

the entire road transport system. Therefore, we must bring together technologies, systems design methods, and business models to supply sustainable mobility solutions at a low cost to consumers and to societies [1].

Table 1.1 Transport and vehicle technologies funded by Horizon 2020 (H2020).

Category	Number of projects	Budget (million €)
FC and hydrogen fuel	21	327
Vehicle propulsion	35	172
EVs	56	119
CAVs	12	81
EV batteries and EMS	23	73
ADAS	23	47
EC systems	12	43
Safety systems	29	39
Information systems	23	31
CAD	5	28
VDM	14	23
MaaS	11	18
EV support technologies	7	14
TMS	21	10
Freight technologies	7	9
Satellite navigation	3	8
Manufacturing processes	9	8
Sensor technologies	7	6
HVAC	4	6
Noise optimization	3	5

Source: Adapted from Joint Research Centre (JRC), European Commission - "The future of road transport: Implications of automated, connected, low-carbon and shared mobility" [13] and TRIMIS database, European Commission [14].

Note: FC = fuel cell; EV = electrified vehicle; CAV = connected and automated vehicle; EMS = energy management strategy; ADAS = advanced driver assistance systems; EC = emission control; CAD = computer aided design; VDM = vehicle design and manufacturing; MaaS = mobility as a service; TMS = traffic management systems; HVAC = heating, ventilation and air-conditioning.

Table 1.1 summarizes the transport and vehicle technologies funded by Horizon 2020 (H2020), the largest ever European funding programme for research and innovation (R&I). The data identifies fuel cell and hydrogen fuel technologies as the category receiving the highest number of grants (€327 million), in which two flagship projects (called H2ME and H2ME2, Hydrogen Mobility Europe) are co-funded with €67 million from H2020 and aim to demonstrate the potential of hydrogen-fuelled road transport. The category of electrified vehicles (EVs) is ranked third in H2020 funding, covers 56 projects, and attracts more attention from small and medium-sized enterprises (SMEs) [13]. Connected

and automated vehicles (CAVs), in the fourth place, potentially forms the backbone of future intelligent transportation systems (ITS). Although representing more established technologies, the category of vehicle propulsion accounts for the second-largest portion of the H2020 budget.

In addition to public spending, private sector investments in relevant technologies have increased significantly, with MaaS, ADAS sensors, CAVs, and EVs being the front-runners. As reported by McKinsey Center for Future Mobility, from 2010 to 2019, investors have poured $220 billion into more than 1,100 companies across ten technology categories [15].

Although much uncertainty remains about how, exactly, future sustainable mobility will unfold, many of the pivotal building blocks, and their potential, are becoming clear. As the key to these developments, four trends, namely, automated, connected, electrified, and shared (usually represented by the acronym ACES or CASE) vehicles, are radically altering the way people and goods move [15]. Summaries of recent advances in these four directions are provided as follows.

1) Automated vehicles

To facilitate communication and collaboration within and across technical and policy domains, the Society of Automotive Engineers (SAE) J3016 standard [16] provides a common taxonomy and definitions for automated vehicles and defines six levels of driving automation spanning from no automation (Level 0) to full automation (Level 5), as illustrated in Figure 1.2. These levels primarily identify the capability of automated driving systems to perform part or all of the dynamic driving task (DDT) on a sustained basis. The DDT includes, but is not limited to, controlling the lateral (steering) and longitudinal (accelerating and braking) motion of the vehicle, monitoring the driving environment (referred to as object and event detection and response, OEDR), manoeuvre planning, and enhancing conspicuity (e.g., lighting and signalizing). In addition, the operational design domain (ODD) in this standard delimits the geographical, road, environmental, traffic, speed, and temporal conditions where the automated driving system is expected to operate parts of the DDT and applies to Levels 1-4 automation (Level 5 automation has an unlimited ODD) [13].

Figure 1.2 suggests that human drivers are still responsible to monitor the surrounding environment at all times, with lower levels of automation (Levels 0-2) such as adaptive

cruise control (ACC, Level 1), lane keeping assist (LKS, Level 1), and Tesla Autopilot (Level 2). A key distinction is between Level 2 and Level 3. At Level 3 and above levels, the automated driving system, instead of the driver, is in charge of monitoring the environment. It is important as this is where the insurance liability will switch from the driver to the manufacturer. As the automation levels increase, the human driver goes from needing to be available to take over when requested, to being "eyes off & hands off", up to Level 5 where the vehicle may not even allow the driver to take over [17].

Source: Adapted from Society of Automotive Engineers (SAE) J3016 standard [16] and Joint Research Centre (JRC), European Commission [13].

Figure 1.2 Different levels of driving automation defined by Society of Automotive Engineers (SAE) J3016 Standard.

2) Connected vehicles

Connected vehicles are another key enabler for future mobility. As digital disruption is transforming the automotive and transport sectors, more and more relevant applications and services in various domains will follow, such as infotainment, telematics, driver assistance, and autonomous driving [6]. Vehicles should therefore be capable of exchanging information not only with other vehicles, but also with entities, e.g., pedestrians, roadside equipment, and the internet. These innovative connectivity features are collectively called

vehicle-to-everything (V2X), which would lend support to a more active role of vehicle in safety and mobility applications, for example, avoiding collisions, monitoring intersections, gathering real-time traffic information, and exchanging incident alerts. The resulting market is expected to increase across the globe and reach around $100 billion in 2025 at a compound annual growth rate (CAGR) of 18% between 2018 and 2025 [18].

According to the type of peer that the vehicle communicates with, V2X communication is a term including many different acronyms, e.g.,

- **Vehicle-to-infrastructure (V2I):** Communicating with roadside units (RSUs), e.g., traffic lights, speed limits, and traffic cameras.

- **Vehicle-to-vehicle (V2V):** Communicating between vehicles, without having to access the telecom network.

- **Vehicle-to-pedestrian (V2P):** Scanning for and communicating with pedestrians or cyclists within close proximity.

- **Vehicle-to-device (V2D):** communicating with electronic devices such as smartphones, smartwatches, and smart keys.

- **Vehicle-to-grid (V2G):** Allowing electrified vehicles (EVs) to communicate with the power grid and to store and discharge electricity, which therefore enables innovative demand management on power-limited grids.

- **Vehicle-to-network (V2N):** Operating in the licensed cellular spectrum (e.g., 5G), which is good for infotainment.

V2X applications often need extreme connectivity performances, e.g., ultra-low latency (<1 ms) for real-time applications, highly secure and reliable connectivity for safety-critical tasks, and high-speed broadband (> 1Gb/s) to support augmented reality (AR) [18]. Different V2X communication standards available on the market can be categorized into two types depending on the underlying technology: WLAN-based (IEEE 802.11p) and cellular-based (C-V2X) [19].

3) Electrified vehicles

International Energy Agency (IEA) reported in 2020 that 17 countries have announced 100% zero-emission vehicle targets or the phase-out of internal combustion engine vehicles

(ICEVs) by 2050 [20]. These decisions are linked to the Paris Climate Agreement signed by more than 190 nations in 2016 [21]. Electrified vehicles, therefore, feature prominently in current and planned policy frameworks to achieve greenhouse gas (GHG) emissions reduction targets [22].

To address the global push towards more environmentally friendly and energy-efficient transport, electrified propulsion systems are evolving with the automotive industry. Table 1.2 overviews five types of commercially available powertrain technologies, which are categorized by their energy sources, and provides an evaluation of how they stack up against key environmental, performance, and economic dimensions [23].

Table 1.2 Pros and cons of electrified vehicles categorized by energy sources.

| | | ICEV | Electrified vehicles | | | |
			HEV	PHEV	BEV	FCEV
Environment	T2W emissions [a]	D	C	B	A	A
	W2W emissions [b]	D	D	B	B	B
	Recycling	B	B	C	D	C
Performance	Range	A	A	A	C	B
	Refueling time [c]	A	A	C	D	B
	Acceleration	B	B	A	A	A
	Top speed	A	A	B	C	C
Economics	TCO today [d]	A	A	B	C	D
	Price today	A	B	C	D	D
	Infrastructure costs	A	A	B	D	C
Key characteristics, indicative	ICE power, kW	50-400	50-400	50-200	-	-
	Electric power, kW	-	<25	<100	>100	>100
	Battery capacity, kWh	-	<2	<30	>40	<10
	T2W CO_2 savings, % CO_2	-	10-20	50-80 [e]	100	100

[a] Tank-to-wheel (T2W) emissions, i.e., tailpipe emissions that a vehicle produces locally via the combustion of fossil fuels; these emissions are subject to current regulations globally.
[b] Well-to-wheel (W2W) emissions, i.e., emissions related to the fuel cycle or generation of electricity, the production of the vehicle and battery, and the use of the vehicle; largely dependent on a country's energy mix.
[c] Considering only the time needed to refuel/charge the vehicle, not infrastructure availability.
[d] Total cost of ownership (TCO), strongly depending on region and vehicle segment.
[e] Estimated CO_2 savings considered for certification tests.
Source: Adapted from McKinsey Center for Future Mobility - "Reboost: A comprehensive view on the changing powertrain component market and how suppliers can succeed" [23].
Note: A = excellent; B = good; C = moderate; D = challenged; ICE(V) = internal combustion engine (vehicle); HEV = hybrid electric vehicle; PHEV = plug-in hybrid electric vehicle; BEV = battery electric vehicles; FCEV = fuel cell electric vehicles.

Internal combustion engine vehicles (ICEVs) are almost exclusively powered by gasoline or diesel and well established in global road transport because of low cost, high power density, proven durability, and fuel use flexibility, and a widespread network of refuelling stations [24]. Over the past decades, advanced engine technologies, such as downsizing, turbocharging, and exhaust after-treatment, have contributed to reducing

tailpipe emissions and energy losses, however, it is widely recognised that little room is left for significant improvements [23].

Hybrid electric vehicles (HEVs) are developed to optimize the use of the internal combustion engine (ICE) through its interplay with electric components such as the low-voltage (LV) battery and the electric motor (EM) [25]. As a result, the ICE can be better managed to avoid low-efficiency and high-emission operations, e.g., idling, cold start, and strong acceleration [26]. Moreover, the EM can serve as a generator in regenerative braking to convert the otherwise wasted kinetic energy into electric energy, which is then used to charge the battery and extend the driving range [27].

Plug-in hybrid electric vehicles (PHEVs) have a similar powertrain architecture to HEVs, however, are usually fitted with a more powerful EM and a much larger battery [28]. The battery can be recharged by plugging it into an external power source (utility grid or renewable energy sources such as solar cells), by the onboard ICE-powered generator, or through regenerative braking [29]. Despite the ICE being used occasionally to assist the propulsion, PHEVs can provide a significant share of the all-electric range (AER), the value of which typically lies between 30 and 60 km today and possibly between 60 and 80 km in the near future [23].

Battery electric vehicles (BEVs), operating only on stored electricity, consist mainly of the high-voltage (HV) battery and the EM. Compared with the ICE, which produces peak torque within a limited range of speed, the EM is able to deliver high starting torque across a broad range of speed [30]. Therefore, many parts, such as the reduction gearbox, the increasingly complex engine management system, and a wide variety of fluids (e.g., engine oil and transmission fluid), are not required for BEVs, meaning lower maintenance costs [31]. Furthermore, as battery prices continue to drop, BEVs are expected to offer lower total cost of ownership (TCO) to customers than the ICE and hybrid vehicles [23].

Fuel cell electric vehicles (FCEVs) use fuel cell (FC) stacks to convert the chemical energy of onboard gaseous hydrogen (H_2) into electricity, which is then stored in a battery to drive the vehicle's EM. The compressed hydrogen demonstrates significantly higher gravimetric and volumetric energy densities than batteries [32]. The refuelling time of a few minutes makes FCEVs well suited for applications with high-power and long-distance requirements, e.g., trucks and commercial vehicles [23]. In addition, from the perspective of life cycle emissions and environmental impacts, FCEVs are more sustainable than BEVs,

ICEVs, and hybrids, with even more room for improvement as technologies of hydrogen production and delivery mature [33].

4) Shared vehicles

Mobility as a service (MaaS) is an innovative transportation strategy, which uses a digital platform to integrate end-to-end trip planning, booking, electronic ticketing, and payment services, across all public and private transport modes such as train, taxi, bus, carsharing, and bikesharing [34]. The overarching goal of MaaS is to make it so convenient for users to travel that they will no longer want to own a personal vehicle [35]. Shared vehicles have the potential to reduce negative impacts commonly associated with road transport, e.g., emissions and congestion [36]. The most common models of shared mobility are described as follows [13].

- **Carsharing:** It is a business model providing self-service car rental by the hour or day and allowing individuals to benefit from car use without costs and responsibilities associated with car ownership [37]. Leading carsharing organisations (CSOs) are usually backed by carmakers, such as Share Now (jointly owned by Daimler and BMW) and Maven (owned by GM). As shown in Table 1.3, the global carsharing membership reached nearly 5 million in 2014, up from around 0.35 million in 2006, and is projected to exceed 23 million worldwide by 2024 [34].

- **Ridesharing**: It is also known as carpooling or vanpooling. Ridesharing companies, e.g., BlaBlaCar, use websites and mobile apps to connect people looking to travel long distances with drivers going the same way [38]. The people travelling together can share the operating expenses and may share the responsibility of driving [39].

- **Ridesourcing:** It is also known as Transportation Network Companies (TNCs), e.g, Uber and Lyft. Ridesourcing allows travellers to request a ride in real-time through mobile applications, which can dispatch the request to nearby drivers based on the location proximity [36]. Unlike ridesharing, ridesourcing drivers operate for profit and typically provide rides not incidental to their own trips [40].

Table 1.3 Global carsharing growth between 2006 and 2014.

	2006	2008	2010	2012	2014
Members ($\times 10^3$)	346.6	670.8	1163.6	1788.0	4842.6
Membership growth rate (%)	-	39	32	24	65
Vehicles ($\times 10^3$)	11.5	19.4	32.0	43.6	104.1
Fleet growth rate (%)	-	30	28	17	55
Member / vehicle ratio	30.1	34.6	36.4	41.1	46.5

Source: Adapted from Deloitte - "The rise of mobility as a service" [34] and Shaheen et al. [41].

1.1.2 Advanced driver assistance systems for automated vehicles (AVs)

Advanced driver assistance systems (ADAS) are intended to help drivers in their driving activities [42]. The market for ADAS is expected to show strong momentum in the coming decades, fueled largely by regulatory and consumer interest in safety solutions that protect drivers and prevent accidents [43]. For example, in 2019, some forty countries, led by the European Union (EU) and Japan, have agreed on a draft United Nations (UN) Regulation making autonomous emergency braking (AEB) systems mandatory for all new vehicles [44]. In addition, current ADAS technologies will ultimately pave the way for fully autonomous vehicles, which are now a major focus of research and development (R&D), public interest, and press coverage [45]. As summarized in Figure 1.3, ADAS features can be categorized into three broad groups: aiding the driver, warning the driver, and assisting the driver in performing certain basic driving functions [46].

1) ADAS aiding features

These features, enabled by sensors such as mono-vision cameras, infrared lights, and lasers, provide additional display or illumination and therefore improve the driver's visibility. For instance, night vision (NV) systems utilize the infrared camera to capture the front view in adverse circumstances, e.g., darkness and poor weather [47]. The rear view camera can alleviate the rear blind spot to facilitate parking and reversing [48]. The adaptive front lighting system (AFS) optimizes the distribution of light from the headlights according to vehicle speed and steering input [49]. The surround view system (SVS) gives drivers a 360 degree surround view to ensure easy, safe, and comfortable parking and manoeuvring [50].

Aiding features, most of which were introduced before 2008, are not newcomers in the automotive field. Their cost to customers is decreasing at an annual rate of 4% to 9% [46].

ADAS FEATURES			PARTIAL AUTOMATION
Aiding	**Warning**	**Assisting**	
Definition Aiding features can improve the driver's visibility by providing additional display or illumination.	Warning features alert the driver to potential danger through sensory cues (auditory, visual or haptic).	Assisting features can engage in steering, acceleration, and/or brake systems if necessary.	Automated features allow the vehicle to be driven/stopped without driver intervention in certain scenarios.
Feature (year) Night vision (NV, 2000) Rear view camera (2002) Adaptive front lighting system (AFS, 2006) Surround view system (SVS, 2007)	Park assist (2002) Forward collision warning (FCW, 2003) Lane departure warning (LDW, 2005) Blind spot detection / rear cross traffic alert (BSD/RCTA, 2006) Driver monitoring system (DMS, 2006)	Adaptive cruise control (ACC, 2007) Lane keeping assist (LKA, 2010) Automatic parking (2006) Autonomous emergency braking (AEB, 2008) Pedestrian avoidance (2014) Intelligent speed adaptation (ISA, 2018)	Single lane highway autopilot (2016) Autonomous valet parking (2017) Traffic jam autopilot (2017) Highway autopilot with lane changing (2018) Urban autopilot (2022)
Technology Mono cameras Infrared (night vision) Laser lights	Mono and stereo cameras Radar (short) Steering inertia Ultrasonic	Mono and stereo cameras Radar (short and long) Lidar Ultrasonic	Mono and stereo cameras Radar (short and long) Lidar GPS/mapping Ultrasonic
Others		Drivers begin to share control	System integration

Source: Adapted from Boston Consulting Group (BCG) - "A roadmap to safer driving through advanced driver assistance systems" [46].

Figure 1.3 Categories of ADAS features.

2) ADAS warning features

Warning features can alert the driver to potential dangers through sensory cues such as audio, visual, and haptic signals. For example, the park assist system uses proximity sensors to measure the distances to nearby objects while parking and alerts the driver of obstacles via a beeping noise [51]. The forward collision warning (FCW) system monitors traffic conditions ahead and provides alerts to the driver when possible forward collisions are detected [52]. The lane departure warning (LDW) system visually tracks lane markers and alerts the driver if the vehicle unintentionally drifts out of the travelling lane [53].

Other warning features include blind spot detection (BSD), rear cross traffic alert (RCTA), and driver monitoring system (DMS), all of which have been commercially available since 2006.

3) ADAS assisting features

Assisting features can actively engage in driving tasks to ensure safety and comfort, such as longitudinal control (e.g., acceleration, braking, and gear shifting) and lateral control (e.g., steering) of the vehicle movement [54]. Such features are usually enabled by advanced digital technologies and intelligent tools, for example, mono- and stereo-vision cameras, short- and long-range radars, as well as light detecting and ranging (lidar, using reflected light signals to assess the driving environment) [46]. ADAS products with assisting features have hit the automotive market in the last decade, some of which are elaborated as follows.

- **Adaptive cruise control (ACC):** Vehicles equipped with ACC systems are now reaching mainstream production [55]. These systems utilize radar and control the throttle and brake pedals of the vehicle, aiming to automatically maintain a safe inter-vehicle spacing in congested traffic or a constant speed (user-specified) in free-flow traffic, which potentially improve the safety, fuel economy, and road capacity [56].

- **Intelligent speed adaptation (ISA):** It uses the onboard global positioning system (GPS) and a digital map to improve the driver's compliance with speed limits [57]. If the vehicle speed exceeds a safe or legally enforced speed, the ISA system can provide early warnings of safety issues or directly control the brake and throttle pedals to prevent speeding [58].

- **Lane keeping assist (LKA):** It is an extended version of the lane departure warning (LDW) system. Instead of alerting the driver to the unintended lane departure, LKA can intervene in the actual driving task by providing steering torque and therefore helping the vehicle return to the centre of the lane [59].

- **Automatic parking:** It uses ultrasonic sensors and/or cameras to scan for a suitable parking space and then moves the vehicle from a traffic lane into the parking spot [59]. The automatic parking system aims to enhance the comfort and safety of driving in constrained environments where much attention and experience is required [60].

- **Autonomous emergency braking (AEB):** It is enabled by sensors (e.g., cameras, radars, and/or lidars) to detect the presence of possible hazards in front of the vehicle [61]. In an emergency, the system can automatically enhance braking effort to prevent the accident or mitigate its severity [62].

1.1.3 Powertrain architectures for electrified vehicles (EVs)

Electrified vehicles (EVs), including battery electric vehicles (BEVs) and hybrids, allow various powertrain architectures created by connecting the main components (e.g., internal combustion engine, electric motor/generator, gearbox, and output shaft) in different ways [63]. As shown in Figure 1.4, typical powertrain architectures for electrified vehicles can be classified into four broad groups: pure electric, series hybrid, parallel hybrid, and power-split hybrid, according to the mechanical configuration [64].

(a) **A pure electric powertrain.**

(b) **A series hybrid powertrain.**

(c) **A parallel hybrid powertrain.**

(d) **A power-split powertrain.**
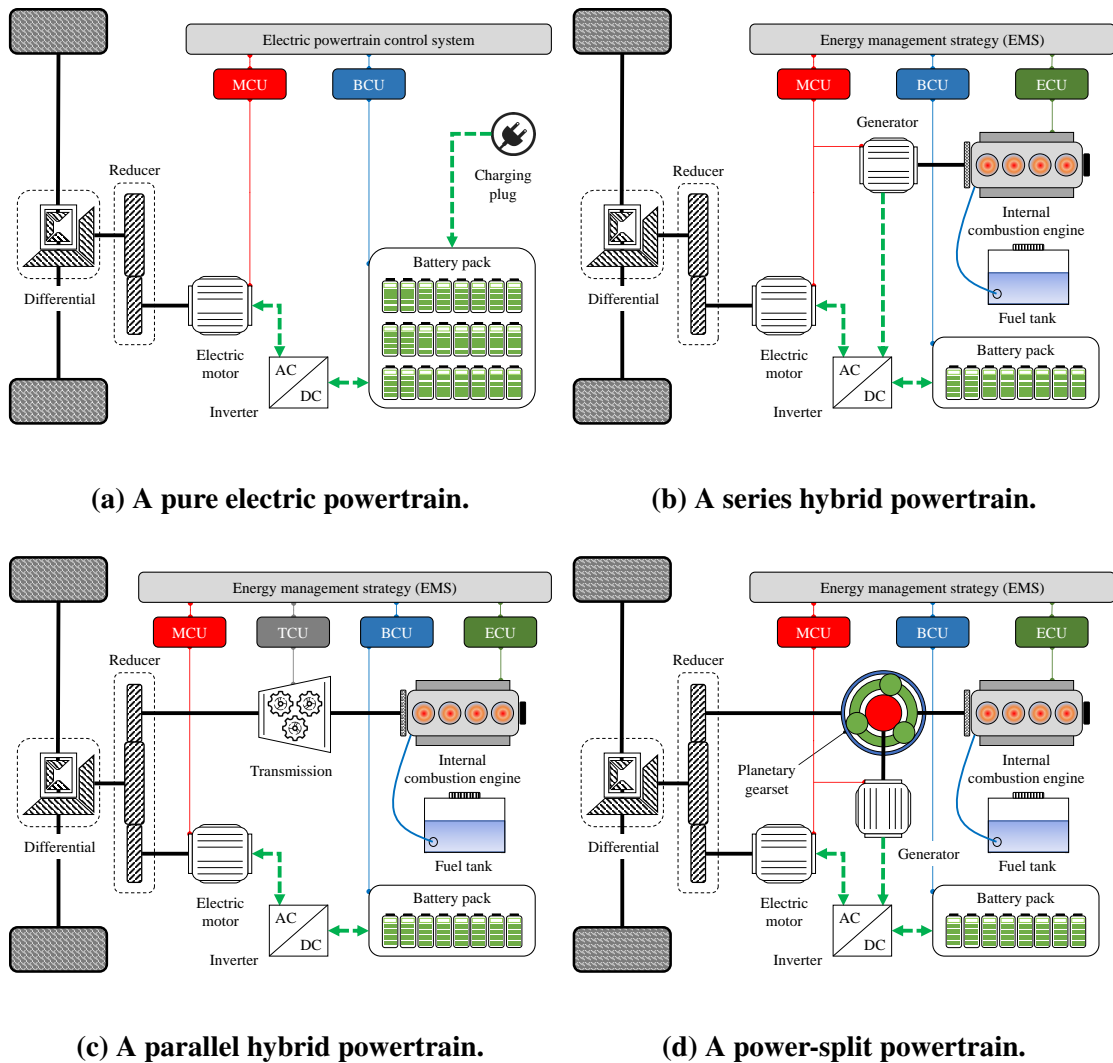
Source: Adapted from Mi et al. [25], Liu et al. [65], Wu et al. [64], and Lucena [66]

Note: MCU = motor control unit; BCU = battery control unit; ECU = engine control unit; TCU = transmission control unit; AC = alternating current; DC = direct current.

Figure 1.4 Typical powertrain architectures for electrified vehicles (EVs).

1) Pure electric powertrain

Figure 1.4 (a) is the simplest pure electric powertrain architecture, but adopted by the majority of battery electric vehicles (BEVs) available in the market, e.g., Nissan Leaf [64]. This layout is relatively similar to conventional internal combustion engine vehicles (ICEVs) except for the absence of clutch and transmission. The battery is the energy source, storing electricity from the grid, and powers the electric motor (EM). The EM converts electricity into mechanical energy and then propels vehicle wheels through the fixed ratio reducer and the differential. In regenerative braking, the EM can be used in reverse as a generator to recover energy, which might otherwise be lost as heat and friction, to charge the battery and extend the driving range [67].

2) Series hybrid powertrain

Figure 1.4 (b) shows the configuration of a series hybrid powertrain. The engine-generator unit (EGU), consisting of an internal combustion engine (ICE) and an electric generator, is the major energy converter, which transforms the chemical energy of the fuel (e.g., gasoline and diesel) into electricity [29]. The EM can use electricity directly generated by the EGU, or that stored in the battery, or both.

Since the engine operation is independent of the vehicle speed and the road load, the series hybrid powertrain possesses numerous advantages. For example, it not only simplifies the energy management strategy (EMS), which coordinates the outputs of multiple power components including the EM and the ICE [25], but, more importantly, allows the ICE to operate at its very narrow optimal region, which leads to improved fuel economy and decreased emissions [68]. However, this architecture has several major limitations as well. The overall energy efficiency is reduced due to multiple energy conversion processes between the EGU, the EM, and the battery [64]. In addition, the EM is the only power source directly propelling the wheels, which means increased costs, weight, and installation space to meet the vehicle's maximum power demand [69].

3) Parallel hybrid powertrain

Figure 1.4 (c) gives the layout of a parallel hybrid powertrain, in which the ICE and the EM are connected with a fixed speed ratio and deliver driving torque to wheels, either

separately or together [64]. The EM can also operate as a generator, which recovers the kinetic energy during braking or absorbs a portion of the engine power output, according to the battery state-of-charge (SoC) and the vehicle power demand [25]. It is worth noting that the parallel hybrid powertrain, unlike the series one, requires the engine to be rigidly attached to wheels when it works [70]. Since the ICE and the EM complement each other to meet the vehicle power demand, both of them can be downsized to reduce the costs, weight, and installation space [66].

4) Power-split hybrid powertrain

Figure 1.4 (d) provides the architecture of a power-split hybrid powertrain, which is a compromise possessing the strengths of both the series and the parallel configurations [64]. The power-split device (PSD), i.e., the planetary gearset (PGS) in this layout, divide the engine power along two paths, namely, the electrical path (to generate electricity) and the mechanical path (to drive the wheels) [65]. Since the ICE can always operate efficiently, this architecture yields significant improvement in fuel economy, and therefore, currently dominants HEV and PHEV markets, e.g., Toyota Prius [64]. Nevertheless, this type of powertrain suffers from some limitations. For instance, the ratio of power split along two paths largely depends on vehicle speed [71], and therefore, the powertrain only retains its high fuel efficiency within a certain speed range, in which the impact of multiple energy conversions is minimized [72]. In addition, it is generally more expensive than the series or parallel counterparts because of increased components and complexity [25].

1.2   Motivations

This research project, partially supported by the Joint Research Centre (JRC) of the European Commission (EC), focuses on emerging automated and electrified vehicles (AEVs) and brings together insights from multiple disciplines, e.g., vehicle studies to design and control AEVs as well as traffic flow studies to describe and evaluate their driving behaviours. In general, the following three questions have directed much of this industry-oriented project.

- How can the driving and powertrain systems of AEVs be optimized for taking advantage of their (mechanical and electrical) components and (energy and driving)

controllers? It is important for bringing collective improvements in energy efficiency, greenhouse gas (GHG) emissions, ride comfort, safety, and cost-effectiveness.

- How can microscopic traffic models be developed for accurately reproducing AEVs' driving behaviours in traffic simulation? It is essential for predicting the impact of AEVs on traffic flow and for maximizing their benefits to the road network.

- How can the driving performances (e.g., energy and safety) of AEVs be evaluated in real-world conditions? It is critical for understanding the properties of commercially available AEVs and for anticipating potential problems associated with their widespread application.

1.3 Objectives

To meet growing stakeholders' interest in automated and electrified vehicles (AEVs) and sustainable transport, this PhD project attempts to shed light on the development and assessment of AEVs from three aspects, namely, optimizing their driving and powertrain systems, modelling their longitudinal driving behaviours in microscopic traffic simulation, and evaluating their driving performance in real-world driving conditions. More specifically, the objectives of this work are as follows.

1) Optimizing the driving and powertrain systems of AEVs

- To develop a flex-fuel hybrid powertrain for electrified vehicles (EVs), and then to explore the optimal sizing of its key components for improving its energy efficiency, GHG emissions, and cost-effectiveness.

- To model AEVs' system dynamics that can simultaneously account for longitudinal driving control and hybrid powertrain operation, and then to perform integrated multi-objective optimization of adaptive cruise control (ACC) and energy management strategy (EMS) for enhancing energy efficiency, ride comfort, and tracking capability.

2) Modelling the longitudinal driving behaviours of AEVs in microscopic traffic simulation

- To introduce electrified powertrain dynamics into microscopic traffic models for EVs, and then to validate the proposed free-flow acceleration model using in-lab

measurements (on a chassis dynamometer), on-road driving trajectories, and vehicle technical specifications.

- To explore the impacts of road curvature and road slope on the free-flow driving behaviour of ACC-equipped vehicles, and then to introduce these effects into microscopic traffic models for automated vehicles (AVs).

- To develop a physics-augmented microscopic modelling framework that introduces mechanical features and controller designs of AVs into traffic flow theory.

3) Assessing the driving performance of AEVs in real-world conditions

- To compare the driving behaviour between ACC vehicles and human-driven vehicles (HDVs) in platooning experiments on public roads, in terms of their energy and safety performances.

- To investigate the impacts of different time-gap settings of commercial ACC systems on the energy consumption of vehicle platoons examined on test tracks.

1.4   Thesis outline

The remainder of this thesis is organized into nine chapters as follows, including Chapter 2 that presents a comprehensive literature review, Chapter 10 that summarizes major findings and recommendations for future research, as well as another seven main chapters that are divided into three parts and discuss the results and original contributions.

Chapter 2:   Energy management strategy (EMS) is the key to operating the electrified powertrain in an energy-efficient way. Adaptive cruise control (ACC) plays a critical role in low-level automated driving. Multi-objective optimization (MOO) is important for a comprehensive improvement in vehicle performance. In addition, microscopic traffic model is essential for describing the vehicle behaviour in traffic simulation and then predicting the impact of AEVs on traffic flow. Consequently, this chapter first covers a brief overview of EMSs that are categorized into three types including rule-based, optimization-based, and learning-based. Some preliminaries on the ACC system are discussed subsequently, with a focus on its spacing policy, control algorithm, and more sophisticated variants including

cooperative ACC (CACC) and ecological ACC (EcoACC). According to different ranking schemes, multi-objective optimization approaches are categorized into two classes, i.e., scalarization methods and Pareto methods. Finally, representative microscopic traffic models in the literature are summarized and compared between and within groups (i.e., kinematics-based and dynamics-based).

Part I: To optimize the driving and powertrain systems of AEVs
Part I of this thesis, consisting of Chapters 3 and 4, is devoted to exploiting the potential of multi-objective optimization (MOO) in component sizing and controller design of AEVs.

Chapter 3: This chapter explores the optimal component sizing for a flex-fuel hybrid powertrain that runs on multiple energy sources including grid electricity, gasoline, and ethanol, aiming to improve its energy efficiency, GHG emissions, and cost-effectiveness. In particular, the empirical ethanol-gasoline blend model is incorporated into the powertrain simulation. We can therefore develop a full picture of the use-phase well-to-wheel (WTW) GHG emissions from ethanol, gasoline, and grid electricity and their energy consumptions. The outcomes of this chapter have been published in *Applied Energy* [29].

Chapter 4: This chapter performs the integrated calibration of control systems including ACC and EMS for AEVs, to simultaneously enhance energy efficiency, ride comfort, and tracking capability. To this end, the augmented system dynamics is introduced to account for the longitudinal driving control and the hybrid powertrain operation. In addition, we compare optimal solutions resulting from different optimization approaches, namely, Pareto frontier and weighted-sum. This work has been published in *IEEE Transactions on Transportation Electrification* [73] and selected as *Front Cover Paper* for Volume 6, Issue 1, 2020 of this journal.

Part II: To model the driving behaviours of AEVs in microscopic traffic simulation

The second part of the thesis, including the following three chapters, focuses on developing microscopic traffic models for describing the observed driving behaviour of AEVs.

Chapter 5: This chapter proposes the first microscopic free-flow model that can explicitly account for the EVs' acceleration and deceleration characteristics in traffic simulation. The developed model is exhaustively validated using in-lab measurements (on a chassis dynamometer), on-road driving trajectories, and vehicle technical specifications. This work has been published in *Transportation Research Record* [74] and awarded *Best Simulation Application Paper* at the Transportation Research Board (TRB) 99th Annual Meeting held in January 2020 in Washington DC, US.

Chapter 6: This chapter proposes a generic approach to extend any of the (free-flow or car-following) microscopic models to capture the impacts of road geometry (e.g., slope and curvature) on driving behaviours of low-level automated vehicles (AVs). To demonstrate its benefit in improving model accuracy, the extended models are calibrated and cross-validated against data sets, which contain empirical trajectories of commercial adaptive cruise control (ACC) systems on different test tracks. This work has been submitted to *IEEE Transactions on Intelligent Transportation Systems* for peer review.

Chapter 7: This chapter investigates the accuracy and robustness of behavioural car-following (CF) and adaptive cruise control (ACC) models to simulate observed driving behaviours of commercial ACC vehicles. To this aim, a general modelling framework is proposed, in which ACC and CF models are incrementally augmented with physics extensions; namely, perception delay, linear or nonlinear vehicle dynamics, and acceleration constraints. The developed models are assessed and compared through a vast calibration and validation experiment against measured trajectory data of low-level automated vehicles (AVs). The findings of this work have been submitted to *Transportation Research Part C: Emerging Technologies* for peer review.

Part III: To evaluate AEVs in real-world driving conditions
This part comprises Chapters 8 and 9 and evaluates the energy and safety performances of ACC vehicles in real-world driving conditions including public roads and test tracks.

Chapter 8: In this chapter, to examine the difference in driving behaviour between ACC vehicles and human-driven vehicles (HDVs), we perform automated (comprising only ACC vehicles) and mixed (consisting of both ACC vehicles and HDVs) platoon

experiments on public roads. It is the first study to investigate the energy and safety performances of commercial ACC systems in real-world car-following scenarios. The outcomes of this work have been published in *European Transport Research Review* and awarded *Best Research Paper* at the 8th Transport Research Arena (TRA) held in April 2020 in Helsinki, Finland.

Chapter 9: This chapter, for the first time, systematically investigates the energy impacts of different time-gap settings of commercial ACC systems in platooning experiments performed on test tracks. To this end, different platoons consisting of 5-7 ACC-equipped vehicles are employed to conduct both speed perturbation and cruising experiments on two test tracks of the ZalaZone proving ground. The outcomes of this work are included as part of a manuscript that has been published in *Transportation Research Part C: Emerging Technologies*.

Chapter 10: In this chapter, the thesis is concluded with major findings and some recommendations for future research.

2 Literature review

This chapter reviews existing studies on automated and electrified vehicles (AEVs) from four perspectives, including energy management strategies (EMSs) for hybrid powertrain operation, adaptive cruise control (ACC) systems for low-level automated driving, multi-objective optimization methods in the development of AEVs, and microscopic traffic models for understanding the vehicle behaviour and its impact on traffic flow dynamics.

The remainder of this chapter is organised as follows. Section 2.1 describes the rule-based, optimization-based, and learning-based EMSs in the literature. Section 2.2 gives some preliminaries on ACC, cooperative ACC (CACC), and ecological ACC (EcoACC). Section 2.3 reviews multi-objective optimization approaches in the development of AEVs, including scalarization and Pareto methods. In Section 2.4, microscopic traffic models are presented, which are grouped into two types, i.e., kinematics-based and dynamics-based.

2.1 Energy management strategies (EMSs) for electrified powertrain

As discussed in Figure 1.4, hybrid powertrain architectures are enabled by multiple energy sources, e.g., gasoline/diesel and electricity, as well as multiple power sources, e.g., the internal combustion engine (ICE) and the electric motor (EM), allowing for more degrees of freedom to supply vehicle's power or torque demand. In this way, hybrid propulsion systems can fully leverage the synergistic benefits of different components, some of which are elaborated as follows.

- The lithium-ion battery represents the most widely used electric energy storage module because of its high energy densities [75], both gravimetric and volumetric. However, its relatively low power density often results in an oversizing, and thus the excess cost, of the battery pack, in order to deal with high power transients in real-world driving scenarios [76]. Furthermore, increased load frequency is reported to reduce battery durability [77].

- The ultracapacitor, on the other hand, has received increasing attention in automotive propulsion [78] mainly due to its high power density, fast charge, and

wide operational range. In the recent study by Zhang et al. [79], the energy storage system comprising batteries and ultracapacitors is demonstrated to prolong battery life and reduce the system weight and manufacturing cost.

- The ICE can use liquid fuels and act as an onboard charging device [80] to address the limitations of electric energy storage devices (e.g., batteries and ultracapacitors), such as range anxiety and lack of charging infrastructure. In addition, various techniques, e.g., ethanol-gasoline blends and engine downsizing, have been employed to make ICEs greener, cleaner, and more efficient [81].

Consequently, the problem of balancing power distribution among multiple onboard components is referred to as energy management [82]. Energy management strategies (EMSs) are related algorithms to solve this problem, usually aiming to improve fuel economy, emissions, and driving mobility [83]. Generally, EMS can be categorized into three broad groups, namely, rule-based, optimization-based, and learning-based strategies [84, 85], which are elaborated as follows.

2.1.1 Rule-based (RB) EMSs

Rule-based (RB) energy management strategies (EMSs) describe a set of rules, which can generate power or torque split control signals according to preset thresholds for state or input variables [82]. These thresholds are usually determined through optimal control analysis based on specific driving cycles, e.g., New European Driving Cycle (NEDC) and Worldwide Harmonised Light Vehicle Test Cycles (WLTC) [86, 87]. RB strategies can hardly achieve optimal control in real-world driving conditions because they are devised for a particular set of driving cycles [82]. Over the past decades, however, they are dominant industrial practices for the energy management of HEVs and PHEVs because these approaches are easy to implement and understand [88]. RB EMSs can be further divided into two types, i.e., deterministic strategies and fuzzy logic (FL) strategies [89].

1) Deterministic strategies

Energy management strategies (EMSs) with deterministic rules mainly include thermostat strategy, power following strategy, and charge depleting - charge sustaining (CD–CS) strategy [82, 89]. The thermostat (or on-off) strategy exerts control by switching the ICE on or off to maintain the battery state-of-charge (SoC) between the predefined upper and

lower bounds [90]. After being switched on, the ICE keeps running at the optimal region with high energy efficiency and low emissions. The power following strategy, adopted by production HEVs including Honda Insight and Toyota Prius, uses the battery as a power buffer to smooth rapid load fluctuations so that the ICE can operate in energy-efficient regions to satisfy the smoothed power demand [91]. The CD-CS strategy is a widely used EMS in PHEV studies and consists of the following two modes [82]. Charge depleting mode aims to exhaust the all-electric range (AER) at the beginning of the trip, and therefore, prioritizes the use of the EM over the ICE. The ICE only operates if the vehicle's power demand exceeds the limits of the EM [92]. Charge sustaining (CS) mode, to which the PHEV switches after the battery has reached the minimum SoC threshold, uses a combination of engine and motor management to maintain the battery SoC at a specified level and at the same time meet the vehicle's power demand [86].

2) Fuzzy logic (FL) strategies

Energy management strategies (EMSs) with fuzzy rules are able to account for numerical uncertainties and high-level linguistic knowledge [89]. Therefore, FL-based EMSs have the advantage that the solution to the problem can be converted into terms that human operators can understand, so that their experience can be used in the design of the controller, making it easier to mechanize tasks that are already successfully performed by humans [93]. For example, an EMS based on FL methods is proposed for a series-parallel hybrid electric bus and can simultaneously handle two tasks, namely, mode switching (between the series and parallel modes) as well as instantaneous power distribution, reducing the energy consumption by 30.3% compared to the conventional approach [94]. Through the vehicle simulation platform ADVISOR, an adaptive fuzzy inference system is developed for the energy management of a parallel hybrid powertrain and reported to strike a good compromise between fuel economy, emissions, and drivability [95].

2.1.2   Optimization-based EMSs

Optimization-based energy management strategies (EMSs) formulate the power/torque distribution of the hybrid powertrain as an optimization problem with one or more objectives, e.g., fuel economy [96], drivability for comfort [97], battery health [98], tailpipe pollutants [99], and life cycle CO_2 emissions [100]. The industrial usefulness of

optimization-based strategies is currently limited by several technical shortcomings including algorithm complexity, high computation effort, robustness, and sensitivity to driving cycle information and characteristics [101]. However, many previous studies have demonstrated that these strategies are superior to rule-based ones, and therefore, a plethora of optimization-based algorithms have been proposed for the energy management of hybrid vehicles and validated in simulation environments or experimental platforms [82].

Dynamic programming (DP) breaks the energy management problem down into a sequence of decision steps over time and guarantees global optimality through an exhaustive search of all control and state grids [90]. However, its computational burden increases exponentially as the dimensionality of the search space increases, also known as "curse of dimensionality" [102]. Moreover, it requires prior knowledge of the entire driving cycle, which is not available in real scenarios [103]. Due to these limitations, DP-based strategies usually serve as the offline benchmark, instead of the real-time control method [82].

To overcome deficiencies of DP-based EMSs, intensive efforts have been devoted to developing real-time optimization-based strategies [104], e.g., equivalent consumption minimization strategy (ECMS) [105] and model predictive control (MPC) [96]. Particularly, as one of the most promising optimization-based strategies for real-time energy management problems, MPC determines the control action by solving the optimal control problem over a finite horizon [106]. This technique can handle linear or nonlinear system dynamics, equality or inequality constraints, and multiple inputs, outputs, or objectives, which make it attractive to the automotive industry [107].

2.1.3   Learning-based EMSs

Because of the ability to automatically improve through experience (also known as data-driven optimization) [108], machine learning (ML) techniques, e.g., neural network (NN) and reinforcement learning (RL), have recently attracted extensive interest as EMSs [109].

NN consists of multiple layers of artificial neurons that are interconnected via edges, where each edge is assigned a weight (representing its relative importance) and each neuron has a bias term and an activation function [110]. In the learning process, the weights are adjusted using training data and the error backpropagation algorithm to minimize the loss function [82]. For instance, two NN modules are employed to minimize the energy consumption of a power-split PHEV, where the training data is derived from DP methods

in various driving conditions [111]. In addition, an NN-based framework is developed to predict the short-term driving environment (e.g., road type and congestion level) and generate control signals for energy management of the HEV [112, 113].

In RL methods, an agent (e.g., EMS) learns how to map input states to optimal control actions (or outputs), typically through a trial and error search process, to maximize the cumulative reward (e.g., fuel economy) [109]. For example, a multi-step RL strategy is proposed for model-free predictive energy management of an off-highway HEV, leading to significant energy savings (more than 7.8%, compared with the MPC strategy) [114]. A double Q-learning strategy is developed for energy management of HEVs in the charge sustaining (CS) mode and demonstrates improved fuel economy and strong learning robustness [115]. A nested RL-based framework is presented to minimize the operating cost of an HEV, in which the inner and outer loops focus on optimizing the fuel cost and the battery replacement cost, respectively [116].

2.2 Adaptive cruise control (ACC) systems for automated driving

Corresponding to Level 1 driving automation as defined by the international standard SAE J3016 (shown in Figure 1.2), adaptive cruise control (ACC) systems have reached the consumer market for over two decades [117, 118]. As presented in Figure 2.1 (a) and (b), these systems are enabled by radar sensors and used to automatically maintain a desired inter-vehicle spacing in congested traffic or a constant speed in free-flow traffic, which potentially improve the safety, capacity, and fuel economy of road transport [119, 120].

Figure 2.1 (c) illustrates the longitudinal kinematics for ACC implementation, which is important for the control problem formulation and can be described by

$$
\begin{cases}
a_n(t) = \dot{v}_n(t) = \ddot{x}_n(t), \\
v_{n-1}(t) = \dot{x}_{n-1}(t), \\
a_{n-1}(t) = \dot{v}_{n-1}(t), \\
s_n(t) = x_{n-1}(t) - x_n(t) - l_{n-1}, \\
\Delta x_n(t) = x_{n-1}(t) - x_n(t), \\
\Delta s_n(t) = s_n(t) - s_{n,des}(t), \\
\Delta v_n(t) = v_{n-1}(t) - v_n(t),
\end{cases}
\tag{2.1}
$$
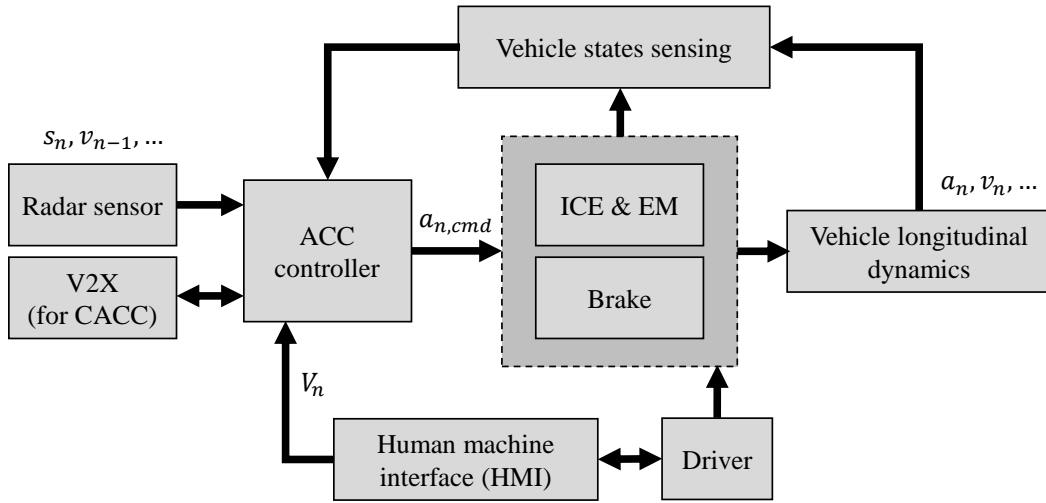
(a) **Control architecture of an ACC system.**
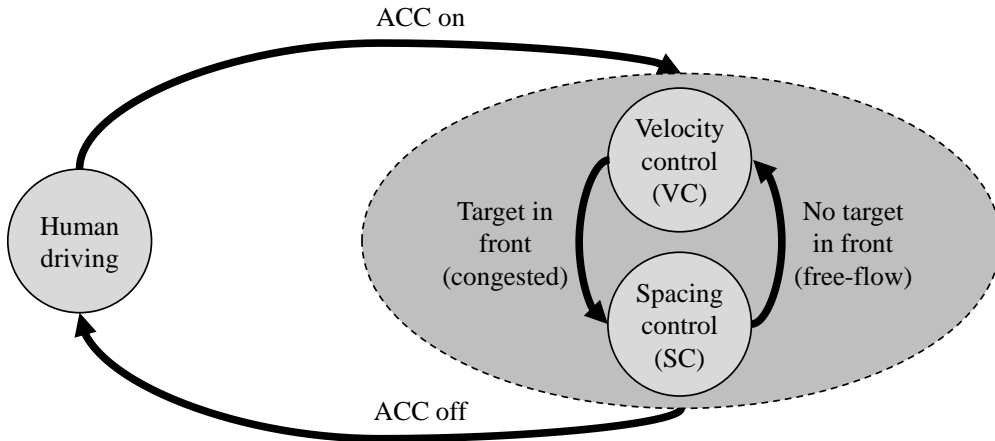
(b) **Operation modes of an ACC system.**
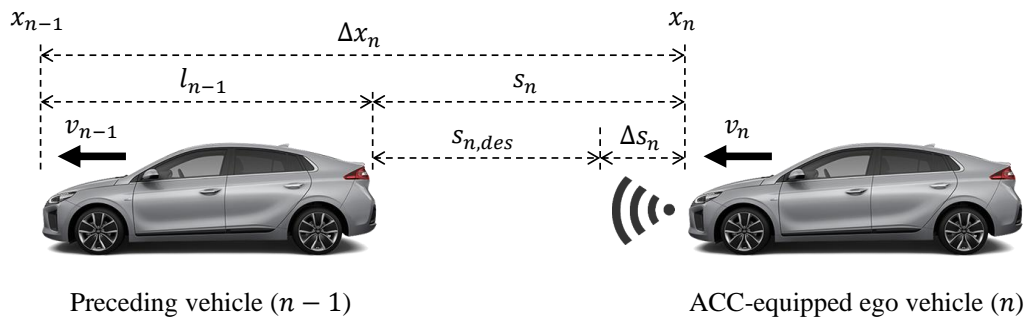
(c) **Longitudinal kinematics for ACC implementation.**

Source: Adapted from Bu et al. [121], Li et al. [106], Wang [122], Bernsteiner [123].
Note: V2X = vehicle-to-everything; ACC = adaptive cruise control; CACC = cooperative adaptive cruise control; ICE = internal combustion engine; EM = electric motor.

Figure 2.1 Overview of an adaptive cruise control (ACC) system.

where subscripts n and $n-1$ represent the ego and the preceding vehicles, respectively; x, v, and a are the vehicle's longitudinal position (m), speed (m/s), and acceleration (m/s^2), respectively; t denotes time (s); l means the vehicle length (m); s_n is the spacing (m) between the front bumper of the ego vehicle and the back bumper of the preceding one; $s_{n,des}$ is the desired spacing determined by the spacing policy inherent in the ACC system; Δx_n is the headway (m); Δs_n represents the spacing error (m) between the actual and desired values; Δv_n is the relative speed (m/s) between the preceding and ego vehicles.

In the remainder of the section, we revisit the literature on spacing policies and control algorithms of ACC systems, followed by a review of studies on cooperative ACC (CACC) and ecological ACC (EcoACC), both of which are more sophisticated variants of ACC.

2.2.1 ACC spacing policies

The spacing policy of ACC determines the desired spacing ($s_{n,des}$) in Equation (2.1) and plays a crucial role in driving safety, traffic throughput, and string stability [124]. String stability means disturbances (e.g., spacing error Δs_n and relative speed Δv_n) of an individual vehicle in a platoon (or vehicle string) do not amplify when they propagate upstream [125].

In previous studies, prevailing spacing policies can be grouped into three types including constant distance (CD), constant time headway (CTH), and nonlinear distance (NLD), as detailed below [106].

1) Constant distance (CD)

In the CD policy, the desired inter-vehicle spacing ($s_{n,des}$) is independent of the driving environment [126, 127], i.e.,

$$s_{n,des}(t) = s_0, \tag{2.2}$$

where s_0 is a positive constant (m). Although potentially increasing traffic capacity [128], this policy cannot guarantee string stability unless the leading vehicle broadcasts its information (e.g., speed and acceleration) via V2V communication to all other vehicles in the platoon [129].

2) Constant time headway (CTH)

In the CTH policy, which is widely used in commercial ACC systems, the desired spacing ($s_{n,des}$) varies as a linear function of the ego vehicle speed (v_n) [130], i.e.,

$$s_{n,des}(t) = s_0 + t_h v_n(t), \tag{2.3}$$

where t_h is the time headway (s) and s_0 is the minimum (or standstill) spacing. This policy is to some extent similar to that of human driver's behaviour [106] and has been used to develop ACC controllers that can guarantee string stability [131]. The major drawback of the CTH policy, however, is poor robustness against traffic flow fluctuation [132, 133].

3) Nonlinear distance (NLD)

In the NLD policy, the desired spacing ($s_{n,des}$) is a nonlinear function of one or multiple state variables (e.g., v_n, v_{n-1}, x_n, and x_{n-1}) associating with the driving environment, the generic mathematical formulation of which can be represented as

$$s_{n,des}(t) = g\big(v_n(t), v_{n-1}(t), x_n(t), x_{n-1}(t), ...\big), \tag{2.4}$$

NLD spacing policies are expected to outperform CD and CTH policies in enhancing both traffic flow stability and traffic capacity [134]. For instance, an NLD policy is developed based on Greenshield's speed-density relationship and demonstrates superior stability and safety properties [132], as given by

$$s_{n,des}(t) = \frac{1}{\rho_{max}\left(1 - \frac{v_n(t)}{v_{free}}\right)} - l_{n-1}, \tag{2.5}$$

where ρ_{max} and v_{free} denote the jam density and free-flow speed of the traffic, respectively [124]. Another NLD spacing policy, which includes a quadratic term of ego vehicle speed (v_n), is proposed and optimized to improve both string stability and traffic flow stability [133], as described by

$$s_{n,des}(t) = 3 + 0.0019 v_n(t) + 0.0448 v_n(t)^2. \tag{2.6}$$

More complicated NLD policies have been discussed in the literature. For example, a safe distance policy is reported to take into account the vehicles' braking capability [135, 136], which can be mathematically expressed as

$$s_{n,des}(t) = s_0 + \tau v_n(t) - \left(\frac{v_n(t)^2}{2a_{min}} - \frac{v_{n-1}(t)^2}{2\hat{a}_{min}} \right), \tag{2.7}$$

where s_0 is the minimum (or standstill) spacing (m); τ is the time constant (s); both a_{min} and $\hat{a}_{min}$ are negative constants (m/s^2), representing the braking capabilities of the ego (n) and preceding ($n-1$) vehicles, respectively.

2.2.2 ACC control algorithms

As shown in Figure 2.1 (b), the ACC system usually operates in two modes, i.e., spacing control (SC, in congested traffic) and velocity control (VC, in free-flow traffic) [122]. The transition between these two modes can be determined by a fixed spacing threshold such as the maximum unambiguous range (MUR) of the radar [137, 138], i.e.,

$$a_{n,cmd}(t) = \begin{cases} a_{n,cmd}^{VC}(t), & s_n(t) > s_{th}, \\ a_{n,cmd}^{SC}(t), & s_n(t) \leq s_{th}, \end{cases} \tag{2.8}$$

where s_{th} is the spacing threshold (m); $a_{n,cmd}$ is the final acceleration command (m/s^2) adopted by the ACC system; while $a_{n,cmd}^{VC}$ and $a_{n,cmd}^{SC}$ are acceleration commands (m/s^2) generated in the VC and SC modes, respectively. Alternatively, most previous studies implicitly implement the mode transition by comparing acceleration commands of two modes, in which the more restrictive choice is adopted [139, 140], i.e.,

$$a_{n,cmd}(t) = \min \left(a_{n,cmd}^{VC}(t), a_{n,cmd}^{SC}(t) \right). \tag{2.9}$$

In free-flow traffic, the ACC velocity control (VC) mode regulates the throttle and brake paddles to follow the set speed, which is specified in advance by the driver via human machine interface (HMI) [118]. This mode is usually accomplished by a linear proportional controller [73, 139, 138], as given by

$$a_{n,cmd}^{VC}(t) = k_0 \left(V_n - v_n(t) \right), \tag{2.10}$$

where k_0 is a positive coefficient (s^{-1}) and V_n is the set speed (m/s) of the ACC system.

In congested traffic, the ACC spacing control (SC) mode aims to maintain a desired inter-vehicle spacing ($s_{n,des}$), which is determined by the spacing policy as previously discussed. In the literature, the development of ACC algorithms is mainly focused on this control mode since congested traffic is a much more challenging environment for ACC operation [122]. Typical ACC spacing control algorithms will be presented as follows.

1) Linear controller

The linear controller is probably the most widely used ACC spacing control (SC) method in either academia or industry because it can facilitate theoretical analyses and hardware implementations [122, 141, 106]. A generic form of linear ACC controller is described by

$$a^{SC}_{n,cmd}(t) = k_s \Delta s_n(t) + k_v \Delta v_n(t), \tag{2.11}$$

where Δs_n and Δv_n are the spacing error (between the actual and desired spacing values) and the relative speed (between the preceding and ego vehicles), respectively, as given by Equation (2.1); while k_s and k_v are positive coefficients (s^{-2} and s^{-1}, respectively). The linear ACC control law using simple spacing policies, e.g., constant distance (CD) or constant time headway (CTH), cannot guarantee collision-free at safety-critical (e.g., approaching a standstill vehicle at high speeds) or dense traffic conditions [137, 142, 143]. In these conditions, the ACC system is switched off in practice [122].

2) Model predictive control (MPC)

Advanced ACC systems usually have multiple design objectives, e.g. minimizing tracking error (also known as spacing regulation error), preserving string stability, increasing ride comfort, and improving fuel economy, some of which are contradictory [144]. In addition, there are often multiple constraints imposed on ACC design solutions, e.g., actuator (the brake and throttle pedals) limit and safety limit [121]. MPC is a control framework that can optimize multiple objectives under different design constraints, and therefore, the MPC-based ACC is usually formulated as a constrained optimization problem [145]. However, existing MPC algorithms suffer from a high computational load [144].

In the literature, a hybrid MPC approach is used to design ACC systems that can improve safety and tracking capability [146, 147]. An MPC-based ACC system is proposed to explicitly include acceleration constraints to meet comfort and safety needs [148]. In addition, a multi-objective MPC-based ACC system is developed to simultaneously address multiple critical issues, including tracking capability, fuel economy, and driver desired response, in which limits on both acceleration and jerk are applied to guarantee ride comfort of the vehicle [144].

3) Sliding mode control (SMC)

SMC is a variable structure control method, which can switch back and forth between two continuous control laws based on the current position in the state space [149]. This switching approach makes SMC robust to nonlinear vehicle dynamics, actuator constraints, and external disturbances [150]. However, the main obstacle for its implementation is the chattering problem (the phenomenon of finite-frequency, finite-amplitude oscillations) [151]. There are some studies employing SMC algorithms to design ACC systems. For example, an ACC system based on the SMC algorithm and the CTH spacing policy is proposed, which can detect the presence of possible hazards in front of the vehicle and then switch between two spacing control modes, i.e., adaptive cruise mode and collision avoidance mode [152]. Similar SMC-based ACC systems are developed to overcome bounded disturbances under different spacing policies [153].

4) Fuzzy logic (FL) controller

In the literature, FL-based ACC systems are proposed in several studies. For instance, an FL-based ACC system adopting the CTH spacing policy is reported to guarantee string stability [154]. An adaptive FL method is used to develop the ACC system that can emulate human drivers' behaviour [155]. Another fuzzy controller is developed for both high-level (to maintain safe spacing) and low-level (to adjust the throttle and brake pedals) control tasks, exhibiting a good performance at a broad range of speeds [156].

2.2.3 Cooperative ACC (CACC)

Using V2V and V2I communications, CACC extends ACC to achieve cooperative manoeuvres [139]. A series of CACC studies, in terms of controller design, stability

analysis, and real-world driving experiments, have been conducted in the California Partners for Advanced Transit and Highways (PATH) program [157, 158]. With the connectivity between vehicles, CACC allows the vehicle to maintain smaller headway compared to ACC [159].

By sharing vehicle operating states, e.g., position, speed, and emergency braking, in a distributed manner, CACC vehicles within a certain geographic area can cooperate with each other, which can maximize the benefits of automated driving in the following ways [160]. First, driving safety is enhanced because the downstream traffic information can be broadcasted to upstream vehicles in advance and therefore the actuation delay is significantly reduced [122]. Second, road capacity is increased owing to the reduced time (or distance) headway between consecutive vehicles [118]. Finally, energy economy and pollutant emissions are improved because both unnecessary speed changes and aerodynamic drag can be reduced [160].

In addition, based on CACC and ACC, the platoon control techniques have attracted extensive interest for decades. Typical research topics of platoon control include spacing policies [161, 133], string stability [162, 163], dynamics heterogeneity [164, 165], time delays [166, 167], communication topologies (e.g., bidirectional) [168, 106], etc.

2.2.4 Ecological ACC (EcoACC)

Increasing concerns over energy consumption and GHG emissions are giving rise to the development of EcoACC [169], which regulates the individual vehicle's speed by minimizing not only spacing error (Δs_n) and relative speed (Δv_n) but also fuel consumption. Most studies on EcoACC focus on internal combustion engine vehicles (ICEVs). For example, using road grade information provided by the high-definition (HD) map, predictive EcoACC systems are proposed to control the inter-vehicle spacing in an energy-efficient manner [170–172].

On the other hand, a few efforts are being made to develop EcoACC systems for HEVs and PHEVs, which can leverage the synergistic benefits of ACC and EMS in improving energy efficiency and exhaust emissions. For instance, a multi-objective EcoACC system is proposed to simultaneously improve fuel economy and ride comfort for an HEV, which adopts a rule-based (RB) energy management strategy (EMS) [173]. Another EcoACC system designed for PHEVs can use the traffic light information to predict the future

trajectory of the preceding vehicle, and then provides optimal speed and power control signals, which can minimize the fuel consumption and satisfy the constraints associated with the vehicle's safety and comfort [174]. By combining an ACC based on action dependent heuristic dynamic programming (ADHDP) and an adaptive EMS, an EcoACC system is developed to achieve near-optimal fuel economy and comfortable driving [175].

2.3 Multi-objective optimization in the development of AEVs

In the development of AEVs, it is necessary to address various needs, e.g., energy efficiency, safety, ride comfort, and traffic throughput [174, 97, 176]. Therefore, different methods are proposed to solve the multi-objective optimization problems in the system design.

2.3.1 Scalarization methods

Scalarization methods (e.g., weighted-sum) aggregate multiple objectives into a single cost function that is then minimized [177]. For example, Zhou et al. [178] developed a particle swarm optimization (PSO) algorithm utilized in the optimal PHEV sizing. In this algorithm, the single cost function aims to minimize the overall volume and maximize energy efficiency. Moreover, Vajedi and Azad [179] proposed an EcoACC system based on nonlinear model predictive control (NMPC). In this system, the safety and the energy targets are integrated into a cost function using a two-dimensional (2D) weight vector.

The scalarization methods cannot, however, determine the weights and the normalization factors that can optimally balance and scale the multiple objective functions for a problem with little or no information [180], which can cause misleading optimization results. For example, in a study on multi-objective ACC and EMS co-optimization [181], the weighted-sum method leads to an over-optimized fuel economy (a fuel saving of 7.07%), which in turn compromises other attributes such as tracking safety (a tracking error increase of 10.5%).

2.3.2 Pareto methods

To address limitations of scalarization methods, Pareto methods offer a set of Pareto-optimal (or non-dominated) solutions [182], where no single solution is better than another in every criterion [183]. For instance, Zhang et al. [79] have employed a non-dominated

sorting genetic algorithm (NSGA) to reduce the manufacturing cost of the energy storage system and prolong battery life for PHEVs. Although incurring a greater computational cost, Pareto methods can provide the performance boundaries and relationships (e.g., conflicting or harmonious) of the objective functions, which are important inputs to the system design process [73].

2.4   Microscopic traffic models to describe vehicle behaviour

Unlike ACC models, which are discussed in Section 2.2 and developed to control the vehicle's longitudinal driving behaviour through mechanical (e.g., ICE, EM, and brake system) and electrical (e.g., radar and camera) components, microscopic car-following (CF) models focus on describing the resulting vehicle behaviour and then estimating its impact on traffic flow dynamics in traffic simulation [184]. Traffic flow theory and microscopic traffic simulation are indispensable tools to maximize the benefits of automated, connected, electrified, and shared (ACES) vehicles to the road network [185].

From the perspective of motion description, existing CF models can be categorized into two groups, namely, kinematics-based (or behavioural) and dynamics-based [186]. The former is simple and concerns only variables derived from trajectories of vehicles, e.g., position, spacing, speed, and acceleration. The latter, however, can take into account variables underlying the vehicle movement, e.g., forces, torque, and energy [74]. It is worth noting that both types of CF models should be able to strike a balance between simplicity and accuracy and therefore feasible for large-scale traffic simulation [187].

2.4.1   Kinematics-based (or behavioural) car-following (CF) models

Kinematics-based (or behavioural) CF models describe the movement of the following vehicle as a function of its kinematic relationship to the preceding vehicle, as depicted in Figure 2.1 (c), and, in the last seven decades, have been studied intensively by model simulation, experimental campaign, and traffic observation [188].

Table 2.1 Typical kinematics-based (or behavioural) car-following (CF) models.

Model	Year	Acceleration or speed equations	Parameters
Reuschel [189]	1950	$v_n(t) = c \cdot s_n(t),$	c
Pipes [190]	1953	$a_n(t) = c \cdot \Delta v_n(t),$	c
Gazis et al. [191] - GHR	1961	$a_n(t+\tau) = c \cdot v_n(t+\tau)^m \cdot \Delta v_n(t)/\left(\Delta x_n(t)\right)^l,$	τ, c, m, l
Newell [192]	1961	$a_n(t) = c \cdot \left(\Delta x_n(t)\right)^l,$ or $a_n(t) = \frac{1}{\tau}\left[V_{opt}(t) - v_{n-1}(t)\right],$ where $V_{opt}(t) = V_n \cdot \left[1 - e^{-\frac{c}{V_n}\left(\Delta x_n(t) - s_0\right)}\right],$	c, l or c, s_0
Bierley [193]	1963	$a_n(t) = \alpha \cdot \Delta v_n(t) + \beta \cdot \left(\Delta x_n(t)\right)^l,$	α, β, l
Gipps [194]	1981	$v_n(t+\tau) \;=\; \min\left\{ v_n(t) + 2.5 a_{max}\tau \cdot \left(1 - \frac{v_n(t)}{V_n}\right)\left(0.025 + \frac{v_n(t)}{V_n}\right)^{0.5}, \right.$ $\left. a_{min}\tau + \sqrt{a_{min}^2\tau^2 - a_{min} \cdot \left[2\left(\Delta x_n(t) - s_0\right) - \tau v_n(t) - \frac{v_{n-1}(t)^2}{\hat{a}_{min}}\right]}\right\},$	$\tau, s_0, a_{max},$ $a_{min}, \hat{a}_{min}$
Leutzbach et al. [195]	1986	$a_n(t+\tau) = \frac{\left(\Delta v_n(t)\right)^2}{2\left(\Delta x_n(t) - s_{safe}\right)} + a_{n-1}(t),$	τ, s_{safe}
Sultan et al. [196]	2004	$a_n(t+\tau) = c \cdot v_{n-1}(t)^m \cdot \frac{\Delta v_n(t)}{\left(\Delta x_n(t)\right)^l} + k_1 a_{n-1}(t) + k_2 a_n(t),$	$\tau, c, m,$ k_1, k_2
Bando et al. [197] - OV	1995	$a_n(t) = c \cdot \left[V_{opt}(t) - v_n(t)\right],$ where $V_{opt}(t) = \frac{V_n}{2}\left[\tanh\left(\Delta x_n(t) - s_0\right) + \tanh(s_0)\right]$	c, s_0
Helbing et al. [198] - GFM [a]	1998	$a_n(t) = c \cdot \left[V_{opt}(t) - v_n(t)\right] + \lambda \cdot H\left(-\Delta v_n(t)\right) \cdot \Delta v_n(t),$ where $V_{opt}(t) = V_1 + V_2\tanh\left[k_1 s_n(t) - k_2\right],$	$c, \lambda, V_1,$ V_2, k_1, k_1
Treiber et al. [199] - IDM	2000	$a_n(t) = a_{max} \cdot \left[1 - \left(\frac{v_n(t)}{V_n}\right)^\delta - \left(\frac{s_{n,des}(t)}{s_n(t)}\right)^2\right],$ where $s_{n,des}(t) = s_0 + \max\left[0, t_h v_n(t) - \frac{v_n(t)\Delta v_n(t)}{2\sqrt{-a_{max}\cdot a_{min}}}\right],$	$\delta, t_h, s_0,$ a_{max}, a_{min}
Jiang et al. [200] - FVDM	2001	$a_n(t) = c \cdot \left[V_{opt}(t) - v_n(t)\right] + \lambda \Delta v_n(t),$	c, λ

[a] $H(\cdot)$ is Heaviside function.

Source: Adapted from Chen et al. [201, 202], Reuschel [189], and Gipps [194]

Note: Subscripts n and $n-1$ indicate the ego and preceding vehicles, respectively; $\Delta x_n(t) = x_{n-1}(t) - x_n(t)$ is the headway (m); $\Delta v_n(t) = v_{n-1}(t) - v_n(t)$ is the relative speed (m/s); $s_n(t) = x_{n-1}(t) - x_n(t) - l_{n-1}$ is the spacing (or gap, m); V_n is the free-flow (or desired) speed; GHR = Gazis-Herman-Rothery model; OV = optimal velocity model; GFM = generalized force model; IDM = intelligent driver model; FVDM = full velocity difference model.

In Table 2.1, typical kinematics-based CF models are listed chronologically with the deterministic acceleration or speed equation and the associated parameters given in the last two columns [201]. In the early 1950s, Reuschel [189] and Pipes [190] did pioneering work on the development of behavioural CF models. Their model formulations only consider either the inter-vehicle spacing (s_n) or the relative velocity (Δv_n, between the preceding and ego vehicles), and therefore, have significant limitations in describing the vehicle behaviour [203]. The Gazis–Herman–Rothery (GHR) model, proposed by Gazis et al. in 1961 [191], defines a nonlinear acceleration equation that considers reaction time (τ) [185]. However, it is built upon strong assumptions, leading to critical drawbacks that are frequently reported by researchers, for example, the model overestimates the vehicle's ability to perceive small changes in the relative speed (Δv_n) and the headway (Δx_n) [204, 205]. Newell's model assumes that the following vehicle's response directly depends on the headway (Δx_n) [192], which, however, might result in unrealistic acceleration behaviour [206].

As a major milestone towards the development of safety distance (or collision avoidance) CF models [206], Gipps model [194] developed in 1981 has been extensively studied [207]. It describes the vehicle speed in a way assuming that the driver leaves enough safe distance in front and thus can safely stop the vehicle in case the preceding vehicle commences an emergency brake [208]. Similar to ACC models given in Equation (2.9), Gipps model consists of two driving regimes, i.e., free-flow and congested, and chooses the more restrictive one from the resulting speeds of these two regimes [209].

The optimal velocity (OV) model, proposed by Bando et al. [197], assumes that the vehicle attempts to follow an optimal (or safe) speed (V_{opt}) that depends on the headway (Δx_n). This model has received considerable attention because of its ability to accurately describe many traffic flow characteristics in the real world, e.g., traffic instability, traffic congestion evolution, and the formation of stop-and-go waves. However, a comparison between the simulated and observed vehicle trajectories indicates that the OV model exhibits significantly high acceleration and unrealistic deceleration [210]. To overcome this limitation, Helbing et al. adopted the basic concept of the OV model, utilized negative velocity difference, and developed the generalized force model (GFM), which demonstrates a good agreement with empirical trajectory data [198], but is poor in predicting the delay time of vehicle movement [210]. Consequently, Jiang et al. [200] modified GFM in 2001

by including the negative and positive velocity differences and then proposed the full velocity difference model (FVDM) [210].

The intelligent driver model (IDM), proposed by Treiber et al. [199] in 2000, is a breakthrough in the development of desired measure CF models, which usually assume that vehicles aim to simultaneously reach both the desired (or free-flow) speed (V_n) and the desired spacing ($s_{n,des}$). Its acceleration equation can ensure a smooth transition between the free-flow and congested driving regime [206]. Nevertheless, IDM does not provide a lower bound for the acceleration, and therefore, may lead to unrealistic large deceleration when the inter-vehicle spacing (s_n) drops significantly (e.g., in cut-in manoeuvres) [211].

2.4.2 Dynamics-based car-following (CF) models

Dynamics-based CF models take into account features, e.g., force, torque, and power, underlying the vehicle movement [74]. As summarized in Table 2.2, it has been a growing field across several disciplines in recent years. Relevant publications remain few, almost all of which focus on conventional ICEVs powered by a gasoline or diesel ICE with a multi-ratio transmission. The pioneering work of Searle et al. [212] is crucial to our wider understanding of this area. In their model, however, the full load (FL) engine power (P_{ice}^{FL}) is assumed to be constant and equal to the peak engine power (P_{ice}^{max}) across the entire engine speed range. Also, the dynamics of the internal driveline (e.g., transmission and engine accessories) and external resistances (i.e., aerodynamic, rolling, and grade) are not considered; instead, their effects on the power losses are all incorporated into a constant, i.e., acceleration efficiency (η_a). Moreover, driving behaviour, that is, how the driver utilizes the vehicle's full load capabilities, is not indicated, thus, the model's output is the maximum acceleration characteristics. In the subsequent study by Rakha et al. [213], the enhanced model accounts for detailed dynamics of the driveline and the resistances. Although the full load engine power (P_{ice}^{FL}) is still constant, the tractive force is upper bounded by the maximum force that can be sustained between the vehicle tires and the road surface. Rakha et al. [214] then developed a variable power dynamics model in 2002 by introducing a power adjustment factor (β), which dealt with the full load power reduction caused by the effect of successive gear shifting at low speeds. The factor β is a ramp function (with a positive intercept) of vehicle speed (v_n), when $v_n \leq v_p$ (v_p is the speed at which maximum power occurs).

Table 2.2 Development of dynamics-based car-following (CF) models.

Model	Year	Full load engine power [a]	Driveline & resistances	Gearshift behaviour [b]	Driving behaviour [c]	Collision avoidance [d]	Traffic stability [d]	Model output
Searle et al. [212]	1999	✗ P_{ice}^{max}	✗	✗	✗	✗	✗	Maximum acceleration
Rakha et al. [213]	2001	✗ P_{ice}^{max}	✓	✗	✗	✗	✗	
Rakha et al. [214]	2002	✗ $\beta(v_n)\cdot P_{ice}^{max}$	✓	✗	✗	✗	✗	
Rakha et al. [215]	2004	✗ $\beta(v_n)\cdot P_{ice}^{max}$	✓	✗	✓ w_{db}	✗	✗	Typical acceleration
Rakha et al. [216] - RPA	2009	✗ $\beta(v_n)\cdot P_{ice}^{max}$	✓	✗	✓ t_{db}	✓ $v_{ca}^{lim}(v_{n-1},s_n)$	✓ $v_{ts}^{lim}(V_n,s_n)$	
Rakha et al. [217]	2012	✓ $P_{ice}^{FL}(v_n,\varphi_g)$	✓	✓ w_{gb}	✓ t_{db}	✗	✗	
Fadhloun et al. [218]	2015	✗ P_{ice}^{max}	✓	✗	✓ $t_{db}(v_n,V_n)$	✗	✗	
Fadhloun et al. [219] - FR	2019	✗ $\beta(v_n)\cdot P_{ice}^{max}$	✓	✗	✓ $w_{db}(v_n,v_{n-1},V_n,s_n)$			
Makridis et al. [187] - MFC	2019	✓ $P_{ice}^{FL}(v_n,\varphi_g)$	✓	✓ $w_{gb}(GS)$	✓ $w_{db}(v_n,V_n,DS)$	✗	✗	

[a] The ICE full load power (P_{ice}^{FL}) across the entire operating speed range can be calculated in three ways: 1) P_{ice}^{max}, which is a constant and equal to the peak power that the ICE can produce; 2) $\beta(v_n)\cdot P_{ice}^{max}$, which is a percentage of the ICE peak power; or 3) $P_{ice}^{FL}(v_n,\varphi_g)$, which is a function of the vehicle speed v_n and the engaged gear ratio φ_g.

[b] The gear shifting points within the vehicle speed range are defined by w_{gb} for each driver.

[c] The driver's typical driving behaviour can be represented as a percentage of the vehicle's full load capabilities in two ways: 1) to multiply the full load ICE power curve by a power reduction (or throttle opening) factor, t_{db}; or 2) to multiply the vehicle's acceleration potential curve by an acceleration reduction factor, w_{db}. Both of the above factors can be a constant or a function (the symbol with arguments in parentheses) for each driver.

[d] Collision avoidance and traffic stability, both of which belong to the interaction term (instead of the free-flow term) of the CF model, can be either formulated as speed limit functions (i.e., v_{ca}^{lim} and v_{ts}^{lim}, respectively) or directly incorporated into the driving behaviour function w_{db}.

Source: Adapted from He et al. [74]

Note: β is the full load power adjustment factor for the ICE; v_n and v_{n-1} are speeds of the ego (n) and preceding ($n-1$) vehicles, respectively; V_n is the desired or free-flow speed; s_n is the inter-vehicle spacing (or gap); GS and DS are calibratable parameters capturing gearshift style and acceleration style, respectively; ICE = internal combustion engine; RPA = Rakha-Pasumarthy-Adjerid model; FR = Fadhloun-Rakha model; MFC = microsimulation free-flow acceleration model.

Rakha et al. [215] are the first of many who have attempted to capture typical driving behaviour and vehicle dynamics at the same time. The typical acceleration output is achieved by introducing an acceleration reduction factor (w_{db}), which denotes the ratio of the driver's actual acceleration to the vehicle's theoretical capability. On the other hand, the model proposed in 2009 by Rakha et al. [216] adopts a power reduction factor (t_{db}) aiming to represent the percentage of the throttle opening, and therefore, the power delivered from the engine can be assumed to be equal to a constant percentage of the full load engine power. Additionally, to capture the interaction of vehicles in the traffic flow, the model considers two speed constraints: $v_{ca}^{lim}(v_{n-1}, s_n)$ to avoid any collisions with the preceding vehicle and $v_{ts}^{lim}(V_n, s_n)$ to maintain cruising in the steady-state traffic stream. Rakha et al. [217] developed the first model that explicitly captures the dynamics of engine power and gearshift. This research is critical, given that the full load engine power (P_{ice}^{FL}) during driving cannot be assumed to be constant over the entire vehicle speed range nor to be adjusted by a ramp function (β) at the low-speed region. In fact, it is well known that the engine power at full load conditions varies as a function of the current vehicle speed (v_n) and the engaged gear ratio (φ_g). Moreover, the gearshift behaviour (w_{gb}) in this model is designed as per a fixed engine speed threshold.

The above three typical acceleration models reported by Rakha et al., however, reproduce the driving behaviour (w_{db} or t_{db}) and the gearshift behaviour (w_{gb}) using constant factors, thus they provide limited information in relation to each driver's unique pattern of driving. Recognizing this deficiency, an enhancement proposed in 2015 by Fadhloun et al. [218] made the model representative of different driving patterns. The basic idea behind their research is to employ a variable throttle opening (t_{db}) as a function of the vehicle speed (v_n) and the driver's desired speed (V_n). In 2019, Fadhloun et al. [219] further improved the model by incorporating the two constraints regarding vehicle interactions (i.e., collision avoidance and steady-state traffic stream) into the driving behaviour function $w_{db}(v_n, v_{n-1}, V_n, s_n)$, which serves as an acceleration reduction factor. Makridis et al. [187] demonstrated the first study to account for different drivers' driving behaviour and gearshift behaviour simultaneously, by introducing two calibratable parameters, i.e., driving style (DS) and gearshift style (GS).

Part I

To optimize the driving and powertrain systems of AEVs

3

Optimal sizing of key components for a flex-fuel hybrid powertrain

Concerns over energy efficiency and greenhouse gas (GHG) emissions are driving research investments into advanced propulsion technologies. Plug-in hybrid electric vehicles (PHEVs) can provide a bridge that connects transport electrification to renewable bioenergy sources such as ethanol. However, it remains unclear how this pathway can simultaneously address economic, energy, and environmental goals. To tackle this challenge, the present study explores, for the first time, the multi-objective optimal sizing of a flex-fuel hybrid powertrain enabled by low-carbon energy sources including grid electricity and ethanol-gasoline blend. The empirical ethanol-gasoline blend model is incorporated into the PHEV simulation. We develop a full picture of the use-phase well-to-wheel (WTW) GHG emissions from ethanol, gasoline and grid electricity and their energy consumptions. Consequently, market-oriented PHEV sizing solutions are provided as per the power utility generation portfolio and automobile fuel properties of the target region. The results indicate that better performances of the PHEV, regarding GHG emissions and energy consumption, are associated with larger battery size and smaller engine displacement but result in a higher cost-to-power ratio. Specifically, for E25-fuelled PHEVs in markets with world average electricity carbon intensity, every 1.0 USD/kW increase in cost-to-power ratio leads to savings of 1.6 MJ energy consumption and 1.7 g CO_2−eq/km WTW GHG emissions. Moreover, a clear benefit of using E25 in the hybrid propulsion system is identified, where the energy consumption and GHG emissions can be reduced by 5.9% and 12.3%, respectively.

3.1 Introduction

Transport is a major source of greenhouse gas (GHG) emissions and unsustainable energy use due to a nearly complete dependence on liquid fossil fuels [220]. Intensive efforts have been directed at battery and biofuel technologies, which have made battery electric vehicles (BEVs) and flex-fuel vehicles (FFVs) potentially important strategies to decarbonize transport [221]. However, the market penetration of BEVs remains marginal owing to

higher cost, increased weight, limited range, and slow charging process [222]. The main barriers to the adoption of FFVs running on ethanol are the high cost relating to powertrain enhancements and the potential to pose a big threat to food security [223]. To overcome these limitations, the view from BYD Auto, a Chinese multinational automaker, is that plug-in hybrid electric vehicles (PHEVs) could provide a bridge that connects powertrain electrification to renewable ethanol. The reason for this is the PHEV can use an onboard battery to travel on electricity from the grid, and it can burn liquid fuel, operating as a traditional hybrid electric vehicle (HEV).

Despite the surging acceptance of PHEVs, little progress has been made to simultaneously address economic, energy, and environmental goals in the design of PHEVs enabled by low-carbon energy sources including electricity and ethanol. In PHEV design, the optimal sizing of the key mechanical and electrical components has significant effects on driving performance and cost-effectiveness [178]. Some valuable insights have been reported in the literature [224, 225], primarily concerned with the optimal sizing of lithium-ion batteries, ultracapacitors, and the internal combustion engine (ICE). For example, Hu et al. [226] presented a battery sizing framework for PHEVs to minimize CO_2 emissions. Wu et al. [227] demonstrated a cost-optimal sizing of drivetrain components including batteries and the ICE, etc.

In addition, ethanol-gasoline blends used in the ICE have attracted considerable attention from both scholars and the wider community [228]. For example, Wang et al., in their recently published articles [229, 230], have demonstrated clear benefits of ethanol addition for the enhancement of engine efficiency and the reduction of emissions. Furthermore, Samaras et al. [231] have stressed that the reduced liquid fuel requirements of PHEVs could utilize limited ethanol resources, without threat to food security. Bradley et al. [232] present the PHEVs design considerations including vehicle component function, energy management systems, and energy storage trade-offs. Some studies on PHEVs have shown larger regional GHG reductions in areas with less GHG-intensive generation portfolios [233].

Therefore, the incorporation of multiple targets, including energy consumption, cost-effectiveness, and emissions, is important when approaching the optimal PHEV component sizing. Using the Pareto-based optimization method (reviewed in Section 2.3.2), this work contributes to the multi-objective PHEV component sizing by including several

aspects omitted by previous studies. First, an empirical ethanol-gasoline blend model is incorporated into the PHEV simulation. Second, we develop a full picture of the use-phase well-to-wheel (WTW) GHG emissions from ethanol, gasoline and grid electricity and their energy consumptions. Third, market-oriented PHEV design solutions can be provided since the power utility generation portfolio and automobile fuel properties of the target market are considered. Finally, the present work highlights the Pareto relationships among the economic, energy, and environmental goals in PHEV design.

The remainder of this chapter is organized as follows. Section 3.2 presents the ethanol-gasoline blend model. Section 3.3 describes the flex-fuel hybrid propulsion system. Section 3.4 gives the multi-objective optimization methodology where the cost-to-power ratio, the energy consumption, and the GHG emissions are simultaneously minimized. Section 3.5 provides the results, followed by the key conclusions summarized in Section 3.6.

3.2 Ethanol-gasoline blend model

An accurate ethanol-gasoline blend model is vitally important because a precise knowledge of ethanol blends and their influencing factors can be instrumental in the implementation of component sizing and energy management. In our recently published articles [229, 230], we have proposed an empirical ethanol-gasoline blend model based on historical and literature data, which is a general method to evaluate the benefits of ethanol use to engine thermal efficiency gains and WTW GHG emissions. Table 3.1 lists the main properties of typical gasoline and ethanol used in automotive applications [229]. What is important for us to recognize here, is that although lower in energy density (i.e., lower heating value, H_v), ethanol has a higher research octane number (N_{RON}) that can lead to an increased compression ratio and thence to enhanced engine thermal efficiency. Moreover, the GHG intensity (E_{GHG}) of ethanol is only about one-third of its gasoline counterpart.

Table 3.1 Fuel properties.

Parameter (unit)	Gasoline	Ethanol
Research octane number, N_{RON}	89	107
Octane sensitivity, S_O	10	18
Fuel density, ρ_f (kg/m^3)	730	790
Lower heating value, H_v (MJ/kg)	42	26.9
WTW GHG emissions, E_{GHG} (g CO$_2$–eq/MJ)	93.2	33.5
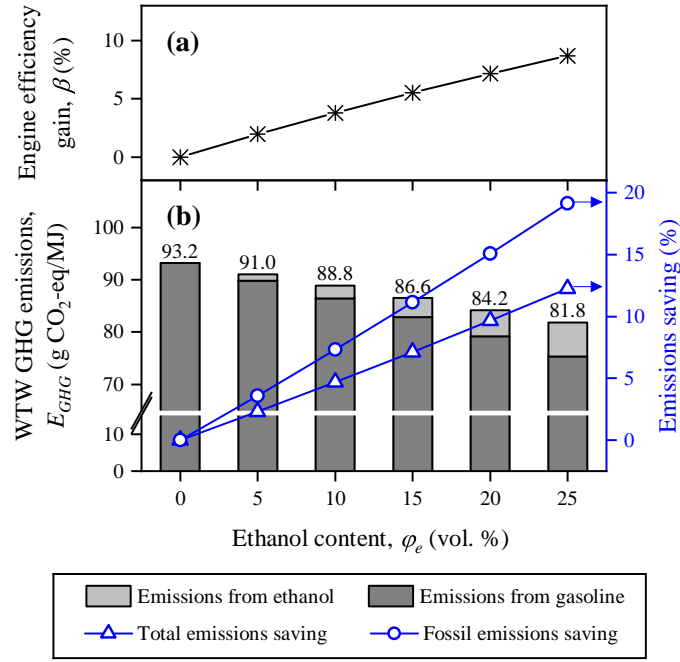
Figure 3.1 The benefits of ethanol-gasoline blends for (a) engine efficiency and (b) GHG emissions.

Figure 3.1 (a) shows the engine thermal efficiency gain (β) due to the beneficial effects of ethanol addition. In the literature on ethanol blends, there are three principal effects of ethanol addition on engine hardware design and fuel consumption: (1) anti-knock; (2) high flame speed; (3) engine downsizing. These are factors contributing to total engine thermal efficiency gain (β) that varies as a function of the ethanol content, described as

$$\beta(\varphi_e) = \beta_{AK}(\varphi_e) + \beta_{FS}(\varphi_e) + \beta_{ED}(\varphi_e), \tag{3.1}$$

where φ_e is the volumetric content of ethanol (vol.%); the subscripts, AK, FS, and ED denote the effects of anti-knock, flame speed, and engine downsizing, respectively. The anti-knock engine efficiency gain can be calculated by

$$\beta_{AK}(\varphi_e) = (k_0 \cdot \Delta N_{RON} + k_1)\varphi_e^2 + (k_2 \cdot \Delta N_{RON} + k_3 \cdot \Delta S_O + k_4)\varphi_e, \tag{3.2}$$

where k_0, k_1, k_2, k_3, and k_4 are coefficients derived from the engine tests using ethanol blends, more details are available in [229]; ΔN_{RON} and ΔS_O are differences between ethanol and gasoline, in terms of research octane number and octane sensitivity, respectively, as

expressed below.

$$\begin{cases} \Delta N_{RON} = N_{RON}^{ethanol} - N_{RON}^{gasoline}, \\ \Delta S_O = S_O^{ethanol} - S_O^{gasoline}, \end{cases} \qquad (3.3)$$

In addition, the contributions of high flame speed and engine downsizing to engine efficiency are quantified as

$$\begin{cases} \beta_{FS}(\varphi_e) = \gamma \cdot \varphi_e, \\ \beta_{ED}(\varphi_e) = (\alpha - 1)\big(\beta_{AK}(\varphi_e) + \beta_{FS}(\varphi_e)\big), \end{cases} \qquad (3.4)$$

where γ and α are factors equal to 0.02 and 1.1, respectively.

Furthermore, the ethanol-gasoline blend model provides the estimation of the GHG intensities (g CO_2−eq/MJ) of ethanol blends, which can be linearly calculated by

$$E_{GHG}^{fuel} = b_0 + b_1 \cdot \varphi_e, \qquad (3.5)$$

where b_0 and b_1 are constant coefficients determined by the gasoline and ethanol properties. As shown in Figure 3.1 (b), with successive increases in ethanol content (φ_e) from 0 to 25 vol.%, the GHG intensity of the fuel blend is decreased from 93.2 to 81.8 g CO_2−eq/MJ, indicating significant reductions in total GHG emissions ($\sim$12%, from blend) and in fossil GHG emissions ($\sim$20%, from gasoline).

The ethanol-gasoline blend model can be applied for up to 70 vol.% ethanol blends [229]. However, the blend whose ethanol content is beyond 25 vol.% cannot be used in regular engines [234], causing high cost relating to engine enhancements. Therefore, the ethanol content (φ_e) in blends ranges between 0 and 25 vol.% in this study.

3.3   Flex-fuel hybrid propulsion system

As illustrated in Figure 3.2, the PHEV propulsion system examined here comprises a set of mechanical and electrical components. The battery pack (BP) and the ultracapacitor pack (UP) can both store grid electricity. The ICE, connected to the liquid fuel tank and the generator, can use chemical energy obtained from the ethanol-gasoline blend to charge batteries and ultracapacitors when their grid electricity is depleted or to propel the wheels via the electric motor. In addition, the kinetic energy harvested by regenerative braking

can also be stored in the BP and the UP. The involved energy conversion and management processes are introduced below.
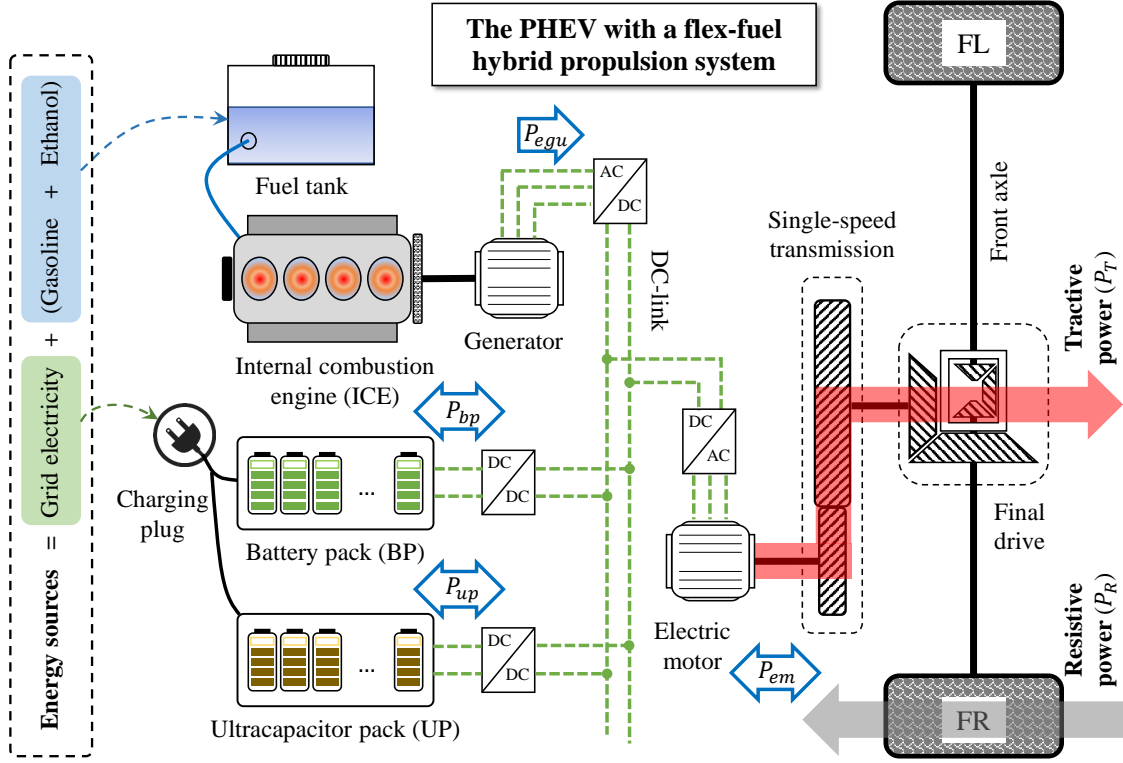
Figure 3.2 The PHEV powertrain configuration and energy sources.

3.3.1 Vehicle dynamics

The vehicle longitudinal dynamics can be described by

$$
\begin{cases}
v(t) = \dot{x}(t), \\
a(t) = \frac{1}{\phi \cdot m}\big(F_T(t) - F_R(t)\big), \\
F_T(t) = \frac{1000 \cdot P_{em}(t) \cdot \eta_d}{v(t)}, \\
F_R(t) = f_0 \cdot \cos\theta + f_1 \cdot v(t) + f_2 \cdot v(t)^2 + mg \cdot \sin\theta,
\end{cases}
\tag{3.6}
$$

where a, v, and x are acceleration (m/s^2), speed (m/s), and travel distance (m), respectively, of the subject vehicle at time t (s); m is the vehicle operating mass (kg); ϕ is the equivalent inertial mass factor; P_{em} denotes the power (kW) of the electric motor; η_d is the driveline efficiency; F_T is the tractive force (N); F_R indicates the resistance forces (N) acting on the vehicle, namely, the aerodynamic, rolling, and grade resistances; f_0, f_1, and f_2 are the road load coefficients (N, kg/s, and kg/m, respectively) [235]; and θ is the road grade (rad).

3.3.2 Internal combustion engine

An empirical 1.0 L engine model from the AVL CRUISE software was selected as the baseline for the component sizing. It is assumed that the engine operation points always lie on the highest efficiency curve across the entire power range of the engine, which is normalized against its maximum power (40 kW) [236]. According to Willan's method adopted by Zhou et al. [178] and Lujan [237], the maximum power of the engine can be scaled by considering its displacement, and thus, its instantaneous fuel consumption rate ($\dot{m}$) can be estimated by

$$
\begin{cases}
\dot{m}(t) = \dfrac{P_{ice}(t)}{H_v(\varphi_e) \cdot \left(1 + \beta(\varphi_e)\right) \cdot \eta_{ice}^{base}(P_{ice}^n)}, \\
P_{ice}^n = P_{ice}(t)/P_{ice}^{max}, \\
P_{ice}^{max}(V_{ice}) = k_s \cdot V_{ice},
\end{cases}
\tag{3.7}
$$

where P_{ice}^{max} is the maximum engine power (kW); V_{ice} indicates the engine displacement (L); k_s is the engine scale factor; $\dot{m}$ is the fuel consumption rate (g/s); P_{ice} is the current engine power output (kW); P_{ice}^n is a dimensionless quantity and denotes the normalized engine power; η_{ice}^{base} is the baseline engine efficiency varying with engine power output, as illustrated in Figure 3.3; H_v is the lower heating value (MJ/kg) of the fuel blend. The cost estimation method for a regular engine, adopted by Wu et al. [227], is expressed as

$$
c_{ice}(V_{ice}) = 12 \cdot P_{ice}^{max}(V_{ice}) + 424,
\tag{3.8}
$$

where c_{ice} is the cost (USD) of the engine depending on the maximum engine power P_{ice}^{max}.
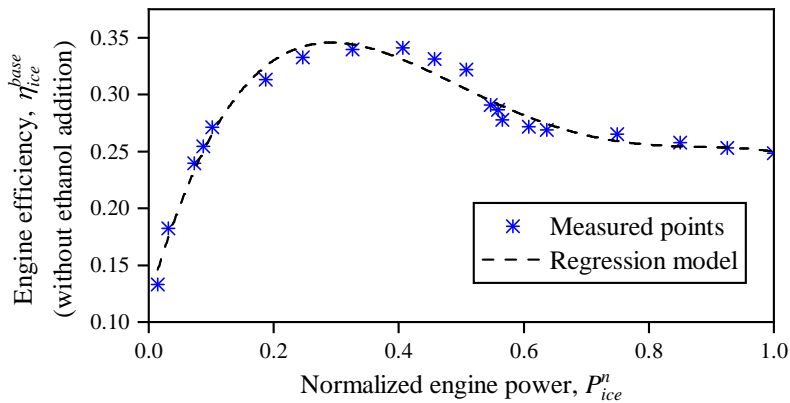
Figure 3.3 Efficiency of the baseline engine fuelled with gasoline (without ethanol addition).

3.3.3 Battery and ultracapacitor

The battery pack (BP) and the ultracapacitor pack (UP) are scaled by their cell numbers, namely, n_{bc} and n_{uc}, respectively. Taken from the study by Zhou et al.[178], the types of lithium-ion battery and ultracapacitor are Panasonic NCR18650BF and NessCap ESHSR-3000C0-002R7A5T, respectively, whose main specifications are summarized in Table 3.2. The battery dynamics is simulated by the model proposed by Chen et al. [238], while the mathematical model adopted for the ultracapacitor simulation is based on the study by Ostadi et al. [224]. To avoid the detrimental effects of overcharge and overdischarge, the operating window of battery state-of-charge (SoC) is from 0.2 to 0.8; while for ultracapacitor, its SoC is bounded between 0.2 and 0.9, following Zhang et al. [79].

Table 3.2 Main specifications of the battery and the ultracapacitor.

Battery cell		Ultracapacitor cell	
Parameter (unit)	Value	Parameter (unit)	Value
Mass, m_{bc} (g)	46.5	Mass, m_{uc} (g)	535
Nominal voltage, V_{bc} (V)	3.6	Nominal voltage, V_{uc} (V)	2.7
Energy capacity, Q_{bc} (As)	11,500	Energy capacity, Q_{uc} (As)	4000
Resistance, R_{bc} (Ω)	0.01	Capacitance, C_{uc} (F)	3000
Cost, c_{bc} (USD)	6.5	Cost, c_{uc} (USD)	32.5

3.3.4 Energy management strategy

Torque/power coordination is essential for realizing PHEVs potentials of low-carbon and high-efficiency [114]. Thus, the hybrid propulsion system needs capable energy management strategies (EMSs) to coordinate the power outputs from the engine-generator unit (EGU), battery pack (BP), and ultracapacitor pack (UP). In this work, charge depleting - charge sustaining (CD-CS) and wavelet transform (WT) are employed to realize the power split among EGU, BP, and UP. The overall power-balance equations are

$$\begin{cases} \frac{P_{em}(t)}{\eta_{em}\eta_i^2} = P_{ice}(t) \cdot \eta_g + P_{ele}(t), \\ P_{ele}(t) = P_{bp}(t) + P_{up}(t), \end{cases} \tag{3.9}$$

where η_{em}, η_i, and η_g are the motor efficiency, the inverter efficiency, and the generator efficiency, respectively; P_{ele} is the power (kW) delivered from the electricity storage

components; and P_{bp} and P_{up} are the power outputs (kW) of the battery pack and the ultracapacitor pack, respectively.

The CD-CS technique [96] is applied to split the mechanical (P_{ice}) and electrical (P_{ele}) power outputs, where the former varies as a stepwise function of the battery SoC.

$$P_{ice}(t) = \begin{cases} 0, & SoC_{bc} \in (0.8, 1] \\ \dfrac{round\left(20 \cdot e^{-\frac{\left(SoC_{bc}(t) - 0.2\right)^2}{2\sigma^2}}\right)}{20} \cdot P_{ice}^{max}, & SoC_{bc} \in [0.2, 0.8] \\ P_{ice}^{max}, & Soc_{bc} \in [0, 0.2) \end{cases} \tag{3.10}$$

where σ is the time constant; SoC_{bc} is the state-of-charge (SoC) of battery cells. The battery dynamics [26, 239] are governed by the following equations, i.e.,

$$\begin{cases} P_{bc}(t) = \dfrac{P_{bp}(t)}{n_{bc}} = U_{bc} \cdot I_{bc}(t) - I_{bc}(t)^2 \cdot R_{bc}, \\ S\dot{o}C_{bc}(t) = -\dfrac{I_{bc}(t)}{Q_{bc}} = -\dfrac{U_{bc} - \sqrt{U_{bc}^2 - 4 \cdot R_{bc} \cdot P_{bc}(t)}}{2 \cdot R_{bc} \cdot Q_{bc}}, \end{cases} \tag{3.11}$$

where P_{bc} and I_{bc} are respectively the power (W) and the current (A) of the battery cell; R_{bc}, Q_{bc}, and U_{bc} denote the internal resistance (Ω), energy capacity (As), and open-circuit voltage (V), respectively; n_{bc} is the cell number in the battery pack.

In addition, the WT technique uses high-pass and low-pass filters to decompose the electrical power signal (P_{ele}) into different localized contributions, each of which represents a portion of the signal from a different frequency band [240]. Consequently, the high-frequency components are dealt with by the highly responsive ultracapacitor pack (UP); while the remaining parts are consigned to the battery pack (BP). This approach, as expressed in the following equations [79], can help to protect battery cells from too much transient charging and discharging.

$$\begin{cases} P_{bp}(t) = f_{\text{low-pass}}\big(P_{ele}(t)\big), \\ P_{up}(t) = f_{\text{high-pass}}\big(P_{ele}(t)\big), \end{cases} \tag{3.12}$$

3.4   Optimization methodology

The working principle of the multi-objective optimal sizing conducted in this study is illustrated in 3.4. The input layer, as presented in 3.4 (a), provides information from the
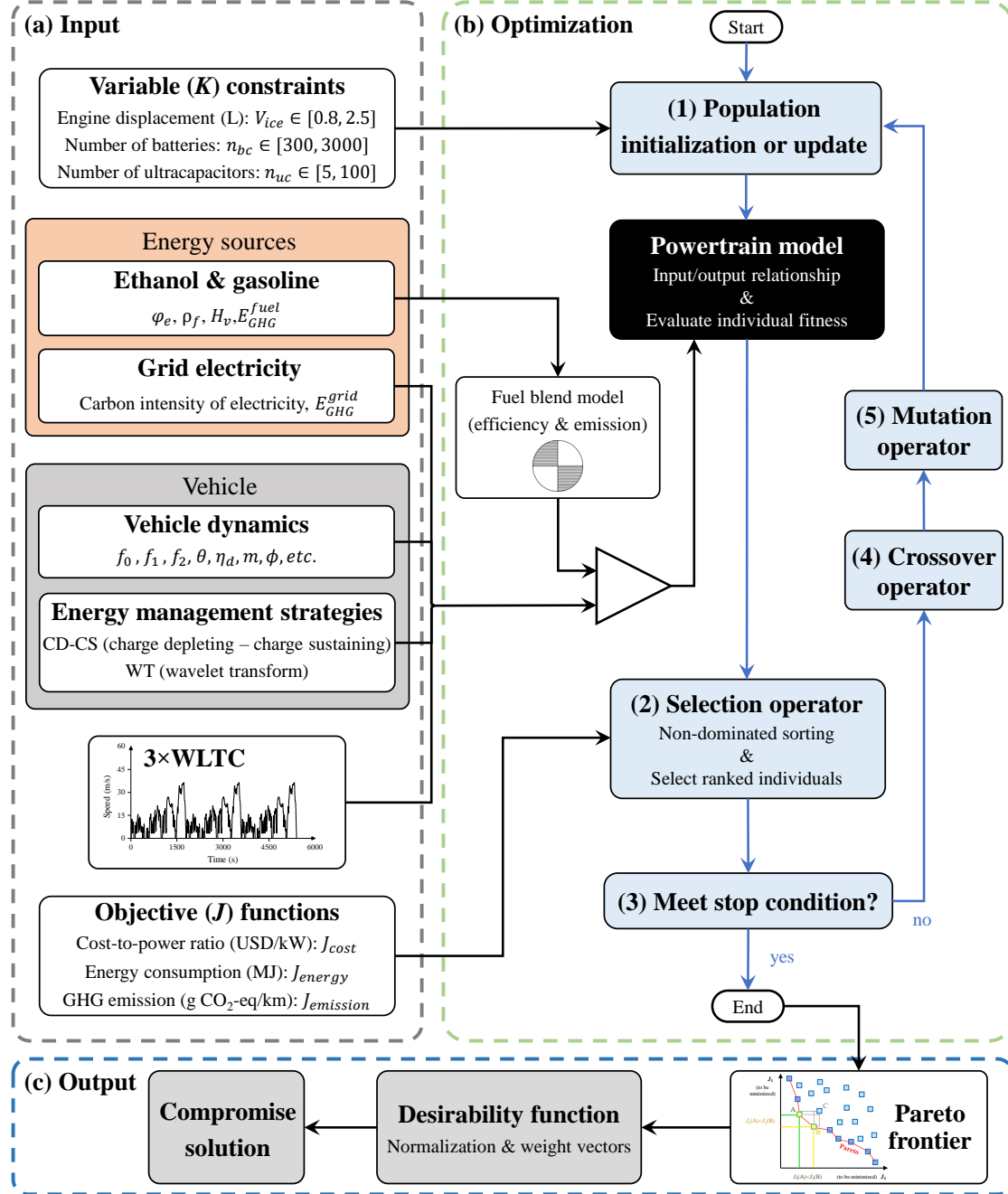
Subplots: (a) The input layer including the real-world measurements, standards, and requirements; (b) the optimization layer implementing the Pareto-based NSGA-III algorithm, which consists of building blocks (1)-(5); (c) the output layer utilizing the desirability function to derive the best compromise solution from the Pareto frontier.

Figure 3.4 Working principle of the multi-objective optimal sizing.

real-world measurements, standards, and requirements, for the formulation of the multi-objective optimization problem (MOOP). The driving cycle used is three consecutive repetitions of the Worldwide Harmonised Light Vehicle Test Cycle (3×WLTC). As mentioned in the previous section, the ethanol and gasoline properties are fed into the fuel blend model for the estimation of engine efficiency and GHG emissions. The optimization layer, given in 3.4 (b), is the flow chart of the non-dominated sorting genetic algorithm III (NSGA-III) employed to solve the formulated MOOP. The output layer, presented in 3.4 (c), utilizes the desirability function to derive the best compromise solution from the Pareto frontier resulting from the NSGA-III optimization.

3.4.1 Optimal sizing problem formulation

The primary goal of this study is to investigate the optimal sizing, i.e., the engine displacement (V_{ice}), the number of batteries (n_{bc}), and the number of ultracapacitors (n_{uc}), of the PHEV using multiple energy streams. To this end, three objective functions, namely cost-to-power ratio (J_{cost}), energy consumption (J_{energy}), and GHG emissions ($J_{emission}$) are defined as follows to encompass economic, efficiency, and environmental needs.

The cost-to-power ratio (USD/kW) is the value of the components' total manufacturing cost divided by the maximum power that the propulsion system can deliver. Its mathematical expression is given by

$$
\begin{cases}
J_{cost} = \dfrac{c_{ice}(V_{ice}) + c_{bc} \cdot n_{bc} + c_{uc} \cdot n_{uc}}{P_{ice}^{max}(V_{ice}) + \varepsilon_{bp} \cdot P_{bc}^{max} \cdot n_{bc} + \varepsilon_{up} \cdot P_{uc}^{max} \cdot n_{uc}}, \\[2ex]
\varepsilon_{bp} = \dfrac{n_{bc} \cdot Q_{bc}}{n_{bc} \cdot Q_{bc} + n_{uc} \cdot Q_{uc}}, \\[2ex]
\varepsilon_{up} = \dfrac{n_{uc} \cdot Q_{uc}}{n_{bc} \cdot Q_{bc} + n_{uc} \cdot Q_{uc}},
\end{cases}
\tag{3.13}
$$

where P_{bc}^{max} and P_{uc}^{max} are the maximum power outputs (kW) of the battery cell and the ultracapacitor cell, respectively. As mentioned in Section 2.1, the ultracapacitor has a high power density but has a much lower energy density when compared with the battery. Considering that the sustainability of their maximum power outputs is limited by the energy available in these two devices, the power adjustment factors ε_{bp} and ε_{up} are incorporated into the cost function.

The energy consumption (MJ) includes the consumed ethanol-gasoline blend and grid electricity during the $3 \times$WLTC test cycle. The expressions are presented as

$$
\begin{cases}
J_{energy} = \frac{1}{1000} \int_{t_0}^{t_f} \left(H_v(\varphi_e) \cdot \dot{m}(t) + P_{bp}(t) + P_{up}(t) \right) dt, \\
P_{bp} = n_{bc} \cdot P_{bc}(t), \\
P_{up} = n_{uc} \cdot P_{uc}(t),
\end{cases}
\tag{3.14}
$$

where t_0 and t_f represent the initial time and final time of the driving cycle.

Life cycle assessment (LCA) is a standardized tool to quantify GHG emissions associated with a product's manufacture, use, and end-of-life [231]. In this work, the use-phase well-to-wheel (WTW) GHG emissions (g CO_2–eq/km), resulting from powering the vehicle with liquid fuel and grid electricity [241], is given below.

$$
J_{emission} = \frac{1}{d} \int_{t_0}^{t_f} \left(E_{GHG}^{fuel}(\varphi_e) \cdot H_v(\varphi_e) \cdot \dot{m}(t) + E_{GHG}^{grid} \cdot \left(P_{bp}(t) + P_{up}(t) \right) \right) dt
\tag{3.15}
$$

where E_{GHG}^{grid} is the carbon intensity (g CO_2–eq/MJ) of the grid electricity stored in batteries and ultracapacitors. For the base-case scenario, grid electricity used to charge PHEVs has the WTW GHG intensity (E_{GHG}^{grid}) similar to the average intensity of the current world power portfolio, or 146.9 g CO_2–eq per MJ of electricity as reported by the International Energy Agency (IEA) [242].

Moreover, according to a dataset of vehicle specifications that contains information relating to 543 commercial hybrid electric vehicles, the multi-objective optimization is subject to the following constraints on the controlled variables.

$$
\begin{cases}
0.8\text{L} \leq V_{ice} \leq 2.5\text{L}, \\
0 \leq n_{uc} \leq 100, \\
300 \leq n_{bc} \leq 3000,
\end{cases}
\tag{3.16}
$$

3.4.2 Optimization using Pareto genetic algorithm

NSGA-III has been recognized to be an effective and efficient algorithm to solve multi-objective optimization problems (MOOPs) [243–245], where an approximation of the Pareto-optimal set can be obtained in a single run. The flow chart of the NSGA-III optimization in this study is illustrated in Figure 3.4 (b). The vector of controlled variables

is expressed as a chromosome where each variable is the gene. There are three fundamental genetic operators: (1) the crossover operator exchanges the gene information of the current generation, in order to share the better gene segment; (2) the mutation operator then randomly alters some genes of the chromosome to perform a local search, attempting to find a better fitness landscape; (3) the selection operator finally determines the survived population for the next generation.

3.4.3 Desirability function

In engineering applications, usually only one PHEV design solution is required, thus, the desirability function is introduced to select the best compromise solution from the Pareto frontier, as shown in Figure 3.4 (c). The method adopted by Pasandideh et al. [246] computes a penalty score (α) for each objective vector in the Pareto-optimal set. Consequently, the solution with the minimum α is the best compromise one. The expressions of the desirability function are presented as follows.

$$\min_{K \in PF} \alpha\big(J(K)\big) = \min_{K \in PF} \sum_{i=1}^{3} w_i \frac{J_i(K) - J_i^{min}}{J_i^{max} - J_i^{min}}, \tag{3.17}$$

$$\begin{cases} J = [J_{cost}, J_{energy}, J_{emission}], \\ K = [V_{ice}, n_{uc}, n_{bc}], \\ \sum_{i=1}^{3} w_i = 1 \ \ \text{and} \ \ w_i \geq 0, \end{cases} \tag{3.18}$$

where J_i^{max} and J_i^{min} are the maximum and minimum values of the objective function J_i on the Pareto frontier (PF); K is the variable vector; w_i means the weight factor given by the decision-maker.

3.5 Results and discussion

The results obtained from the multi-objective component sizing are presented and discussed in the section below from three perspectives: (1) the Pareto analysis seeks to elicit relationships (e.g., conflicting and harmonious) between different objective functions, and thus to provide guidance for the selection of the weight vector w in the desirability function; (2) the performance analysis demonstrates the reliability of the best

compromise solution when implemented in the PHEV propulsion system; and (3) the analysis of the energy and emission benefits from the ethanol use is presented.
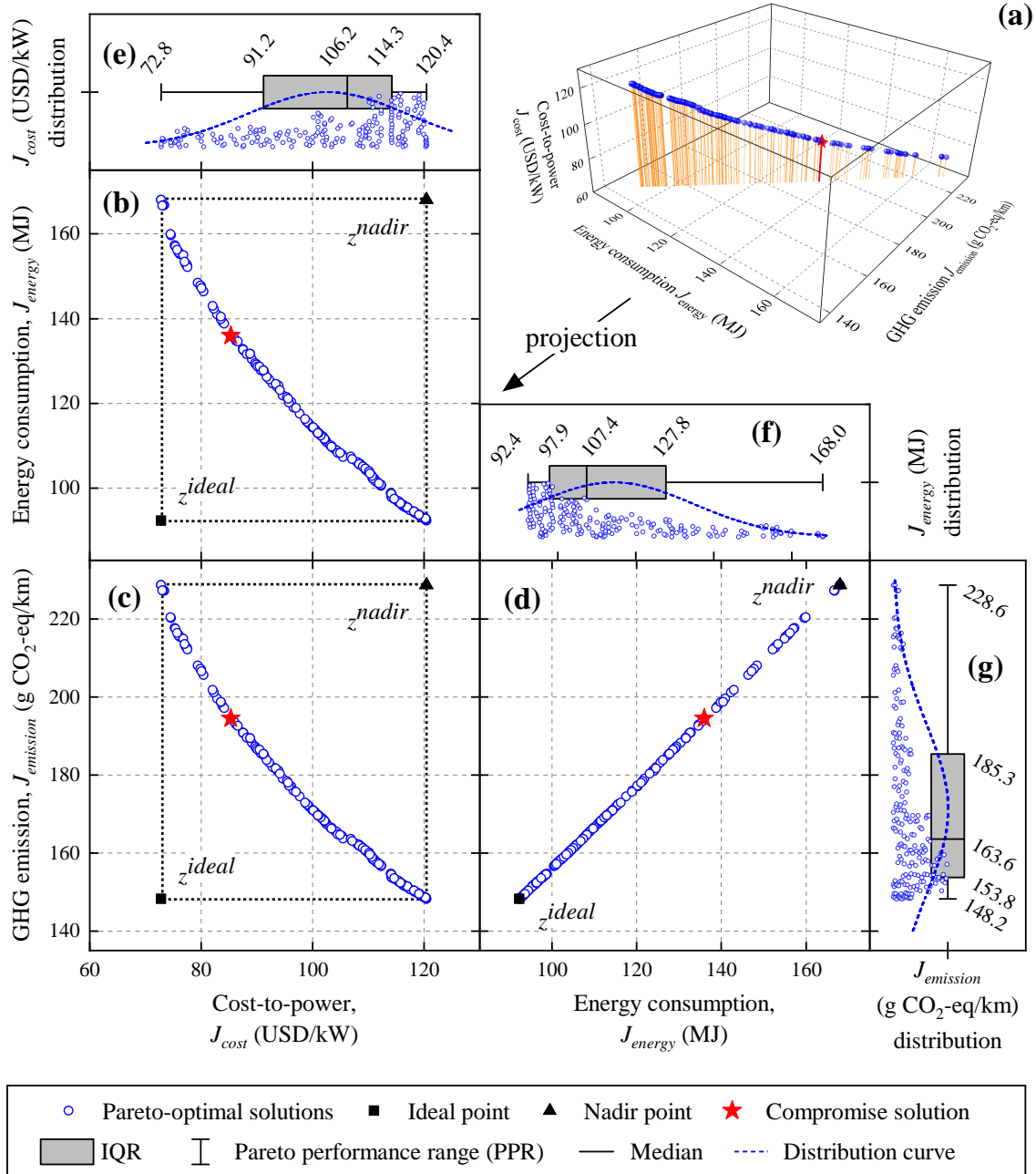
Subplots: (a) Pareto frontier (PF) in 3D space; (b)-(d) PF projections onto 2D planes; (e)-(g) marginal distributions.

Figure 3.5 The Pareto frontier (PF) resulting from the multi-objective optimization.

3.5.1 Pareto analysis

Figure 3.5 (a) presents the Pareto-optimal set achieved by NSGA-III optimization when the ethanol content (φ_e) is equal to 25% (E25). For visualization and analysis purposes, the

three-dimensional (3D) objective space is projected onto the 2D scatter plots, i.e., Figure 3.5 (b)-(d), where the ideal point (black square, z^{ideal}) and the nadir point (black triangle, z^{nadir}) correspond to the lower and upper boundaries of the Pareto performance range (PPR). The relationships among different objective functions are analyzed as below.

Intuitively with the projection in Figure 3.5 (b), a trade-off (or conflicting relationship) can be identified between the manufacturing cost (J_{cost}) and the energy consumption (J_{energy}) targets, because one of them will deteriorate when the other is improved in the Pareto-optimal set. Moreover, there exists a similar trade-off between the cost (J_{cost}) and the emission ($J_{emission}$) targets, as shown in Figure 3.5 (c). However, looking at Figure 3.5 (d), the optimization of J_{energy} is in harmony with that of $J_{emission}$, where the reduction of any one is rewarded with a simultaneous decrease in the other.

According to the relationships of objective functions mentioned above, the weight vector is assigned as $w = [0.50, 0.25, 0.25]$ in this work, because the energy and the emission targets are both in conflict with the cost objective. After the implementation of the desirability function, the best compromise solution is obtained and identified as a pentagram symbol in Figure 3.5.

Table 3.3 Distribution of each objective on the Pareto frontier.

Objective (unit)	PPR[a]	Median
cost-to-power ratio, J_{cost} (USD/kW)	47.6	106.2
energy consumption, J_{energy} (MJ)	75.6	107.4
GHG emission, $J_{emission}$ (g CO_2−eq/km)	80.4	163.6

[a] PPR = Pareto performance range.

The box-whisker diagrams in Figure 3.5 (e)-(g) provide the statistical distributions of the Pareto-optimal set regarding each objective. The height of the box is the interquartile range (IQR) between the first quartile (Q1, 25%) and the third quartile (Q3, 75%). The median, the band inside the box, denotes the second quartile (Q2, 50%). The ends of the whisker represent the Pareto performance range (PPR), namely, the range between the ideal point and the nadir point in every objective dimension. As summarized in Table 3.3, the cost (J_{cost}), energy (J_{energy}), and emission ($J_{emission}$) objectives have a median value of 106.2 USD/kW, 107.4 MJ, and 163.6 g CO_2−eq/km, respectively, in the Pareto-optimal set. More importantly, the PPR data from this table indicates that, for the design of PHEVs

fuelled with E25, every 1.0 USD/kW increase in cost-to-power ratio leads to savings of 1.6 MJ energy consumption and 1.7 g CO_2−eq/km WTW GHG emissions.

Figure 3.6 displays the parallel coordinates, offering more details in correlating the controlled variables (V_{ice}, n_{bc}, and n_{uc}) with the design objectives (J_{cost}, J_{energy}, and $J_{emission}$). Each dimension is visualized on a vertical axis and each Pareto-optimal solution is presented as a curve connecting the respective values on the vertical axis. In addition, the black dash curve denotes the compromise solution, which is consistent with the preference expressed by the weight vector (w). The findings in the parallel coordinates further indicate that better performances of the PHEV propulsion system with respect to GHG emissions and energy consumption are associated with larger battery size and smaller engine displacement, which, conversely, result in a higher cost-to-power ratio.
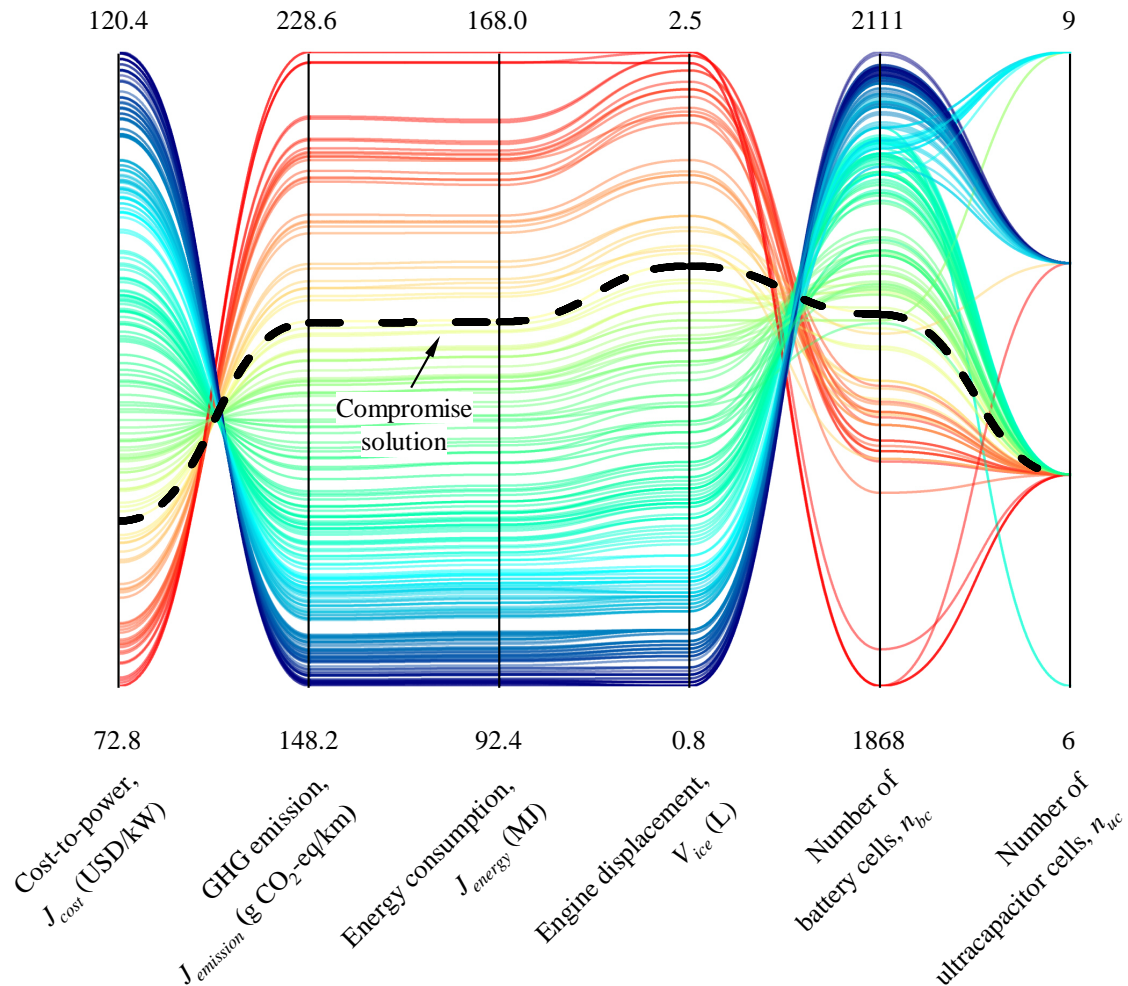
Figure 3.6 Parallel coordinates of the Pareto-optimal solutions.

3.5.2 Performance analysis

Figure 3.7 demonstrates the performances of the PHEV propulsion system after implementing both the compromise solution for component sizing (as discussed above) and the EMS described in Section 3.3.4.
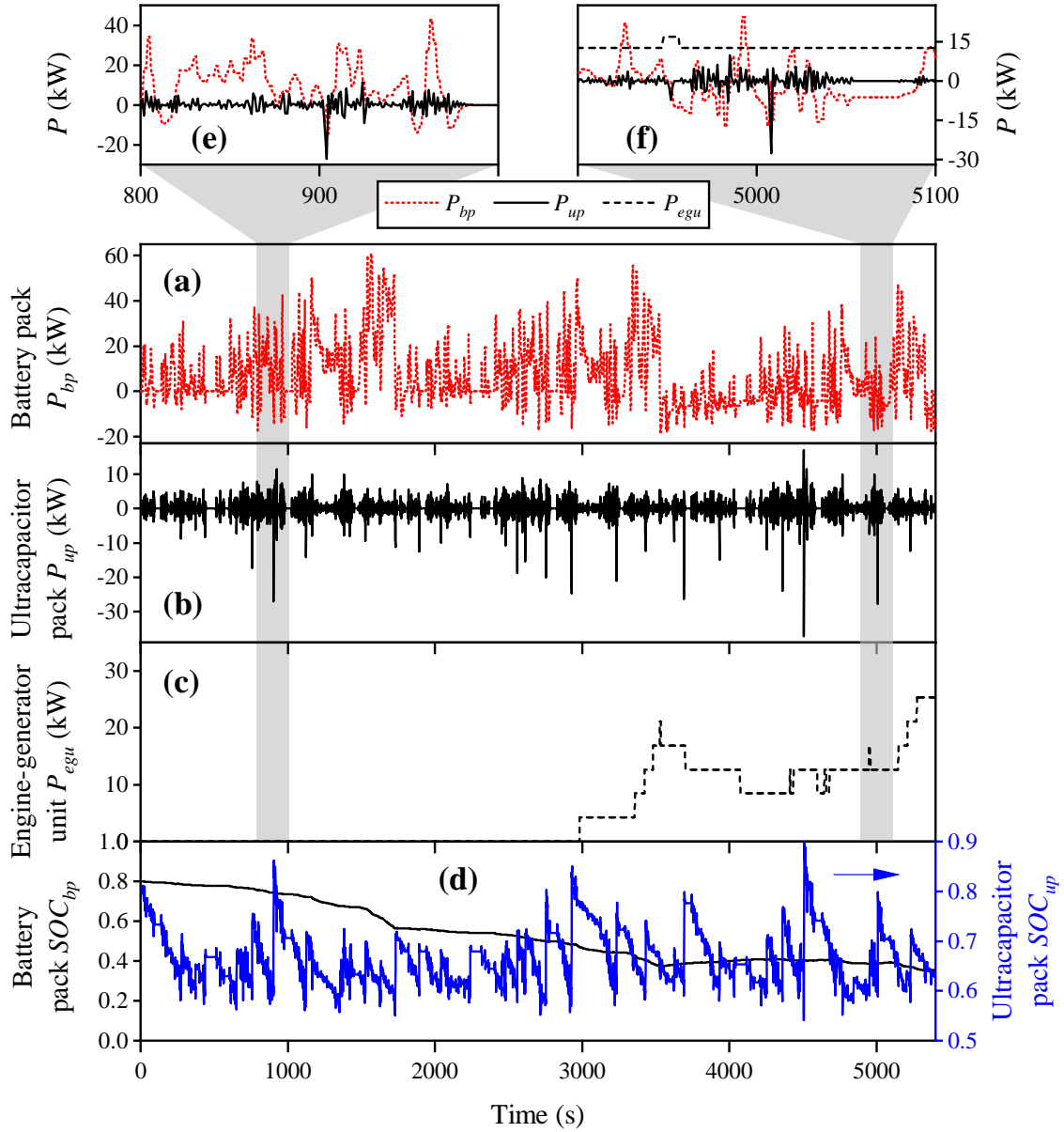
Figure 3.7 The power coordination and the performances of propulsion components.

Figure 3.7 (a)-(c) show the power profiles of the battery pack (BP), the ultracapacitor pack (UP), and the engine-generator unit (EGU), respectively. To compare their power transients, two gray sections (time intervals 800-1000 s and 4900-5100 s) are zoomed in and put into the same time-power coordinates, as shown in Figure 3.7 (e) and (f). The above figures reveal that power coordination among different mechanical and electrical propulsion

components can be achieved by the employed CD-CS and WT energy management strategies. The BP has a smooth power profile together with reduced power levels, while the UP assists to share the dynamic transients during the aggressive accelerations and decelerations. The EGU starts to work at ~3000 s and operates constantly in high-efficiency and low-emission areas since the hybrid powertrain has multiple power sources and makes it easy to adjust the engine operation points [176]. Figure 3.7 (d) illustrates the battery SoC and ultracapacitor SoC profiles during the 3×WLTC test cycle, where detrimental overcharge and overdischarge are avoided.
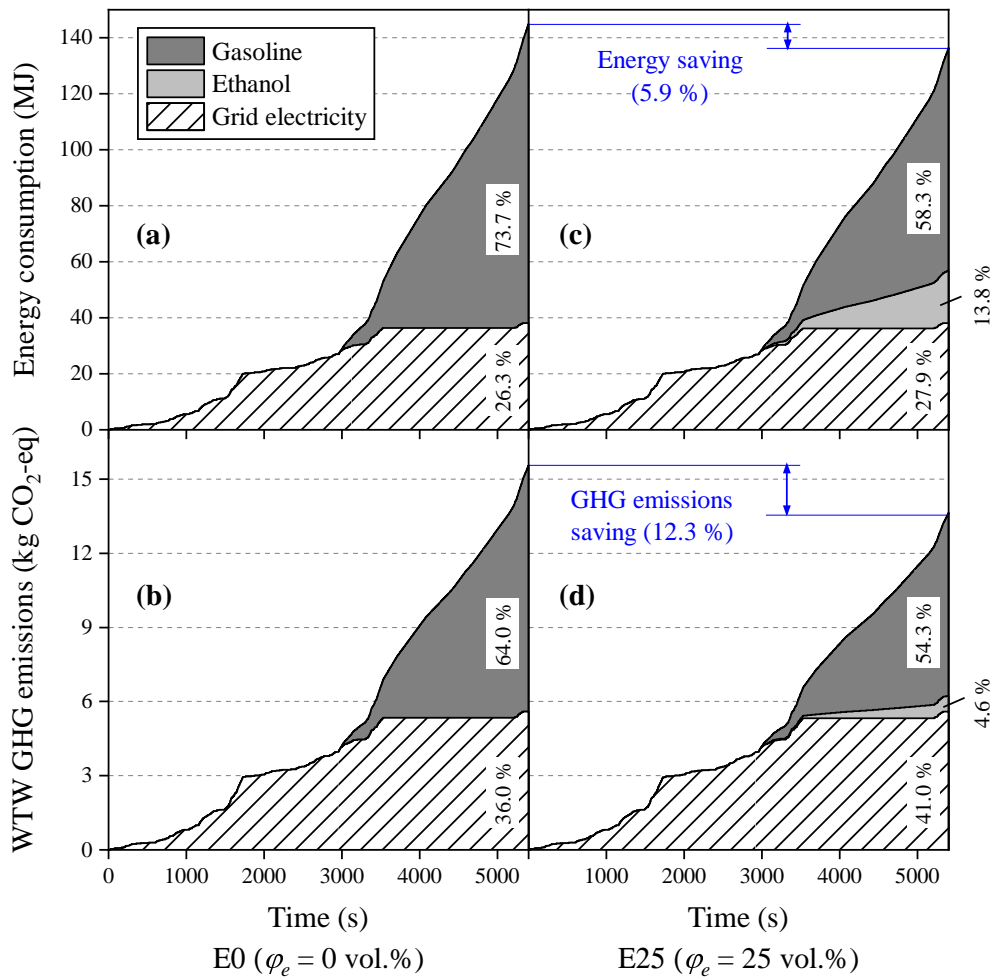
Subplots: (a) and (b) E0-fuelled PHEV; (c) and (d) E25-fuelled PHEV.

Figure 3.8 Energy and emission benefits from ethanol use during 3×WLTC driving cycle.

3.5.3 Analysis of energy and emission benefits

To analyze the impact of ethanol use on the performance of the optimized PHEV, Figure 3.8 compares the cumulative energy consumption and GHG emissions for E0 (without ethanol addition, i.e., ethanol content $\varphi_e = 0$ vol.%,) and E25 ($\varphi_e = 25$ vol.%) scenarios.

Figure 3.8 (a) and (b) present results from the simulation of the E0 scenario. It can be seen that the energy consumption and the GHG emissions from $3\times$WLTC cycle are $\sim$145 MJ and $\sim$15.6 kg CO_2−eq, respectively, where gasoline accounts for 73.7% of the total energy consumed and 64.0% of the overall GHG emissions. When using the low-carbon E25 fuel blend, an overview of the PHEV energy consumption is displayed in Figure 3.8 (c), where the saving of the total energy consumption is 5.9%, while the corresponding contribution from gasoline is reduced to 58.3%. Moreover, the emission benefit from ethanol use is provided in Figure 3.8 (d), where the saving of total GHG emissions is 12.3%, and the percentage of fossil GHG emissions is reduced to 54.3%. What is interesting about the data in Figure 3.8 (c) and (d) is that ethanol only contributes to 4.6% of the total GHG emissions although it provides 13.8% of the total energy.

3.6 Summary

To combat climate change and enhance energy security, plug-in hybrid electric vehicles (PHEVs) can provide a bridge that connects transport electrification to renewable ethanol. However, little progress has been made to simultaneously address economic, energy, and environmental goals in the design of PHEVs powered by low-carbon energy sources including electricity and ethanol. This study has thoroughly examined the synergistic benefits of both electric and ethanol low-carbon propulsion techniques within the framework of multi-objective component sizing for a flex-fuel hybrid powertrain. The cost-to-power ratio, energy consumption, and use-phase WTW GHG emissions are selected as optimization objectives. Major contributions and conclusions are as follows:

- An empirical ethanol-gasoline blend model is incorporated into the PHEV powertrain simulation. Then we develop a full picture of the use-phase WTW GHG emissions from ethanol, gasoline and grid electricity and their energy consumptions.

- The proposed PHEV component sizing approach can provide market-oriented PHEV design solutions targeted at the power utility generation portfolio and the automobile fuel properties of the market region.

- More specifically, for E25-fuelled PHEVs in markets with world average (146.9 g CO_2−eq/MJ) electricity carbon intensity, every 1.0 USD/kW increase in cost-to-power ratio leads to savings of 1.6 MJ energy consumption and 1.7 g CO_2−eq/km WTW GHG emissions.

- A clear benefit of using E25 in the hybrid propulsion system is identified, where the energy consumption and the WTW GHG emissions can be reduced by 5.9% and 12.3%, respectively.

- When using E25 in the PHEV, the moderate proportion of ethanol, can contribute to 13.8% of the total energy used but counts only 4.8% of the WTW GHG emissions.

4 Integrated multi-objective optimization of ACC and EMS for AEVs

Automated and electrified vehicles (AEVs) are gathering momentum in the automotive and transport sectors, but there are escalating concerns over their need for co-optimization to improve energy efficiency, traffic safety, and ride comfort. Previous approaches to these multi-objective co-optimization problems often overlook trade-offs and scale differences between the objectives, resulting in misleading optimizations. To overcome these limitations, this study marks the first attempt to utilize the Pareto-based approach to investigate multi-objective co-optimization of the adaptive cruise control (ACC) and the energy management strategy (EMS) for AEVs. The high-level Pareto knowledge assists in finding the best compromise solution. The results suggest that the energy and the comfort targets are harmonious, but both conflict with the safety target. Validation using real-world driving data shows that the Pareto optimum for ACC and EMS systems, relative to the baseline, can reduce energy consumption (by 7.57%) and tracking error (by 68.94%), while simultaneously satisfying ride comfort needs. In contrast to the weighted-sum method, the Pareto method can optimally balance and scale the multiple objective functions. In addition, sensitivity analysis proves that the vehicle reaction time impacts significantly on tracking safety, but its effect on energy saving is trivial.

4.1 Introduction

Energy, environmental, and safety challenges are exacerbated by rising transport demand [13]. To tackle these problems, vehicle electrification, automation, and connectivity are gathering momentum worldwide [247–249], but there are escalating concerns over their synergistic impacts on the control design of vehicles that fuse mechatronics with new informatics, such as automated and electrified vehicles (AEVs).

Plug-in hybrid electric vehicles (PHEVs) are widely promoted as an efficient and clean solution that combines an internal combustion engine (ICE) with an electric motor (EM) and a large rechargeable battery. This hybrid powertrain enables all-electric driving for extended periods of time and overcomes the concern of range anxiety [178, 114]. Intensive

efforts on PHEVs have developed energy management strategies (EMS) for coordinating the power split in a fuel-efficient way [250]. However, the performance of EMS is often compromised by the complexity and uncertainty of driving conditions. It is therefore desirable to synergize internal powertrain coordination and external driving behaviour [28]. Meanwhile, the longitudinal driving task gradually shifts from the human driver to in-vehicle automated systems. For example, the radar-aided adaptive cruise control (ACC) and the communication-enabled cooperative ACC (CACC) can regulate the vehicle speed to maintain a safe inter-vehicles spacing or reach the user-specified speed [251–253]. These automated driving systems are designed to improve energy efficiency, road safety, and traffic throughput by optimizing velocity trajectories, and can be integrated with the EMS to further boost fuel economy [254]. Consequently, the multi-objective co-optimization of ACC and EMS is gaining traction among automakers and policymakers [82].

Vehicles may operate in two longitudinal driving conditions of car-following and platooning. Accordingly, studies on multi-objective co-optimization of ACC and EMS can be divided into the following two groups [255]:

1) Studies on car-following scenarios [175, 179, 174] mainly address constraints of the movement of the preceding vehicle, to improve fuel economy, tracking safety, etc. For instance, a predictive car-following power management system for PHEVs is demonstrated to simultaneously coordinate battery state-of-charge (SoC) planning, inter-vehicle spacing, and power split in a cost-optimal manner [97]. Adopting similar techniques, a deep fusion method with ACC and EMS claims to reduce fuel consumption by 5% [176].

2) Studies on platooning scenarios [256, 257] are primarily concerned with interactions between multiple vehicles. In a study on integrated optimization of internal powertrain energy management and external driving coordination for multiple hybrid electric vehicles (HEVs), the optimal results indicate a fuel saving of 17.9% compared with their baseline counterparts [26]. A two-layer hierarchical control system is constructed for a set of connected HEVs on a hilly terrain [258]. The top layer is tasked with cooperative driving and battery SoC planning; the bottom layer determines the power split and the gear shifting strategy.

All the studies reviewed so far use weighted-sum methods to solve the multi-objective ACC and EMS co-optimization problems, by converting the multiple objectives into

a single cost function. As discussed in Section 2.3.1, these methods cannot, however, determine the weights and the normalization factors that can optimally balance and scale the multiple objective functions for a problem with little or no information [180], which can cause misleading optimization results. To overcome these limitations, we propose a Pareto-based framework dealing with the multi-objective ACC and EMS co-optimization for PHEVs. The high-level knowledge (e.g., trade-offs and scale differences between objectives) of the Pareto frontier (PF) assists in finding the best compromise solution.

The rest of this chapter is structured as follows. Section 4.2 describes the integrated ACC and EMS control framework as well as the augmented system dynamics for car-following and power-split. Section 4.3 presents the multi-objective problem and optimization methods. In Section 4.4, optimization results from the Pareto and the weighted-sum methods are compared. Section 4.5 concludes the work by summarizing the main findings.

4.2   Integrated control framework

Figure 4.1 illustrates the integrated ACC and EMS control framework as well as the augmented system dynamics for car-following and power-split. Their mathematical models are elaborated as follows.
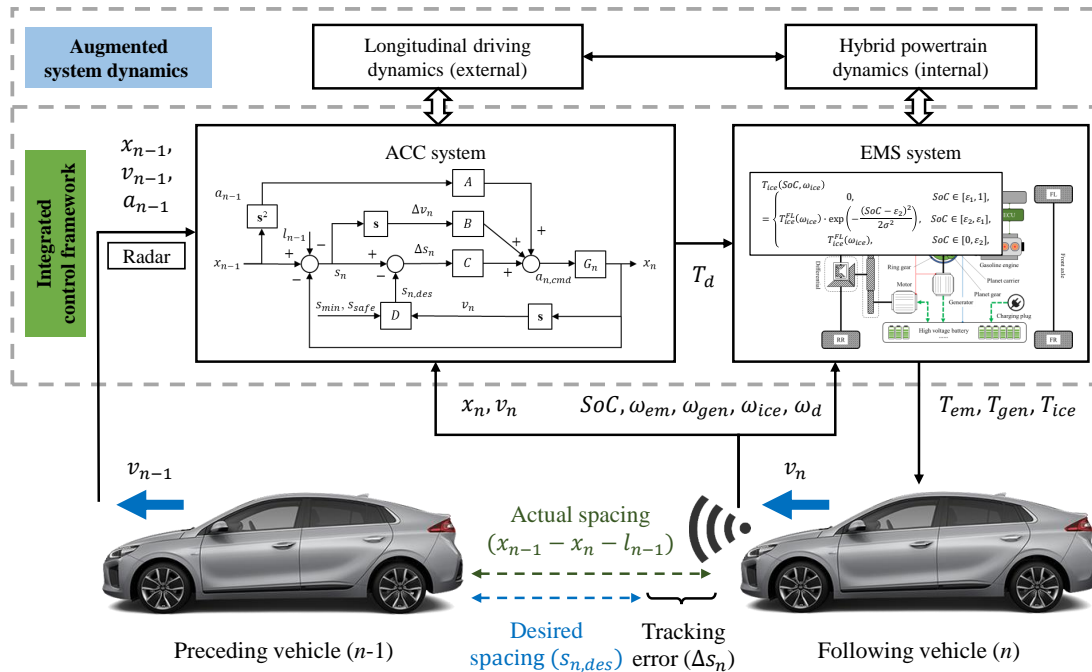
Figure 4.1 The augmented system dynamics and the integrated control framework.

4.2.1 Longitudinal driving dynamics

The longitudinal motion dynamics of the following vehicle is described by the equations,

$$\begin{cases} v_n(t) = \dot{x}_n(t), \\ a_n(t) = \dot{v}_n(t), \\ \tau_a \cdot \dot{a}_n(t) + a_n(t) = a_{n,cmd}(t), \\ m \cdot a_n(t) = \frac{1}{r_w} T_d(t) - \frac{1}{2} \rho C_d A_n \cdot v_n(t)^2 - f \cdot mg \cdot \cos\theta - mg \cdot \sin\theta, \end{cases} \tag{4.1}$$

where x_n, v_n, and a_n denote the following vehicle's longitudinal position (m), velocity (m/s), and acceleration (m/s^2), respectively; $a_{n,cmd}$ is the acceleration command (m/s^2) of the ACC system; τ_a means the actuation delay (s); r_w is the wheel radius (m); T_d represents the driving torque (Nm) on the wheel axle; m is the vehicle operating mass (kg); ρ is the air density (kg/m^3); C_d stands for the air drag coefficient; A_n is the vehicle effective frontal area (m^2); θ is the road slope (rad); g is the gravitational constant (9.81 m/s^2); and f is the rolling resistance coefficient.

4.2.2 Adaptive cruise control (ACC)

According to ACC systems reported in previous studies [139, 259], the acceleration command ($a_{n,cmd}$) can be computed in two ways: (1) $a_{n,cmd}^x$ based on the inter-vehicle spacing and the relative speed or (2) $a_{n,cmd}^y$ based on the difference between the actual speed and the maximum safe speed. Consequently, the ACC system adopts the more restrictive choice, i.e.,

$$\begin{cases} a_{n,cmd}(t) = \min\left(a_{n,cmd}^x(t), a_{n,cmd}^y(t)\right), \\ a_{n,cmd}^x(t) = a_{n-1}(t - \tau_p) + k_v \cdot \left(v_{n-1}(t - \tau_p) - v_n(t - \tau_p)\right) \\ \qquad\qquad + k_s \cdot \left(s_n(t - \tau_p) - s_{n,des}(t - \tau_p)\right), \\ a_{n,cmd}^y(t) = \left(v_n^{max}(t - \tau_p) - v_n(t - \tau_p)\right)/t_s, \end{cases} \tag{4.2}$$

where a_{n-1} and v_{n-1} are the preceding vehicle's acceleration (m/s^2) and speed (m/s), respectively. t_s represents the control sample time (0.1 s); s_n is the spacing (m) from the front bumper of the following vehicle to the back bumper of the preceding one; $s_{n,des}$ is the desired inter-vehicle spacing (m); v_n^{max} is the maximum safe speed (m/s); and k_v and k_s

are gain factors to minimize the speed difference and the tracking error, respectively. Here τ_p is the reaction time (s) indicating the perception or sensing delays. Previous studies revealed that reaction time has considerable impacts on the performance of ACC systems, particularly on stability [163, 260, 167]. For example, Wang et al. [261] showed both the local and string stability of ACC platoons deteriorate with the increase of reaction time.

The desired spacing, $s_{n,des}$, is the maximum among three values: s_{hw}, according to the time headway setting; the safe following distance, s_{safe}, considering the deceleration capabilities of the vehicles; and the minimum allowed distance, s_{min}, as given by

$$
\begin{cases}
s_{n,des}(t) = \max \left(s_{hw}(t), s_{safe}(t), s_{min} \right), \\
s_{hw}(t) = v_n(t) \cdot t_{hw}, \\
s_{safe}(t) = \frac{v_n(t)^2}{2} \cdot \left(\frac{1}{a_{min}} - \frac{1}{\hat{a}_{min}} \right),
\end{cases}
\tag{4.3}
$$

where s_{min} is the minimum clearance (2.0 m) in the standstill situation; t_{hw} is the system-specified time headway (s); and $\hat{a}_{min}$ and a_{min} are negative numbers indicating the maximum braking decelerations (m/s^2) of the leader and the follower, respectively.

The maximum safe speed v_n^{max} is important for avoiding rear-end collisions when the preceding vehicle initiates emergency braking, which can be expressed as

$$
\begin{cases}
v_n^{max}(t) = \sqrt{-2a_{min} \cdot s_0(t)}, \\
s_0(t) = \left(x_{n-1}(t) - x_n(t) - l_{n-1} \right) - v_n(t)\tau_p - \frac{v_{n-1}(t)^2}{2\hat{a}_{min}},
\end{cases}
\tag{4.4}
$$

where x_{n-1} and l_{n-1} are the preceding vehicle's position (m) and length (m), respectively.
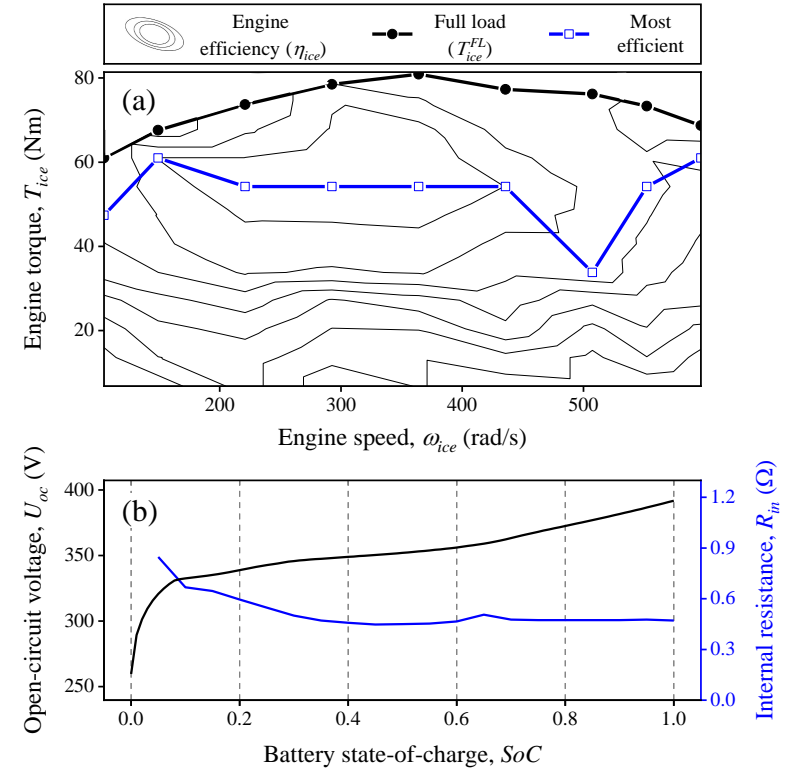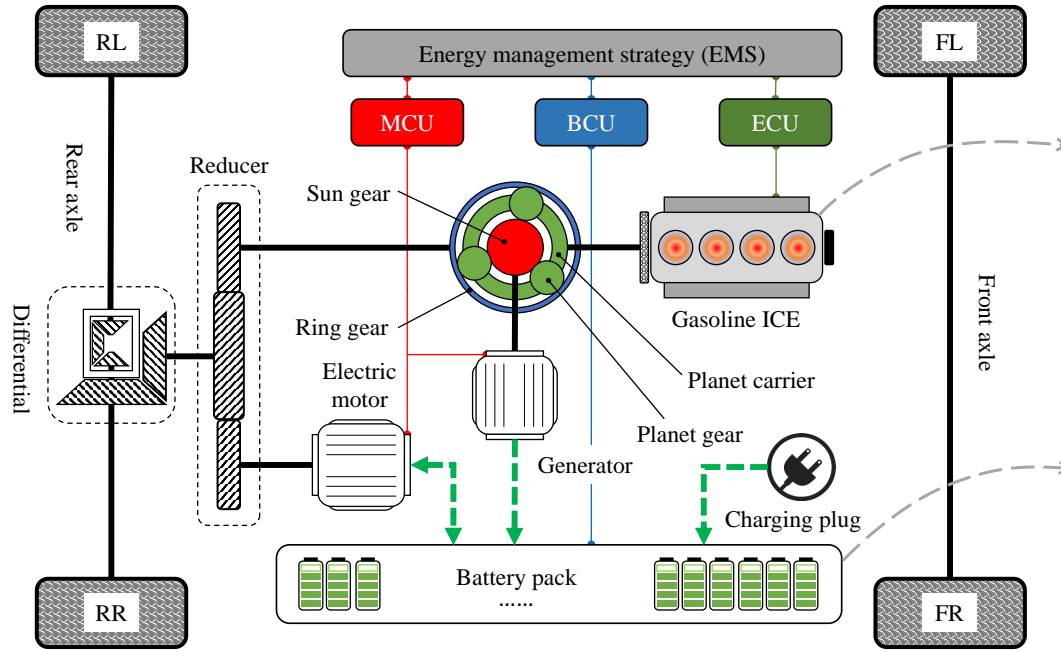
Note: MCU = motor control unit; BCU = battery control unit; ECU = engine control unit; ICE = internal combustion engine; RL = rear-left wheel; RR = rear-right wheel; FL = front-left wheel; FR = front-right wheel.

Figure 4.2 The power-split PHEV powertrain (left) and the dynamics of (a) the ICE and (b) the battery pack.

4.2.3 Hybrid powertrain dynamics

Figure 4.2 (left) shows the PHEV powertrain with a power-split configuration [26]. This system divides the engine power along two paths through a planetary gearset (PGS); one path goes to the generator to produce electricity while the other one drives the wheels. The PGS includes a planet carrier, a sun gear, and a ring gear, which are connected to the gasoline ICE, the generator, and the reducer, respectively. Their torque balance is given by

$$
\begin{cases}
T_{em}(t) = -\left(\frac{r_r}{r_s+r_r}\right)T_{ice}(t) + \frac{1}{\kappa_c \cdot \kappa_f}T_d(t), \\
\omega_{em}(t) = \kappa_c\kappa_f \cdot \omega_d(t), \\
T_{gen}(t) = -\left(\frac{r_r}{r_s+r_r}\right)T_{ice}(t), \\
\omega_{ice}(t) = \left(\frac{r_r}{r_s+r_r}\right)\omega_{em}(t) + \left(\frac{r_s}{r_s+r_r}\right)\omega_{gen}(t),
\end{cases}
\tag{4.5}
$$

where T_{ice}, T_{em}, and T_{gen} indicate torques (Nm) that are respectively delivered from the ICE, the electric motor (EM), and the generator; ω_{ice}, ω_{em}, ω_{gen}, and ω_d are respectively the angular velocities (rad/s) of the ICE, the EM, the generator, and the driveline; κ_c and κ_f are fixed gear ratios of the reducer and the differential, respectively; and r_s and r_r are respectively the radii of the sun gear and the ring gear.

The 1.5 L gasoline ICE is modeled using its empirical performance map, as displayed in Figure 4.2 (a). According to the data in the map, the instantaneous fuel consumption rate ($\dot{m}_f$, g/s) is calculated by

$$
\dot{m}_f(t) = \frac{T_{ice}(t) \cdot \omega_{ice}(t)}{H_v \cdot \eta_{ice}(t)},
\tag{4.6}
$$

where H_v is the lower heating value (J/g) of gasoline and η_{ice} is the ICE thermal efficiency.

The high voltage (HV) battery pack consists of lithium-ion 18650-type cells. The battery dynamics are governed by the following equations [239, 262], i.e.,

$$
\begin{cases}
P_b(t) = U_{oc}I_b(t) - I_b(t)^2 R_{in}, \\
\dot{SoC}(t) = -\frac{I_b(t)}{Q_b} = -\frac{U_{oc}-\sqrt{U_{oc}^2-4R_{in}P_b(t)}}{2R_{in}Q_b},
\end{cases}
\tag{4.7}
$$

where I_b and P_b are respectively the current (A) and the power (W) of the battery pack; R_{in} and U_{oc} respectively denote the internal resistance (Ω) and the open-circuit voltage

(V), whose dynamic characteristics are displayed in Figure 4.2 (b) (assuming batteries operate at a constant temperature of 35 °C); Q_b is the nominal capacity (As) of the battery pack. The battery SoC is subject to the constraints ($SoC \in [0.2, 0.8]$), to ensure safe battery operation and prolong its service life [263]. According to power balance, the battery power P_b is given by

$$P_b(t) = \frac{\eta_{em}^{\delta}}{r_w} T_d(t) v_n(t) - \eta_{gen} T_{ice}(t) \omega_{ice}(t) - \frac{\kappa_c \kappa_f r_r \cdot (\eta_{em}^{\delta} - \eta_{gen})}{r_w(r_r + r_s)} T_{ice}(t) v_n(t), \quad (4.8)$$

where η_{em} and η_{gen} represent the efficiency factors of the EM and the generator, respectively. The EM can either drive the wheels (δ = -1) or charge the battery by performing regenerative braking (δ = 1).

Table 4.1 Main specifications of the power-split PHEV.

Parameter	Value	Parameter	Value
m	1350 kg	r_w	0.28 m
A_n	2.2 m^2	ρ	1.225 kg/m^3
C_d	0.3	f	0.021
r_s	0.03 m	r_r	0.078 m
κ_c	3.9	κ_f	3.2
Q_b	90000 As	H_v	42000 J/g

4.2.4 Energy management strategy (EMS)

Charge depleting - charge sustaining (CD-CS) is a well-proved EMS [264], taking advantage of the PHEV's extended all-electric (or zero-emissions) range and protecting battery cells from overcharge or overdischarge. Moreover, this strategy is favoured by its simplicity and ease of implementation. According to the CD-CS model defined in our previously published study [96], the engine power demand, P_{ice}, is computed as a function of the battery SoC, i.e.,

$$P_{ice}(SoC) = \begin{cases} 0, & SoC \in [\varepsilon_1, 1], \\ P_{ice}^{FL} \cdot \exp\left(-\frac{(SoC - \varepsilon_2)^2}{2\sigma^2}\right), & SoC \in [\varepsilon_2, \varepsilon_1], \\ P_{ice}^{FL}, & SoC \in [0, \varepsilon_2], \end{cases} \quad (4.9)$$

where σ is a constant factor; ε_1 and ε_2 are two thresholds that are equal to 0.8 and 0.2, respectively; and P_{ice}^{FL} is the full load power of the engine. The PHEV main specifications mentioned in this section are summarized in Table 4.1.

4.3 Multi-objective problem formulation

Figure 4.3 gives an overview of the multi-objective ACC and EMS co-optimization problem. The decision vector (or solution), the objective vector (or outcome), and the state vector are exemplified in subplots. Different driving cycles of the preceding vehicle are provided for optimization and validation purposes. The formulated optimization problem is solved by the Pareto method or the weighted-sum method (serving as a benchmark), by guiding a population of candidate solutions towards better solutions that simultaneously minimize multiple objectives.

4.3.1 Multi-objective problem formulation

Figure 4.3 (c) indicates that the decision vector $K = [k_v, k_s, \sigma]$ consists of the principal control parameters in ACC and EMS systems. k_v and k_s are gain factors in Equation (4.2), that determine the car-following behaviour; the variable, σ, in Equation (4.9) governs the torque (or power) split. Previous studies [96, 259] have given the recommended value, $K_{base} = [0.58, 0.10, 0.10]$, that is utilized as the baseline scheme in this work.

(a) Driving cycles

For optimization

5×WLTC

10×NEDC

For validation

JRC real-world (with varying road slope)

J = [tracking capability J_1 (m), ride comfort J_2 (m/s^2), power consumption J_3 (kW)]   Objective vector (outcome)

(b) Augmented system dynamics

State vector

Position,
Speed,
Acceleration,
Spacing,
.
.
.
Battery SoC,
Battery current,
Engine speed,
Engine torque,
Motor speed,
Generator speed,
.
.
.
.

(c) Integrated control framework

ACC & EMS

Control parameters

Decision vector (solution)

$K=[k_v, k_s, \sigma]$

(d) Multi-objective co-optimization

Non-dominated sorting

Crossover & mutation

Random initial population

Parent population

Offspring population

F1
F2
F3
F4
F5

Reference-point-based selection

F3
F4
F5

New generation

F1
F2
F3

F3
F2
F1

Pareto method

(Simultaneously $\min_K J_1$, $\min_K J_2$, $\min_K J_3$)

Weighted-sum method

($\min_K F = w_1 \frac{J_1}{n_1} + w_2 \frac{J_2}{n_2} + w_3 \frac{J_3}{n_3}$)

Global Best Solution

Pareto Best Solution

Note: WLTC = Worldwide Harmonised Light Vehicle Test Cycle; NEDC = New European Driving Cycle; JRC = Joint Research Centre; ACC = adaptive cruise control; EMS = energy management strategy.

Figure 4.3 Multi-objective co-optimization using the Pareto method and the weighted-sum method.

As an image of the decision vector K through the optimization algorithm, the objective vector $J = [J_1, J_2, J_3]$ is mainly concerned with tracking safety, ride comfort, and energy efficiency, which can be described by

$$\begin{cases} \min_K J_1 = \frac{1}{t_f - t_0} \int_{t_0}^{t_f} \|s_n(t) - s_{n,des}(t)\|_2 \, dt, \\ \min_K J_2 = \frac{1}{t_f - t_0} \int_{t_0}^{t_f} \|a_n(t)\|_2 \, dt, \\ \min_K J_3 = \frac{1}{1000 \, (t_f - t_0)} \Big(\int_{t_0}^{t_f} \dot{m}_f(t) H_v \, dt + \big(SoC(t_f) - SoC(t_0)\big) Q_b U_b \Big), \end{cases} \tag{4.10}$$

where t_0 and t_f are respectively the start and end time (s) of the driving cycle adopted. Each element of the objective vector is defined as follows:

1) Tracking capability, J_1, (m) is a 2-norm function of tracking error [146] and an important indicator for improving car-following safety and traffic throughput [144].

2) Ride comfort, J_2, (m/s^2) is defined as a 2-norm function of the following vehicle's longitudinal acceleration. Although some studies utilize jerk as the indicator of ride comfort [176], acceleration is a more intuitive measure of the driver's sensation when driving on the road [181].

3) Power consumption, J_3, (kW) is the average power demand to complete the driving cycle. The terms inside the parentheses represent the total energy consumption (J) including the consumed gasoline and the battery charge depletion [181].

Figure 4.3 (a) shows the preceding vehicle's driving cycles: 1) 5×WLTC indicates 5 consecutive repetitions of the Worldwide Harmonised Light Vehicle Test Cycle; 2) 10×NEDC means 10 consecutive repetitions of the New European Driving Cycle; 3) JRC real-world, published by the Joint Research Centre (JRC) of the European Commission, is a highway driving trajectory with varying road slope: this field test was conducted on a section of Autostrada A26 (Italy) between Ispra and Vicolungo, a 40-km trip, to collect driving data under actual traffic conditions. Among these driving cycles, the first one (5×WLTC) is applied in the multi-objective optimization process; the other two (10×NEDC and JRC real-world) are utilized to validate the reliability and robustness of the resulting optimal solutions.

4.3.2 Multi-objective optimization methods

As demonstrated in Figure 4.3 (d), the Pareto method and the weighted-sum method, for solving the above optimization problem, are two evolutionary algorithms (EAs) generating high-quality solutions by relying on bio-inspired operators such as mutation, crossover, and selection. However, the two methods have different selection schemes, i.e., different approaches to ordering the objective vectors in each generation.

1) Pareto method

In the formulated multi-objective ACC and EMS co-optimization problem, a single solution that simultaneously optimizes each objective is nonexistent. Instead, there exist a number of (possibly infinite) Pareto optimal solutions, in which one objective cannot be improved without degrading at least one of the other objectives. A solution K^1 is said to dominate (or Pareto) another solution K^2 (in notation, $K^1 \preceq K^2$) if the following conditions are met [180], as described by,

$$
\begin{cases}
J_i(K^1) \leq J_i(K^2), \forall\, i \in [1,2,3], \\
J_j(K^1) < J_j(K^2), \exists\, j \in [1,2,3],
\end{cases}
\tag{4.11}
$$

The solutions that are not dominated by others are called Pareto optimal K_{PF}. Their corresponding outcomes (or objective vectors J_{PF}) are represented by a Pareto frontier (PF). The high-level knowledge (e.g., trade-offs and scale differences between objectives) of the Pareto set (K_{PF}, J_{PF}) assists in finding a best compromise solution. To find an approximation of the entire Pareto frontier, a non-dominated sorting genetic algorithm (NSGA-III) [243, 244] is employed in this work.

2) Weighted-sum method

Serving as a benchmark, the weighted-sum method integrates different objectives into a single cost function using configurable weights. After the scalarization, the objective vectors can be ordered as per the composite cost value. Mathematically, the weighted-sum method can be represented by

$$
\min_K F = \sum_{i=1}^{3} w_i \frac{J_i(K)}{N_i} \text{ for } w_i \geq 0 \text{ and } \sum_{i=1}^{3} w_i = 1,
\tag{4.12}
$$

where w_i is the weight factor, and N_i is the normalization factor. Although this method is computationally efficient, it cannot determine the factors w_i and N_i that can optimally balance and scale the objective functions for a problem with little or no prior information [180]. In this work, a particle swarm optimization (PSO) algorithm [178] is applied to minimize the cost function, F, and find the corresponding optimal solution, K_{WS}.

4.4 Results and discussion

This section will be divided into four parts. Firstly, the Pareto frontier (K_{PF}, J_{PF}) reveals the high-level knowledge, e.g., trade-offs and scale differences between the objectives, for the ACC and EMS co-optimization problem. Secondly, the Pareto knowledge assists in finding a best compromise solution K_{PF}^*, whose safety and energy benefits are validated by comparing with the baseline scheme (K_{base}) in various driving conditions. Thirdly, the weighted-sum optimal solutions with (K_{WS}^P) and without (K_{WS}^B) the Pareto knowledge, highlight that the weighted-sum method cannot optimally scale the objective functions if the Pareto information is unknown. Finally, we compare the sensitivities of the objective functions to variations in the reaction time (τ_p, s).

4.4.1 The Pareto frontier

Figure 4.4 shows the representative Pareto frontier (PF) approximated by NSGA-III. For visualization and analysis purposes, the three-dimensional (3D) objective vectors are projected onto the 2D scatter plots of Figure 4.4 (a)-(c). The ideal (z^{ideal}) and the nadir (z^{nadir}) vectors correspond to the lower and the upper boundaries, respectively. Figure 4.4 (a) presents a trade-off between tracking capability, J_1, and ride comfort, J_2, since one of them will deteriorate when the other is improved on the PF. Figure 4.4 (b) shows a similar relationship between tracking capability, J_1, and power consumption, J_3. However, Figure 4.4 (c) demonstrates a harmonious relationship between ride comfort, J_2, and power consumption, J_3, because the reduction of any one is rewarded with a simultaneous decrease in the other. It also suggests that acceleration levels of the PHEV impact significantly on its energy consumption [144].

Marginal distributions of the objectives are illustrated by the box-whisker diagrams in Figure 4.4 (d)-(f). The height of the box is the interquartile range (IQR) between the
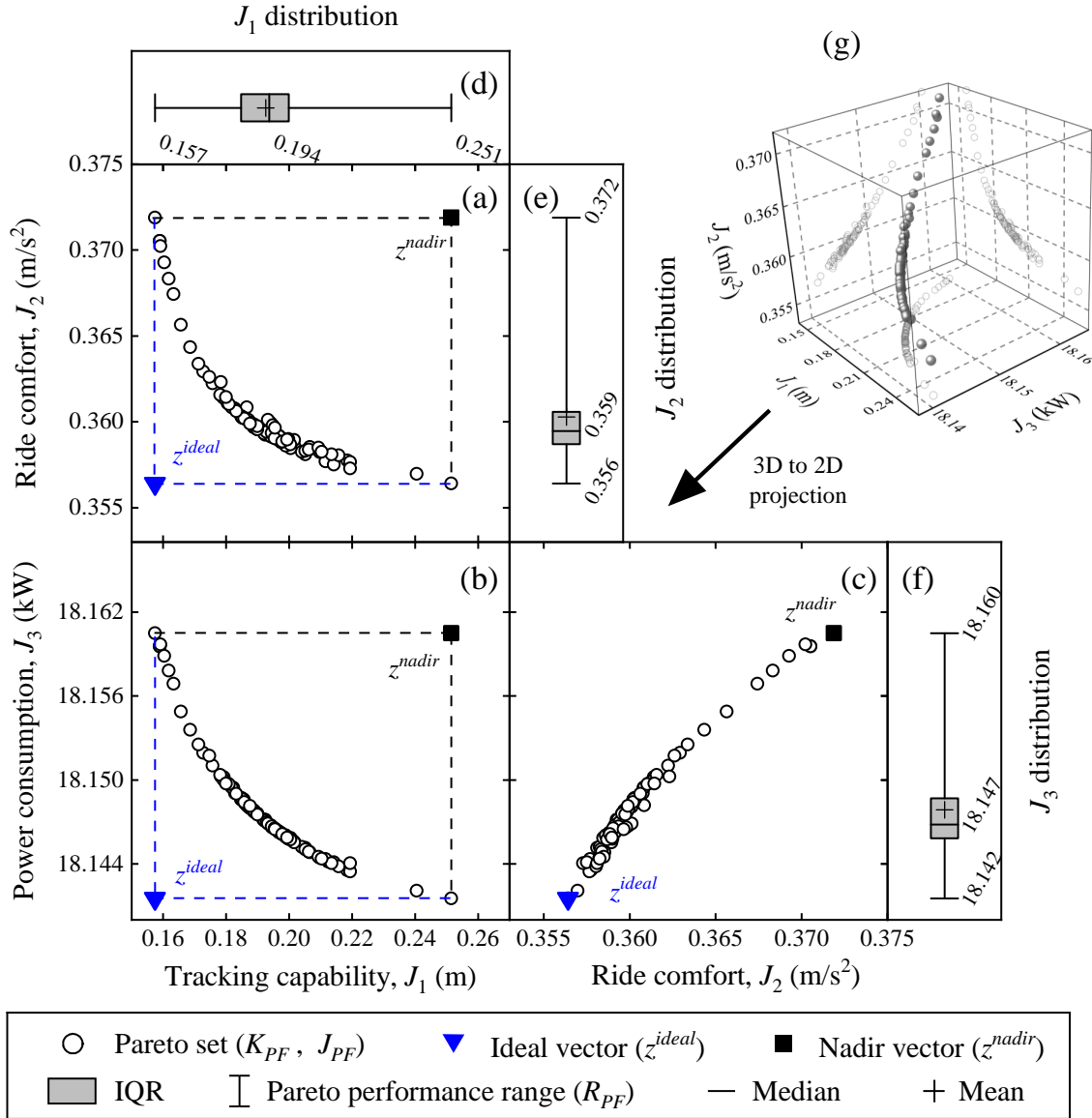
Figure 4.4 The representative Pareto frontier (PF) approximated by NSGA-III.

first quartile (Q1, 25%) and the third quartile (Q3, 75%). The median (the band inside the box) denotes the second quartile (Q2, 50%). The ends of the whisker represent the Pareto performance range ($R_{PF} = z^{nadir} - z^{ideal}$). Table 4.2 summarizes the R_{PF} values and the medians of the PF, indicating that different objective functions are measured on different scales. For example, the median of power consumption, J_3, is two orders of magnitude larger than that of the tracking capability, J_1.

4.4.2 Benefits of the Pareto optimum

Usually, only one solution is required but all Pareto solutions (K_{PF}) are considered equally good because their objective vectors, J_{PF}, cannot be ordered directly. To find a best

Table 4.2 Marginal distributions of objectives on the Pareto frontier.

Objective	R_{PF}	Median
Tracking capability, J_1	0.094	0.194
Ride comfort, J_2	0.016	0.359
Power consumption, J_3	0.018	18.147

compromise solution, a penalty function, u, utilizes the above high-level Pareto knowledge to rank the Pareto set [246], i.e.,

$$\min_{K \in PF} u\Big(J(K)\Big) = \min_{K \in PF} \sum_{i=1}^{3} w_i \frac{J_i(K) - z_i^{ideal}}{z_i^{nadir} - z_i^{ideal}}, \tag{4.13}$$

where z_i^{ideal} and z_i^{nadir} adjust objectives measured on different scales to a notionally common scale; and the weight factor w_i represents the decision maker's preferences, whose value is assigned as $w = [0.5, 0.25, 0.25]$ to balance trade-offs between the objectives. Consequently, the Pareto solution with the minimum penalty, u, is the best compromise one, $K_{PF}^* = [1.22, 1.06, 0.05]$ in this study and defined as the Pareto optimum.

Figure 4.5 draws a comparison between the Pareto optimum (K_{PF}^*) and the baseline scheme (K_{base}) in terms of their car-following and power-split performances in the $5 \times$WLTC driving test. Figure 4.5 (i) displays a zoomed portion of the inter-vehicle spacing (m), s_n, profiles of Figure 4.5 (a). It can be seen from these two graphs that K_{PF}^* can always meet the minimum spacing requirement in Equation (4.3), namely, $s_n \geq 2.0$ m; this constraint, however, is violated by the K_{base} control design. Moreover, Figure 4.5 (b) shows that K_{PF}^* can significantly reduce tracking error, $s_n - s_{n,des}$, thus enhancing car-following safety. Figure 4.5 (c) and (d) illustrate the following vehicle's speed and acceleration, respectively. Figure 4.5 (e)-(h) compare the power-split dynamics of the two control schemes. For the K_{base} design, the engine and the generator started to work at $\sim$1700 s, i.e. switching to the CS mode; the battery SoC was then kept at $\sim$0.4. For the K_{PF}^* design, however, the CS mode was postponed until $\sim$3000 s and the battery SoC was controlled at the lower level of $\sim$0.3.

Table 4.3 compares the control performances J_i between the Pareto optimum, K_{PF}^*, and the baseline scheme, K_{base}, in the optimization ($5 \times$WLTC) and validation ($10 \times$NEDC and JRC real-world) driving cycles. The data highlight that the Pareto optimal solution for ACC and EMS design can provide considerable and consistent benefits in different driving
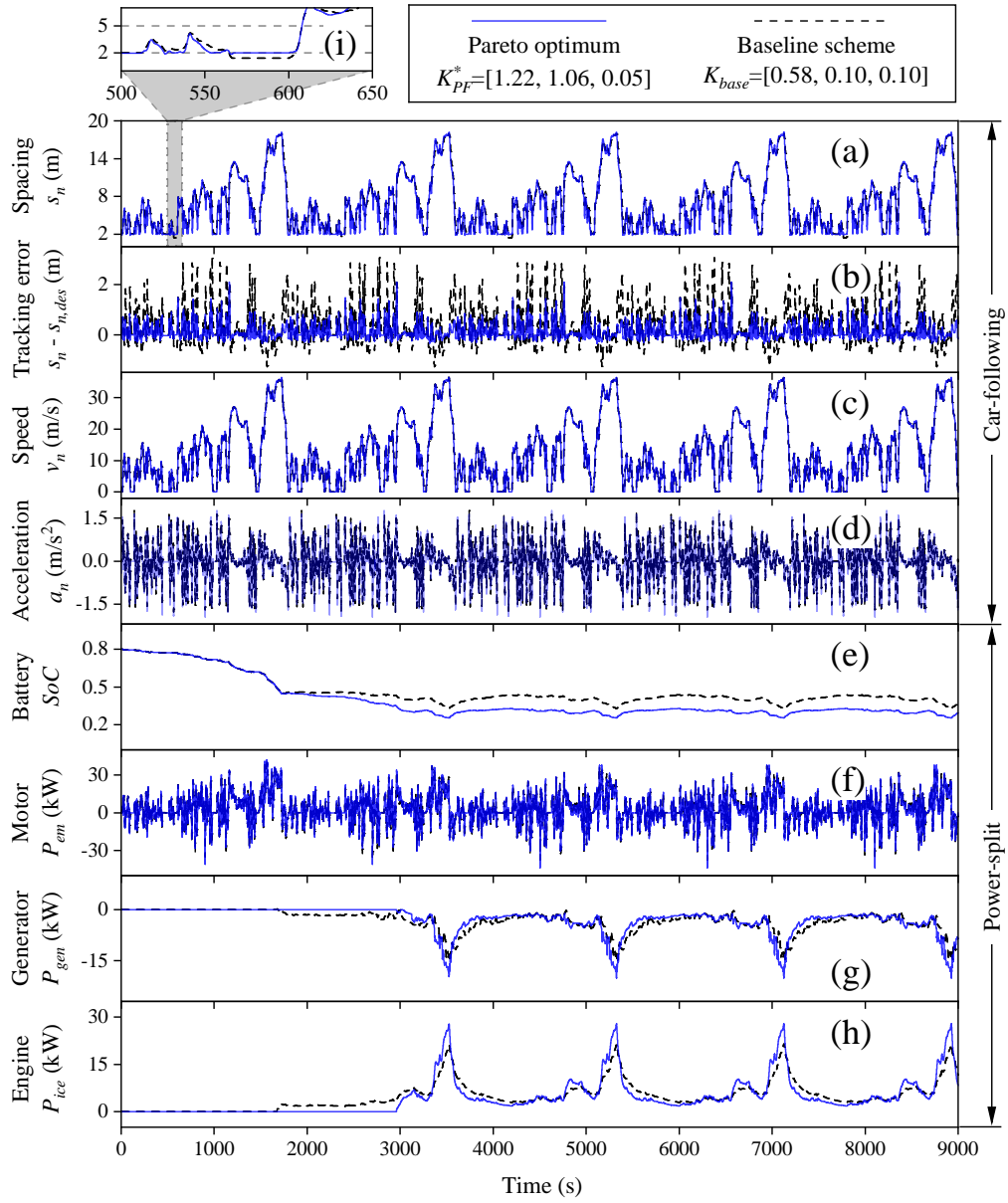
Figure 4.5 Comparison of control performances between the Pareto optimum and the baseline scheme.

conditions. For example, in the JRC real-world driving cycle with varying road slope, the Pareto optimum, K_{PF}^*, can reduce energy consumption (by 7.57%) and tracking error (by 68.94%), while at the same time satisfying ride comfort needs.

Table 4.3 The benefits of the Pareto optimum.

	5×WLTC			10×NEDC			JRC real-world		
	J_1 (m)	J_2 (m/s^2)	J_3 (kW)	J_1 (m)	J_2 (m/s^2)	J_3 (kW)	J_1 (m)	J_2 (m/s^2)	J_3 (kW)
K_{base}	0.5640	0.3638	19.2638	0.3710	0.2588	12.9026	0.9462	0.4831	47.5019
K_{PF}^*	0.1858	0.3602	18.1484	0.0936	0.2634	11.7137	0.2939	0.4915	43.9082
Reduction (%)	67.06	0.99	5.79	74.77	-1.78	9.21	68.94	-1.74	7.57

4.4.3 Weighted-sum optimums

Serving as a benchmark, the weighted-sum method uses the same weight vector, $w = [0.5, 0.25, 0.25]$, as the Pareto method to balance the trade-offs between the objectives. For comparison purposes, the weighted-sum method in this work utilizes two different normalization techniques [265]:

1) Normalization (without the Pareto knowledge) by objective values at the baseline point, $N = J(K_{base})$. The corresponding weighted-sum optimum is (K_{WS}^B, J_{WS}^B).

2) Normalization (with the Pareto knowledge) by the Pareto performance range, $N = R_{PF} = z^{nadir} - z^{ideal}$. The corresponding weighted-sum optimum is (K_{WS}^P, J_{WS}^P).

Figure 4.6 (a)-(c) illustrate the evolutions of J_{WS}^P and J_{WS}^B during 30 PSO iterations. It is obvious that the weighted-sum method is computationally efficient because the objectives converged rapidly (within 20 generations). However, different normalization techniques lead to different final optimums. In Figure 4.6 (d)-(f), the weighted-sum optimums are projected onto 2D planes and compared with the Pareto frontier (PF). It is worth noting that J_{WS}^P is located on the PF and very close to the Pareto optimum, J_{PF}^*. In contrast, J_{WS}^B presents an over-optimized tracking capability, J_1, which can, in turn, compromise the other performance measures, i.e. the ride comfort, J_2, and the power consumption, J_3. Table 4.4 summarizes the final optima through the Pareto method as well as the weighted-sum methods with differing normalization.

These comparisons reveal that the weighted-sum method cannot determine the normalization factors that can optimally scale the objective functions if the high-level Pareto knowledge is unknown before the optimization begins. The Pareto method can overcome this limitation by producing a set of Pareto optimal solutions. These solutions
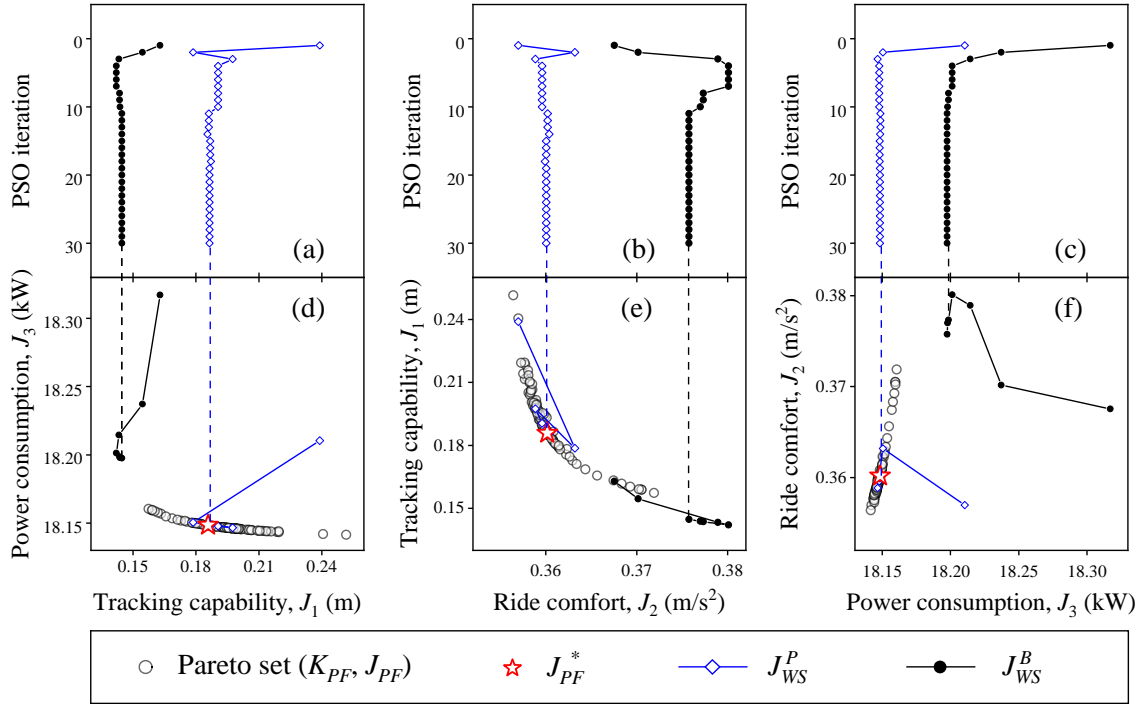
Figure 4.6 Multi-objective optimization using weighted-sum methods.

Table 4.4 Comparison between the Pareto and the weighted-sum optimums.

	K_{PF}^{*} [1.22, 1.06, 0.05]	K_{WS}^{P} [1.23, 1.06, 0.05]	K_{WS}^{B} [1.89, 2.49, 0.05]
J_1 (m)	0.1858	0.1864	0.1447
J_2 (m/s^2)	0.3602	0.3601	0.3758
J_3 (kW)	18.1484	18.1483	18.1976
Penalty, u	30.2384	30.2640	50.0000

Note: The results are based on the 5×WLTC driving cycle.

indicate trade-offs and scale differences between objectives and assist in finding a best compromise solution.

4.4.4 Sensitivities to the reaction time

Representing the sensing or perception delay, the reaction time, τ_p, in Equations (4.2) and (4.4) is a major factor that impacts tracking safety, ride comfort, and fuel economy. This section demonstrates the sensitivities of the objectives to τ_p variations and compares the performance robustness of the Pareto and the weighted-sum optima.
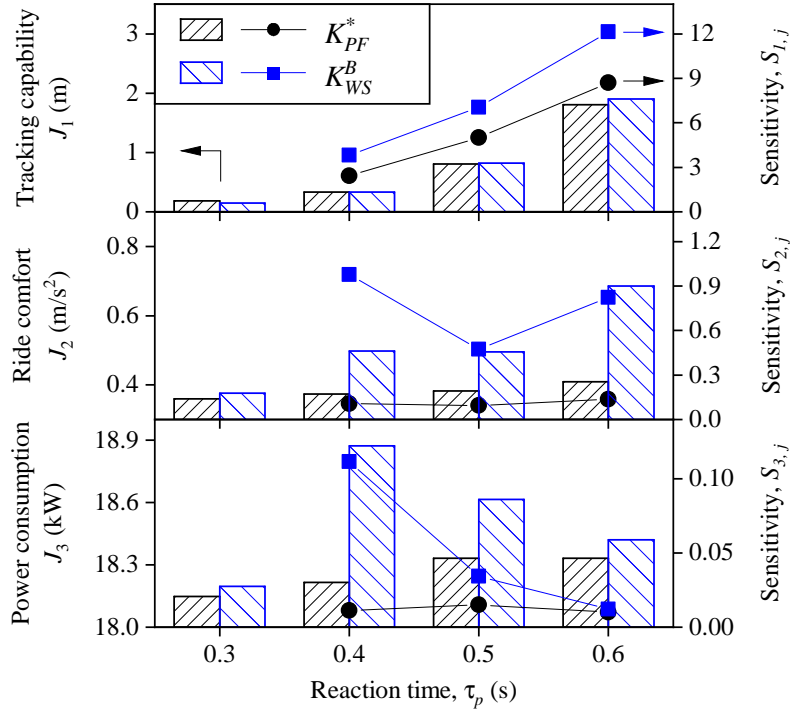
Figure 4.7 Sensitivities of the objectives to reaction time τ_p variations.

The sensitivity of each objective to the reaction time variation is given by [178]

$$S_{i,j} = \left| \frac{\left(J_i(\tau_p^j) - J_i(\tau_p^0)\right)/J_i(\tau_p^0)}{(\tau_p^j - \tau_p^0)/\tau_p^0} \right|, \tag{4.14}$$

where $S_{i,j}$ is the sensitivity of the i-th objective J_i ($i = 1, 2, 3$) to the variation of the j-th reaction time, $\tau_p^j \in [0.3, 0.4, 0.5, 0.6]$ s. $J_i(\tau_p^0)$ is chosen as the reference corresponding to the situation when $\tau_p^j = \tau_p^0 = 0.3$ s. The larger the sensitivity value, the more significant the influence of reaction time on the outcome.

In Figure 4.7, the tracking capability (J_1) shows the highest sensitivity to variation in τ_p. Its sensitivity, $S_{1,j}$, increases with increasing reaction time. The power consumption, J_3, is the least sensitive criterion, whose sensitivity is two orders of magnitude smaller than that of J_1. Therefore, the reaction time impacts significantly on tracking safety, but its effect on energy saving is trivial. In addition, compared with the weighted-sum counterpart, K_{WS}^B, the Pareto optimum, K_{PF}^*, always exhibits less sensitivity to τ_p variation for every objective, indicating a higher level of performance robustness against a range of operational delays in various driving scenarios.

4.5   Summary

In vehicle control design, the co-optimization of electrification, automation, and connectivity is gaining traction among automakers and policymakers. Previous approaches such as weighted-sum methods overlook trade-offs and scale differences inherent in these multi-objective problems, resulting in misleading optimizations. To overcome these limitations, this study proposes a Pareto-based framework demonstrated to optimize system parameters of adaptive cruise control (ACC) and energy management strategy (EMS) for automated and electrified vehicles (AEVs). The high-level knowledge of the Pareto frontier (PF) assists in finding a best compromise solution. The optimized systems can be directly applied in real applications. The results of this study are as follows:

- The Pareto frontier (PF) suggests that the comfort and the energy targets are harmonious, but they both conflict with the safety target. Their objective values are measured on different scales.

- In the validation using real-world driving data, the Pareto optimum, K_{PF}^*, for ACC and EMS systems, compared with the baseline scheme, K_{base}, can reduce energy consumption (by 7.57%) and tracking error (by 68.94%), while at the same time satisfying ride comfort needs.

- In contrast to the weighted-sum method, the Pareto method can optimally balance and scale multiple objective functions, and therefore, help a decision maker identify a solution achieving satisfactory trade-offs among multiple conflicting criteria.

- Sensitivity analysis proves that the vehicle reaction time impacts significantly on tracking safety, but its effect on energy saving is trivial.

Part II

To model driving behaviours of AEVs in traffic simulation

5 Introducing EV dynamics into microscopic traffic models

Many studies have highlighted the added value of incorporating vehicle dynamics into microsimulation. Such models usually focus on simulation of conventional internal combustion engine vehicles (ICEVs), failing to account for the acceleration dynamics of electrified vehicles (EVs) that have different power characteristics from those of ICEVs. In addition, none of them has explicitly dealt with the vehicle's deceleration characteristics. Although it is not commonly considered critical how vehicles decelerate, unrealistic behaviours in simulations can distort both traffic flow and emissions results. The present work builds on the lightweight microsimulation free-flow acceleration (MFC) model and proposes an extension, marking the first attempt to address these research gaps. First, the methodology of the MFC model to capture the dynamics of EVs is described. Then, the experimental setup in different dimensions is introduced for the model validation and implementation. Finally, the results of this study indicate that: (1) the acceleration and deceleration potential curves underlying the MFC model can accurately represent real dynamics of EVs tested on the chassis dynamometer; (2) smooth transitions can be guaranteed after implementing the MFC model in microsimulation; (3) when reproducing the on-road driving trajectories, the MFC model can deliver significant reductions in root mean square error (RMSE) of speed (by $\sim$69%) and acceleration (by $\sim$50%) compared with benchmarks; (4) the MFC model can accurately predict the vehicle 0-100 km/h acceleration specifications, with RMSE 49.4% and 56.8% lower than those of the Gipps model and the intelligent driver model (IDM), respectively.

5.1 Introduction

Developing mathematical models to accurately reproduce vehicles' acceleration behaviour is important for assessing the impacts of emerging technologies (e.g., electrified and automated vehicles) on the performances (e.g., safety, congestion, and emissions) of future road transport [266, 267]. Transportation systems comprise many complex elements (vehicles, infrastructure, drivers, control systems, etc.) that might interact with each other

[73]. The interactions within such systems introduce high stochasticity [268], which in some cases makes the production of quantifiable results difficult or even impossible. Consequently, simplistic behavioural car-following (CF) models such as the Gipps model and the intelligent driver model (IDM) are usually preferred, because of their reduced computational complexity which makes them ideal for large microsimulation studies. However, modelling based on vehicle dynamics has attracted considerable interest lately. According to Ciuffo et al. [252], although behavioural models can correctly replicate traffic dynamics, their capability to reproduce vehicle dynamics and their consequent assessments on emissions and energy consumption are questionable. Recently, lightweight models have been proposed that are quite accurate in reproducing vehicle dynamics, and lightweight enough to be used in large-scale microsimulations, such as the Fadhloun-Rakha model [219] and the microsimulation free-flow acceleration (MFC) model [187]. There is still room for improvement. For example, recent studies show that the relation between fuel consumption and average speed for internal combustion engine vehicles (ICEVs) is questionable for plug-in electric vehicles, for which higher energy consumption is related to free-flow test cases [269]. Thus, more fundamental and explicit characterization of system dynamics in CF models is not only essential but also mandatory for the provision of reliable and robust conclusions. Moreover, the validity and suitability of a certain CF model for engineering applications depend on capturing the observed driving and traffic behaviours with the smallest number of calibration parameters.

Mathematical expressions of state-of-the-art CF models generally comprise two branches [270, 194, 199]: (a) the free-flow branch, regulating the subject vehicle on a free road, which asymptotically approaches its desired speed; and (b) the vehicle interaction branch, governing the subject vehicle in congested conditions, where rear-end collision and traffic instability need to be avoided. Over the past few decades, various CF models have been developed to generate vehicle trajectories that mimic empirical driving behaviour as realistically as possible [219]. Several systematic reviews of widely used CF models have been undertaken [252, 188, 271, 272].

Based on whether vehicle dynamics are explicitly involved in their expressions, the models observed in the literature can be categorized into two groups: kinematics-based and dynamics-based. First, the kinematics-based (or behavioural) models, such as the Gipps model [194], the intelligent driver model (IDM) [199], the Newell model [273], and

the Gazis-Herman-Rothery (GHR) model [191], attempt to replicate the empirical vehicle acceleration behaviour during driving. These models suffer from a notable methodological weakness, however; namely, they ignore the mechanical characteristics of the vehicle. Second, dynamics-based models, e.g., the Searle model [212], the Rakha-Pasumarthy-Adjerid (RPA) model [216], the Fadhloun-Rakha (FR) model [219], and the MFC free-flow model [187], explicitly incorporate vehicle dynamics into their mathematical expressions to ensure that vehicle accelerations are realistic. However, it is questionable whether such models are lightweight and flexible enough to be used in large-scale microscopic simulation studies. Table 2.2 traces the development of dynamics-based models.

None of the studies reviewed so far, however, accounted for the acceleration dynamics of electrified vehicles (EVs), which have significantly different power characteristics from those of conventional ICEVs [269, 114] and are representative of an emerging trend in sustainable transportation [29, 274]. Furthermore, previous studies have not explicitly dealt with the vehicle's deceleration characteristics. The present research builds on the MFC free-flow acceleration model [187] and proposes an extension to introduce the dynamics of EVs for free-flow microsimulation modelling. The developed model is extensively tested in the following dimensions:

- Validation of acceleration and deceleration potential curves underlying the MFC model, using laboratory chassis dynamometer tests of an electrified vehicle.

- Implementation of the MFC model in microsimulation with various acceleration and deceleration scenarios.

- Calibration and validation of the MFC, Gipps, and IDM models using on-road driving trajectories.

- Validation based on the official 0-100 km/h acceleration time from the vehicle specification database that contains information relating to 59 commercial EVs.

This chapter is organized as follows. In Section 5.2, a comprehensive description of the proposed model is presented. Section 5.3 then describes the experimental setup, which includes chassis dynamometer tests in the Vehicle Emissions Laboratories (VELA) of the European Commission, the on-road experimental campaign, the publicly available specifications of EVs, and two behavioural models (Gipps and IDM) that are used in the

validation workflow for comparison purposes. Afterwards, Section 5.4 presents the results and Section 5.5 discusses the conclusions as well as future work.

5.2 Model description

To the authors' best knowledge, the enhanced MFC model proposed in this study is hitherto the only free flow model that incorporates the electrified vehicle's power and deceleration dynamics. It has three key functional components: the acceleration potential (a_{ap}) curve, the deceleration potential (a_{dp}) curve, and the driving behaviour (w_{db}) function. The logic behind them is straightforward to understand. The model computes the vehicle's theoretical capabilities, namely, a_{ap} and a_{dp} curves, according to its official specifications and chassis dynamometer tests. The percentage of these capabilities that drivers typically use is then formulated as the driving behaviour function w_{db}.
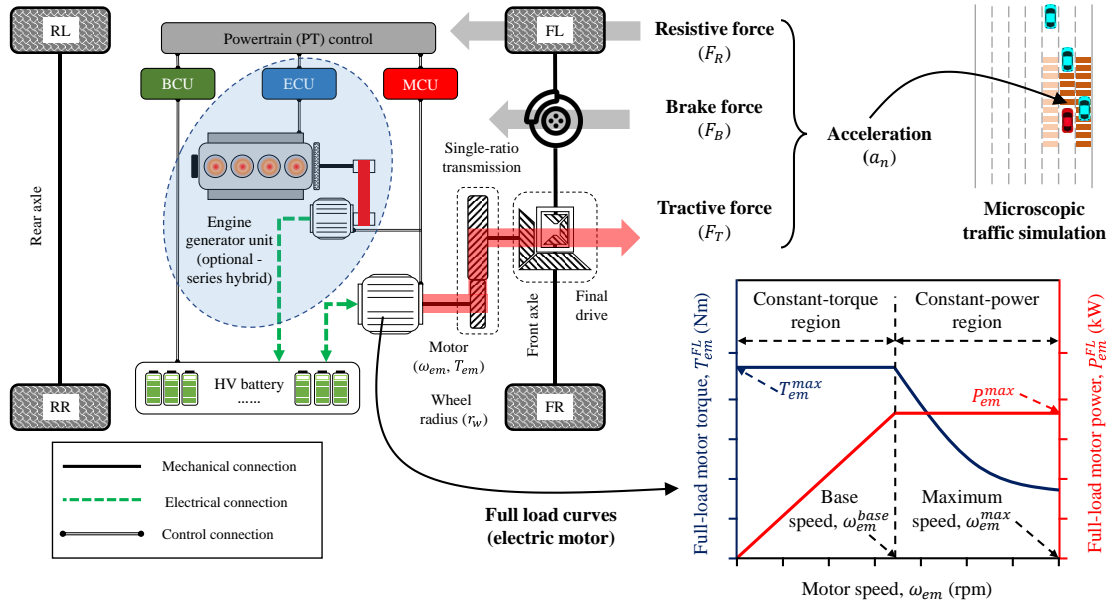
Note: RL = rear-left wheel; RR = rear-right wheel; FL = front-left wheel; FR = front-right wheel; BCU = battery control unit; ECU = engine control unit; MCU = motor control unit; HV = high-voltage.

Figure 5.1 Introducing dynamics of electrified vehicles (EVs) into microsimulation.

The model presented in this study is applicable to the battery (or pure) electric and series hybrid electric vehicles (i.e., BEVs and series-HEVs). However, the same principles can be used to simulate any electrified vehicle. After all, the underlying MFC methodology was designed to offer as broad vehicle coverage as possible. As shown in Figure 5.1 (left), BEV and series-HEV are directly driven by the electric motor (EM), and adopt the

single-ratio transmission gearbox because the motor has a larger operating speed range than that of the ICE, thus, no gear shift effects are involved. It is worth noting that the ICE in a series-HEV, instead of driving the wheels, merely acts as an onboard charging component. The more advanced MFC model for complex hybrid configurations, e.g., power-split [26], involving speed and torque coupling between the EM and the ICE, are still under development and will not be discussed in this work. The examined vehicles adopt the single-ratio transmission, as mentioned above, so the gearshifting functionality of the MFC model was not elaborated further in the present study.

5.2.1 Acceleration potential curve

The acceleration potential (a_{ap}) curve captures the maximum acceleration across the entire vehicle speed range and varies as a function of the vehicle speed, as described by

$$
\begin{cases}
a_{ap}(v_n) = \frac{F_T^{FL}(v_n) - F_R(v_n)}{\phi \cdot m}, \\
F_T^{FL}(v_n) = \min\left(\frac{T_T^{FL}(v_n)}{r_w}, \mu \cdot m_{ta} \cdot g\right),
\end{cases}
\tag{5.1}
$$

where v_n is the current vehicle speed (m/s); m is the vehicle operating mass (kg); ϕ is the equivalent inertial mass factor; r_w is the wheel radius (m); F_R is the total resistance force (N), including the aerodynamics, the rolling and the grade resistances; μ is the coefficient of friction between wheels and roadway surface; m_{ta} is the mass of the vehicle on the tractive axle (kg); g is the gravitational acceleration (m/s^2); F_T^{FL} and T_T^{FL} respectively denote the vehicle's tractive force (N) and tractive torque (Nm) at full load conditions. As mentioned in the previous paragraphs, a single-ratio transmission gearbox is adopted, thus, T_T^{FL} can be directly derived from the full load characteristics of the electric motor, i.e.,

$$
T_T^{FL}(v_n) = T_{em}^{FL}(\omega_{em}) \cdot \varphi_g \cdot \eta_d,
\tag{5.2}
$$

$$
\omega_{em}(v_n) = \frac{60 \cdot \varphi_g \cdot v_n(t)}{2\pi \cdot r_w},
\tag{5.3}
$$

where ω_{em} and T_{em}^{FL} are the rotational speed (rpm) of the electric motor, and the maximum achievable (full load) motor torque (Nm) at this speed, respectively; φ_g is the fixed gear ratio of the transmission gearbox; and η_d is driveline efficiency. Equation (5.3) presents the relation between the vehicle motion speed (v_n) and the motor rotational speed (ω_{em}).

Figure 5.1 (bottom right) qualitatively explains the speed-torque-power characteristics of the normal electric motor at full load conditions [30]. From this graph, two distinct motor operation regions are observed. First, in the lower speed region ($\omega_{em} < \omega_{em}^{base}$) or the constant-torque region, the full load motor torque T_{em}^{FL} is constant and equal to the motor's peak torque T_{em}^{max}; however, the full load motor power P_{em}^{FL} is directly proportional to the motor speed. Second, in the higher speed region or the constant-power region, P_{em}^{FL} is constant and equal to the motor's peak power P_{em}^{max}, but T_{em}^{FL} varies as a reciprocal function of the motor speed. Accordingly, the motor's full load torque T_{em}^{FL} can be described as a stepwise function of its rotational speed ω_{em}, i.e.,

$$T_{em}^{FL}(\omega_{em}) = \begin{cases} T_{em}^{max}, & 0 \leq \omega_{em}(t) < \omega_{em}^{base} \\ \frac{6 \times 10^4 \cdot P_{em}^{max}}{2\pi \cdot \omega_{em}(t)}, & \omega_{em}^{base} \leq \omega_{em}(t) < \omega_{em}^{max} \end{cases} \tag{5.4}$$

where T_{em}^{max} and P_{em}^{max} are the motor's peak torque (Nm) and peak power (kW), respectively; ω_{em}^{max} is the motor's maximum permissible speed (rpm); ω_{em}^{base} is the motor base speed (rpm), representing the split point between constant-torque and constant-power regions, which can be calculated by

$$\omega_{em}^{base} = \frac{6 \times 10^4 \cdot P_{em}^{max}}{2\pi \cdot T_{em}^{max}}, \tag{5.5}$$

The model also computes the variable resistance force F_R that acts on the vehicle, as provided by

$$F_R(v_n) = f_0 \cdot \cos\theta + f_1 \cdot v_n(t) + f_2 \cdot v_n(t)^2 + mg \cdot \sin\theta, \tag{5.6}$$

where θ is the road grade (rad); f_0, f_1, and f_2 are road load coefficients (N, kg/s, and kg/m, respectively). A dedicated method for the calculation of the vehicle's road load coefficients presented by Tsiakmakis et al. [275] is adopted in this work.

5.2.2 Deceleration potential curve

The deceleration potential (a_{dp}) curve is an essential upgrade for the MFC model [187] and marks the first attempt to incorporate the vehicle's deceleration characteristics explicitly in CF models. According to Fadhloun et al. [219], the vehicle's deceleration capability has to be bounded by the deceleration limit a_d^{lim} (namely, the product of the gravitational

acceleration g and the road friction coefficient μ), as calculated by

$$a_d^{lim} = \mu \cdot g, \tag{5.7}$$

Besides the theoretical capability, the a_{dp} curve should account for the deceleration rates that are acceptable to drivers in the field. A reasonable approach to tackle this issue could be to introduce a reduction factor ξ that varies with the vehicle speed (v_n), as given in Equations (5.8) and (5.9). The factor ξ uses a quadratic functional form proposed and validated by Akhilesh et al. [276] for typical passenger cars examined in this work.

$$a_{dp}(v_n) = \xi(v_n) \cdot a_d^{lim}, \tag{5.8}$$

$$\xi(v_n) = d_0 + d_1 \cdot v_n(t) + d_2 \cdot v_n(t)^2, \tag{5.9}$$

where the theoretical deceleration limit a_d^{lim} is assumed to be constant and equal to 7.72 m/s^2 in this study; d_0, d_1, and d_2 are coefficients equal to -0.2439, -0.0221, and 0.0006, respectively, based on the data from chassis dynamometer deceleration tests, which ensure that vehicle decelerations are realistic.

5.2.3 Driving behaviour function

To make the model representative of different driving patterns, the driving behaviour function (w_{db}) is incorporated as a variable reduction factor multiplied by a_{ap} and a_{dp} curves. The resulting formula, as demonstrated in Equation (5.10), allows modelling of the typical acceleration and deceleration behaviours that follow different driver characteristics.

$$a_n(t) = \begin{cases} w_{db}\big(v_n(t)\big) \cdot a_{ap}\big(v_n(t)\big), & 0 \leq \frac{v_n(t)}{V_D(t)} < 1 \\ w_{db}\big(v_n(t)\big) \cdot a_{dp}\big(v_n(t)\big), & \frac{v_n(t)}{V_D(t)} \geq 1 \end{cases} \tag{5.10}$$

where V_D is the desired (or roadway free-flow) speed (m/s); w_{db} is the driving behaviour function, whose expression is given by

$$
w_{db}\big(v_n(t)\big) = \begin{cases} DS \cdot \left(1 - c_1 \cdot \left(1 - \frac{v_n(t)}{V_D(t)} \right)^{c_0} \right), & 0 \leq \frac{v_n(t)}{V_D(t)} < 0.5 \\ DS \cdot \left(1 - \left(1 + \frac{v_n(t) - V_D(t)}{c_3} \right)^{c_2} \right), & 0.5 \leq \frac{v_n(t)}{V_D(t)} < 1 \\ DS \cdot \left(1 - \left(1 - \frac{v_n(t) - V_D(t)}{c_3} \right)^{c_2} \right), & \frac{v_n(t)}{V_D(t)} \geq 1 \end{cases} \tag{5.11}
$$

where the factor DS represents the driving style and ranges between 0 and 1, determining the driver's overall willingness to change the driving speed; the coefficients c_0, c_1, c_2, and c_3 determine the way in which drivers approach the desired speed and are set as 60, 0.8, 100, and 50, respectively [187]. What is important to recognize here is that the driving behaviour function is different from that of the original MFC model [187], to incorporate the deceleration potential curve and offer a much smoother acceleration profile.

Table 5.1 Variables and parameters of the enhanced MFC model.

	Acceleration potential (a_{ap}) curve	Deceleration potential (a_{dp}) curve	Driving behaviour function (w_{db})
Equations	(5.1)-(5.6)	(5.7)-(5.9)	(5.10)-(5.11)
State variables	a_n, v_n, t, θ		
Available in or determined by publicly available specifications	$F_T^{FL}(v_n), F_R(v_n), T_T^{FL}(v_n),$ $T_{em}^{FL}(\omega_{em}), \omega_{em}(v_n); m, \phi, g,$ $\mu, m_{ta}, r_w, \varphi_g, \eta_d, T_{em}^{max},$ $P_{em}^{max}, \omega_{em}^{base}, \omega_{em}^{max}, f_0, f_1, f_2$	a_d^{lim}	na
Determined by chassis dynamometer tests	na	$\xi(v_n), d_0, d_1, d_2$	na
From microsimulation	na	na	$V_D(t); c_0, c_1, c_2, c_3$
Determined by model calibration	na	na	DS

Note: na = not applicable; MFC = microsimulation free-flow acceleration model.

Main symbols: F = force; T = torque; P = power; a = acceleration; v = velocity; ω = rotational speed; t = time; θ = road grade; m = mass; ϕ is the equivalent inertial mass factor; g = gravitational acceleration; μ = coefficient of friction; f, d, and c = constant coefficients; DS = driving style; ξ = reduction factor.

Main subscripts: n = the subject vehicle; T = tractive; R = resistance; ta = tractive axle; em = electric motor; ap = acceleration potential; dp = deceleration potential; db = driving behaviour.

Main superscripts: FL = full load; max = maximum; lim = limit; $base$ = base.

Other variables or parameters: r_w = wheel radius; φ_g = gear ratio; η_d = driveline efficiency; V_D = desired (or free-flow) speed; a_d^{lim} = deceleration limit.

Table 5.1 summarizes all the variables and parameters in the enhanced MFC model, categorizes them into different groups according to their sources, and explains their main symbols, subscripts, and superscripts. Most of the elements involved in this model are derived directly from the publicly available specifications, the data in chassis

dynamometer tests, and the predefined microsimulation scenarios. Table 5.1 highlights that the proposed model requires the calibration of only one parameter, namely, driving style (*DS*), completely ruling out the effect of the number of calibration parameters on any potential increase in model complexity.

5.3 experimental setup

This section describes the experimental setup, which includes chassis dynamometer tests in the VELA laboratory, the on-road experimental campaign, the publicly available electrified vehicle specifications, and two behavioural models (Gipps and IDM) that are used in the validation workflow for comparison purposes.

5.3.1 Validation using VELA data

To validate the reliability of the acceleration and deceleration potential curves (i.e., a_{ap} and a_{dp}), chassis dynamometer tests were carried out at the VELA Joint Research Centre (JRC). A 2016 Hyundai Ioniq electric vehicle, whose main specifications are listed in Table 5.2, was selected to conduct 46 consecutive acceleration-deceleration test cycles. More specifically, the vehicle was tested within a speed range between 20 and 120 km/h, in relation to three different drive modes (i.e., normal, eco, and sport), three different pedal positions (i.e., mild, normal, and full), and four levels of regenerative braking. The testbed can collect data with a 10 Hz measurement rate.

Table 5.2 Main specifications of the electrified vehicle under test.

Specifications	Symbols	Units	Values
Vehicle operating mass	m	kg	1420
Motor's peak torque	T_{em}^{max}	Nm	295
Motor's peak power	P_{em}^{max}	kW	88
Single-speed gear ratio	φ_g	na	7.412
Wheel radius	r_w	m	0.316
Vehicle speed limit	v^{lim}	km/h	165
Height	H	m	1.45
Width	W	m	1.82
0–100 km/h acceleration time	$T_{0-100km/h}$	s	9.9

Note: na = not applicable.

5.3.2 Calibration and validation using on-road data

Figure 5.2 illustrates the on-road campaign carried out in typical highway driving scenarios. Therefore, unusual circumstances such as traffic crashes and congestions are not considered. Field tests were conducted on a section of Autostrada A26 (Italy) between Vicolungo and Ghemme, a 32 km round trip, to collect driving data under real-world traffic conditions for the model calibration and validation. The test vehicle was equipped with a multi-constellation global navigation satellite system (GNSS) receiver, able to collect GNSS data with a 10 Hz measurement rate. The horizontal accuracy reported by the receiver is less than 50 cm. The GNSS active antenna was mounted on the roof of the vehicle, to ensure maximum satellite visibility and avoid signal attenuation from the vehicle body. At each time instant, the geographic coordinates (latitude, longitude, and altitude) of the vehicle were recorded, which were then transformed into a local east, north, and up (ENU) Cartesian reference frame. The outliers were filtered using typical moving average post-processing. The test section comprises various uphill and downhill segments, providing an appropriate environment to examine different tractive load conditions. The elevation profile of the test route is extracted using GPS Visualizer. The road grade varies approximately between -8% and 8%.

Figure 5.2 (a) and (b) show the northbound (Cycle I) and southbound (Cycle II) driving profiles, respectively, where the speed varies between 10 and 40 m/s and the acceleration ranges from -4 to 2 m/s^2. The MFC model is calibrated and validated, using Cycles I and II, respectively, against the other two widely used behavioural models (Gipps and IDM), whose expressions will be subsequently introduced. Figure 5.2 (c) demonstrates the model calibration and validation procedures. The model parameters are calibrated using the on-road data (Cycle I) and the LMFIT (non-linear least-squares minimization and curve-fitting) optimization tool. After determining the optimal parameters, the models are then tested using Cycle II to further validate the models' robustness and reliability. According to the method discussed in the work of Treiber and Kesting [277], the calibration objective function is defined based on the sums of squared errors, as described by

$$V^{rel}(M_{\hat{\chi}}) = \sum_{j=1}^{n} \left(\ln \left(\frac{v_{M_{\hat{\chi}}(j)}}{v_N(j)} \right) \right)^2, \forall M, \hat{\chi} \tag{5.12}$$

where j is a distance instance (every 2 m along the predefined path); v_N is the measured speed from the naturalistic on-road driving; $v_{M_{\hat{\chi}}}$ is the simulated speed by the model M with a parameter vector $\hat{\chi}$. The calibration parameters and their respective constraints are summarized in Table 5.3.

Table 5.3 Calibration parameters and their constraints.

Model	Parameters		
Gipps	$a_{max} \in [0.5, 4]$,	$\lambda \in [0.001, 5]$,	$\gamma \in [0.5, 4]$
IDM	$a_{max} \in [0.5, 4]$,	$\delta \in [0.1, 4]$	
MFC	$DS \in [0.1, 1]$		

Note: IDM = intelligent driver model; MFC = microsimulation free-flow acceleration model.
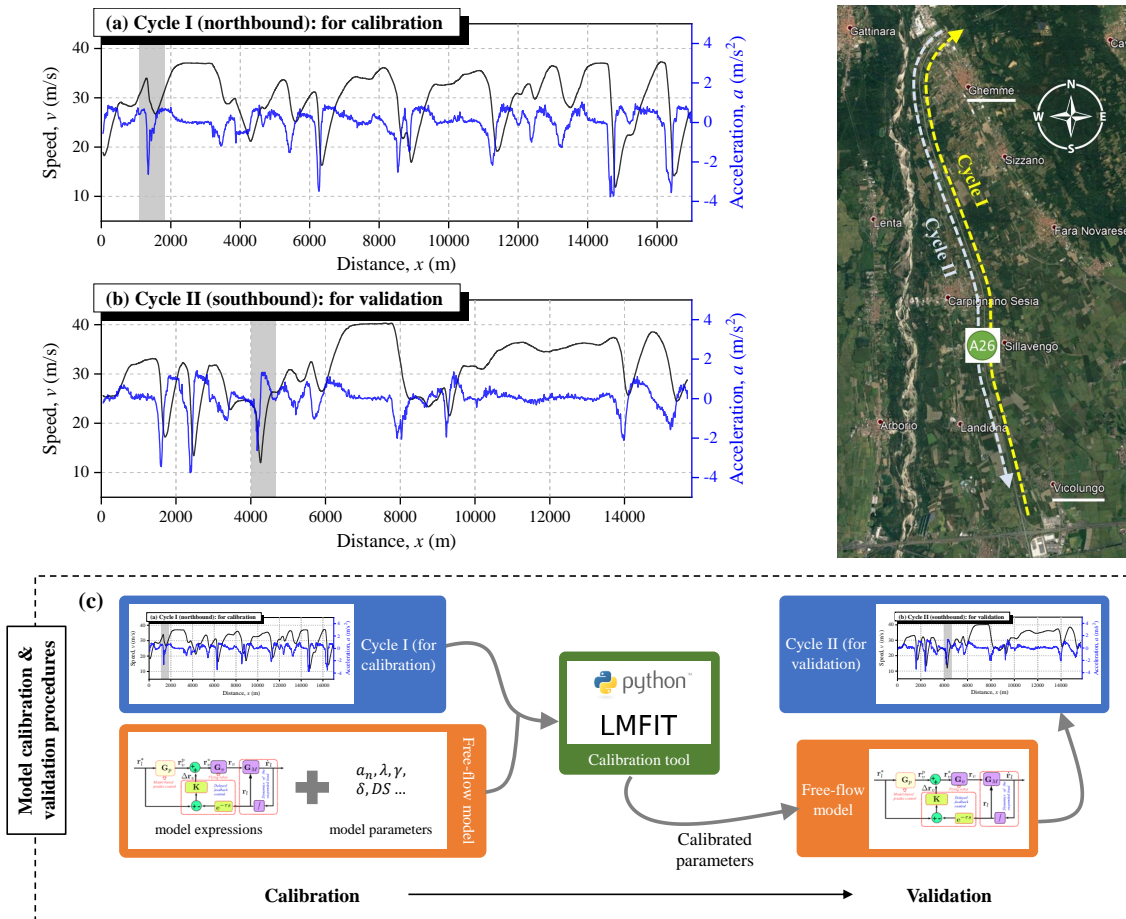
Subplots: (a) Northbound (Cycle I) and (b) southbound (Cycle II) driving profiles; and (c) model calibration and validation procedures.

Figure 5.2 On-road driving campaign for model calibration and validation.

5.3.3 Validation using 0-100 km/h Acceleration Specifications

A vehicle specification dataset developed by JRC contains information relating to 59 commercial electrified vehicles. Figure 5.3 exhibits the main specifications associated with their acceleration performances, including the power, torque, and speed limits of the electric motor, the vehicle mass, the wheel radius, and the transmission gear ratio. What is interesting about the data in this parallel plot is that positive correlations can be found among P_{em}^{max}, T_{em}^{max}, ω_{em}^{max}, and m, suggesting that stronger performances of the electric motor are usually associated with a larger vehicle mass. Furthermore, better motor performances (i.e., P_{em}^{max}, T_{em}^{max}, ω_{em}^{max}) can significantly reduce the 0-100 km/h acceleration time ($T_{0-100\text{km/h}}$), whose value ranges from 2.7 to 14.5 s. As elaborated in Table 5.1, specifications including P_{em}^{max}, T_{em}^{max}, ω_{em}^{max}, m, r_w, and φ_g in this dataset are underlying model parameters and subsequently utilized to validate the proposed model against the specified $T_{0-100\text{km/h}}$ values.
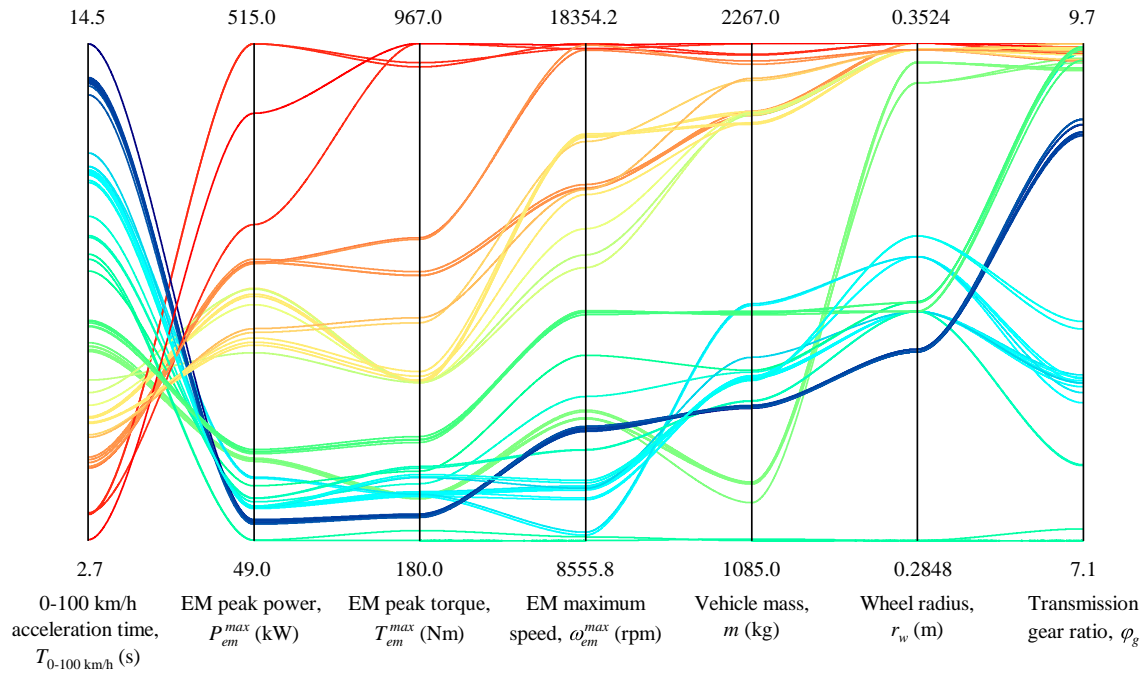
Note: EM = electric motor.

Figure 5.3 Main specifications of 59 electrified vehicles from the dataset.

5.3.4 Benchmark models

The enhanced MFC model is validated against another two state-of-the-art behavioural models: Gipps and IDM. The expression of the Gipps model's free-flow branch is given by

$$a_n(t) = \max\left(\alpha \cdot a_{max} \cdot \left(1 - \frac{v_n(t)}{V_D}\right) \cdot \left(\lambda + \frac{v_n(t)}{V_D}\right)^\gamma, a_{min} \right), \tag{5.13}$$

where v_n (m/s) and a_n (m/s^2) are the state variables at time t (s); V_D is the desired speed (m/s); a_{max} is the maximum acceleration (m/s^2); and a_{min} indicates the vehicle's maximum deceleration rate and is equal to -3 m/s^2. Ciuffo et al. [207] reported that the constant parameters, α, λ, and γ in the Gipps model have the following relationship.

$$\alpha = \frac{(1+\gamma)^{1+\gamma}}{\gamma^\gamma \cdot (1+\lambda)^{1+\gamma}}, \tag{5.14}$$

IDM is another benchmark model, whose free-flow driving behaviour is similar to the work conducted by Schakel et al. [278], as described by

$$a_n(t) = \max\left(a_{max} \cdot \left(1 - \frac{v_n(t)}{V_D}\right)^\delta, a_{min} \right), \tag{5.15}$$

where δ is a constant parameter. It is important to stress that many dynamics-based models in Table 2.2 are claimed to outperform the above benchmark models (i.e., Gipps and IDM) in generating realistic vehicle trajectories [279], but all of them are developed for conventional ICEVs. It is therefore time-consuming to adapt these models for electrified vehicles and recalibrate their parameters. Moreover, these dynamics-based models are often not widely implemented or extensively validated in commercial microscopic simulation software (e.g., AIMSUN, VISSIM, and PARAMICS). Therefore, in this work, the proposed MFC model is not benchmarked against these dynamics-based models, which, however, can be considered in the authors' future studies.

5.4 Results and discussion

This section presents a critical analysis of the results from the experimental and simulation tests described above.
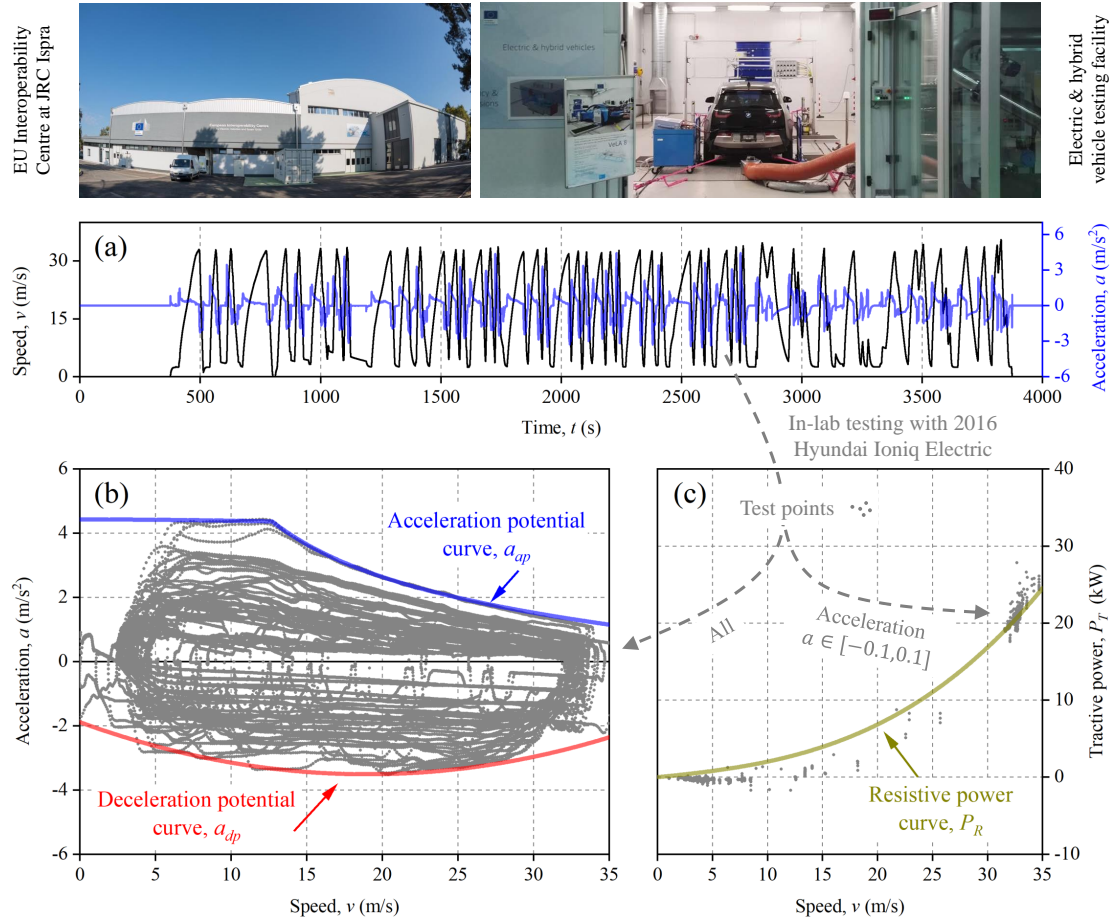
Subplots: (a) Testing facilities and driving profiles; (b) the validation of the acceleration and deceleration potential curves; and (c) the validation of the vehicle's theoretical resistive power.
Note: EU = European Union; JRC = Joint Research Centre.

Figure 5.4 Chassis dynamometer tests of an electrified vehicle for the model validation.

5.4.1 Validation using VELA data

Figure 5.4 displays the validation of the vehicle's acceleration and deceleration potential curves in the MFC model, using the data recorded during chassis dynamometer testing in the VELA laboratory. Figure 5.4 (a) reports the 46 consecutive acceleration-deceleration test cycles that the vehicle performed. From the results achieved, Figure 5.4 (b) compares the observed data points with the a_{ap} and a_{dp} curves resulting from the enhanced MFC model. It is worth noting that there are few test points in the low-speed (less than $\sim$5 m/s) region because the speed range for the acceleration test is between 20 and 120 km/h. The theoretical a_{ap} curve, derived directly from vehicle specifications, demonstrates a good correlation with the upper boundary test points. Besides, the empirical a_{dp} curve is very close to the lower boundary test points. Figure 5.4 (c) selects the test points, whose

acceleration rates are close to zero (namely, $a \in [-0.1, 0.1]$). In this condition, according to Equation (5.1), the tractive power P_T (kW) is approximately equal to the resistance power P_R (kW). The observed correlation between the simulated P_R curve and the observed P_T points can provide further support for the reliability of the MFC model.

5.4.2 Model implementation in microsimulation

Figure 5.5 presents the implementation of the enhanced MFC model in microsimulation, where changes in driving style factor DS (in driving behaviour function w_{db}) are compared. Three indicative driving styles are selected for the same vehicle: (i) $DS = 1$, the dynamic driver who utilizes the full acceleration and deceleration potentials when possible; (ii) $DS = 0.8$, the normal one; and (iii) $DS = 0.6$, the timid driver.
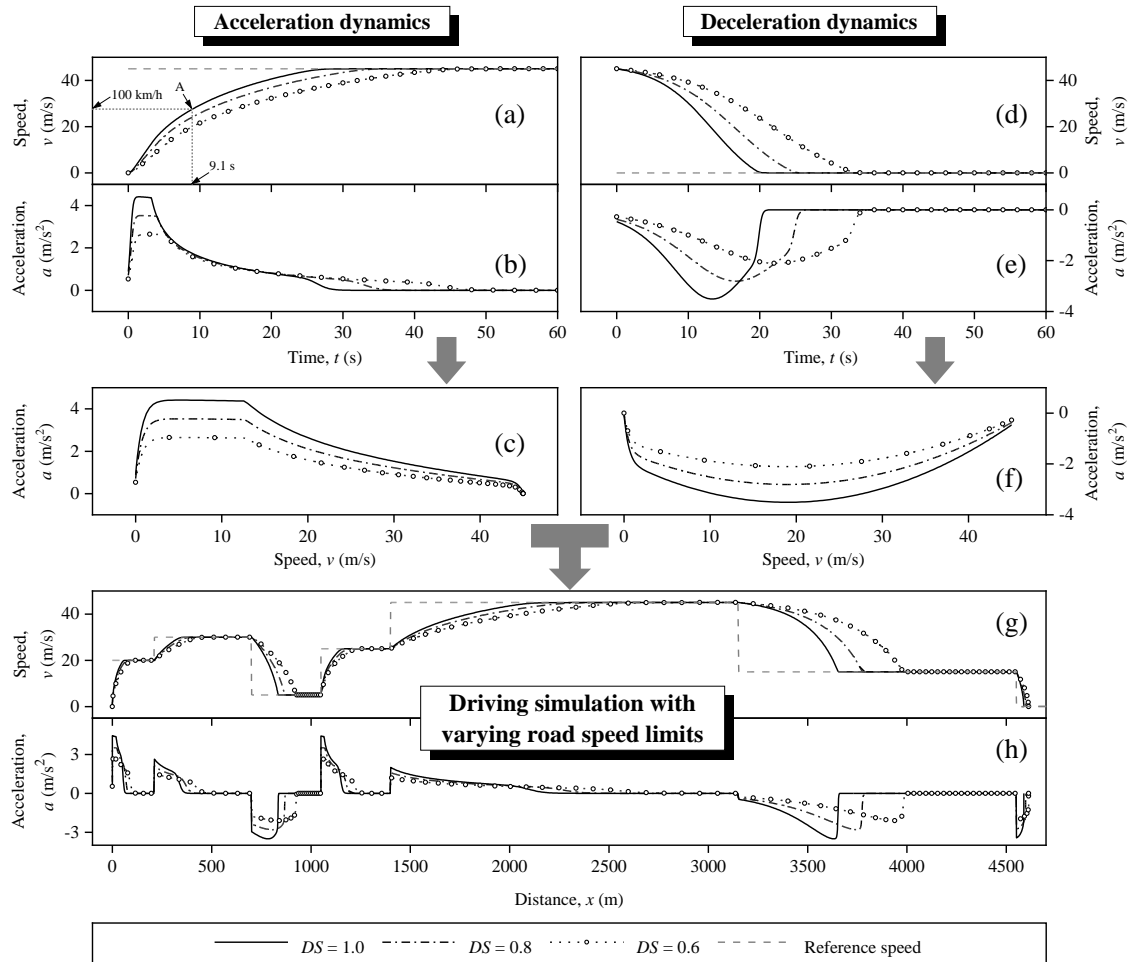
Subplots: (a) Speed-time, (b) acceleration-time, and (c) acceleration-speed profiles in the vehicle acceleration scenario; (d)-(f) corresponding profiles in the vehicle deceleration scenario; and (g) speed-distance and (h) acceleration-distance profiles in driving simulation with varying road speed limits.
Note: MFC = microsimulation free-flow acceleration model; DS = driving style factor.

Figure 5.5 Implementation of the enhanced MFC model in microsimulation.

Figure 5.5 provides the driving profiles of different drivers, during scenarios of both acceleration (from 0 to 45 m/s) in Figure 5.5 (a)-(c) and deceleration (from 45 to 0 m/s) in Figure 5.5 (d)-(f). Moreover, Figure 5.5 (g)-(h), show the results from the driving simulation with varying road speed limits. The results in these plots suggest that the enhanced MFC model can ensure a smooth transition between different acceleration and deceleration levels while avoiding obvious oscillations or overshoots when approaching the reference speed. This smooth feature is praiseworthy given that significant and omnipresent acceleration cliffs are observed in many well-known car-following models [219]. Additionally, the result is significant at point A in Figure 5.5 (a) because it represents that the most aggressive driver ($DS = 1$) can accelerate from 0 to 100 km/h in 9.1 s, very close to the vehicle's specification ($T_{0-100\text{km/h}} = 9.9$ s) given in Table 5.2.

5.4.3 Calibration and validation using on-road data

Figure 5.6 (a)-(d) and Figure 5.6 (e)-(h) show the statistical results from the model calibration and validation, respectively. Figure 5.6 (a) and (e) compare the observed average speed $\bar{v}$ from on-road driving and its corresponding predictions from three different models (MFC, Gipps, and IDM). Although small, the absolute percentage errors of these models in relation to average speed prediction are different, where the MFC model demonstrates the smallest prediction errors ($\sim 0.06\%$) and the best robustness. The RMSE (root mean square error) between the observed and predicted speed profiles are presented in Figure 5.6 (b) and (f). A clear benefit of the MFC model in the reduction of RMSE for speed could be identified in these graphs. For example, when tested with the validation cycle, the speed RMSE of the MFC model (0.37 m/s) is 68.8% and 68.5% lower than those of the Gipps model (1.18 m/s) and the IDM model (1.17 m/s), respectively.

From the perspective of acceleration profiles, Figure 5.6 (c) and (g) compare on-road observations and corresponding model predictions, in relation to the average absolute acceleration $\overline{|a|}$. The MFC model leads to excellent $\overline{|a|}$ predictions, whose absolute percentage errors (0.30% and 0.50% in calibration and validation cycles, respectively) are an order of magnitude lower than those of the benchmark models. Figure 5.6 (d) and (h) compare the RMSE of acceleration in different model predictions. The MFC model's advantage of accurately predicting the real acceleration behaviour is demonstrated in these

charts. In the validation test, for instance, the MFC model results in an acceleration RMSE equal to 0.17 m/s^2, which is 49.8% and 49.0% lower than those of benchmark models.
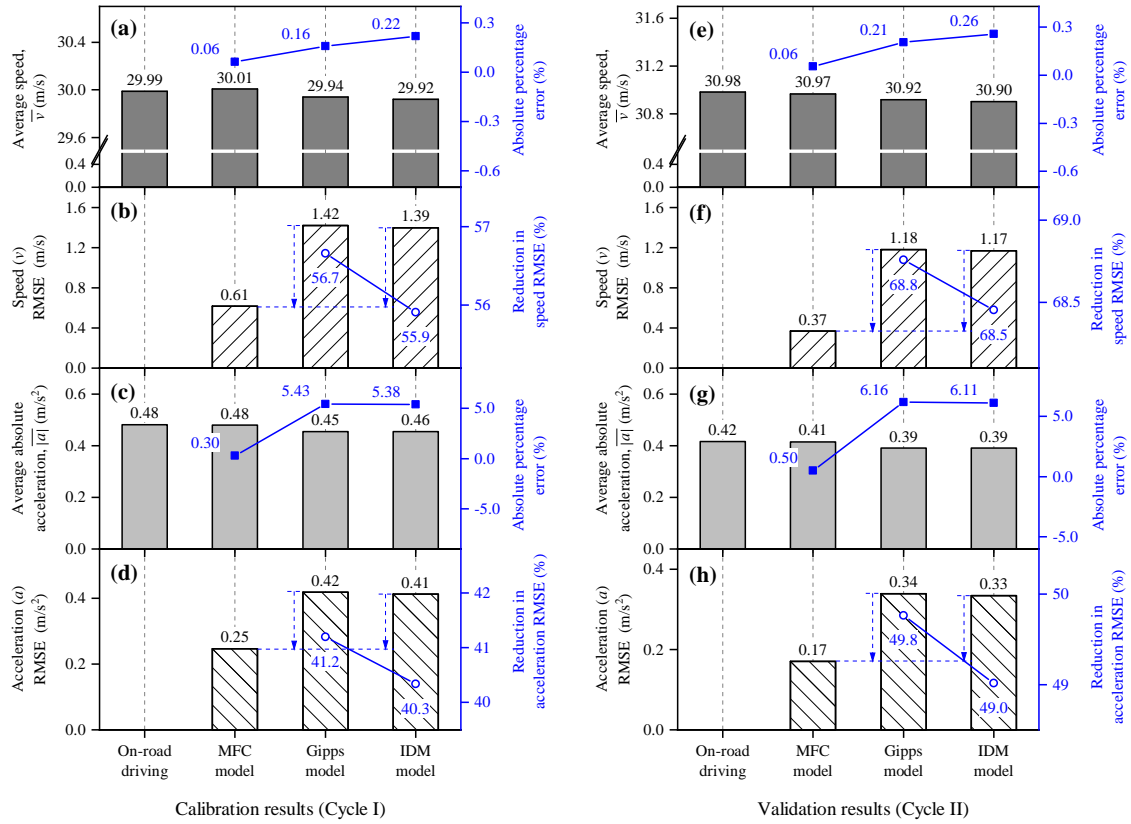
Subplots: (a) The error of the average speed, (b) the RMSE of speed, (c) the error of the average absolute acceleration, and (d) the RMSE of acceleration in model calibration; (e)-(h) corresponding results in model validation.
Note: MFC = microsimulation free-flow acceleration model; IDM = intelligent driver model; RMSE = root mean square error.

Figure 5.6 Statistical results of the model calibration and validation using on-road driving trajectories.

To offer a closer inspection of transient results, Figure 5.7 (left) and (right) present parts (the gray sections in Figure 5.2) of the distance-speed-acceleration profiles from calibration and validation cycles, respectively. As mentioned in the literature review, free-flow models regulate the subject vehicle by asymptotically approaching the desired speed V_D, such as MFC, Gipps, and IDM, as respectively defined in Equations (5.11), (5.13), and (5.15). Consequently, a time delay exists between the speed prediction of the model and the desired speed (V_D). On the other hand, the driver's perception-response time delay in the free-flow driving experiments (illustrated in Figure 5.2) is not considered in this study. It is therefore assumed that the desired speed V_D is approximately the same as the driver's on-road driving speed for simplification purposes. This explains why time lags

between the model predictions and the on-road trajectory are observed in Figure 5.7. As shown in this graph, the three models appear successfully to produce a driving profile that emulates the on-road driving data. The Gipps and IDM models have very similar driving behaviours, and both introduce an obvious delay. However, the enhanced MFC model can capture both the speed and the acceleration dynamics much better. These results further support the findings in Figure 5.6.
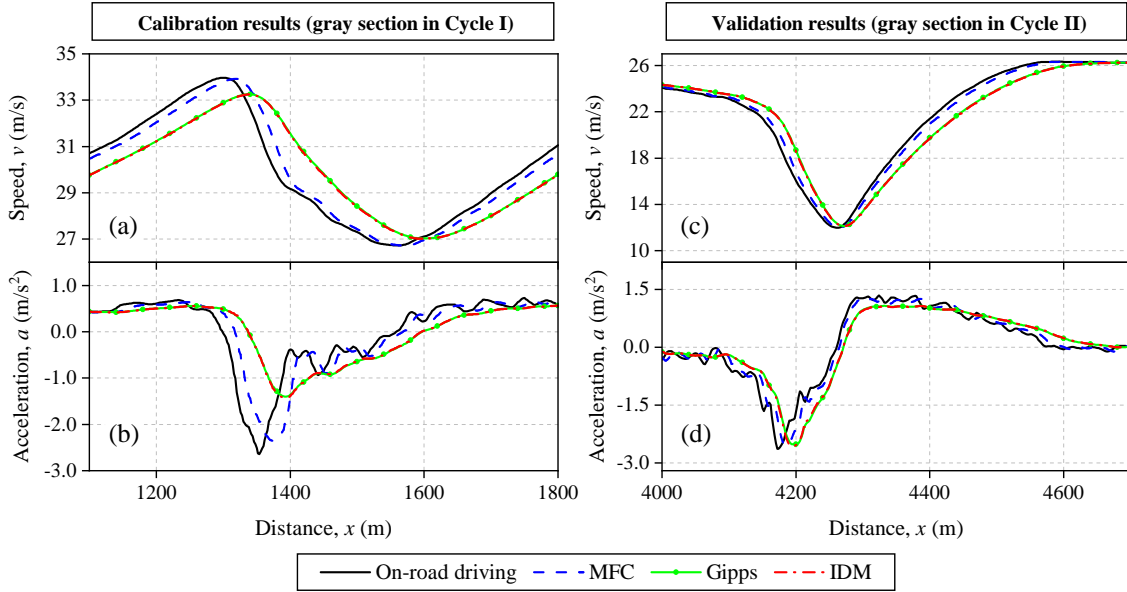
Subplots: (a) and (c) Speed-distance profiles in the part of the Cycle I and Cycle II, respectively; (b) and (d) corresponding acceleration-distance profiles.
Note: MFC = microsimulation free-flow acceleration model; IDM = intelligent driver model.

Figure 5.7 Transient results of the on-road observations and model predictions.

5.4.4 Validation using 0-100 km/h acceleration specifications

In Figure 5.8, the models are further validated using vehicle acceleration specifications summarized in Figure 5.3, namely, 0-100 km/h acceleration time ($T_{0-100\text{km/h}}$). Figure 5.8 (a) is a scatter plot of the acceleration time $T^{model}_{0-100\text{km/h}}$ from model predictions versus the acceleration time $T^{VS}_{0-100\text{km/h}}$ from the vehicle specification dataset, with varying marker color determined by the vehicle maximum power P^{max}_{em}. It can be seen that the cluster resulting from the MFC model is closely located around the diagonal, suggesting small errors between the predicted and specified values. On the other hand, as circled by the black boxes, Gipps and IDM models both significantly underestimate $T_{0-100\text{km/h}}$ values at the low P^{max}_{em} region. Furthermore, the Gipps model gives rise to overestimated predictions when P^{max}_{em} ranges from ~200 to ~300 kW.
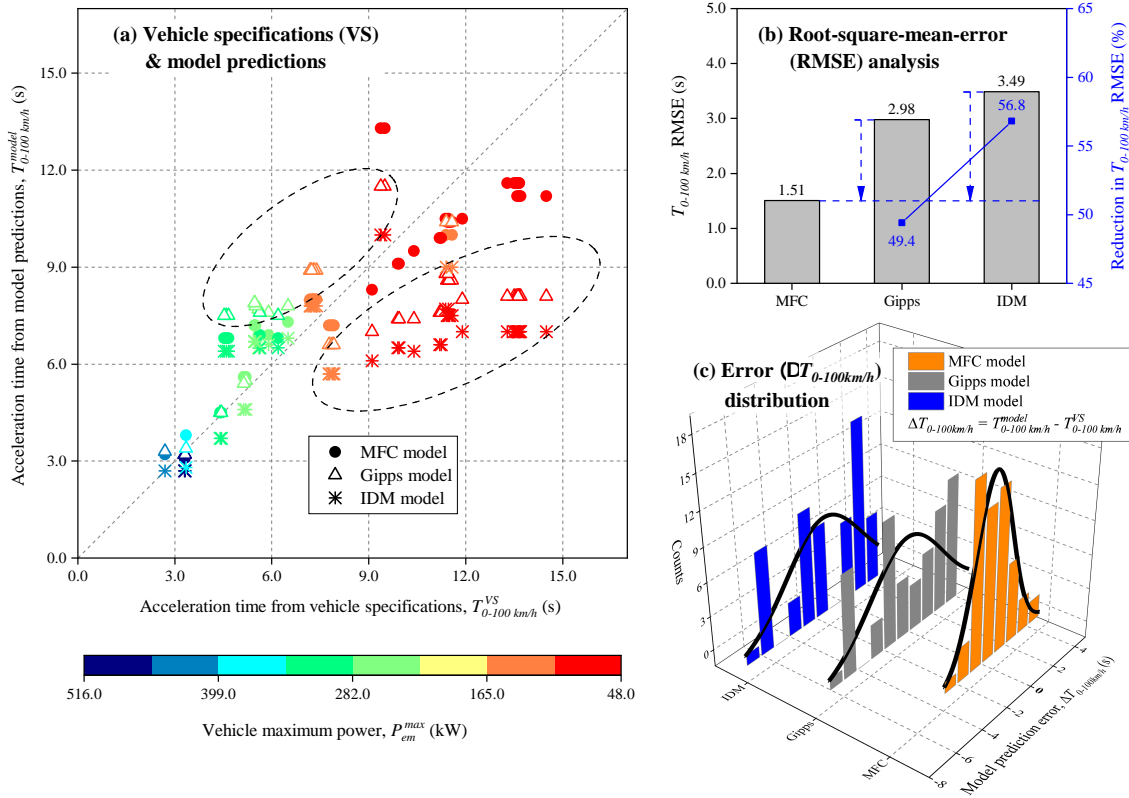
Subplots: (a) Comparison of 0-100 km/h acceleration time between model predictions and vehicle specifications; (b) RMSE of 0-100 km/h acceleration time from model predictions; and (c) the distribution of models' prediction errors.

Note: MFC = microsimulation free-flow acceleration model; IDM = intelligent driver model.

Figure 5.8 Model validation using official 0-100 km/h acceleration specifications.

Figure 5.8 (b) shows the RMSE of the acceleration time $T_{0-100\text{km/h}}$ predicted by the three models. The benchmark models (Gipps and IDM) result in a $T_{0-100\text{km/h}}$ RMSE of 2.98 s and 3.49 s, respectively. Alternatively, the proposed MFC model can produce a much more accurate $T_{0-100\text{km/h}}$ prediction, whose RMSE is equal to 1.51 s and is 49.4% and 56.8% lower than those of Gipps and IDM, respectively. Figure 5.8 (c) illustrates the distributions of the models' prediction errors. The peak in MFC distribution is higher and most of the sample points are concentrated around zero, suggesting that the prediction error is significantly reduced.

5.5   Summary

This work builds on the MFC model and proposes an enhancement for the microsimulation of electrified vehicles (EVs), whose acceleration capabilities are different from those of traditional ICEVs. Furthermore, this research develops an improved deceleration

model to capture the deceleration capabilities of EVs at a given speed, imposing realistic decelerations in microsimulation. The results of this study show that:

- The acceleration and deceleration potential curves underlying the enhanced MFC model can accurately represent the real dynamics of the electrified vehicle tested on the chassis dynamometer;

- In the microsimulation implementation, the enhanced MFC model can ensure a smooth transition between different acceleration and deceleration levels while avoiding obvious oscillations or overshoots when approaching the reference speed;

- When reproducing the on-road driving trajectories, the enhanced MFC model can deliver significant reductions in RMSE of speed (by $\sim$69%) and acceleration (by $\sim$50%) compared with benchmarks;

- The enhanced MFC model can accurately predict the vehicle 0–100 km/h acceleration specifications, where its RMSE is 49.4% and 56.8% lower than those of Gipps and IDM models, respectively.

The study makes several contributions to the current literature:

- This work provides the first comprehensive review and comparison of dynamics-based car-following (including free-flow) models, as summarized in Table 2.2;

- The enhanced MFC model is hitherto the only car-following model that accounts for acceleration dynamics of EVs;

- The enhanced MFC model marks a first attempt to incorporate explicitly the vehicle's deceleration characteristics in microsimulation.

However, to develop a more capable dynamics-based MFC model used in microsimulation, additional studies will be needed, as follows:

- The current deceleration potential curve is empirically derived from the data in chassis dynamometer tests, limiting its flexibility in the implementation of microsimulation. Thus, it would be better if a theoretical method could be proposed;

- A more advanced MFC model is needed that can deal with the speed and torque coupling between the internal combustion engine and the electric motor in complex hybrid powertrain configurations;

- The proposed MFC model is validated in typical highway driving scenarios. However, unusual circumstances, such as traffic crashes and congestion, should also be considered when validating the model with regard to reproducing the empirical driver and vehicle behaviour;

- The authors have started working on a project to couple the proposed dynamics-based car-following model (MFC) with their previously developed fuel consumption and emission model (CO2MPAS). The resulting open-source Python package has been published to PyPI (https://pypi.org/project/co2mpas-driver). However, more effort is required to validate the performance of the MFC model extensively for predicting the vehicle's fuel consumption and emissions.

6

Introducing road geometry into microscopic traffic models for AVs

Road geometry (e.g., slope and curvature) has significant impacts on driving behaviours of low-level automated vehicles (AVs), but it has been largely ignored in microscopic traffic models. To capture these effects, this study proposes a generic approach to extend any of the (free-flow or car-following) microscopic models characterized by acceleration functions. To this end, three model extensions are developed, each of which can use different submodels for comparison. Their effectiveness is demonstrated with a microscopic free-flow model that represents the AVs' control logic. Finally, all possible combinations of the microscopic model and the model extensions are calibrated and cross-validated against data sets, which contain empirical trajectories of commercial adaptive cruise control (ACC) systems on different test tracks. The results suggest that two submodels, i.e., the nonlinear vehicle dynamics (NVD) and the radius difference method (RDM), can extend the microscopic model to effectively capture the effects of road slope and road curvature, respectively, on automated driving. Specifically, the NVD is the dominant factor contributing to increasing (by 34.9% on average) model accuracy. In addition, when simulating reckless turning behaviours (i.e., the vehicle turns at high speeds), the inclusion of the developed RDM is significant for model performance, and the models extended with both the NVD and the RDM can achieve the largest accuracy gains (39.6%).

6.1 Introduction

The safety, stability, and efficiency of road transport are strongly influenced by road geometry such as curvature and slope. For example, sharp curve and steep slope sections account for 14% of accident-prone locations according to a statistical analysis of 1448 traffic accidents on highways [280]. Furthermore, it is well known that traffic bottlenecks formed by sags (where slope varies significantly from downhill to uphill) [281, 282] and horizontal curves [283] can induce undesired traffic instability and capacity drop, and therefore, worsen traffic congestion and throughput.

With the increasing penetration of advanced driver assistance systems (ADAS), e.g., adaptive cruise control (ACC), automated driving has received considerable attention because automated vehicles (AVs) have some unique features compared to human-driven vehicles (HDVs). For example, control logics of AVs are expected to be deterministic, however, human behaviour is inherently stochastic, i.e., given the same situation, drivers may not necessarily take the same action every time [284]. In addition, due to limitations of existing sensing technologies, perception systems of most AVs cannot anticipate future traffic situations in the same way as those of human drivers [285].

Once these unique properties are acknowledged, two important questions arise, how the road geometry affects AVs' driving behaviours, and how microscopic traffic models can be developed to capture these effects. The answers to these questions are crucial for determining the influence of a growing number of AVs on the overall traffic flow.

The impacts of road geometry on automated driving behaviour have been investigated in the past. For example, in the free-flow condition (i.e., there is no vehicle detected ahead [286]), the field experiment is conducted on AVs equipped with conventional cruise control (CCC) [287]. The results demonstrate that uphill and downhill sections of the roadway can lead to significant deviations from the target cruise speed (or set speed). Another study publishes the OpenACC database consisting of car-following trajectories of commercial ACC systems in car platoons [288]. The data suggest that ACC car-following behaviour depends not only on the vehicle ahead but also on road geometry, e.g., slope and curvature. Moreover, the leading vehicle's small speed perturbations resulting from the road geometry can cause stop-and-go waves, due to the string unstable ACC behaviour (i.e., speed deviations are amplified through the upstream followers) [289].

However, road geometry has been largely ignored in prevailing microscopic traffic models, e.g., intelligent driver model (IDM) [199] and Gipps' model [194], which, therefore, cannot reproduce the aforementioned safety and stability issues in traffic networks. Although in some traffic simulation software, microscopic models are reported to be able to reproduce the impacts of road geometry (e.g., the maximum and minimum acceleration of models in AIMSUN can vary depending on road slope) [290], the methodologies behind those approaches are rarely published or justified. Consequently, in the literature, there is a clear and growing interest in developing microscopic traffic models to capture the impacts of road geometry (i.e., slope and/or curvature) on vehicle behaviour.

To account for the influences of road slope, in 2008, the seminal work of Li et al. [291] presents an extended optimal velocity model (OVM), in which the optimal velocity is determined by both headway and road slope. Komada et al. [292] consider the gravitational force acting on the vehicle and then develop another extended OVM to include the effects of road slope on acceleration behaviour, which can help to derive fundamental diagrams of traffic flow at the sag, uphill, and downhill sections. Similarly, Zhou et al. [293] extend the full velocity difference model (FVDM) to include the gravitational force and therefore the impacts of road slope. Li et al. [294] propose another FVDM-based model that incorporates the effects of both road slope and lateral gap on the vehicle acceleration on a road without lane discipline. Nevertheless, the aforementioned models suffer from the same drawback that the model formulation and/or parameters necessarily depend on the vertical profile of the road (i.e., level, uphill, or downhill), making them difficult to implement in practice [295]. Ros et al. [296] extend the IDM to include an additional term, which considers the negative influence of road slope on vehicle acceleration and assumes that drivers compensate gradually for the increase in grade resistance force at sags. However, this model is only verified with a specific sag in simulation [297].

On the other hand, there are few models developed to handle the effects of road curvature. Based on the centrifugal force acting on the vehicle, Liang and Su [298] introduce the curvature and superelevation into the modified cellular automaton (CA) model to investigate the traffic flow at curved sections. Some studies extend the OVM [299, 300] or FVDM [301, 302] model to describe the impacts of side friction factor and turning radius of curved roads on acceleration behaviour. Sun et al. [303] propose another extended FVDM to explore the impacts of curved roads, considering not only the side friction factor and the turning radius but the driver's desire for smooth driving.

Recent advances in microscopic traffic models also allow for simultaneously capturing the impacts of both the slope and curvature of the road. To this end, the OVM [304] and the FVDM [305] are extended using a similar approach, which, however, relies on a strong assumption that the road section is simplified as part of a circular equidistant helix.

Despite growing efforts to extend existing microscopic traffic models for capturing the effects of road geometry (i.e., slope and curvature) on vehicle acceleration, to the best of our knowledge, studies discussed so far suffer from three major limitations. First, the methods to extend the microscopic models are not sufficiently generic, i.e., usually only

applicable to specific ones (e.g., OVM and FVDM, in particular). Second, microscopic models examined in these studies are originally developed to simulate human driving, not considering the control logic behind automated driving. Third, none of the extended models is calibrated and validated to quantitatively compare the model outputs with empirical trajectory data.

To address these research gaps, this study proposes a generic cascade approach to extend any of the (free-flow or car-following) microscopic models characterized by acceleration functions. Specifically, three model extensions are developed, each of which can use different submodels. Their effectiveness is demonstrated with a microscopic free-flow model for automated driving, which has a linear formulation [118] and is derived from the proportional-integral-derivative (PID) control logic [306]. Finally, all possible combinations of the microscopic model and the model extensions are calibrated and validated against empirical data collected across multiple ACC vehicles and test tracks to provide statistically reliable conclusions. It is worth noting that, to avoid interference effects due to vehicle interactions in car-following conditions, the experimental design and theoretical modelling of the present work only consider free-flow driving conditions (i.e., there is no target vehicle detected in front) so that we can clearly identify and simulate the impacts of road geometry on vehicle acceleration.

The remainder of this chapter is outlined as follows. In Section 6.2, the generic cascade approach to extend microscopic traffic models is described. Section 6.3 details the field free-flow driving experiments with ACC vehicles. The design of calibration tests is introduced in Section 6.4. Finally, in Section 6.5, the calibration and cross-validation results are presented and discussed. Section 6.6 draws the main conclusions.

Cascade model extensions for capturing characteristics of both the vehicle and the road

Microscopic traffic model

Defining the driving control logic and giving the acceleration command

1) PID: Eq. (6.2)
…   …

$a_{n,cmd}(t)$

Turning manoeuvre (TM)

Defining negative effects of the curved road on the acceleration command

1) None: Eq. (6.3)
2) RDM: Eq. (6.4)

$a_{n,des}(t)$

Vehicle dynamics (VD)

Defining the longitudinal vehicle response to the acceleration control input

1) None: Eq. (6.5)
2) Linear: Eq. (6.6)
3) Nonlinear: Eq. (6.7)

$a_n(t)$

Acceleration constraints (AC)

Defining capabilities of the vehicle's propulsion and braking systems

1) None: Eq. (6.8)
2) Constant: Eq. (6.9)
3) MFC: Eq. (6.10)

$v_n(t), v_0$ ...

Movement kinematics

Describing the longitudinal vehicle motion

Eq. (6.1)

$a_n(t)$

Note: PID = proportional, integral, and derivative; RDM = radius difference method; MFC = microsimulation free-flow acceleration boundary.

Figure 6.1 Flow diagram of the generic cascade approach to extend microscopic traffic models.

6.2 Generic approach to extend models

Figure 6.1 is the flow diagram illustrating the generic cascade approach to extend microscopic traffic models for capturing the characteristics of both the vehicle and the road. In this framework, the microscopic traffic model defines the control logic of either the ACC system or the human driver and gives the acceleration command ($a_{n,cmd}$). The vehicle actual acceleration (a_n), however, cannot follow exactly this command due to the influences of vehicle mechanical features and road conditions. To describe these influences, three extensions are proposed and introduce submodels between these two variables (i.e., $a_{n,cmd}$ and a_n). Specifically, the turning manoeuvre (TM) converts $a_{n,cmd}$ into $a_{n,des}$ to account for the negative effects of the curved road on the acceleration control. The modified control signal ($a_{n,des}$) is the input of the vehicle dynamics (VD) that describes the vehicle's longitudinal response and computes the vehicle acceleration (a_n). In addition, this value (a_n) is bounded by acceleration constraints (AC) based on the practical capabilities of the vehicle's propulsion and braking systems. Each of the three extensions can use different submodels for comparison. Although as explained in the introduction, this study demonstrates the effectiveness of these extensions only with the microscopic free-flow traffic model, they can also be integrated seamlessly with car-following models. The building blocks of this framework are elaborated as follows.

6.2.1 Movement kinematics

The kinematics describes the motion of a vehicle and provides physical relationships between key variables (e.g., speed and acceleration) of the vehicle trajectory, i.e.,

$$\begin{cases} v_n(t) = \dot{x}_n(t), \\ a_n(t) = \dot{v}_n(t), \end{cases} \tag{6.1}$$

where x_n, v_n, and a_n are the position (m), speed (m/s), and acceleration (m/s^2) of the ego vehicle, respectively; t is the simulation time (s).

6.2.2 Microscopic traffic model

The microscopic traffic model explains the ACC control logic in response to the change of kinematic states given in Equation (6.1). Since this study only considers free-flow driving conditions (i.e., there is no target vehicle detected in front), the model generates the acceleration command ($a_{n,cmd}$) that adjusts the vehicle speed (v_n) to match the ACC set speed (v_0). Among many previously established ACC control algorithms, the one adopted as the microscopic traffic model in this work has a linear formulation [118] and is derived from the proportional-integral-derivative (PID) control logic [306], because it is easy to implement and close to industrial practices. Its mathematical formulations are

$$
\begin{cases}
a_{n,cmd}(t) = k_p \cdot e(t) + k_i \cdot \int_0^{t_f} e(t)dt + k_d \cdot \frac{de(t)}{dt}, \\
e(t) = v_0 - v_n(t),
\end{cases}
\tag{6.2}
$$

where v_0 is the set speed (m/s, or target cruise speed) of the ACC system; e is speed error (m/s) calculated as the difference between the ACC set speed (v_0) and the measured vehicle speed (v_n); k_p, k_i, and k_d are gain factors of the proportional (s^{-1}), integral (s^{-2}), and derivative terms, respectively; $a_{n,cmd}$ is the acceleration command (m/s^2) generated by the ACC system; t_f is the end time (s) of the driving simulation.

6.2.3 Turning manoeuvre (TM)

ACC systems usually cannot anticipate future road conditions in the same way as human drivers due to the limitations of current sensing technologies [285]. Therefore, when negotiating a curved road, the ACC vehicle could operate at a severe longitudinal velocity if the ACC set speed is large in free-flow conditions or the ACC radar loses track of the preceding vehicle in car-following conditions [307]. Consequently, the ACC vehicle that turns at a high speed may lose its lateral stability and cause safety issues [308]. To address this problem, stability control systems are introduced in practice, such as direct yaw moment control (DYC), which, however, often have negative effects on the vehicle's acceleration capabilities [307]. The turning manoeuvre (TM) aims to extend microscopic traffic models to reproduce these effects on vehicle behaviour. The following two submodels are presented for comparison.

1) None

It is assumed that the turning manoeuvre has no effect on the acceleration command ($a_{n,cmd}$) generated by the ACC, i.e.,

$$a_{n,des}(t) = a_{n,cmd}(t), \tag{6.3}$$

where $a_{n,des}$ is the desired acceleration (m/s^2).

2) Radius difference method (RDM)

To capture the negative impacts of the turning manoeuvre on the vehicle acceleration, this work proposes the radius difference method (RDM) that utilizes a deceleration term based on the minimum turning radius [309] to modify the acceleration command ($a_{n,cmd}$), i.e.,

$$\begin{cases} a_{n,des}(t) = a_{n,cmd}(t) - b_T \cdot \frac{R_{min}(t)}{R(t)}, \\ R_{min}(t) = \frac{v_n(t)^2}{g \cdot (0.01 s_e + f_s)}, \\ R(t) = \frac{1}{|K(t)|}, \end{cases} \tag{6.4}$$

where b_T is the turning factor (m/s^2, positive); K is road curvature (m^{-1}); R is the turning radius (m) and equal to the reciprocal of the absolute value of the road curvature (K); g is the gravitational acceleration (9.81 m/s^2); s_e is the superelevation (%, or the banking angle), which is the inward transverse inclination provided to counteract the effect of centrifugal force acting on the moving vehicle; f_s is the side friction factor [309]; R_{min} is the minimum turning radius (m) in the road geometric design for a given design speed, as defined by the American Association of State Highway and Transportation Officials (AASHTO) [310].

6.2.4 Vehicle dynamics (VD)

Vehicle dynamics describes the response of a vehicle to the longitudinal acceleration manoeuvre ($a_{n,des}$), which results from the ACC system, i.e., Equation (6.2), and the stability control system, i.e., Equation (6.3) or (6.4). The following three submodels describing vehicle dynamics are commonly reported in the literature.

1) None

It is the simplest case, which can significantly facilitate the theoretical analysis of ACC control strategies [106]. This method assumes that the vehicle's actual acceleration (a_n) is exactly equal to the control input (i.e., the acceleration manoeuvre, $a_{n,des}$), as given by

$$a_n(t) = a_{n,des}(t), \tag{6.5}$$

2) Linear

The linear vehicle dynamics (LVD) introduces a first-order lag between the acceleration control input ($a_{n,des}$) and the vehicle response (a_n) to describe the inertial delay of the powertrain system [138, 311], i.e.,

$$\tau_a \cdot \dot{a}_n(t) + a_n(t) = a_{n,des}(t), \tag{6.6}$$

where τ_a is the actuation lag (s).

3) Nonlinear

The nonlinear vehicle dynamics (NVD) can capture both the internal (i.e., powertrain) and external (i.e., resistances of aerodynamic, rolling, and grade) influential factors [312, 73]. Consequently, this submodel can reproduce the effects of road slope on the vehicle acceleration behaviour, as described by

$$\begin{cases} a_n(t) = \frac{F_T(t) - F_R(t)}{\phi \cdot m}, \\ F_R(t) = f_0 \cdot \cos\theta(t) + f_1 \cdot v_n(t) + f_2 \cdot v_n(t)^2 + mg \cdot \sin\theta(t), \\ F_T(t) = \frac{T_T(t)}{r_w} = m \cdot a_T(t), \\ \tau_a \cdot \dot{a}_T(t) + a_T(t) = a_{n,des}(t), \\ m = m_0 + m_l, \end{cases} \tag{6.7}$$

where F_R is the total resistance force (N), including resistances of aerodynamics, rolling, and grade; f_0, f_1, and f_2 are road load coefficients (N, kg/s, and kg/m, respectively) [29, 275]; θ is the road grade (rad); F_T, T_T, and a_T respectively indicate the tractive force (N), the tractive torque (Nm), and the tractive acceleration (m/s^2), acting on the wheels; r_w

is the wheel radius (m); τ_a is the actuation lag (s); ϕ is the equivalent inertial mass factor; m, m_0, and m_l are the operating mass (kg), the unladen mass (kg), and the mass of vehicle loads (kg, such as passengers and measuring instruments), respectively.

6.2.5 Acceleration constraints (AC)

Acceleration constraints define the maximum capabilities of the vehicle's propulsion and braking systems, and therefore, determine the upper and lower bounds of vehicle acceleration (a_n). Three types of submodels explaining acceleration constraints are provided as follows.

1) None

It is assumed that there are no constraints on the vehicle acceleration (a_n), which can be expressed by

$$-\infty \leq a_n(t) \leq +\infty, \tag{6.8}$$

2) Constant

The vehicle acceleration (a_n) is assumed to be bounded by constant values, as presented by

$$a_{lb} \leq a_n(t) \leq a_{ub}, \tag{6.9}$$

where a_{lb} and a_{ub} are respectively the lower and upper bounds of the vehicle acceleration and set to -7 and 5 m/s^2 based on the OpenACC database created by Makridis et al [288].

3) Microsimulation free-flow acceleration boundary (MFC)

It is well known that the vehicle's propulsion and braking capabilities may differ significantly across vehicle speeds [185]. The MFC boundary model, therefore, serves to define dynamic bounds for the vehicle acceleration (a_n), in which both the lower and the upper bounds vary with the vehicle speed (v_n), i.e.,

$$a_{dp}\big(v_n(t)\big) \leq a_n(t) \leq a_{ap}\big(v_n(t)\big), \tag{6.10}$$

where a_{ap} and a_{dp} are nonlinear curves defining the acceleration potential (m/s^2) and the deceleration potential (m/s^2), respectively. Their calculation methods are elaborated in the authors' previous studies [74, 187].

6.2.6 Model summary

In general, the microscopic traffic model for AVs, i.e., Equation (6.2), is extended to include turning manoeuvre (TM), vehicle dynamics (VD), and acceleration constraints (AC) using a generic cascade approach. Each extension can use different submodels for comparison, for example, the VD can adopt Equation (6.5), (6.6) or (6.7). To clearly identify influential factors affecting vehicle acceleration behaviour, as summarized in Table 6.1, this work investigates all possible combinations of the basic microscopic model and the extensions, namely, the base model (ID = 1) and its extended variants (IDs = 2-18).

Table 6.1 Model configurations

Model ID [b]	Movement kinematics	Microscopic traffic model	Model extensions [a]			Calibration parameters
			Turning manoeuvre (TM)	Vehicle dynamics (VD)	Acceleration constraints (AC)	
1	Eq. (6.1)	Eq. (6.2), PID	Eq. (6.3), None	Eq. (6.5), None	Eq. (6.8), None	k_p, k_i, k_d
2	Eq. (6.1)	Eq. (6.2), PID	Eq. (6.3), None	Eq. (6.5), None	Eq. (6.9), Constant	k_p, k_i, k_d
3	Eq. (6.1)	Eq. (6.2), PID	Eq. (6.3), None	Eq. (6.5), None	Eq. (6.10), MFC	k_p, k_i, k_d
4	Eq. (6.1)	Eq. (6.2), PID	Eq. (6.3), None	Eq. (6.6), Linear	Eq. (6.8), None	k_p, k_i, k_d, τ_a
5	Eq. (6.1)	Eq. (6.2), PID	Eq. (6.3), None	Eq. (6.6), Linear	Eq. (6.9), Constant	k_p, k_i, k_d, τ_a
6	Eq. (6.1)	Eq. (6.2), PID	Eq. (6.3), None	Eq. (6.6), Linear	Eq. (6.10), MFC	k_p, k_i, k_d, τ_a
7	Eq. (6.1)	Eq. (6.2), PID	Eq. (6.3), None	Eq. (6.7), Nonlinear	Eq. (6.8), None	$k_p, k_i, k_d, \tau_a, m_l, f_0, f_1, f_2$
8	Eq. (6.1)	Eq. (6.2), PID	Eq. (6.3), None	Eq. (6.7), Nonlinear	Eq. (6.9), Constant	$k_p, k_i, k_d, \tau_a, m_l, f_0, f_1, f_2$
9	Eq. (6.1)	Eq. (6.2), PID	Eq. (6.3), None	Eq. (6.7), Nonlinear	Eq. (6.10), MFC	$k_p, k_i, k_d, \tau_a, m_l, f_0, f_1, f_2$
10	Eq. (6.1)	Eq. (6.2), PID	Eq. (6.4), RDM	Eq. (6.5), None	Eq. (6.8), None	k_p, k_i, k_d, b_T
11	Eq. (6.1)	Eq. (6.2), PID	Eq. (6.4), RDM	Eq. (6.5), None	Eq. (6.9), Constant	k_p, k_i, k_d, b_T
12	Eq. (6.1)	Eq. (6.2), PID	Eq. (6.4), RDM	Eq. (6.5), None	Eq. (6.10), MFC	k_p, k_i, k_d, b_T
13	Eq. (6.1)	Eq. (6.2), PID	Eq. (6.4), RDM	Eq. (6.6), Linear	Eq. (6.8), None	$k_p, k_i, k_d, b_T, \tau_a$
14	Eq. (6.1)	Eq. (6.2), PID	Eq. (6.4), RDM	Eq. (6.6), Linear	Eq. (6.9), Constant	$k_p, k_i, k_d, b_T, \tau_a$
15	Eq. (6.1)	Eq. (6.2), PID	Eq. (6.4), RDM	Eq. (6.6), Linear	Eq. (6.10), MFC	$k_p, k_i, k_d, b_T, \tau_a$
16	Eq. (6.1)	Eq. (6.2), PID	Eq. (6.4), RDM	Eq. (6.7), Nonlinear	Eq. (6.8), None	$k_p, k_i, k_d, b_T, \tau_a, m_l, f_0, f_1, f_2$
17	Eq. (6.1)	Eq. (6.2), PID	Eq. (6.4), RDM	Eq. (6.7), Nonlinear	Eq. (6.9), Constant	$k_p, k_i, k_d, b_T, \tau_a, m_l, f_0, f_1, f_2$
18	Eq. (6.1)	Eq. (6.2), PID	Eq. (6.4), RDM	Eq. (6.7), Nonlinear	Eq. (6.10), MFC	$k_p, k_i, k_d, b_T, \tau_a, m_l, f_0, f_1, f_2$

[a] Model extensions that can capture the characteristics of both the vehicle and the road. Each extension can use different submodels, e.g., vehicle dynamics (VD) can adopt Equation (6.5), (6.6) or (6.7).

[b] All possible combinations of the microscopic traffic model and the extensions, namely, the base model (ID = 1, not considering any of the extensions) and its extended variants (IDs = 2-18).

6.3   Field experiments with ACC vehicles on test tracks

To compare the above 18 microscopic models in terms of their capabilities to reproduce empirical driving trajectories of commercial ACC systems, free-flow driving campaigns are conducted with different ACC vehicles on different test tracks. This is necessary for drawing reliable conclusions, especially considering that ACC systems are becoming

increasingly more versatile and can be used in various conditions (e.g., country road and motorway) due to other emerging ADAS features, e.g., curve speed adaption (CSA) [313].

6.3.1 Geometric characteristics of test tracks

To ensure a wide range of testing conditions for ACC free-flow driving campaigns, we select two test tracks that have different characteristics of road geometry.

1) ZalaZone Handling Course

ZalaZone Handling Course (HC) in Zalaegerszeg, Hungary, shown in Figure 6.2 (left), is designed for various test elements, e.g., steering (or turning) and electronic stability control (ESC), at low and high speeds. Its straight and curved sections enable reaching a top speed of 120 km/h. Figure 6.2 (a) illustrates its track layout and satellite view. Figure 6.2 (b) gives the key geometric characteristics of the test track, including slope ($\sin \theta$) and curvature (K, m^{-1}), against its longitudinal coordinate (X, m), whose origin ($X = 0$ m) and positive direction are indicated by the location icon and the black arrow in Figure 6.2 (a), respectively.

The road geometric data in Figure 6.2 (b) suggests that the length of the test track is about 1.8 km; while the road slope ($\sin \theta$) and road curvature (K) range from -0.05 to 0.03 and from -0.03 and 0.01 m^{-1}, respectively. It is worth noting that, in this test track, a large road slope is often accompanied by a large road curvature such as the region of X between 900 and 1500 m. Additionally, since most road curves have a curvature (K) of about 0.01 m^{-1}, the typical turning radius (R_T) of ZalaZone HC is about 100 m.

2) AstaZero Rural Road

AstaZero Rural Road (RR) in Sandhult, Sweden, shown in Figure 6.2 (right), is designed to test future traffic safety solutions. The posted speed limit is 70 km/h. Figure 6.2 (c) provides the track layout and the satellite view. Figure 6.2 (d) presents the road geometric characteristics of the AstaZero RR, whose track length is about 5.7 km. The road slope ($\sin \theta$) of this test track varies between -0.03 and 0.03, the range of which is close to that of ZalaZone HC. However, the road curvature (K) ranges from -0.003 to 0.004 m^{-1}, much smaller than that of ZalaZone HC. Therefore, the typical turning radius (R_T) of AstaZero RR is much larger (about 350 m).

(a)

(b) *Note*: Typical turning radius $R_T \approx 100$ m ($R = 1/|K|$).

Slope, $\sin\theta$ / Curvature, K (m^{-1})

— Slope
-- Curvature

Longitudinal coordinate of ZalaZone Handling Course (Hungary), X (m)

ZalaZone Handling Course (HC)

(c)

(d) *Note*: Typical turning radius $R_T \approx 350$ m ($R = 1/|K|$).

Slope, $\sin\theta$ / Curvature, K (m^{-1})

— Slope
-- Curvature

Longitudinal coordinate of AstaZero Rural Road (Sweden), X (m)

AstaZero Rural Road (RR)
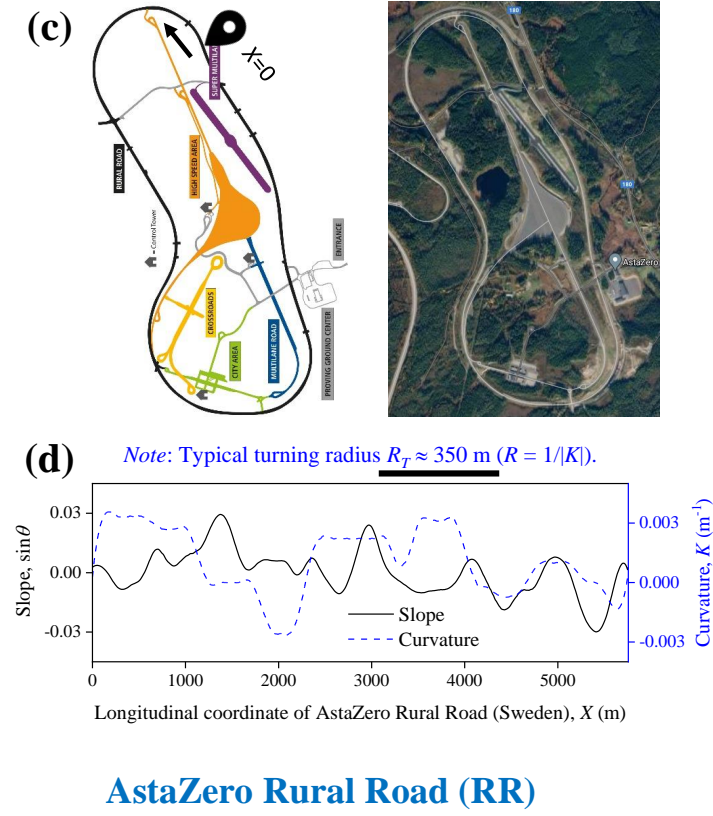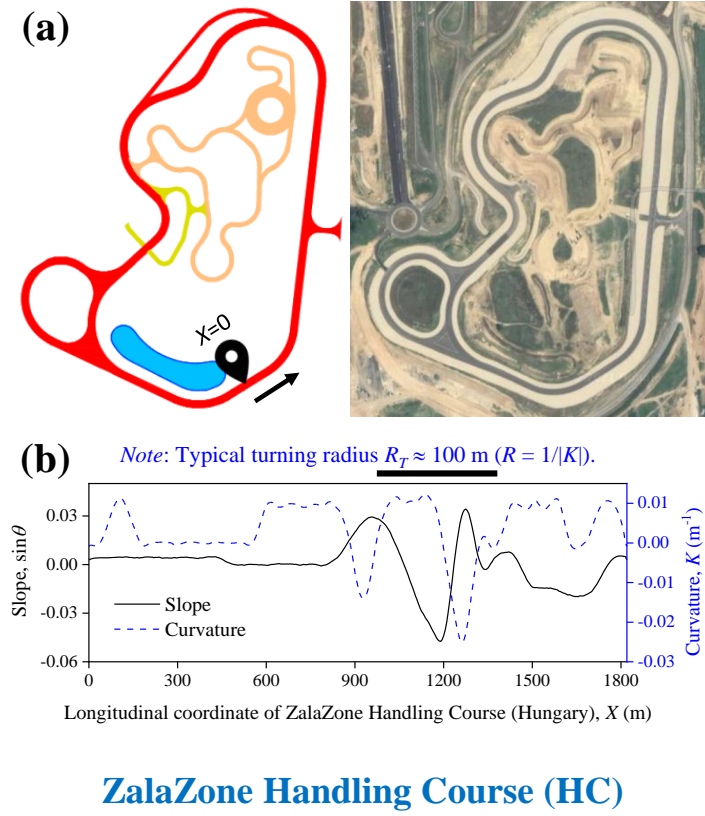
Subplots: The left is ZalaZone Handling Course (HC) in Zalaegerszeg, Hungary; the right is AstaZero Rural Road (RR) in Sandhult, Sweden: (a) and (c) track layout and satellite view; (b) and (d) road geometric characteristics including curvature (K, m^{-1}) and slope ($\sin\theta$).

Figure 6.2 Two test tracks for free-flow driving campaigns with vehicles equipped with commercial adaptive cruise control (ACC).

6.3.2 Vehicle specifications and data acquisition

The vehicle types tested on ZalaZone HC and AstaZero RR are Skoda Octavia 2019 and Audi A8 2018, respectively, whose main specifications are listed in Table 6.2. These specifications are necessary to implement the nonlinear vehicle dynamics in Equation (6.7) and the MFC boundary model in Equation (6.10).

Table 6.2 Vehicle specifications

Specifications	Units	Skoda Octavia [a]	Audi A8 [b]
Unladen mass, m_0	kg	1365	1940
Wheel radius, r_w	m	0.320	0.345
Equivalent inertial mass factor, ϕ	-	1.077	1.052
Length	m	4.685	5.051
Width	m	1.814	1.894
Height	m	1.449	1.444
0-100 km/h acceleration time	s	6.8	6.7
Maximum speed	m/s	249	250
Maximum power	kW	169	202
Maximum torque	Nm	350	650

[a] ACC-equipped vehicle tested on ZalaZone Handling Course.

[b] ACC-equipped vehicle tested on AstaZero Rural Road.

The data acquisition is accomplished by a commercial multi-constellation global navigation satellite system (GNSS) receiver. The GNSS active antenna is mounted on the roof of the vehicle, to ensure maximum satellite visibility and avoid signal attenuation due to the vehicle body. The data of geographic coordinates (i.e., latitude, longitude, and altitude) of the vehicle are recorded, which can guarantee precisions of 0.02 m/s and 0.02 m for speed and localization, respectively [288].

6.3.3 Field data of ACC free-flow driving

Figure 6.3 shows the measured speed and acceleration of the ACC vehicle driven on the test track of ZalaZone HC in free-flow conditions. The collected data are divided into three sets according to the ACC set speed (v_0), in which the Data sets I, II, and III have v_0 of 30, 50, and 70 km/h, respectively. Each data set contains $n = 2$ driving trajectories.

In each subplot, although the set speed (v_0) remains constant, the ACC vehicle's free-flow speed and acceleration vary significantly due to the joint influence of road slope and road curvature. This phenomenon is in line with the observations in previous field studies

[287, 170]. Moreover, the variations of speed and acceleration are found to increase rapidly with an increasing ACC set speed (v_0). For example, the range of the speed variation ($\Delta v = v_{max} - v_{min}$) is 1.35 m/s at v_0 of 30 km/h, increases to 2.12 m/s at v_0 of 50 km/h, and reaches 4.29 m/s at v_0 of 70 km/h. The minimum acceleration is -0.27, -0.67, and -1.14 m/s^2 at set speed (v_0) of 30, 50, and 70 km/h, respectively.

ZalaZone Handling Course (v_0 = 30, 50, and 70 km/h)
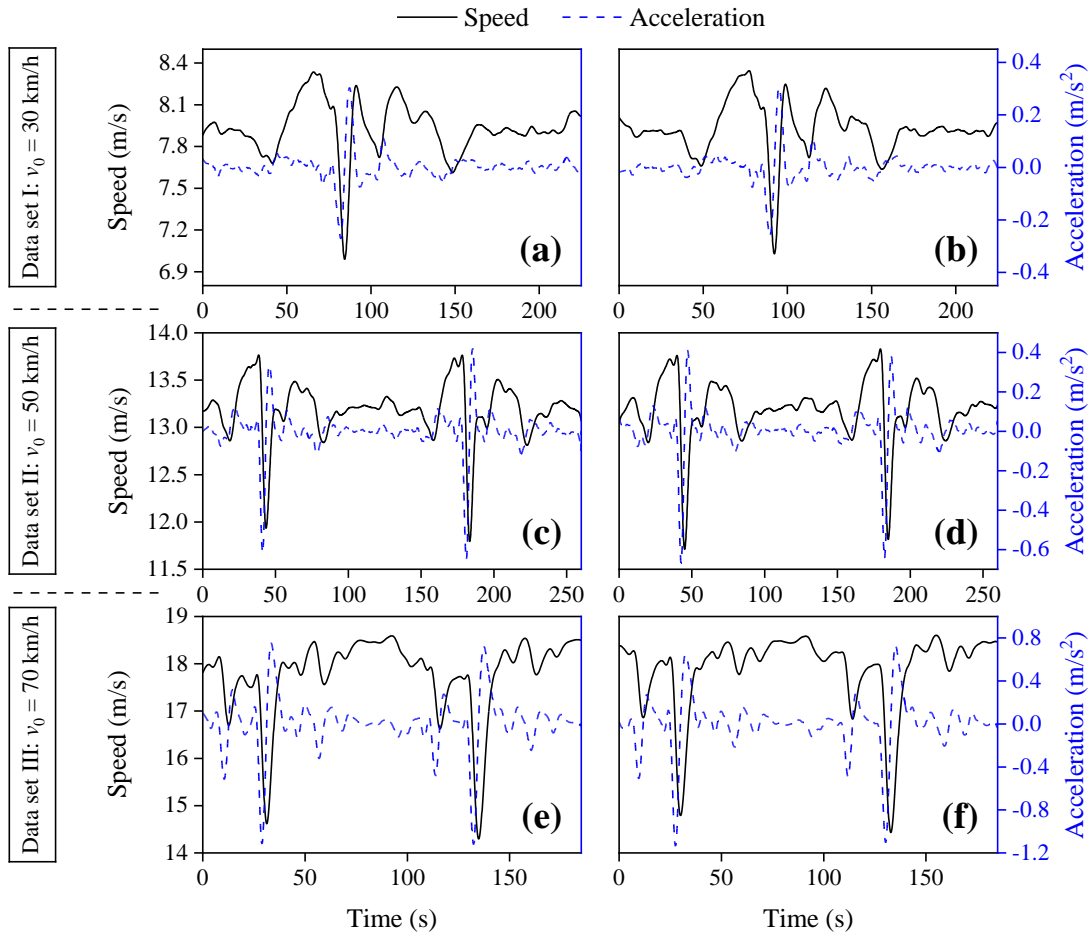
Figure 6.3 ACC free-flow driving trajectories at different set speed (v_0) on the test track of ZalaZone Handling Course: (a) and (b) Data set I (v_0 = 30 km/h); (c) and (d) Data set II (v_0 = 50 km/h); (e) and (f) Data set III (v_0 = 70 km/h).

Figure 6.4 (a)-(d) are the Data set IV containing n = 4 driving trajectories of the ACC vehicle at v_0 of 70 km/h on the test track of AstaZero RR in free-flow conditions. Compared with Data set III, although both data sets have the same set speed (v_0), Data set IV has much smoother curves of speed and acceleration. Specifically, in Data set IV, the range of the speed variation (Δv) is 0.87 m/s, while the minimum acceleration is -0.12 m/s^2. The most plausible reason why Data set IV has more stable free-flow driving behaviour is

that AstaZero RR has a larger typical turning radius (R_T = 350 m) than that (R_T = 100 m) of ZalaZone HC, as described in Figure 6.2 (b) and (d). Except for the impacts of road geometry, different vehicle and ACC characteristics may also contribute to the differences between these two data sets.

AstaZero Rural Road (v_0 = 70 km/h)
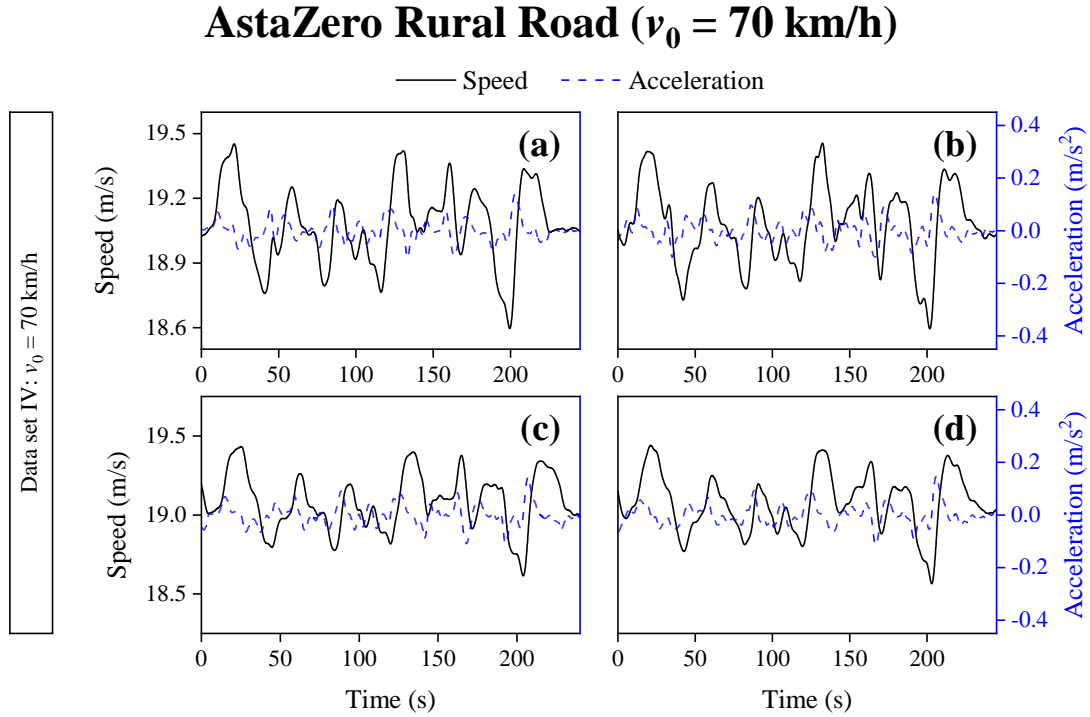
Figure 6.4 ACC free-flow driving trajectories on the test track of AstaZero Rural Road: (a)-(d) Data set IV (v_0 = 70 km/h).

6.3.4 Turning behaviour analysis

According to Data sets I-IV in Figures 6.3 and 6.4, the ACC free-flow driving behaviour largely depends on three factors including ACC set speed (v_0), road slope ($\sin \theta$), and road curvature (K, or turning radius R). In addition, Figure 6.2 (b) and (d) suggest that the road slope data of both ZalaZone HC and AstaZero RR are in a similar range. Therefore, it is necessary to analyse the turning behaviour of AVs by comparing the above four data sets in terms of the set speed (v_0) of the ACC vehicle and the typical turning radius (R_T) of the test track.

In Figure 6.5, the turning characteristics (v_0, R_T) of Data sets I-IV (blue circles) are projected onto the plane defined by the geometric design of highways and streets, in which the curve (marked by the black square) is the minimum radius (R_{min}, m) for a given design

speed (V_{dsg}, km/h), assuming a constant superelevation of 1%. The detailed relationship between R_{min} and V_{dsg} is provided by the American Association of State Highway and Transportation Officials (AASHTO) [310, 309]. The hatched area is here defined as reckless turning because the vehicle speed exceeds the design or (maximum) speed that the curved road is designed to accommodate. Therefore, only Data Set III exhibits reckless turning behaviour based on its turning characteristics (v_0, R_T).
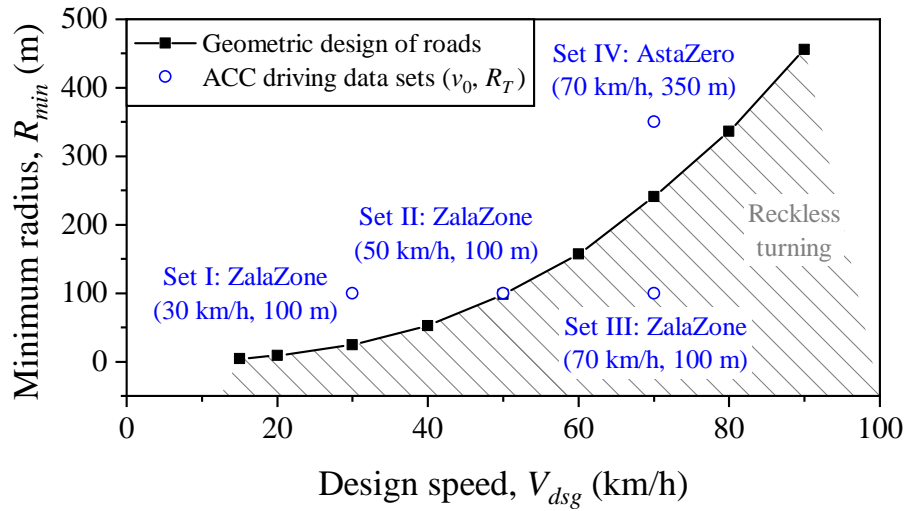
Figure 6.5 The geometric design of highways and streets (black curve), adapted from the American Association of State Highway and Transportation Officials (AASHTO), and the turning characteristics of ACC free-flow driving (blue circles, Data sets I-IV).

6.4 Design of calibration tests

Model calibration is the process of estimating the unknown parameters of the model with the help of observed data. It is important not only for correctly using microscopic traffic models in microsimulation but also for comparing the abilities of different models to reproduce empirical driving trajectories. In this study, 18 microscopic traffic models (listed in Table 6.1), including the base one (ID = 1) and its extended variants (IDs = 2-18), are calibrated and cross-validated against each of the four data sets (shown in Figures 6.3 and 6.4), to demonstrate the effectiveness of different extension combinations in improving model accuracy.

By converting a constrained optimization problem to minimization of a scalar function, the general formulation of the model calibration can be defined as

$$\min_{\boldsymbol{\beta}} f\left(Y^{obs}, Y^{sim}(\boldsymbol{\beta})\right), \tag{6.11}$$

subject to:

$$\begin{cases} Y^{sim}(\boldsymbol{\beta}) = F(\boldsymbol{\beta}), \\ LB_{\boldsymbol{\beta}} \leq \boldsymbol{\beta} \leq UB_{\boldsymbol{\beta}}, \\ \boldsymbol{G}(\boldsymbol{\beta}) \leq 0, \end{cases} \tag{6.12}$$

where F is one of the 18 microscopic traffic models; $\boldsymbol{\beta}$ denotes the vector of model parameters to be calibrated, the dimension of which depends on the model configuration, as summarized in Table 6.1; f is the goodness-of-fit (GoF) function, e.g., root mean square error (RMSE) and Theil's U [208, 314]; Y^{obs} and Y^{sim} respectively represent the observed and simulated measure of performance (MoP), e.g., speed and acceleration; $LB_{\boldsymbol{\beta}}$ and $UB_{\boldsymbol{\beta}}$ are the lower and upper bounds of parameters in $\boldsymbol{\beta}$, respectively; $\boldsymbol{G}$ is a vector of constraint functions.

6.4.1 GoF and MoPs

Punzo et al. [314] propose guidelines for calibration settings by reviewing and comparing all combinations of $GoFs$ and $MoPs$ used in the literature so far. The selection of $GoFs$ and $MoPs$ can significantly affect calibration results, for example, $GoFs$ based on a single MoP (i.e., speed or acceleration) display large variances across different trajectory data. According to their recommendations for achieving Pareto-efficient solutions, this study adopts a GoF function (f) of the normalized RMSE (NRMSE) based on two $MoPs$ (Y), i.e., speed and acceleration, as described by

$$GoF : f = \text{NRMSE}(v, a), \tag{6.13}$$

$$MoPs : Y \in [v, a], \tag{6.14}$$

subject to:

$$
\begin{cases}
\text{NRMSE}(v,a) = \alpha_0 \text{NRMSE}(v) + \alpha_1 \text{NRMSE}(a), \\
\text{NRMSE}(Y) = \text{RMSE}(Y)/\sqrt{\frac{1}{N}\sum_{i=1}^{N}\left(Y_i^{obs}\right)^2}, \\
\text{RMSE}(Y) = \sqrt{\frac{1}{N}\sum_{i=1}^{N}\left(Y_i^{sim} - Y_i^{obs}\right)^2},
\end{cases}
\tag{6.15}
$$

where v and a are the vehicle's speed (m/s) and acceleration (m/s^2), respectively; α_0 and α_1 are weight factors and both equal to 1 in this work; N is the number of data points, proportional to the travel time (t_f, s) of a given trajectory data sampled at a fixed interval of 0.1 s.

6.4.2 Bounds of model parameters

Table 6.3 gives the lower (*LB*) and upper (*UB*) bounds of all calibration parameters shared among 18 models in Table 6.1.

Table 6.3 Bounds of calibration parameters

Parameter	Unit	Lower bound (*LB*)	Upper bound (*UB*)
k_p	s^{-1}	0.01	2
k_i	s^{-2}	0	1
k_d	-	0	1
τ_a	s	0.3	0.8
m_l	kg	230	300
f_0	N	[128.3, 174.0] [a]	[156.8, 212.6] [a]
f_1	kg/s	[0.50, 0.63] [a]	[0.62, 0.77] [a]
f_2	kg/m	[0.028, 0.026] [a]	[0.034, 0.032] [a]
b_T	m/s^2	-5	-0.01

[a] The two-dimensional vector includes bounds for two ACC vehicles: (left) Skoda Octavia on the test track of ZalaZone Handling Course; and (right) Audi A8 on the test track of AstaZero Rural Road.

Most of the *LB* and *UB* values are determined based on previous studies, e.g., gain factors (i.e., k_p, k_i, and k_d) of the ACC free-flow driving control [315], the vehicle actuation lag (τ_a) [316], the deceleration factor (b_T) associated with turning manoeuvre [288]. Others are estimated from the experimental setup and vehicle specifications. For example, the mass of vehicle loads (m_l, including passengers and measuring instruments). In addition, according to Tsiakmakis et al. [275], road load coefficients (f_0, f_1, and f_2) are derived from vehicle specifications in Table 6.2. The ranges of these coefficients are kept small

($\pm 10\%$) around the estimated values to avoid overfitting in calibration [317]. Their bounds are written as a two-dimensional vector since these coefficients differ with the vehicle type.

6.5 Results and discussion

In this work, 18 models (in Table 6.1) are derived from all possible combinations of a basic microscopic traffic model (representing the ACC control logic) and the model extensions, which captures turning manoeuvre (TM), vehicle dynamics (VD), and acceleration constraints (AC). In addition, four data sets (in Figures 6.3 and 6.4) contain ACC free-flow driving trajectories at different set speeds (v_0) on different test tracks. Each model is calibrated and cross-validated against each data set. Specifically, based on the method described by Punzo and Simonelli [208], for a given data set consisting of n observed trajectories (e.g., $n = 2$ and 4 for Data sets I and IV, respectively), model parameters are calibrated using each trajectory, i.e., n calibrations per model. The resulting optimal parameters are then cross-validated against each of the remaining trajectories in this data set, i.e., $n \times (n-1)$ validations per model.

The results presented in this section are divided into three parts. First, the calibration and cross-validation *GoF* values give an overview of the 18 models' abilities to fit (in calibrations) and predict (in validations) empirical driving trajectories. Second, to reveal how model accuracy can benefit from introducing road geometry, we conduct a controlled comparison of speed and acceleration errors between models that are extended to include road slope, road curvature, or both. Finally, the calibrated values of turning factor (b_T) are examined to understand how the radius difference method (RDM) can be improved to capture the impacts of road curvature over the full speed range.

6.5.1 GoF Results

Figure 6.6 (a)-(d) show the *GoF* results of the base model (ID = 1) and its extended variants (IDs = 2-18) in calibrations (black bars) and cross-validations (green bars) against Data sets I, II, III, and IV, respectively. The data of the bar plots represent mean ± standard deviation (SD). The descriptive text (grey) below the x-axis tick labels (Model ID) gives each model's configuration of extensions as discussed in Table 6.1. The base model (ID = 1) considers none of these extensions.

Figure 6.6 The calibration and cross-validation GoF results of 18 models against each of the four ACC driving data sets.

Note: A, B, C = Equations (6.8)-(6.10), respectively, which are different AC submodels (none, constant, and MFC, respectively); MFC = microsimulation free-flow acceleration boundary; RDM = radius difference method; GoF = goodness-of-fit.

The findings indicate that the inclusion of any submodels of acceleration constraints (AC), i.e., Equation (6.8), (6.9), or (6.10), has trivial influences on models' performance.The main reason for this is that, as shown in Figures 6.3 and 6.4, the acceleration of the ACC vehicle in free-flow driving conditions does not vary significantly, and therefore, can hardly reach the upper or lower boundary defined by any of these equations. Results of Models 4-6 suggest, linear vehicle dynamics (LVD), which only accounts for the inertial delay of the powertrain, cannot yield noticeable improvements in minimizing calibration GoF and even deteriorates the model accuracy in most validation cases.

Models 7-9 are extended to include nonlinear vehicle dynamics (NVD), capturing both powertrain dynamics and road load forces (including the one caused by road slope). They exhibit significantly better ability to reproduce ACC driving trajectories. Specifically, these models lead to validation GoF values on average 34.9% less than those of the base model (ID = 1) over four data sets.

Models 10-12 incorporate the RDM submodel, and therefore, can deal with the effects of road curvature on vehicle behaviour. Figure 6.6 (a)-(c) show that based on Data sets I, II, and III (collected from ZalaZone HC with a smaller typical turning radius, i.e., R_T = 100 m), these models result in an average reduction of 21.6% (compared with the base model) in the validation GoF values. On the other hand, Figure 6.6 (d) suggests the RDM submodel provides marginal benefits to these models' accuracy when using Data set IV with a larger R_T (350 m).

Models 16-18, enabled by both the NVD and the RDM, can simultaneously account for the effects of road slope and road curvature on vehicle driving behaviour. In Figure 6.6 (c), these models lead to the lowest validation GoF values about 39.6% less than those of the base model, outperforming Models 7-9 that consider road slope only. The findings suggest that impacts of road curvature on ACC free-flow driving behaviours are substantial when the set speed (v_0) is high and the turning radius (R_T) is small, i.e., the reckless turning as defined in Figure 6.5.

6.5.2   Impacts on the speed and acceleration errors

As discussed in Figure 6.6, submodels NVD and RDM can introduce road geometry (i.e., slope and curvature, respectively) into microscopic traffic models, but have different effects

on model accuracy. Therefore, Table 6.4 demonstrates a controlled comparison of the effectiveness of capturing road slope (Model 7), road curvature (Model 10), and the slope plus curvature (Model 16) in reducing root mean square errors of speed and acceleration, i.e., RMSE(v) and RMSE(a). Data in this table represent the percentage reductions (%) in RMSE(v) and RMSE(a) of selected models (IDs = 7, 10, and 16) compared with those of the base model (ID = 1).

The calibration (left) and validation (right) results in Table 6.4 are consistent with each other. As for Data sets I, II, and IV, Model 7 and Model 16 have similar results in terms of reducing both RMSE(v) and RMSE(a), indicating that the NVD submodel (or the inclusion of road slope) is the dominant factor contributing to better model performance. On the other hand, when reproducing reckless turning behaviours (i.e., Data set III), Model 10 (capturing road curvature) can achieve comparable or even better performance than Model 7 (capturing road slope) in decreasing RMSE(v) and RMSE(a). In addition, Model 16 (considering both curvature and slope) can lead to the greatest reductions in RMSE(v) and RMSE(a) in validations, i.e., 26.0% and 40.2%, respectively. It is worth noting that both submodels (NVD and RDM) are not only generic, i.e., they can be used to extend any of the (free-flow or car-following) microscopic models characterized by acceleration functions, e.g., Equation (6.2), but also lightweight enough for microsimulation because they only respectively incur five and one additional parameter(s) that need to be calibrated, as shown in Table 6.1.

Table 6.4 Percentage reduction in speed and acceleration errors relative to the base model

Data sets #	Calibration (model ID)			Validation (model ID)		
(v_0, R_T) [a]	7 [b]	10 [c]	16 [d]	7 [b]	10 [c]	16 [d]
Reduction in speed error (%): $[RMSE_{ID}(v) - RMSE_1(v)]/RMSE_1(v) \times 100$						
I (30, 100)	-48.2	-6.7	-47.3	-49.2	-9.1	-48.3
II (50, 100)	-54.2	5.9	-52.1	-54.2	4.7	-52.2
III (70, 100)	-12.9	-21.7	-23.6	-15.9	-24.2	-26.0
IV (70, 350)	-54.6	3.1	-54.3	-58.9	-6.2	-58.6
Reduction in acceleration error (%): $[RMSE_{ID}(a) - RMSE_1(a)]/RMSE_1(a) \times 100$						
I (30, 100)	-27.6	-11.9	-27.8	-32.8	-18.6	-32.8
II (50, 100)	-36.7	-16.3	-38.0	-37.9	-17.8	-38.9
III (70, 100)	-24.2	-22.0	-34.1	-32.1	-29.5	-40.2
IV (70, 350)	-32.8	0.1	-32.6	-36.5	-3.1	-36.4

[a] v_0 and R_T are the ACC set speed (km/h) and the typical turning radius (m) of the test track, respectively.
[b] ID = 7, the model extended with the nonlinear vehicle dynamics (NVD) to capture the effects of road slope.
[c] ID = 10, the model extended with the radius difference method (RDM) to capture the effects of road curvature.
[d] ID = 16, the model extended with the NVD and the RDM to capture the effects of both slope and curvature.

6.5.3 Calibrated parameter of turning factor

As described in Equation (6.4), the turning factor (b_T) provides the weight for the deceleration term, and therefore, determines the effectiveness of the RDM's response to the change in road curvature. Figure 6.7 compares the optimal b_T values resulting from the calibration of each extended model (with RDM) against each data set.
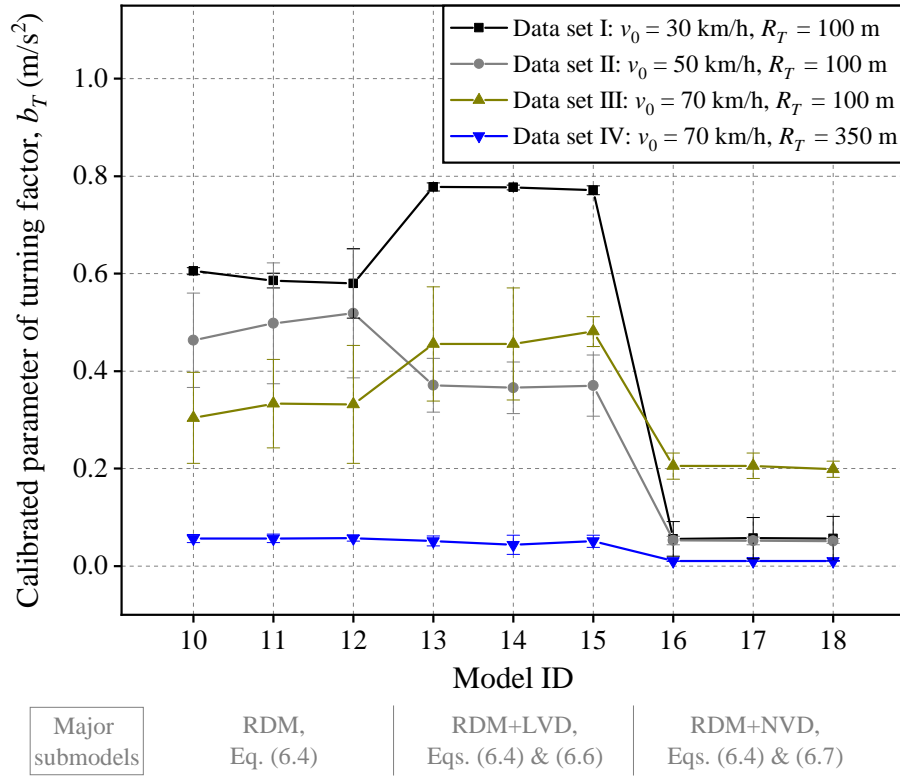
Note: RDM = radius difference method; LVD = linear vehicle dynamics; NVD = nonlinear vehicle dynamics.

Figure 6.7 Calibrated values of turning factor (b_T).

The findings in Figure 6.7 show that, for any given data set, calibrated b_T values of Models 10-15, which consider road curvature only (i.e., extended with RDM or RDM+LVD), are larger than those of Models 16-18, which consider both road curvature and road slope (i.e., extended with RDM+NVD). It suggests that, compared with the former group of models, the latter can make a less severe response to the varying road curvature but generally deliver better performance (see Figure 6.6) due to the inclusion of road slope. In addition, the results of Models 16-18 in Figure 6.7 show that the calibrated b_T values may differ significantly between different data sets used for calibration. For example, Data set III, which represents reckless turning (see Figure 6.5), can lead to much larger calibrated b_T values ($\sim$0.2 m/s^2) than those (0.01-0.06 m/s^2) resulting from other

data sets. Therefore, to better implement the RDM over the full speed range in the future, the turning factor b_T can be transformed into a parameter adaptable to a wide variety of speeds and turning radii, instead of being a constant one as given in Equation (6.4).

6.6   Summary

Some efforts have been devoted to extending microscopic traffic models to capture the effects of road geometry (i.e., slope and curvature) on vehicle driving behaviour. However, there is still substantial room for improvement. For example, previous methods to extend the microscopic models are not sufficiently generic (i.e., usually only applicable to specific models). Microscopic models examined in these studies do not consider the control logic of automated vehicles (AVs). Moreover, none of the extended models is calibrated and validated against empirical trajectory data.

To address these research gaps, this study proposes a generic cascade approach to extend any of the (free-flow or car-following) microscopic models characterized by acceleration functions. Specifically, three model extensions are developed, i.e., turning manoeuvre (TM), vehicle dynamics (VD), and acceleration constraints (AC), each of which can use different submodels for comparison. Their effectiveness is demonstrated with a microscopic free-flow model that is used to simulate adaptive cruise control (ACC). Finally, all possible combinations of the microscopic model and the model extensions are calibrated and cross-validated against each of four data sets, which contain driving trajectories of ACC vehicles on different test tracks.

The results suggest that two submodels, i.e., the nonlinear vehicle dynamics (NVD) and the radius difference method (RDM), can extend the microscopic model to capture the effects of road slope and road curvature, respectively, on AVs' acceleration behaviour. More specifically, the NVD submodel is the dominant factor contributing to increasing (by 34.9% on average) model accuracy. Meanwhile, when reproducing reckless turning behaviours (i.e., the vehicle moves at a high speed and a small turning radius), the inclusion of the RDM is significant for model performance, and the models extended with both the NVD and the RDM can achieve the largest accuracy gains (about 39.6%). In addition, the relationship between R_{min} and V_{dsg}, provided by the American Association of State Highway and Transportation Officials (AASHTO), has shown potential to identify cases of reckless turning, in which the inclusion of the RDM can be beneficial for microsimulation.

Despite these promising results, several issues remain that should be addressed through further studies and refinement of the proposed approach. First, to clearly identify the effects of road geometry on vehicle behaviour, the developed extensions are only demonstrated with the free-flow model in this work. However, their effectiveness should also be assessed through car-following models. Second, the turning factor b_T in the current submodel RDM is constant, nevertheless, it can be transformed into a parameter or function adaptable to a wide variety of driving conditions in order to better implement the RDM over the full speed range.

7 Physics-augmented models to simulate the behaviour of commercial ACC

This chapter investigates the accuracy and robustness of behavioural car-following (CF) and adaptive cruise control (ACC) models to simulate observed driving behaviours of commercial ACC vehicles. To this aim, a general modelling framework is proposed, in which ACC and CF models have been incrementally augmented with physics extensions; namely, perception delay, linear or nonlinear vehicle dynamics, and acceleration constraints. The framework has been applied to the intelligent driver model (IDM), the Gipps model, and to three basic ACC models. These ACC models are a linear controller coupled with three different spacing policies, i.e., the constant time headway (CTH), the IDM-desired, and the Gipps-equilibrium, the latter two of which are derived from the traffic flow theory. The ninety models, resulting from the combination of the five base models and the aforementioned physics extensions, have been assessed and compared through a vast calibration and validation experiment against measured trajectory data of low-level automated vehicles (AVs). When a single extension has been applied, perception delay and linear vehicle dynamics have been the extensions to mostly increase modelling accuracy, whatever the base model considered. Concerning models, Gipps-based ones have outperformed all other CF and ACC models in calibration. Even among ACC models, the linear controllers coupled with the Gipps-equilibrium spacing policy have been the best performing models. On the other hand, IDM-based models have been by far the most robust in validation, showing almost no crash when calibrated parameters have been used to simulate different trajectories. Overall, this study shows the importance of cross-fertilization between traffic flow and vehicle studies.

7.1 Introduction

Accurate simulation of mixed traffic, including human-driven vehicles (HDVs) and automated vehicles (AVs), is crucial to the development of cooperative, connected, and automated mobility (CCAM) technologies and to the assessment of their impacts on traffic efficiency and safety [13]. In traffic simulation, car-following (CF) and adaptive cruise

control (ACC) models have been proposed to mimic behaviours of HDVs and AVs, respectively.

There is a vast literature on modelling HDVs through behavioural car-following (CF) models. Since the true underlying human driving process is unknown, several formulations coexist in the field literature, though based on completely different assumptions [206]. Theoretical properties, advantages, and drawbacks of these models have been confronted and very well known, however, it has never been demonstrated the dominance of one model over the others in terms of performances, i.e., as to the difference between the simulated and observed HDV trajectories [208]. Previous studies have shown that, when calibrating models against trajectories, modelling errors vary more from one trajectory to another, than from one model to another. That is to say, there are trajectories that are reasonably reproduced by most of the models, and others that all models fail to mimic at an acceptable degree of accuracy [208, 314]. Basic CF models have been applied also to emulate the behaviour of vehicles equipped with adaptive cruise control (ACC), though these models were rarely calibrated against field trajectories [118, 253, 318–320]. In general, behavioural CF models barely consider detailed lower-level dynamics concerning characteristics of the vehicle, the sensor, the road, etc. In fact, they are conceived as stimulus-response relationships, which phenomenologically describe the vehicle motion, without making explicit the control and dynamics of the car-following system [185].

On the other hand, a plethora of ACC models have been studied to understand the behaviour of AVs [184]. Most of these models are coupled with lower-level dynamics at different levels of detail for simulating the car-following behaviour of ACC vehicles [106, 321]. Opposite to studies on behavioural CF models, calibration of ACC models against observed trajectories has not generally been a subject of investigation, since the objective of previous ACC studies was to design automated logic to replace the human one, and not to mimic it. ACC models proposed in the literature have been also widely applied to represent the behaviour of AVs and assess their impacts on the efficiency and safety of mixed traffic [322, 119].

If we neglect lower-level dynamics, behavioural CF models and ACC models are conceptually equivalent. In fact, behavioural CF models can be treated as upper-level controllers (like ACC controllers) because they provide the ego vehicle with the desired acceleration or speed, as a function of its kinematic relationships to the preceding vehicle.

Conversely, we may think of ACC models as elementary CF models. Once acknowledged that behavioural CF models and ACC models are equivalent, several questions arise.

First, one may wonder what the impact is, on behavioural CF models' performances, of augmenting them with the detailed lower-level dynamics, which accounts for physical characteristics of the vehicle, the sensor, the road, and etc [285, 187, 74].

Second, one may concern the ability of ACC models to capture actual behaviours of commercial ACC vehicles. Since ACC models in the literature are integrated with lower-level dynamics at different levels of detail, a systematic investigation is necessary to assess the contribution of each physical extension to the model accuracy.

Eventually, one might compare performances of behavioural CF models and ACC models, once augmented with the same physical extensions, and verify whether significant differences emerge from the two classes of models.

To answer these questions, this work develops a comparison framework that allows confronting different models, each one augmented with physical extensions of increasing complexity. To this end, all possible combinations of five base models (CF and ACC) with different extensions, including perception delay, linear or nonlinear vehicle dynamics, and acceleration constraints, are calibrated against measured vehicle trajectory data.

As base models, two CF models, namely, the intelligent driver model (IDM) [199] and the Gipps model [194], as well as three ACC models have been examined. Applied ACC models are a linear controller [106] coupled with three different spacing policies, i.e., the constant time headway (CTH) [141], the IDM-desired, and the Gipps-equilibrium, the latter two of which are derived from the traffic flow theory. To the best of our knowledge, the approach of coupling a linear control law with spacing policies derived from the car-following theory is novel in the literature. Finally, the resulting 90 different models have been calibrated, each one against open-source trajectories gathered in 7 platooning experiments with four high-end vehicles controlled by ACC systems (Audi, Tesla, Mercedes, and BMW), following a platoon leader [288]. Models calibrated against a vehicle trajectory in a platoon, have been also cross-validated against trajectories of the same vehicle taken from other platoons.

The remainder of this chapter is organized as follows. Section 7.2 describes the unified modelling framework adopted in this study, which includes five base models and three types of physics extensions. Section 7.3 introduces the field platoon data applied for

model calibration and validation. Section 7.4 provides the methodology and the design of experiments. Sections 7.5 and 7.6 discuss the calibration and validation results, respectively. Afterwards, Section 7.7 draws the conclusions.

7.2 Modelling framework

The modelling framework is presented in Figure 7.1 and applied to both behavioural CF models and ACC models. Through this framework, we can clarify the equivalence, from a modelling standpoint, between behavioural CF models and ACC models. In addition, it also shows how both types of models can be augmented with lower-level dynamics of increasing complexity.

The five base models examined are the IDM and the Gipps model, and three ACC models that adopt a linear control law coupled either with a CTH spacing policy (L-CTH), or with other two new spacing policies derived from the IDM and the Gipps model (L-IDM and L-Gipps, respectively). Each base model is formulated as 18 variants, which account for all possible combinations of the base model with physics enhancements, including perception delay, vehicle dynamics and acceleration constraints.

The models share the same kinematics that describes the motion of the ego vehicle and its microscopic relationships to the preceding vehicle [308], i.e.,

$$
\begin{cases}
v_n(t) = \dot{x}_n(t), \\
v_{n-1}(t) = \dot{x}_{n-1}(t), \\
a_n(t) = \dot{v}_n(t), \\
s_n(t) = x_{n-1}(t) - x_n(t) - l_{n-1}, \\
\Delta v_n(t) = v_{n-1}(t) - v_n(t),
\end{cases}
\tag{7.1}
$$

where subscripts n and $n-1$ denote the ego and the preceding vehicles, respectively; t is the simulation time (s); x, v, and a respectively represent the position (m), speed (m/s), and acceleration (m/s^2) of the vehicle in the longitudinal direction; s_n is the spacing (m) between the front bumper of the ego vehicle and the back bumper of the preceding one; l_{n-1} means the length (m) of the preceding vehicle; Δv_n is the relative speed (m/s) between the preceding and the ego vehicles.

| **Perception delay** | | **Base model** | | **Vehicle dynamics** | | **Acceleration constraints** |

Perception delay

Defining the time delay of the ACC radar sensor(s)

1) None: Eq. (7.15)
2) Constant: Eq. (7.16)

$v_n(t - \tau_p),$
$v_{n-1}(t - \tau_p),$
$\Delta v_n(t - \tau_p),$
$s_n(t - \tau_p)...$

Base model

Defining the acceleration command of ACC in response to perceived kinematic states

1) IDM: Eq. (7.2) & (7.3)
2) Gipps: Eq. (7.4) & (7.5)
3) L-CTH: Eq. (7.6) & (7.7)
4) L-IDM: Eq. (7.6) & (7.3)
5) L-Gipps: Eq. (7.6) & (7.8)

$a_{n,cmd}(t)$

Vehicle dynamics

Defining the vehicle's response to ACC acceleration command

1) None: Eq. (7.9)
2) Linear: Eq. (7.10)
3) Nonlinear: Eq. (7.11)

$a_n(t)$

Acceleration constraints

Defining the upper and lower bounds of the vehicle acceleration

1) None: Eq. (7.12)
2) Constant: Eq. (7.13)
3) MFC: Eq. (7.14)

$v_n(t), v_{n-1}(t), \Delta v_n(t), s_n(t)...$

Car-following kinematics

Defining the movements and the microscopic relationships of vehicles

Eq. (7.1)

$a_n(t)$

Note: IDM = intelligent driver model; L-CTH, L-IDM, and L-Gipps = linear control law with the spacing policies of constant time headway (CTH), IDM-desired, and Gipps-equilibrium, respectively; MFC = microsimulation free-flow acceleration boundary.

Figure 7.1 Diagram of the unified modelling framework.

7.2.1 Base models

In the proposed modelling framework, the base model defines the ACC acceleration command ($a_{n,cmd}$) in response to the perceived kinematic states (e.g., s_n and Δv_n) given by Equation (7.1). The five base models studied in this work are presented as follows.

1) IDM model

The intelligent driver model (IDM) is developed by Treiber et al., [199] and widely investigated in previous studies [323–326], as described by

$$a_{n,cmd}(t) = a_{max} \cdot \left(1 - \left(\frac{v_n(t)}{v_0} \right)^{\delta} - \left(\frac{s_{n,des}(t)}{s_n(t)} \right)^2 \right), \tag{7.2}$$

where $a_{n,cmd}$ is the acceleration command (m/s^2) that is generated by ACC and then transformed into control signals of the throttle and brake pedals of the ego vehicle; a_{max} indicates the maximum acceleration (m/s^2, positive); v_0 is the desired speed (m/s), which represents the set speed of the onboard ACC system in this work; $s_{n,des}$ indicates the desired inter-vehicle spacing (m); δ is the exponent factor.

The spacing policy defines the desired geometry formation of the car-following system and is formulated as the desired spacing ($s_{n,des}$) in the IDM model. The IDM-desired spacing policy is calculated as

$$s_{n,des}(t) = d_0 + \max \left[0, t_h v_n(t) - \frac{v_n(t)\Delta v_n(t)}{2\sqrt{-a_{max} \cdot a_{min}}} \right], \tag{7.3}$$

where d_0 is the minimum desired (or standstill) spacing (m); t_h denotes the desired time headway (s); a_{min} is the comfortable braking deceleration (m/s^2, negative).

2) Gipps model

The Gipps model specifies a safe inter-vehicle spacing and plans the vehicle speed for the following instants [207]. Therefore, the acceleration command ($a_{n,cmd}$) is derived from the speed planned by the Gipps model and the speed at the current time, i.e.,

$$a_{n,cmd}(t) = \left(v_{n,cmd}(t + t_h) - v_n(t) \right) / t_h \tag{7.4}$$

where t_h is the reaction time (s) and $v_{n,cmd}$ denotes the safe speed (m/s) planned by Gipps model that includes two driving regimes. The former is a free-flow regime where a vehicle is trying to reach its desired speed based on a given acceleration pattern. The latter is a congested regime where the planned speed allows the vehicle to avoid rear-end collision even in the occurrence of sudden deceleration of the preceding vehicle. The vehicle chooses the minimum between speeds resulted from these two regimes [327], i.e.,

$$
\begin{aligned}
v_{n,cmd}(t+t_h) = \min \Bigg\{ & v_n(t) + 2.5 a_{max} t_h \cdot \left(1 - \frac{v_n(t)}{v_0} \right) \left(0.025 + \frac{v_n(t)}{v_0} \right)^{0.5}, \\
& a_{min} \cdot \left(\frac{t_h}{2} + \gamma \right) + \sqrt{a_{min}^2 \cdot \left(\frac{t_h}{2} + \gamma \right)^2 - a_{min} \cdot \left(2\big(s_n(t) - d_0\big) - t_h v_n(t) - \frac{v_{n-1}(t)^2}{\hat{a}_{min}} \right)} \Bigg\},
\end{aligned}
$$

(7.5)

where a_{max} indicates the maximum acceleration (m/s^2, positive); a_{min} is the comfortable braking deceleration (m/s^2, negative); $\hat{a}_{min}$ is the estimated comfortable braking deceleration (m/s^2, negative) of the preceding vehicle; d_0 is the minimum desired (or standstill) spacing (m); v_0 is the desired speed (m/s); γ is an additional delay (s) inserted to avoid braking always at the maximum rate.

3) Linear ACC models

Linear control laws are commonly used in studies of ACC, cooperative ACC (CACC), and vehicular platoons because these models can significantly simplify hardware implementations and the theoretical analysis of controller designs [141, 106, 73]. This work utilizes three linear base models that couple the linear control law with different spacing policies. The general linear formulation is described by

$$
\begin{cases}
a_{n,cmd}(t) = \min \left[k_v \cdot \Delta v_n(t) + k_s \cdot \Delta s_n(t), k_0 \cdot \big(v_0 - v_n(t) \big) \right], \\
\Delta s_n(t) = s_n(t) - s_{n,des}(t),
\end{cases}
$$

(7.6)

where $s_{n,des}$ is the desired inter-vehicle spacing (m); Δs_n denotes the error (m) between the actual (s_n) and the desired ($s_{n,des}$) spacing values; k_s is the gain factor (s^{-2}) for the spacing error (Δs_n); k_v is the gain factor (s^{-1}) for the relative speed between the ego and the

preceding vehicles (Δv_n); k_0 is the gain factor (s^{-1}) for the error between the ego vehicle speed (v_n) and the ACC set speed (v_0).

The desired spacing ($s_{n,des}$) is determined by the spacing policy, which has a considerable influence on traffic flow. Many researchers have studied spacing policies from the microscopic or macroscopic perspective, aiming to improve car-following safety, driver acceptance, and stability performance [328, 124]. For comparison purposes, in this study, three spacing policies are coupled with the linear control law in Equation (7.6).

First, the constant time headway (CTH) spacing policy calculates the desired spacing ($s_{n,des}$) as a linear function of the ego vehicle speed (v_n), in which the slope and the intercept are time headway (t_h, s) and standstill spacing (d_0, m), respectively, i.e.,

$$s_{n,des}(t) = d_0 + t_h \cdot v_n(t), \tag{7.7}$$

In addition, two new spacing policies are tested in this work, which are referred to as IDM-desired and Gipps-equilibrium because they are derived from the IDM and the Gipps model, respectively. These two spacing policies are a novel contribution to the literature on ACC models. The former is given by Equation (7.3) as per the IDM. The latter implements the safe-to-stop spacing strategy of the Gipps model and can be defined as [209]

$$s_{n,des}(t) = d_0 + (t_h + \gamma)v_n(t) - 0.5v_n(t)^2 \left(\frac{1}{a_{min}} - \frac{1}{\hat{a}_{min}} \right), \tag{7.8}$$

For simplicity, the linear control law, i.e., Equation (7.6), coupled with the spacing policies described in Equations (7.7), (7.3), and (7.8), are hereafter abbreviated as L-CTH, L-IDM, and L-Gipps, respectively.

7.2.2 Physics extensions

Most of the studies on behavioural CF models do not consider lower-level dynamics (with some exceptions, e.g., He et al., [74]). While most of the ACC studies account for these dynamics at different levels of detail. The resulting literature is puzzled, with three major extensions variously applied, i.e., vehicle dynamics (e.g., actuation lag), acceleration constraints, and perception delay.

Two types of vehicle dynamics (i.e., linear and nonlinear) are observed to extend CF models in the literature, both of which can strike a balance between simplicity and accuracy

(and thus are feasible for large-scale traffic simulation) [312]. Linear vehicle dynamics (LVD) represents the response of the powertrain system by introducing the first-order lag between the desired acceleration generated by ACC and the actual acceleration of the ego vehicle [311, 138], whereas the effects of external factors cannot be captured. On the other hand, nonlinear vehicle dynamics (NVD) can simulate both internal (e.g., powertrain) and external (e.g., resistances of aerodynamic, rolling, and grade) influential factors [322, 145], in which varying road slope can therefore be considered.

Acceleration constraints (AC) are specified to avoid unrealistic acceleration beyond the vehicle's practical capabilities. In most CF models, the upper and lower acceleration bounds are set as constants or not fully implemented. For example, the IDM only has a constant upper bound for acceleration and therefore may lead to unrealistic large deceleration when the inter-vehicle spacing drops significantly (e.g., in cut-in manoeuvres) [211]. Similar issues are observed with the Gipps model. However, the vehicle's upper and lower acceleration bounds are not constant [185] and affected by many factors such as engine, braking system, and road loads [310]. Consequently, as summarized in Table 2.2, many newly proposed CF models account for adaptive acceleration constraints that vary as functions of speed, e.g., Rakha-Pasumarthy-Adjerid (RPA) model [216], Fadhloun-Rakha (FR) model [219], and microsimulation free-flow acceleration (MFC) model [187].

Perception delay (PD) represents the dynamics of human senses or automated sensors in data gathering and processing. It plays an important role in traffic properties, e.g., string stability [329]. For example, experimental studies exhibit that the linear ACC models with perception delay can accurately capture the string instability of ACC platoons in field tests [330]. Concerning CF models, the IDM, for instance, has been extended to include perception delay [285].

The formulations of the aforementioned physics extensions are presented in the following subsections.

1) Vehicle dynamics

Vehicle longitudinal dynamics defines how the vehicle responds to the acceleration command generated by ACC [106]. Different types of vehicle dynamics utilized in this study can be categorized as follows.

None: It is the simplest case and assumes that the ego vehicle can behave exactly as the acceleration command of ACC, i.e.,

$$a_n(t) = a_{n,cmd}(t), \tag{7.9}$$

Linear: It can capture the actuation lag (τ_a) of the powertrain system, i.e.,

$$\tau_a \cdot \dot{a}_n(t) + a_n(t) = a_{n,cmd}(t), \tag{7.10}$$

where τ_a is the actuation lag (s).

Nonlinear: It can reproduce nonlinear features inherent in vehicles, including the internal powertrain system and the external road loads. The following equations and their variants are widely employed to model the nonlinear longitudinal dynamics, i.e.,

$$\begin{cases} a_n(t) = \frac{F_T(t) - F_R(t)}{\phi \cdot m}, \\ F_R(t) = f_0 \cdot \cos \theta(t) + f_1 \cdot v_n(t) + f_2 \cdot v_n(t)^2 + mg \cdot \sin \theta(t), \\ F_T(t) = \frac{T_T(t)}{r_w} = m \cdot a_T(t), \\ \tau_a \cdot \dot{a}_T(t) + a_T(t) = a_{n,cmd}(t), \\ m = m_0 + m_l, \end{cases} \tag{7.11}$$

where F_R is the total resistance force (N), including resistances of aerodynamics, rolling, and grade; f_0, f_1, and f_2 are road load coefficients (N, kg/s, and kg/m, respectively) [29]; θ is the road grade (rad); g is the gravitational acceleration (9.81 m/s^2); F_T, T_T, and a_T respectively indicate the tractive force (N), the tractive torque (Nm), and the tractive acceleration (m/s^2), acting on the wheels; r_w is the wheel radius (m); τ_a is the actuation lag (s); ϕ is the equivalent inertial mass factor; m, m_0, and m_l respectively represent the operating mass (kg), the unladen mass (kg), and the mass of vehicle loads (kg, such as passengers and measuring instruments).

2) Acceleration constraints

Acceleration constraints define the maximum capabilities of the vehicle's propulsion and braking systems in various conditions. The modelling framework in this work considers three types of acceleration constraints.

None: There are no physical constraints on the acceleration of the ego vehicle, which can be expressed as

$$-\infty \leq a_n(t) \leq +\infty, \tag{7.12}$$

Constant: It assumes that the acceleration of the ego vehicle is always bounded by constant values, as presented by

$$a_{lb} \leq a_n(t) \leq a_{ub}, \tag{7.13}$$

where a_{lb} and a_{ub} are respectively the lower and upper bounds of ego vehicle acceleration and set to -7 and 5 m/s^2 in this work [288].

Microsimulation free-flow acceleration boundary (MFC): The MFC boundary model serves to define dynamic bounds for the ego vehicle acceleration, in which both the lower and the upper bounds change with the vehicle speed (v_n) at the current instant (t). The constraints can be described by

$$a_{dp}\big(v_n(t)\big) \leq a_n(t) \leq a_{ap}\big(v_n(t)\big), \tag{7.14}$$

where a_{ap} and a_{dp} are nonlinear curves representing acceleration potential (m/s^2) and deceleration potential (m/s^2) of the ego vehicle, respectively. Their calculation methods are elaborated in our previous studies [74, 187].

3) Perception delay

Perception delay is a significant feature of AVs enabled by sensors and/or V2X techniques. To capture characteristics of ACC radar sensors, the modelling framework introduces the factor τ_p to represent the time delay (s) of sensor perception. Consequently, the time instance (t) should be replaced with the delayed time instance ($t - \tau_p$) for all the state

Table 7.1 Configurations of investigated car-following (CF) models.

Model group	Model ID	Control law	Spacing policy	Perception delay (PD) [b]	Vehicle dynamics (VD) [b]	Acceleration constraints (AC) [b]	Calibration parameters
IDM-based models	1 [a]	IDM	IDM-desired	None	None	None	$\delta, v_0, d_0, t_h, a_{max}, a_{min}$
	2	IDM	IDM-desired	None	None	Constant	$\delta, v_0, d_0, t_h, a_{max}, a_{min}$
	3	IDM	IDM-desired	None	None	MFC	$\delta, v_0, d_0, t_h, a_{max}, a_{min}$
	4	IDM	IDM-desired	None	Linear	None	$\delta, v_0, d_0, t_h, a_{max}, a_{min}, \tau_a$
	5	IDM	IDM-desired	None	Linear	Constant	$\delta, v_0, d_0, t_h, a_{max}, a_{min}, \tau_a$
	6	IDM	IDM-desired	None	Linear	MFC	$\delta, v_0, d_0, t_h, a_{max}, a_{min}, \tau_a$
	7	IDM	IDM-desired	None	Nonlinear	None	$\delta, v_0, d_0, t_h, a_{max}, a_{min}, \tau_a, m_l, f_0, f_1, f_2$
	8	IDM	IDM-desired	None	Nonlinear	Constant	$\delta, v_0, d_0, t_h, a_{max}, a_{min}, \tau_a, m_l, f_0, f_1, f_2$
	9	IDM	IDM-desired	None	Nonlinear	MFC	$\delta, v_0, d_0, t_h, a_{max}, a_{min}, \tau_a, m_l, f_1, f_2$
	10	IDM	IDM-desired	Constant	None	None	$\delta, v_0, d_0, t_h, a_{max}, a_{min}, \tau_p$
	11	IDM	IDM-desired	Constant	None	Constant	$\delta, v_0, d_0, t_h, a_{max}, a_{min}, \tau_p$
	12	IDM	IDM-desired	Constant	None	MFC	$\delta, v_0, d_0, t_h, a_{max}, a_{min}, \tau_p$
	13	IDM	IDM-desired	Constant	Linear	None	$\delta, v_0, d_0, t_h, a_{max}, a_{min}, \tau_p, \tau_a$
	14	IDM	IDM-desired	Constant	Linear	Constant	$\delta, v_0, d_0, t_h, a_{max}, a_{min}, \tau_p, \tau_a$
	15	IDM	IDM-desired	Constant	Linear	MFC	$\delta, v_0, d_0, t_h, a_{max}, a_{min}, \tau_p, \tau_a$
	16	IDM	IDM-desired	Constant	Nonlinear	None	$\delta, v_0, d_0, t_h, a_{max}, a_{min}, \tau_p, \tau_a, m_l, f_0, f_1, f_2$
	17	IDM	IDM-desired	Constant	Nonlinear	Constant	$\delta, v_0, d_0, t_h, a_{max}, a_{min}, \tau_p, \tau_a, m_l, f_0, f_1, f_2$
	18	IDM	IDM-desired	Constant	Nonlinear	MFC	$\delta, v_0, d_0, t_h, a_{max}, a_{min}, \tau_p, \tau_a, m_l, f_0, f_1, f_2$
Gipps-based models	19 [a]	Gipps	None	None	None	None	$\gamma, v_0, d_0, t_h, a_{max}, a_{min}, \hat{a}_{min}$
	20	Gipps	None	None	None	Constant	$\gamma, v_0, d_0, t_h, a_{max}, a_{min}, \hat{a}_{min}$
	21	Gipps	None	None	None	MFC	$\gamma, v_0, d_0, t_h, a_{max}, a_{min}, \hat{a}_{min}$
	22	Gipps	None	None	Linear	None	$\gamma, v_0, d_0, t_h, a_{max}, a_{min}, \hat{a}_{min}, \tau_a$
	23	Gipps	None	None	Linear	Constant	$\gamma, v_0, d_0, t_h, a_{max}, a_{min}, \hat{a}_{min}, \tau_a$
	24	Gipps	None	None	Linear	MFC	$\gamma, v_0, d_0, t_h, a_{max}, a_{min}, \hat{a}_{min}, \tau_a$
	25	Gipps	None	None	Nonlinear	None	$\gamma, v_0, d_0, t_h, a_{max}, a_{min}, \hat{a}_{min}, \tau_a, m_l, f_0, f_1, f_2$
	26	Gipps	None	None	Nonlinear	Constant	$\gamma, v_0, d_0, t_h, a_{max}, a_{min}, \hat{a}_{min}, \tau_a, m_l, f_0, f_1, f_2$
	27	Gipps	None	None	Nonlinear	MFC	$\gamma, v_0, d_0, t_h, a_{max}, a_{min}, \hat{a}_{min}, \tau_a, m_l, f_1, f_2$
	28	Gipps	None	Constant	None	None	$\gamma, v_0, d_0, t_h, a_{max}, a_{min}, \hat{a}_{min}, \tau_p$
	29	Gipps	None	Constant	None	Constant	$\gamma, v_0, d_0, t_h, a_{max}, a_{min}, \hat{a}_{min}, \tau_p$
	30	Gipps	None	Constant	None	MFC	$\gamma, v_0, d_0, t_h, a_{max}, a_{min}, \hat{a}_{min}, \tau_p$
	31	Gipps	None	Constant	Linear	None	$\gamma, v_0, d_0, t_h, a_{max}, a_{min}, \hat{a}_{min}, \tau_p, \tau_a$
	32	Gipps	None	Constant	Linear	Constant	$\gamma, v_0, d_0, t_h, a_{max}, a_{min}, \hat{a}_{min}, \tau_p, \tau_a$
	33	Gipps	None	Constant	Linear	MFC	$\gamma, v_0, d_0, t_h, a_{max}, a_{min}, \hat{a}_{min}, \tau_p, \tau_a$
	34	Gipps	None	Constant	Nonlinear	None	$\gamma, v_0, d_0, t_h, a_{max}, a_{min}, \hat{a}_{min}, \tau_p, \tau_a, m_l, f_0, f_1, f_2$
	35	Gipps	None	Constant	Nonlinear	Constant	$\gamma, v_0, d_0, t_h, a_{max}, a_{min}, \hat{a}_{min}, \tau_p, \tau_a, m_l, f_0, f_1, f_2$
	36	Gipps	None	Constant	Nonlinear	MFC	$\gamma, v_0, d_0, t_h, a_{max}, a_{min}, \hat{a}_{min}, \tau_p, \tau_a, m_l, f_0, f_1, f_2$
L-CTH-based models	37 [a]	Linear	CTH	None	None	None	$k_s, k_v, k_0, v_0, d_0, t_h$
	38	Linear	CTH	None	None	Constant	$k_s, k_v, k_0, v_0, d_0, t_h$
	39	Linear	CTH	None	None	MFC	$k_s, k_v, k_0, v_0, d_0, t_h$
	40	Linear	CTH	None	Linear	None	$k_s, k_v, k_0, v_0, d_0, t_h, \tau_a$
	41	Linear	CTH	None	Linear	Constant	$k_s, k_v, k_0, v_0, d_0, t_h, \tau_a$
	42	Linear	CTH	None	Linear	MFC	$k_s, k_v, k_0, v_0, d_0, t_h, \tau_a$
	43	Linear	CTH	None	Nonlinear	None	$k_s, k_v, k_0, v_0, d_0, t_h, \tau_a, m_l, f_0, f_1, f_2$
	44	Linear	CTH	None	Nonlinear	Constant	$k_s, k_v, k_0, v_0, d_0, t_h, \tau_a, m_l, f_0, f_1, f_2$
	45	Linear	CTH	None	Nonlinear	MFC	$k_s, k_v, k_0, v_0, d_0, t_h, \tau_a, m_l, f_0, f_1, f_2$
	46	Linear	CTH	Constant	None	None	$k_s, k_v, k_0, v_0, d_0, t_h, \tau_p$
	47	Linear	CTH	Constant	None	Constant	$k_s, k_v, k_0, v_0, d_0, t_h, \tau_p$
	48	Linear	CTH	Constant	None	MFC	$k_s, k_v, k_0, v_0, d_0, t_h, \tau_p$
	49	Linear	CTH	Constant	Linear	None	$k_s, k_v, k_0, v_0, d_0, t_h, \tau_p, \tau_a$
	50	Linear	CTH	Constant	Linear	Constant	$k_s, k_v, k_0, v_0, d_0, t_h, \tau_p, \tau_a$
	51	Linear	CTH	Constant	Linear	MFC	$k_s, k_v, k_0, v_0, d_0, t_h, \tau_p, \tau_a$
	52	Linear	CTH	Constant	Nonlinear	None	$k_s, k_v, k_0, v_0, d_0, t_h, \tau_p, \tau_a, m_l, f_0, f_1, f_2$
	53	Linear	CTH	Constant	Nonlinear	Constant	$k_s, k_v, k_0, v_0, d_0, t_h, \tau_p, \tau_a, m_l, f_0, f_1, f_2$
	54	Linear	CTH	Constant	Nonlinear	MFC	$k_s, k_v, k_0, v_0, d_0, t_h, \tau_p, \tau_a, m_l, f_0, f_1, f_2$
L-IDM-based models	55 [a]	Linear	IDM-desired	None	None	None	$k_s, k_v, k_0, v_0, d_0, t_h, a_{max}, a_{min}$
	56	Linear	IDM-desired	None	None	Constant	$k_s, k_v, k_0, v_0, d_0, t_h, a_{max}, a_{min}$
	57	Linear	IDM-desired	None	None	MFC	$k_s, k_v, k_0, v_0, d_0, t_h, a_{max}, a_{min}$
	58	Linear	IDM-desired	None	Linear	None	$k_s, k_v, k_0, v_0, d_0, t_h, a_{max}, a_{min}, \tau_a$
	59	Linear	IDM-desired	None	Linear	Constant	$k_s, k_v, k_0, v_0, d_0, t_h, a_{max}, a_{min}, \tau_a$
	60	Linear	IDM-desired	None	Linear	MFC	$k_s, k_v, k_0, v_0, d_0, t_h, a_{max}, a_{min}, \tau_a$
	61	Linear	IDM-desired	None	Nonlinear	None	$k_s, k_v, k_0, v_0, d_0, t_h, a_{max}, a_{min}, \tau_a, m_l, f_0, f_1, f_2$
	62	Linear	IDM-desired	None	Nonlinear	Constant	$k_s, k_v, k_0, v_0, d_0, t_h, a_{max}, a_{min}, \tau_a, m_l, f_0, f_1, f_2$
	63	Linear	IDM-desired	None	Nonlinear	MFC	$k_s, k_v, k_0, v_0, d_0, t_h, a_{max}, a_{min}, \tau_a, m_l, f_0, f_1, f_2$
	64	Linear	IDM-desired	Constant	None	None	$k_s, k_v, k_0, v_0, d_0, t_h, a_{max}, a_{min}, \tau_p$
	65	Linear	IDM-desired	Constant	None	Constant	$k_s, k_v, k_0, v_0, d_0, t_h, a_{max}, a_{min}, \tau_p$
	66	Linear	IDM-desired	Constant	None	MFC	$k_s, k_v, k_0, v_0, d_0, t_h, a_{max}, a_{min}, \tau_p$
	67	Linear	IDM-desired	Constant	Linear	None	$k_s, k_v, k_0, v_0, d_0, t_h, a_{max}, a_{min}, \tau_p, \tau_a$
	68	Linear	IDM-desired	Constant	Linear	Constant	$k_s, k_v, k_0, v_0, d_0, t_h, a_{max}, a_{min}, \tau_p, \tau_a$
	69	Linear	IDM-desired	Constant	Linear	MFC	$k_s, k_v, k_0, v_0, d_0, t_h, a_{max}, a_{min}, \tau_p, \tau_a$
	70	Linear	IDM-desired	Constant	Nonlinear	None	$k_s, k_v, k_0, v_0, d_0, t_h, a_{max}, a_{min}, \tau_p, \tau_a, m_l, f_0, f_1, f_2$
	71	Linear	IDM-desired	Constant	Nonlinear	Constant	$k_s, k_v, k_0, v_0, d_0, t_h, a_{max}, a_{min}, \tau_p, \tau_a, m_l, f_0, f_1, f_2$
	72	Linear	IDM-desired	Constant	Nonlinear	MFC	$k_s, k_v, k_0, v_0, d_0, t_h, a_{max}, a_{min}, \tau_p, \tau_a, m_l, f_0, f_1, f_2$
L-Gipps-based models	73 [a]	Linear	Gipps-equilibrium	None	None	None	$k_s, k_v, k_0, v_0, d_0, t_h, \gamma, a_{min}, \hat{a}_{min}$
	74	Linear	Gipps-equilibrium	None	None	Constant	$k_s, k_v, k_0, v_0, d_0, t_h, \gamma, a_{min}, \hat{a}_{min}$
	75	Linear	Gipps-equilibrium	None	None	MFC	$k_s, k_v, k_0, v_0, d_0, t_h, \gamma, a_{min}, \hat{a}_{min}$
	76	Linear	Gipps-equilibrium	None	Linear	None	$k_s, k_v, k_0, v_0, d_0, t_h, \gamma, a_{min}, \hat{a}_{min}, \tau_a$
	77	Linear	Gipps-equilibrium	None	Linear	Constant	$k_s, k_v, k_0, v_0, d_0, t_h, \gamma, a_{min}, \hat{a}_{min}, \tau_a$
	78	Linear	Gipps-equilibrium	None	Linear	MFC	$k_s, k_v, k_0, v_0, d_0, t_h, \gamma, a_{min}, \hat{a}_{min}, \tau_a$
	79	Linear	Gipps-equilibrium	None	Nonlinear	None	$k_s, k_v, k_0, v_0, d_0, t_h, \gamma, a_{min}, \hat{a}_{min}, \tau_a, m_l, f_0, f_1, f_2$
	80	Linear	Gipps-equilibrium	None	Nonlinear	Constant	$k_s, k_v, k_0, v_0, d_0, t_h, \gamma, a_{min}, \hat{a}_{min}, \tau_a, m_l, f_0, f_1, f_2$
	81	Linear	Gipps-equilibrium	None	Nonlinear	MFC	$k_s, k_v, k_0, v_0, d_0, t_h, \gamma, a_{min}, \hat{a}_{min}, \tau_a, m_l, f_1, f_2$
	82	Linear	Gipps-equilibrium	Constant	None	None	$k_s, k_v, k_0, v_0, d_0, t_h, \gamma, a_{min}, \hat{a}_{min}, \tau_p$
	83	Linear	Gipps-equilibrium	Constant	None	Constant	$k_s, k_v, k_0, v_0, d_0, t_h, \gamma, a_{min}, \hat{a}_{min}, \tau_p$
	84	Linear	Gipps-equilibrium	Constant	None	MFC	$k_s, k_v, k_0, v_0, d_0, t_h, \gamma, a_{min}, \hat{a}_{min}, \tau_p$
	85	Linear	Gipps-equilibrium	Constant	Linear	None	$k_s, k_v, k_0, v_0, d_0, t_h, \gamma, a_{min}, \hat{a}_{min}, \tau_p, \tau_a$
	86	Linear	Gipps-equilibrium	Constant	Linear	Constant	$k_s, k_v, k_0, v_0, d_0, t_h, \gamma, a_{min}, \hat{a}_{min}, \tau_p, \tau_a$
	87	Linear	Gipps-equilibrium	Constant	Linear	MFC	$k_s, k_v, k_0, v_0, d_0, t_h, \gamma, a_{min}, \hat{a}_{min}, \tau_p, \tau_a$
	88	Linear	Gipps-equilibrium	Constant	Nonlinear	None	$k_s, k_v, k_0, v_0, d_0, t_h, \gamma, a_{min}, \hat{a}_{min}, \tau_p, \tau_a, m_l, f_0, f_1, f_2$
	89	Linear	Gipps-equilibrium	Constant	Nonlinear	Constant	$k_s, k_v, k_0, v_0, d_0, t_h, \gamma, a_{min}, \hat{a}_{min}, \tau_p, \tau_a, m_l, f_0, f_1, f_2$
	90	Linear	Gipps-equilibrium	Constant	Nonlinear	MFC	$k_s, k_v, k_0, v_0, d_0, t_h, \gamma, a_{min}, \hat{a}_{min}, \tau_p, \tau_a, m_l, f_0, f_1, f_2$

[a] Five base models (without physics extensions).

Acronyms: IDM = intelligent driver model; CTH = constant time headway; MFC = microsimulation free-flow acceleration boundary [74, 187].

Symbols: δ = exponent factor of IDM; v_0 = desired speed (m/s, user-specified); d_0 = minimum desired inter-vehicle spacing (m); t_h = desired time headway (s); a_{max} = maximum acceleration (m/s^2); a_{min} = comfortable braking deceleration (m/s^2); τ_p = perception delay (s); τ_a = actuation lag (s); m_l = mass (kg) of vehicle loads; f_0, f_1, and f_2 = road load coefficients (N, kg/s, and kg/m, respectively); γ = delay factor (s) of Gipps model; $\hat{a}_{min}$ = estimated comfortable braking deceleration (m/s^2) of the preceding vehicle; k_s = the gain factor (s^{-2}) for the spacing error (Δs_n); k_v is the gain factor (s^{-1}) for the relative speed between the ego and the preceding vehicles (Δv_n); k_0 is the gain factor (s^{-1}) for the error between the ego vehicle speed (v_n) and the ACC set speed (v_0).

variables in Equations (7.2), (7.3), and (7.5)-(7.8), including $v_n(t)$, $v_{n-1}(t)$, $\Delta v_n(t)$, $s_n(t)$, $s_{n,des}(t)$, and $\Delta s_n(t)$. This study provides two options of perception delay as follows.

None: Perception delay is not taken into account, i.e.,

$$\tau_p = 0, \tag{7.15}$$

Constant: Perception delay is considered and set as a positive constant, i.e.,

$$\tau_p > 0, \tag{7.16}$$

7.2.3 Model summary

The full list of tested models is summarized in Table 7.1. 90 models are derived by combining the five base models with three vehicle dynamics formulations, three acceleration constraints functions, and two perception delay types, in a full factorial design. In the table, model variants relative to the same base model are sorted by increasing level of complexity.

7.3 Field platoon data

Trajectory data used in this study were collected in platooning experiments carried out on the Rural Road of the AstaZero proving ground (Sweden) in 2019. The test track is 5.7 km long, with road slope ($\sin\theta$) ranging from -0.03 to 0.03, as shown in Figure 6.2 (right).

Table 7.2 Composition of platoons.

Vehicle position	Platoons						
	P1	P2	P3	P4	P5	P6	P7
Leader	Audi A8	Audi A8	Audi A8	Audi A8	Audi A8	Audi A8	Audi A8
Follower 1	Audi A6	Audi A6	Tesla	Tesla	Tesla	Mercedes	Mercedes
Follower 2	BMW	BMW	BMW	BMW	BMW	BMW	BMW
Follower 3	Mercedes	Mercedes	Audi A6	Audi A6	Audi A6	Tesla	Tesla
Follower 4	Tesla	Tesla	Mercedes	Mercedes	Mercedes	Audi A6	Audi A6

The tested platoon was composed of five high-end vehicles from different manufacturers (Audi, Tesla, Mercedes, and BMW), all equipped with commercial ACC. Trajectory data were acquired with the RT-Range S multiple target ADAS measurements
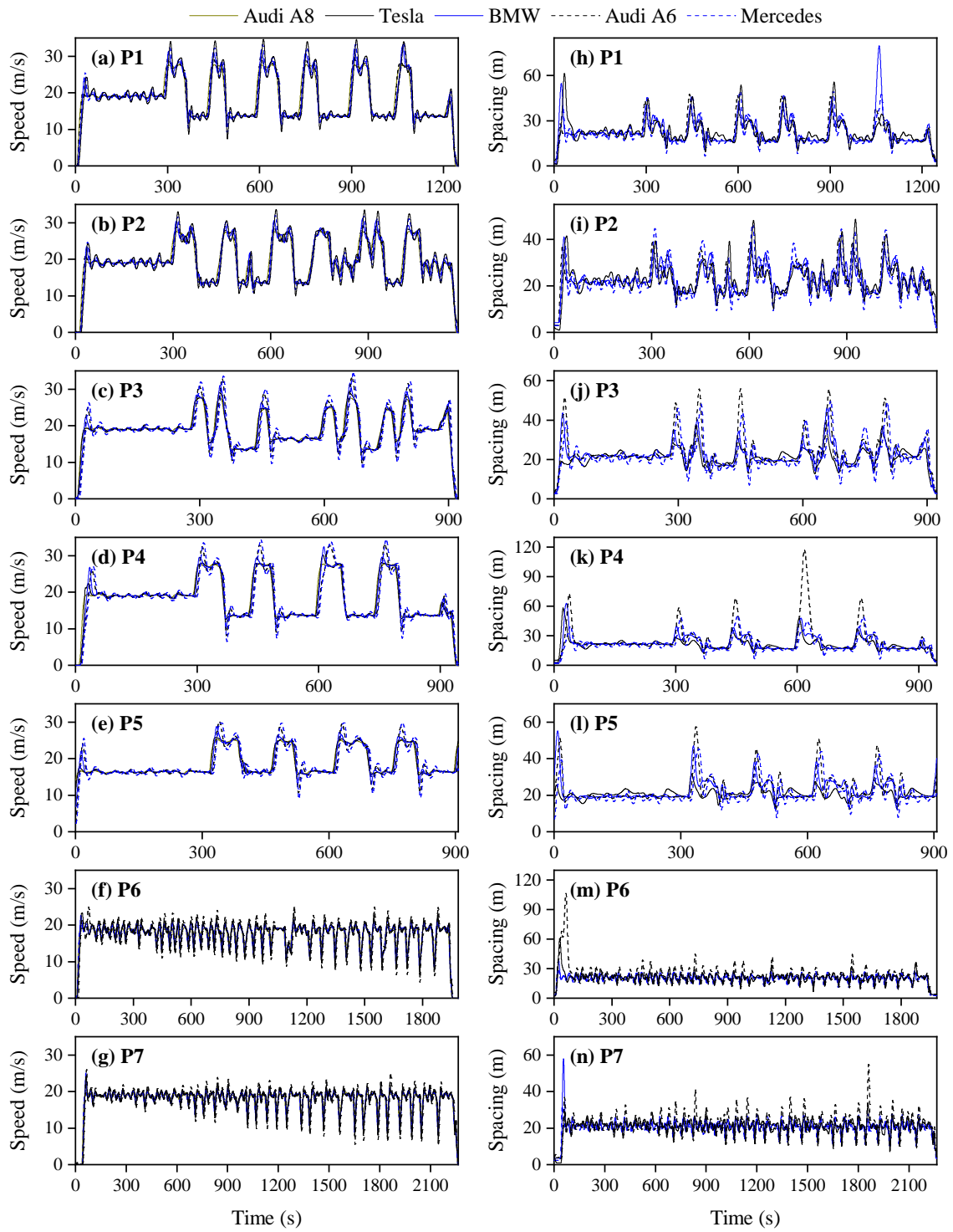
Note: Open-source trajectory data collected by the Joint Research Centre (JRC) of the European Commission in 7 platooning experiments [288].

Figure 7.2 Field data of seven platoons tested on the AstaZero proving ground: (a)-(g) speed (m/s) and (h)-(n) spacing (m).

solution, supplied by Oxford Technical Solutions Company. The system has a sampling rate of 100 Hz (trajectory data were down-sampled to 10 Hz), and guarantees precisions of 0.02 m/s and 0.02 m for speed and position measurements, respectively [288].

Table 7.2 lists the vehicle compositions (platoon leader and four followers) in 7 platoons (some platoons shared the same composition). Data analysis showed that the platoon was in car-following regime during the whole experiment, i.e., the following vehicle's behaviour was influenced more by the preceding vehicle trajectory, vehicle characteristics, and onboard ACC system setup, than by road geometry such as slope.

Figure 7.2 illustrates vehicle trajectory data of 7 platoons tested on the AstaZero proving ground. Figure 7.2 (a)-(g) provide the speed profiles of the platoon leader and four following vehicles. Figure 7.2 (h)-(n) give the corresponding spacing profiles. In the tests, the platoon leader (always an Audi A8), was instructed to keep a predefined speed value (via the onboard ACC system), in order to prevent speed fluctuations caused by human driving. Speed perturbations were then introduced in the platoon by changing the set speed (v_0) of the leading vehicle's ACC system. For safety purposes, the ACC set speed lies between 13.9 and 16.7 m/s in curves and between 25 and 27.8 m/s in straight sections.

7.4 Methodology and design of experiments

To appraise the impact of increasingly complex lower-level dynamics on models' ability to reproduce observed ACC vehicle behaviour, models listed in Table 7.1 have been calibrated against ACC trajectory data. By comparing calibration errors among the variants of each base model, the contribution of every physics extension to model accuracy has been outlined. In addition, by comparing variants of different base models, it has been possible to verify which model is more likely to reproduce observed ACC vehicle trajectory.

To investigate the robustness of calibrated models in terms of transferability of model parameters, cross-validation experiments have been also conducted. In these experiments, the vehicle trajectory in a platoon has been simulated using the set of parameter values obtained by calibrating the model against the trajectory of the same vehicle in a different platoon. The cross-validation analysis has revealed which model is more likely to avoid vehicle collisions, i.e., generation of negative inter-vehicle spacing [326, 325].

7.4.1 Methodology

A general formulation of the model calibration problem is described by [314]

$$\min_{\boldsymbol{\beta}} f\left(Y^{obs}, Y^{sim}(\boldsymbol{\beta})\right), \tag{7.17}$$

subject to:

$$\begin{cases} Y^{sim}(\boldsymbol{\beta}) = F(\boldsymbol{\beta}), \\ LB_{\boldsymbol{\beta}} \leq \boldsymbol{\beta} \leq UB_{\boldsymbol{\beta}}, \\ \boldsymbol{G}(\boldsymbol{\beta}) \leq 0, \end{cases} \tag{7.18}$$

where f is the goodness-of-fit (*GoF*) function (also known as the cost function) in calibration, which measures the overall performance of the car-following model; $\boldsymbol{\beta}$ represents a vector of model parameters to be calibrated; Y^{obs} and Y^{sim} respectively indicate the observed and simulated measure of performance (*MoP*); F is a car-following model; $LB_{\boldsymbol{\beta}}$ and $UB_{\boldsymbol{\beta}}$ respectively denote lower and upper bounds of parameters in $\boldsymbol{\beta}$; and $\boldsymbol{G}$ is a vector of inequality constraint functions.

Based on the findings of the work by Punzo et al. [314], the normalized root mean square error of spacing (s), speed (v), and acceleration (a), i.e., NRMSE(s, v, a), has been adopted as the *GoF* function in model calibration. In fact, in their study, NRMSE(s, v, a) was proved to be the most preferable objective function to be used in a CF calibration problem, according to theoretical arguments and wide empirical evidence. The formulation of NRMSE(s, v, a) is expressed as

$$GoF : f = \text{NRMSE}(Y), \tag{7.19}$$

$$MoPs : Y \in [s, v, a], \tag{7.20}$$

subject to:

$$\begin{cases} \text{NRMSE}(s, v, a) = \alpha_0 \text{NRMSE}(s) + \alpha_1 \text{NRMSE}(v) + \alpha_2 \text{NRMSE}(a), \\ \text{NRMSE}(Y) = \text{RMSE}(Y) / \sqrt{\frac{1}{N} \sum_{i=1}^{N} \left(Y_i^{obs}\right)^2}, \\ \text{RMSE}(Y) = \sqrt{\frac{1}{N} \sum_{i=1}^{N} \left(Y_i^{sim} - Y_i^{obs}\right)^2}, \end{cases} \tag{7.21}$$

where s, v, and a are inter-vehicle spacing (m), ego vehicle speed (m/s), and ego vehicle acceleration (m/s^2), respectively; α_0, α_1, and α_2 are weight factors and all assumed to be equal to 1, in accordance with Punzo et al. [314]; N is the number of data points.

In order to assess the ability of the whole calibration setting (e.g., optimization algorithm and *GoF* function) to find robust solutions, 10 replicates of each model calibration experiment have been performed. By comparing *GoF* value among replicates, we have verified whether the algorithm was able to converge to the same minimum at each calibration replication. The optimization algorithm used in this study is the genetic algorithm (GA) in Python (https://pypi.org/project/geneticalgorithm/).

Additionally, to compare the robustness of the chosen calibration *GoF* with those of alternative *GoFs*, models have been calibrated also by means of the following *GoFs*: RMSE(s), RMSE(v), Theil's U(s,v), Theil's U(s,v,a), and NRMSE(s,v) (for their definitions, see Punzo et al. [314]).

Finally, to investigate the accuracy of calibrated models in validation, performances have been evaluated via the NRMSE(s,v,a).

7.4.2 Design of experiments

The calibration and validation experiments have been conducted for the 90 models listed in Table 7.1, against trajectory data of 4 following vehicles in 7 platoons.

To allow a better understanding of the design of experiments, an index of (VT, P_{cal}, P_{val}) is introduced for representing both calibration and validation experiments, where VT $\in$ [Tesla, BMW, Audi A6, Mercedes] is the vehicle type; P_{cal} and $P_{val} \in$ [P1, P2, P3, P4, P5, P6, P7] denote platoons used for calibration and validation, respectively. For example, the experiment index (Tesla, P2, P6) means that model parameters have been calibrated against the trajectory of vehicle Tesla in platoon P2, and the resulting optimal parameters have been adopted to simulate the trajectory of the same vehicle in platoon P6.

Therefore, experiments with $P_{cal} = P_{val}$ denote calibration experiments, which are 28 per model, i.e., 4 vehicles $\times$ 7 platoons. A total of 2520 calibration experiments (28 trajectories $\times$ 90 models) have been performed.

Experiments with $P_{cal} \neq P_{val}$ refer to validation experiments, which are 168 per model, i.e., 28 sets of calibrated parameters (4 vehicles $\times$ 7 platoons) $\times$ 6 simulations (where 6 is the maximum number of platoons in which the same vehicle is observed, other than P_{cal}).

In addition, each simulation has been performed following the guidelines provided by Punzo et al. [314], i.e.,

1) Time step consistency: The time step of the car-following model simulation is consistent with the resolution (equal to 0.1 s in this work) of trajectory data.

2) Data internal consistency: The trajectory data, consisting of GPS position, speed, and acceleration, should be derived using the same integration scheme applied for the model numerical integration, as provided in Equation (7.1).

Table 7.3 lists the lower and the upper bounds of all calibration parameters, as presented in Table 7.1, shared among the 90 models. Since road load coefficients (f_0, f_1, and f_2) vary with the vehicle type, their bounds are written as a four-dimensional vector. The medians of their ranges have been estimated on the chassis dynamometer so that the ranges have been intentionally kept small around the estimated values (wider ranges could cause overfitting in model calibration [314]).

Table 7.3 Bounds of calibration parameters.

Parameter	Unit	Lower bound (*LB*)	Upper bound (*UB*)
δ	-	0.1	10
v_0	m/s	30	35
d_0	m	1	5
t_h	s	0.1	3
a_{max}	m/s^2	0.5	5
a_{min}	m/s^2	-5	-0.5
$\hat{a}_{min}$	m/s^2	-5	-0.5
γ	s	0	3
τ_a	s	0.3	0.8
τ_p	s	0.1	0.8
m_l	kg	230	300
f_0	N	[185.1, 190.3, 154.9, 139.5] [a]	[226.3, 232.6, 189.4, 170.4] [a]
f_1	kg/s	[0, -0.63, 0.64, 0.56] [a]	[0, -0.52, 0.78, 0.69] [a]
f_2	kg/m	[0.025, 0.042, 0.026, 0.027] [a]	[0.031, 0.051, 0.031, 0.033] [a]
k_s	s^{-2}	0.01	5
k_v	s^{-1}	0.01	5
k_0	s^{-1}	0.01	5

[a] Bounds for different vehicle types (Tesla, BMW, Audi A6, and Mercedes, respectively).

7.5 Calibration results

7.5.1 Robustness of the calibration setting

In CF model calibration, the strong model nonlinearity, the high-dimensional solution space, and the stochasticity of certain optimization algorithms, raise the possibility of trapping the algorithm in a local optimum and of causing poor reproducibility of results.

To address this concern, we have run 10 replicates of each calibration experiment and adopted the coefficient of variation (CV, %) [331] of obtained NRMSE(s, v, a) values at optimum as a measure of relative variability across the replicates. The analysis of CV distribution of all calibration experiments (i.e., 2520 calibration experiments) allowed us to assess the ability of the calibration setting to find robust solutions in terms of *GoF* value. In fact, if the CV distribution result is highly concentrated at zero, i.e., the standard deviation of *GoF* values among replicas is very close to zero in each experiment, calibration results almost do not change when running the same experiment multiple times.
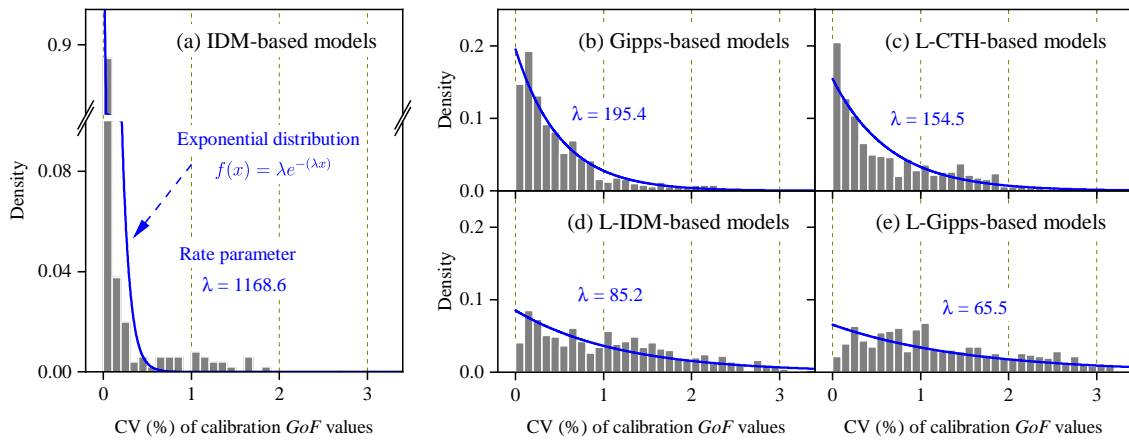
Note: CV = coefficient of variation (defined as the ratio of the standard deviation to the absolute mean value [331]); GoF = goodness-of-fit represented by NRMSE(s, v, a) in this work; IDM = intelligent driver model; L-CTH, L-IDM, and L-Gipps = linear models with the spacing policies of constant time headway (CTH), IDM-desired, and Gipps-equilibrium, respectively.

Figure 7.3 Distribution of the coefficient of variation (CV) of calibration GoF results.

CV distributions are shown in Figure 7.3 and grouped by model class. In each subplot, the distribution of 504 CV values is presented, each value measuring the *GoF* variation across 10 replicates of each of the 504 calibration experiments (18 models × 4 vehicle types × 7 platoons).

Focusing on the range of CV values, findings suggest that calibration *GoF* values at optimum, for all five model classes, are highly reproducible (CVs are always less than 3%). To infer the zero-value concentration, data have been also fitted by an exponential distribution with a decay rate parameter λ, which measures how rapidly the density declines as the CV value increases. IDM-based models stand out prominently in terms of the reproducibility of calibration results, showing a λ value that is almost one order of magnitude higher than the λ values of the other model classes.

7.5.2 Comparison of base models across vehicles and platoons

Figure 7.4 compares the errors of the five base models after calibration against the trajectories of the 4 vehicles in the 7 platoons. Each subplot shows the variability of errors across the 4 vehicles in a specific platoon (sorted according to Table 7.2). For a given vehicle, the first (white) and the last (gold) bars, show the minimum and maximum NRMSE(s, v, a) values achieved by all 90 models. They are the best/worst values that can be achieved with either base models or their variants. The five bars in the middle of each group give the calibration errors of the five base models.
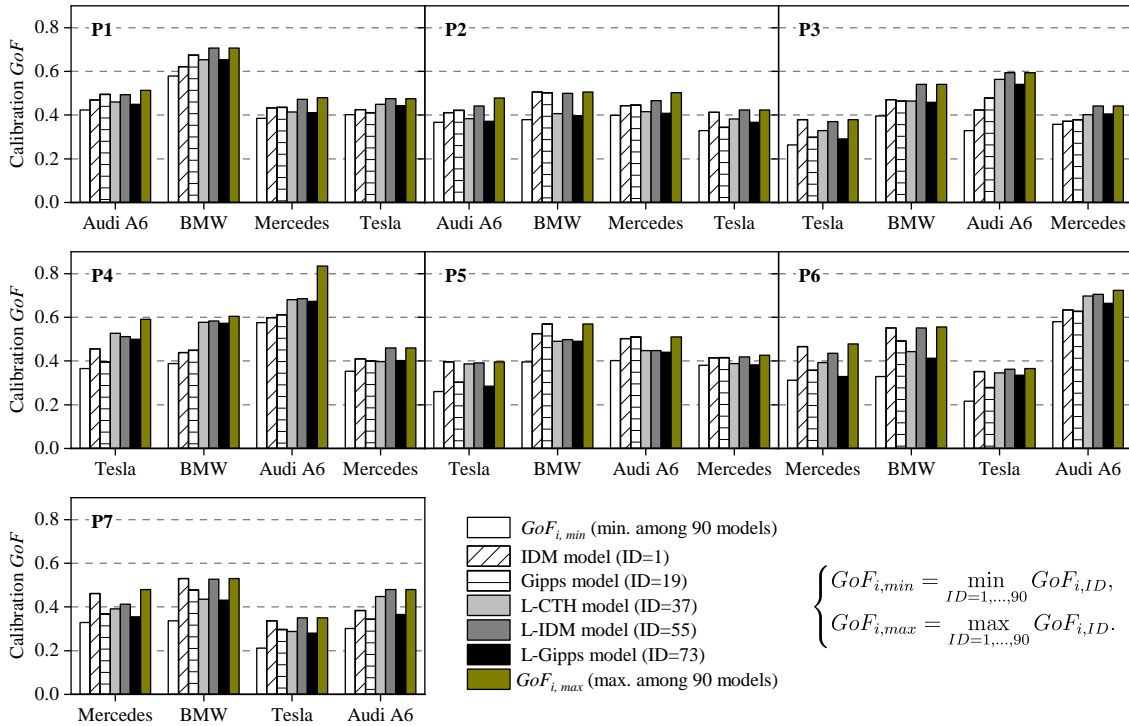
Note: GoF = goodness-of-fit represented by NRMSE(s, v, a) in this work; IDM = intelligent driver model; L-CTH, L-IDM, and L-Gipps = linear models with the spacing policies of constant time headway (CTH), IDM-desired, and Gipps-equilibrium, respectively.

Figure 7.4 Variability of calibration errors of the five base models across the 28 trajectories.

Different trajectory data can lead to very different calibration errors for the same model, which is in accordance with previous studies [208]. Specifically, in Figure 7.4, there are clearly visible *GoF* peaks with values above 0.60 for the vehicle BMW in platoon P1 as well as the vehicle Audi A6 in platoons P4 and P6. These *GoF* peaks highlight the significant effect of trajectory data on calibration errors because, compared with Figure 7.2, these *GoF* peaks seem to be associated with anomalous ACC car-following behaviours. For example, Figure 7.2 (k) and (m) show that Audi A6 in platoons P4 and P6 caused distinctive high peaks of inter-vehicle spacing within time intervals from 600 to 900 s and from 0 to 200 s, respectively.

Moreover, the results in Figure 7.4 reveal that neither vehicle order nor vehicle type can exhibit consistent patterns within or across all platoons in terms of their impacts on calibration errors.

7.5.3 Comparison of model variants

Figure 7.5 shows a box-whisker plot of normalized calibration errors, i.e., $\widetilde{GoF}_{i,ID}$, of the 90 models, as described by

$$\widetilde{GoF}_{i,ID} = \frac{GoF_{i,ID} - GoF_{i,min}}{GoF_{i,min}}, \tag{7.22}$$

$$\begin{cases} i \in [1,...,28], \\ ID \in [1,...,90], \\ GoF_{i,min} = \min_{ID=1,...,90} GoF_{i,ID}, \end{cases} \tag{7.23}$$

where $GoF_{i,ID}$ indicates the calibration error of the *ID*-th model for the *i*-th trajectory; $GoF_{i,min}$ is the minimum calibration error achieved by all 90 models for the *i*-th trajectory. Through this normalization method, we can rule out the direct effect of trajectory data variability, which results in very different calibration errors among trajectories and makes impossible a model comparison. In addition, in model comparison, we do not care about the absolute performance of a model, but we are interested in its performance relative to those of other models in the same calibration experiment/trajectory.
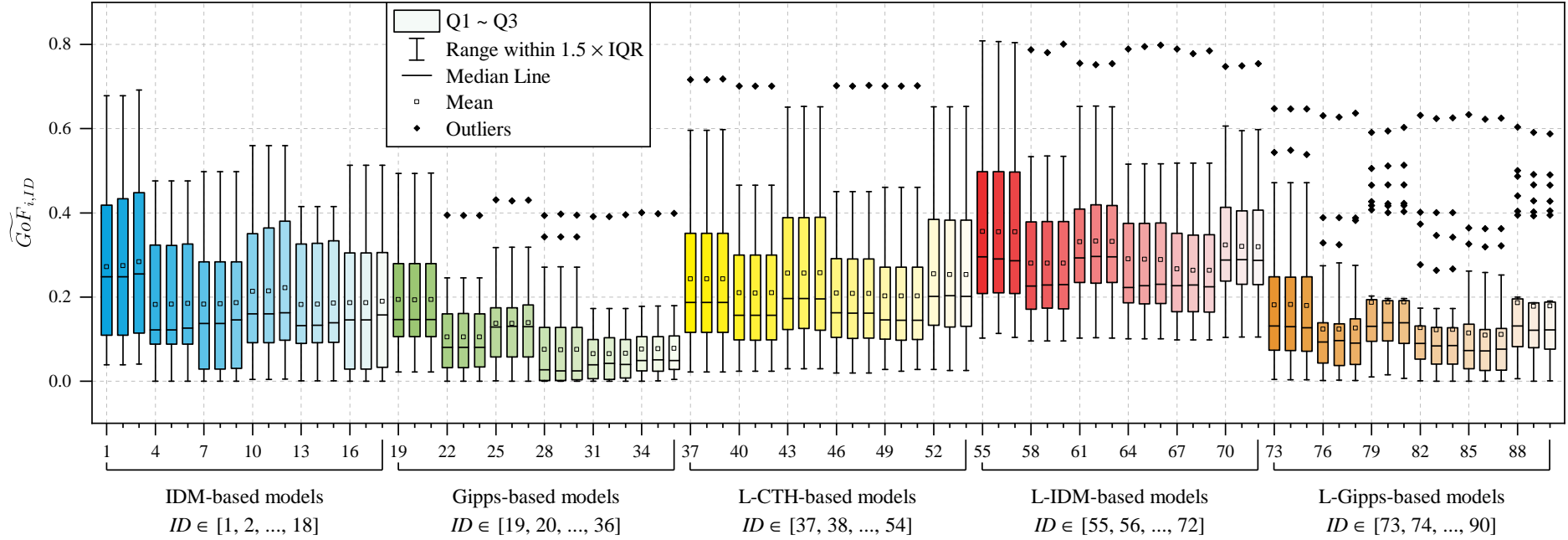
$$\widetilde{GoF}_{i,ID} = \frac{GoF_{i,ID} - GoF_{i,min}}{GoF_{i,min}} \quad \text{and} \quad GoF_{i,min} = \min_{ID=1,\dots,90} GoF_{i,ID}, \quad \text{for } i \in [1, \dots, 28] \text{ and } ID \in [1, \dots, 90]$$

Note: $GoF_{i,ID}$ = goodness-of-fit value of the *ID*-th model for the *i*-th trajectory, calculated by NRMSE(s, v, a); IDM = intelligent driver model; L-CTH, L-IDM, and L-Gipps = linear models with the spacing policies of constant time headway (CTH), IDM-desired, and Gipps-equilibrium, respectively; IQR = interquartile range; Q = quartile.

Figure 7.5 Variability of normalized calibration errors within each model (individual box plot) and among models.

In Figure 7.5, the horizontal line and the square within each box respectively indicate the median and the mean values of normalized calibration errors. The bottom and the top edges of the box represent the 1st (Q1) and 3rd (Q3) quartiles, respectively. The maximum whisker lengths correspond to 1.5 times the interquartile range (IQR). Outliers, i.e., calibration experiments returning a normalized error greater than 1.5IQR plus the third quartile, are marked with black diamonds.

Box plots are grouped into five base model classes and are coloured accordingly. The values of $\widetilde{GoF}_{i,ID}$ range from 0 to 0.81 across 90 models. IDM-based models contain no outliers, suggesting more robust calibration performances. Gipps-based and L-Gipps-based models demonstrate the best overall calibration $\widetilde{GoF}_{i,ID}$ results (both median and mean values are always less than 0.2). Furthermore, L-Gipps-based models are less robust than Gipps-based ones, as to the number of outliers. If we focus on linear controllers, L-Gipps-based models perform better than linear controllers with the IDM-desired or the CTH spacing policy.

Table 7.4 lists the median and median reduction (relative to the base model, %) of $\widetilde{GoF}_{i,ID}$) values in Figure 7.5, which are compared across 90 models. We can therefore investigate both the individual and combined effects of different extensions on the accuracy of base models. The former refers to the impacts of any single physical extension, i.e., perception delay (PD), (linear or nonlinear) vehicle dynamics (LVD or NVD), or acceleration constraints (AC). While the latter denotes the joint effects of multiple extensions. The combined effect is not simply equal to the sum of individual effects because the car-following process is a nonlinear dynamical system. In this table, the rows are grouped by combinations of PD and LVD/NVD (as indicated in the first column) since the effects of different AC types are trivial, which can be attributed to non-aggressive driving behaviours of ACC vehicles observed in the field platoon tests and suggests that their acceleration can hardly reach the upper or lower boundary defined by Equation (7.12), (7.13), or (7.14).

This table reveals several findings regarding the individual effects. Firstly, all base models can achieve a sensible improvement in calibration performance when perception delay (PD) is added in their formulations, which leads to reductions in $\widetilde{GoF}_{i,ID}$ median ranging from 13% to 84% across five model groups.

Table 7.4 Median and median reduction (compared to the base model, %) of $\widetilde{GoF}_{i,ID}$ in calibration.

Main extensions	\multicolumn{3}{c}{IDM-based models}			\multicolumn{3}{c}{Gipps-based models}			\multicolumn{3}{c}{L-CTH-based models}			\multicolumn{3}{c}{L-IDM-based models}			\multicolumn{3}{c}{L-Gipps-based models}		
	ID	$\widetilde{GoF}_{i,ID}$ median	$(\widetilde{GoF}_{i,ID}$ - base)/base, %	ID	$\widetilde{GoF}_{i,ID}$ median	$(\widetilde{GoF}_{i,ID}$ - base)/base, %	ID	$\widetilde{GoF}_{i,ID}$ median	$(\widetilde{GoF}_{i,ID}$ - base)/base, %	ID	$\widetilde{GoF}_{i,ID}$ median	$(\widetilde{GoF}_{i,ID}$ - base)/base, %	ID	$\widetilde{GoF}_{i,ID}$ median	$(\widetilde{GoF}_{i,ID}$ - base)/base, %
	1 [a]	0.248	-	19 [a]	0.147	-	37 [a]	0.187	-	55 [a]	0.295	-	73 [a]	0.131	-
	2	0.248	0	20	0.147	0	38	0.187	0	56	0.291	-2	74	0.130	-1
	3	0.255	3	21	0.147	0	39	0.187	0	57	0.286	-3	75	0.127	-3
LVD	4	0.122	-51	22	0.080	-46	40	0.157	-16	58	0.226	-24	76	0.093	-29
	5	0.122	-51	23	0.080	-45	41	0.157	-16	59	0.229	-23	77	0.097	-26
	6	0.126	-49	24	0.080	-45	42	0.157	-16	60	0.230	-22	78	0.091	-31
NVD	7	0.137	-45	25	0.129	-12	43	0.197	5	61	0.293	-1	79	0.130	0
	8	0.137	-45	26	0.130	-11	44	0.196	5	62	0.296	0	80	0.139	6
	9	0.146	-41	27	0.129	-12	45	0.195	4	63	0.296	0	81	0.139	6
PD	10	0.160	-36	28	0.027	-82	46	0.162	-13	64	0.223	-25	82	0.089	-32
	11	0.160	-36	29	0.025	-83	47	0.162	-14	65	0.227	-23	83	0.084	-36
	12	0.163	-34	30	0.024	-84	48	0.162	-13	66	0.230	-22	84	0.084	-36
PD+LVD	13	0.132	-47	31	0.039	-73	49	0.145	-22	67	0.227	-23	85	0.073	-45
	14	0.132	-47	32	0.042	-71	50	0.145	-23	68	0.229	-23	86	0.072	-45
	15	0.139	-44	33	0.039	-73	51	0.145	-23	69	0.224	-24	87	0.077	-42
PD+NVD	16	0.146	-41	34	0.049	-67	52	0.202	8	70	0.288	-3	88	0.132	0
	17	0.146	-41	35	0.051	-65	53	0.203	9	71	0.289	-2	89	0.121	-8
	18	0.158	-36	36	0.049	-66	54	0.202	8	72	0.287	-3	90	0.121	-7

[a] Base models.

Additionally, introducing linear vehicle dynamics (LVD) yields a clear enhancement for all base models, which is comparable to that resulting from PD. More specifically, the LVD extension can reduce the $\widetilde{GoF}_{i,ID}$ medians of the base models (ID = 1, 19, 37, 55, 73) by ∼50%, ∼45%, ∼16%, ∼23%, and ∼29%, respectively.

Conversely, the individual effect of nonlinear vehicle dynamics (NVD) is not consistent across different base models. This extension can result in accuracy gains of ∼44% and ∼12% for the base IDM and the base Gipps model, respectively, however, cannot improve the base ACC linear models (i.e., L-CTH, L-IDM, and L-Gipps). Furthermore, it is clear that the $\widetilde{GoF}_{i,ID}$ benefit of adding NVD is lower than that of adding LVD. A possible cause for the generally poor outcomes of the NVD can be found in the calibration ranges of road load coefficients in Table 7.3, which were kept small to avoid model overfitting. Small ranges of these coefficients may limit the solution space and the calibration performance.

Eventually, the combined effect of PD+LVD or PD+NVD is often similar to the individual effect of PD or LVD/NVD. For instance, Model 13 (PD+LVD) and Model 16 (PD+NVD) have approximately the same $\widetilde{GoF}_{i,ID}$ medians as their counterparts without PD, i.e., Model 4 (LVD) and Model 7 (NVD), respectively. A possible explanation for this is that the actuation lag (τ_a) of LVD/NVD and the delay factor (τ_p) of PD can largely compensate for each other's absence. However, some exceptions to this pattern are found, e.g., Model 85 (PD+LVD) can outperform its counterparts extended by corresponding individual extensions, namely, Model 82 (PD) and Model 76 (LVD).

7.6 Validation results

7.6.1 Robustness to vehicle collision

In validation experiments, models calibrated on a trajectory are used to simulate a different trajectory, which can yield a collision (i.e., a negative inter-vehicle spacing). Since observed vehicle trajectory data in all platoons are collision-free, the emergence of a collision in simulation suggests that calibrated parameters, although optimal for the specific trajectory used in calibration, cannot be transferred to simulate different trajectories.

Figure 7.6 Collision frequency (F_c) **over 168 validation experiments.**
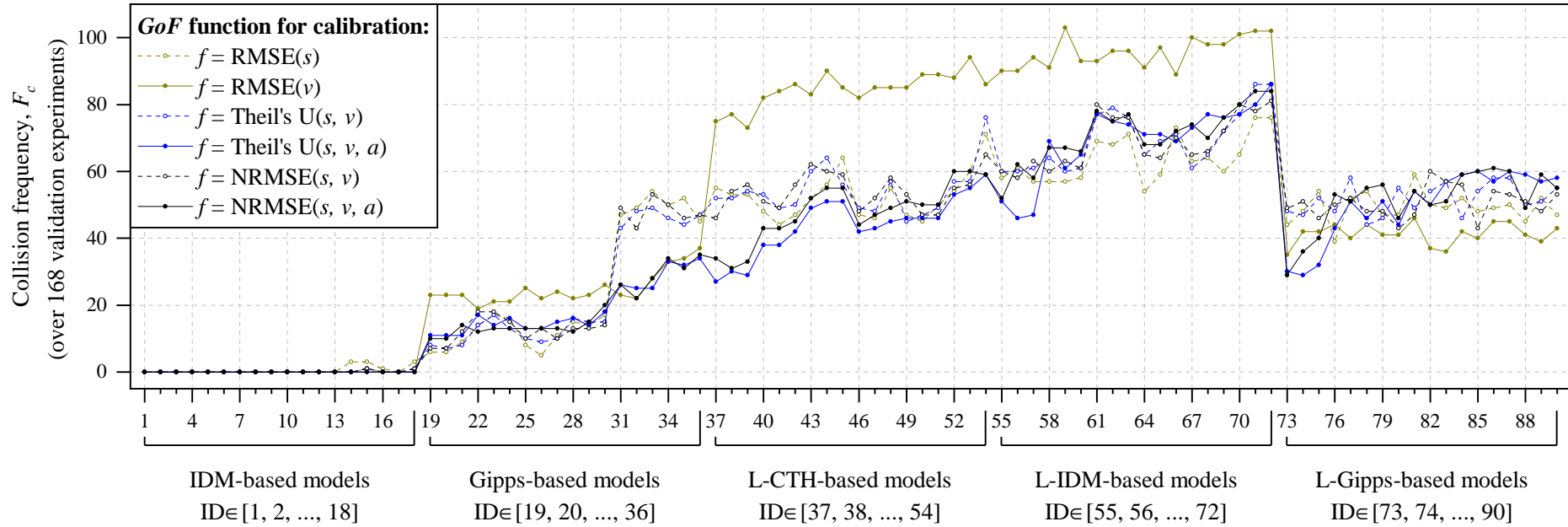
Note: GoF = goodness-of-fit function; IDM = intelligent driver model; L-CTH, L-IDM, and L-Gipps = linear models with the spacing policies of constant time headway (CTH), IDM-desired, and Gipps-equilibrium, respectively.

Therefore, the frequency of collisions measured in validation experiments is an index of model robustness and parameter transferability [332]. Figure 7.6 shows the collision frequency (F_c) of each model over the 168 validation experiments (4 vehicles $\times$ 7 platoons $\times$ 6 simulations/trajectories; see Section 7.4.2). To evaluate also the impact of different calibration settings on parameter robustness and transferability, we have plotted six curves, each one corresponding to a calibration performed with a different *GoF*.

NRMSE(s, v, a) and Theil's U(s, v, a) lead to the least number of collisions, for all 90 models. This result extends the validity of the recommendations given by Punzo et al. [314]. In their work, it has been shown that these two are the most preferable *GoFs* for CF model calibration in terms of accuracy, among the Pareto efficient ones (they also outperform *GoFs* with a single *MoP*). Figure 7.6 shows that the two mentioned *GoFs* guarantee also the highest robustness and transferability of calibrated parameters.

On the other hand, when a single *MoP* is applied, i.e., RMSE(v) and RMSE(s), plotted results show that, also in terms of robustness and transferability of calibrated parameters, spacing is preferable to speed [333]. In fact, the RMSE(v) displays the worst performances, since it sensibly increases the collision frequency in L-CTH-based and L-IDM-based models (and in most of the Gipps-based models).

Figure 7.6 allows us also to compare model variants in terms of robustness. IDM-based models are the most robust, outperforming all other models regarding collision frequency (which is almost zero). Concerning all other models, the higher the model complexity, the higher the collision frequency. Gipps-based models have been the second-best. As to the linear controllers, the Gipps-equilibrium spacing policy has yielded more robust results than other spacing policies.

7.6.2 Comparison of model variants

Table 7.5 reports the calibration (left half) and validation (right half) errors of the 90 models, computed based on RMSE(s), RMSE(v), and RMSE(a). These errors are expressed as median percentage variation from the base model. They measure the model ability to reproduce the observed spacing, speed, and acceleration data, relative to the base model performances. In each half of the table, the NRMSE(s, v, a) percentage variation from the base model is also reported, representing a global performance score since it sums up the errors on spacing, speed, and acceleration.

Table 7.5 Median percentage variation (%) in RMSE(s), RMSE(v), RMSE(a), and NRMSE(s,v,a) from the base models in calibration and validation experiments.

Class	Main extensions	ID	28 calibration experiments, %				collision-free validation experiments [c], %				# of collisions in validation
			[RMSE(s)-base]/base	[RMSE(v)-base]/base	[RMSE(a)-base]/base	[GoF [b]-base]/base	[RMSE(s)-base]/base	[RMSE(v)-base]/base	[RMSE(a)-base]/base	[GoF [b]-base]/base	
IDM-based models		1 [a]	-	-	-	-	-	-	-	-	0/168
		2	0.01	0.00	0.00	0.00	0.01	0.00	0.00	0.00	0/168
		3	0.03	0.00	0.00	0.00	-0.01	-0.01	-0.01	-0.01	0/168
	LVD	4	-1.19	-6.85	-7.10	-6.33	-0.06	-1.65	-2.04	-0.88	0/168
		5	-1.19	-6.80	-7.11	-6.38	-0.15	-1.61	-2.06	-0.86	0/168
		6	-1.17	-6.42	-6.02	-4.89	-0.02	-1.64	-1.76	-0.74	0/168
	NVD	7	-2.35	-7.05	-7.12	-5.04	-1.29	-5.07	-4.20	-4.34	0/168
		8	-2.41	-7.05	-7.11	-5.03	-1.14	-4.99	-4.21	-4.24	0/168
		9	-2.05	-6.35	-7.03	-4.74	-1.99	-5.44	-4.41	-4.82	0/168
	PD	10	-0.89	-4.68	-4.41	-3.57	0.24	-0.74	-0.55	-0.25	0/168
		11	-0.59	-4.46	-4.41	-3.56	-0.02	-0.92	-0.58	-0.32	0/168
		12	-0.54	-4.02	-4.42	-3.54	0.13	-1.03	-0.79	-0.30	0/168
	PD+LVD	13	-1.49	-6.79	-6.84	-5.92	0.19	-1.83	-1.60	-0.43	0/168
		14	-1.48	-6.84	-6.89	-5.96	0.31	-1.63	-1.42	-0.22	0/168
		15	-1.46	-6.42	-5.75	-4.59	0.33	-1.54	-1.56	-0.25	0/168
	PD+NVD	16	-2.35	-6.62	-7.16	-5.05	-0.74	-4.77	-3.44	-3.35	0/168
		17	-2.23	-6.63	-7.14	-5.05	-1.19	-4.89	-3.48	-3.34	0/168
		18	-1.46	-6.12	-7.03	-4.70	-1.00	-5.09	-3.80	-3.74	0/168
Gipps-based models		19 [a]	-	-	-	-	-	-	-	-	10/168
		20	0.05	0.02	-0.03	-0.01	0.03	0.02	-0.01	0.05	14/168
		21	0.09	0.01	0.00	0.00	0.21	-0.11	-0.04	0.02	15/168
	LVD	22	-3.77	-5.27	-5.48	-5.83	-0.96	-3.32	-3.53	-3.89	14/168
		23	-3.84	-5.80	-4.87	-5.72	-1.69	-3.88	-3.91	-4.13	14/168
		24	-3.55	-5.60	-5.45	-5.61	-1.50	-3.04	-3.88	-3.93	15/168
	NVD	25	0.47	-4.13	-3.63	-3.02	-1.06	-1.53	-1.46	-1.28	12/168
		26	0.48	-4.89	-3.73	-3.09	-0.54	-1.07	-1.41	-1.10	14/168
		27	0.92	-4.22	-3.58	-3.05	-1.25	-0.84	-1.43	-1.31	13/168
	PD	28	-7.71	-9.24	-7.15	-10.63	-6.06	-7.36	-4.31	-6.72	15/168
		29	-8.39	-9.30	-7.09	-10.60	-6.25	-7.59	-4.47	-7.20	13/168
		30	-7.51	-9.19	-7.13	-10.62	-6.34	-7.69	-3.81	-7.05	16/168
	PD+LVD	31	-7.96	-9.34	-4.68	-8.97	-4.89	-7.10	-3.91	-6.42	29/168
		32	-9.90	-9.28	-5.70	-9.00	-5.80	-6.96	-3.46	-7.03	26/168
		33	-8.16	-8.79	-5.95	-9.01	-5.94	-7.67	-2.82	-6.94	27/168
	PD+NVD	34	-12.91	-8.51	-5.57	-8.00	-6.79	-5.64	-1.86	-4.49	37/168
		35	-12.02	-8.14	-5.31	-8.25	-6.94	-4.95	-1.51	-4.17	32/168
		36	-11.00	-8.05	-5.94	-8.34	-6.53	-6.22	-1.44	-4.65	38/168
L-CTH-based models		37 [a]	-	-	-	-	-	-	-	-	34/168
		38	0.02	0.03	-0.01	0.00	0.03	0.01	-0.03	-0.04	33/168
		39	-0.01	0.04	0.00	0.00	-0.08	0.06	0.02	0.08	33/168
	LVD	40	-0.97	-0.99	-2.12	-1.43	-0.32	-1.26	-2.52	-1.47	45/168
		41	-0.87	-0.99	-2.06	-1.64	-0.36	-1.23	-2.69	-1.46	45/168
		42	-0.98	-1.12	-2.02	-1.63	0.05	-1.15	-2.86	-1.77	45/168
	NVD	43	3.66	1.84	-0.35	0.40	4.20	2.56	0.20	1.28	55/168
		44	3.39	2.00	-0.36	0.40	3.07	0.47	-0.12	0.44	55/168
		45	3.73	1.88	-0.26	0.78	2.48	1.16	0.38	0.87	56/168
	PD	46	-1.05	-0.91	-1.92	-1.64	-0.18	-0.93	-2.46	-1.55	49/168
		47	-1.05	-0.93	-2.07	-1.89	0.14	-1.08	-2.92	-1.76	50/168
		48	-1.16	-0.89	-2.07	-1.87	0.35	-0.56	-2.52	-1.38	49/168
	PD+LVD	49	-1.20	-1.54	-2.36	-1.57	-0.04	-2.07	-2.85	-1.44	49/168
		50	-1.24	-1.60	-2.31	-1.74	-0.10	-1.97	-3.53	-1.89	51/168
		51	-1.27	-1.46	-2.32	-1.77	0.05	-1.39	-3.28	-1.96	52/168
	PD+NVD	52	4.36	1.96	-0.14	1.19	6.15	3.01	1.04	1.36	57/168
		53	4.63	2.36	-0.41	0.90	4.93	1.94	-0.54	1.05	58/168
		54	4.54	2.17	-0.33	1.08	3.47	1.00	-0.12	1.36	58/168
L-IDM-based models		55 [a]	-	-	-	-	-	-	-	-	57/168
		56	-0.07	-0.17	-0.07	-0.02	-0.30	-0.24	-0.13	-0.17	59/168
		57	0.01	0.04	-0.06	-0.01	-0.11	-0.09	-0.05	-0.05	56/168
	LVD	58	-1.87	-4.75	-5.12	-5.08	-0.68	-3.56	-4.29	-2.62	65/168
		59	-1.30	-4.68	-5.55	-4.83	-0.70	-4.45	-5.33	-3.90	67/168
		60	-0.88	-4.45	-4.93	-5.13	-0.25	-3.50	-4.87	-2.86	68/168
	NVD	61	2.53	-1.50	-3.00	-1.06	6.06	3.66	2.04	2.06	72/168
		62	1.14	-0.72	-2.78	-0.85	5.14	3.31	0.74	2.27	76/168
		63	1.63	-0.70	-3.14	-0.29	5.46	2.99	1.38	2.85	79/168
	PD	64	-1.14	-3.06	-3.65	-2.80	-0.79	-2.37	-2.75	-2.32	71/168
		65	-1.68	-2.74	-3.24	-2.96	-1.38	-3.26	-3.93	-2.98	70/168
		66	-1.63	-3.68	-3.19	-3.38	-0.96	-3.26	-3.38	-2.46	70/168
	PD+LVD	67	-1.37	-5.20	-6.35	-5.50	-0.78	-4.47	-4.83	-3.26	74/168
		68	-2.15	-5.66	-6.22	-5.51	-0.19	-3.53	-3.77	-2.10	74/168
		69	-1.94	-5.52	-6.22	-5.32	0.04	-3.43	-4.34	-2.90	74/168
	PD+NVD	70	0.98	-0.62	-3.07	-0.71	5.85	3.19	1.19	2.30	80/168
		71	1.35	-1.61	-3.39	-0.61	6.96	3.17	2.32	3.52	83/168
		72	0.99	-0.89	-2.72	-1.27	5.19	4.06	2.54	3.35	83/168
L-Gipps-based models		73 [a]	-	-	-	-	-	-	-	-	35/168
		74	-0.26	0.09	0.12	-0.03	0.02	0.03	0.27	0.11	32/168
		75	-0.32	-0.18	0.13	-0.05	-0.10	-0.24	0.05	-0.10	38/168
	LVD	76	-1.26	-3.42	-3.83	-3.70	2.27	-1.38	-4.56	-1.39	56/168
		77	-0.74	-3.03	-3.72	-3.74	-0.05	-2.76	-4.76	-2.68	54/168
		78	-0.36	-3.26	-3.28	-3.49	1.00	-2.15	-4.31	-1.78	56/168
	NVD	79	6.63	1.02	-0.03	1.52	6.35	0.87	-0.03	1.77	54/168
		80	10.08	0.50	-0.31	1.49	2.43	1.10	-0.59	0.45	45/168
		81	8.64	0.37	0.02	1.41	4.76	2.26	-0.19	1.22	50/168
	PD	82	-0.72	-3.59	-3.87	-3.74	1.14	-1.96	-3.53	-1.66	56/168
		83	-1.53	-3.30	-3.99	-3.62	-0.17	-2.84	-4.13	-2.02	55/168
		84	-0.81	-3.49	-3.63	-3.73	-0.15	-2.62	-4.69	-2.19	60/168
	PD+LVD	85	-1.25	-3.38	-3.76	-3.96	0.62	-2.76	-4.41	-2.17	62/168
		86	-1.02	-3.38	-4.58	-4.40	-0.31	-3.88	-5.17	-2.80	61/168
		87	-0.96	-3.37	-4.42	-4.62	0.31	-4.72	-5.35	-4.00	57/168
	PD+NVD	88	9.49	0.78	-0.17	1.15	3.22	1.80	-0.61	1.61	53/168
		89	7.96	0.65	-0.21	1.16	5.01	0.46	-1.46	1.00	59/168
		90	9.11	0.36	-0.74	0.73	6.27	-0.46	-1.03	1.69	60/168

[a] Base models of five model classes, i.e., IDM-based, Gipps-based, L-CTH-based, L-IDM-based, and L-Gipps-based.
[b] GoF = goodness-of-fit function represented by NRMSE(s,v,a) in this work.
[c] The number of collision-free validation experiments, in which all 18 models in the same class do not cause any collision.

Table rows are grouped by base model class. Concerning validation results, it is worth noting that only the validation experiments that are collision-free for all 18 models in a class have been selected for statistical analysis. Moreover, the rightmost column shows the number of collisions that occurred in model validation. The numbers correspond to the collision frequency depicted by the NRMSE(s, v, a) curve in Figure 7.6.

Results show that, in general, physics extensions increase model accuracy in validation less than in calibration.

This trend is exacerbated in the IDM-based models, especially when linear vehicle dynamics (LVD) or perception delay (PD) is added to the base model. The contributions of these extensions to the base model accuracy are less evident in validation than in calibration. In contrast to calibration results, nonlinear vehicle dynamics (NVD) contributes to increasing model accuracy more than linear vehicle dynamics (LVD). Corresponding model variants retained the highest reduction in modelling errors.

Concerning the Gipps-based models, validation results confirm the trends found in calibration, about the contribution of LVD and NVD (the former increases the base model accuracy more than the latter). Among variants, adding PD produces the highest increase in the base model accuracy.

The linear controllers also show consistent results between calibration and validation. LVD was found to have a higher impact on model accuracy than NVD. Concerning spacing policies, it is worth mentioning that the impact of physics extensions on performances of L-CTH-based models between calibration and validation experiments was the same, i.e., the percentage variations of base model accuracy in validation were very close to the ones found in calibration.

7.7 Summary

A comparison framework has been developed to investigate behavioural CF models and ACC models, which are incrementally augmented with physics extensions including perception delay (PD), linear or nonlinear vehicle dynamics (LVD/NVD), and acceleration constraints (AC). All possible combinations of five base models (CF and ACC) with different extensions, i.e., 90 different model variants, have been calibrated and validated against open-source trajectory data, which are collected by the Joint Research Centre (JRC) of the European Commission in 7 platooning experiments with four high-end vehicles

controlled by commercial ACC systems (Audi, Tesla, Mercedes, and BMW), following a platoon leader.

The five base models examined in this framework are two CF models, namely, the intelligent driver model (IDM) and the Gipps model, as well as three ACC models that couple a linear controller with three different spacing policies, i.e., the constant time headway (CTH), the IDM-desired, and the Gipps-equilibrium, the latter two of which are derived from the traffic flow theory. To the best of our knowledge, the proposed approach to couple controllers with spacing policies derived from car-following theory is novel in the field.

More importantly, this study makes several contributions to the current literature. First, by comparing the calibration and validation results among the derived 90 models, we have provided the first comprehensive assessment of the contribution of each physics extension to the base model accuracy (i.e., the model's ability to reproduce the observed trajectory data of ACC vehicles). Second, we have compared performances of CF models and ACC models, when they are augmented with the same extensions, and have highlighted the differences that emerged.

Results suggest that when a single extension has been applied, perception delay and linear vehicle dynamics have been the extensions to mostly increase modelling accuracy, whatever the base model considered. Concerning models, Gipps-based ones have outperformed all other CF and ACC models in calibration. Even among ACC models, the linear controllers coupled with the Gipps-equilibrium spacing policy have been the best performing models. On the other hand, IDM-based models have been by far the most robust in validation, showing almost no crash when calibrated parameters have been used to simulate different trajectories. Overall, this study shows the importance of cross-fertilization between traffic flow and vehicle studies.

Part III

To evaluate AEVs in real-world driving conditions

CHAPTER 8

Comparing energy and safety performances between ACC and human driving behaviours

Surging acceptance of adaptive cruise control (ACC) across the globe is further escalating concerns over its energy and safety impacts. Two questions have directed much of this work: how to distinguish ACC driving behaviour from that of the human driver and how to identify ACC energy and safety impacts. As opposed to simulations or test-track experiments in previous studies, this work is unique because it was performed in real-world car-following scenarios with a variety of vehicle specifications, propulsion systems, drivers, and road and traffic conditions. Tractive energy consumption serves as the energy performance indicator, ruling out the effect of the propulsion system. To further isolate the driving behaviour as the only possible contributor to tractive energy differences, two techniques are offered to normalize heterogeneous vehicle specifications and road and traffic conditions. Finally, ACC driving behaviour is compared with that of the human driver from transient and statistical perspectives. Its impact on tractive energy consumption is then evaluated from individual and platoon perspectives. Our data suggest that, unlike human drivers, ACC followers lead to string instability. Their inability to absorb the speed overshoots may partly be explained by their high responsiveness from a control theory perspective. Statistical results might imply the followers in the automated or mixed traffic flow generally perform worse in reproducing the driving style of the preceding vehicle. On the individual level, ACC followers have tractive energy consumption 2.7-20.5% higher than those of human counterparts. On the platoon level, the tractive energy values of ACC followers tend to consecutively increase (11.2-17.3%). In general, therefore, ACC impacts negatively on tractive energy efficiency. This research provides a feasible path for evaluating the energy impact of ACC in real-world applications. Moreover, the findings have significant implications for ACC safety design when handling the stability-responsiveness trade-off.

8.1   Introduction

Rising transport demand exacerbates the energy, environmental, and safety challenges [334]. Motivated to solve these problems, advanced driver assistance systems (ADAS) gain traction among automakers and consumers. Adaptive cruise control (ACC), as one of the most widely used ADAS features, can automatically adjust the vehicle speed to maintain a safe inter-vehicle spacing or reach the set speed (user-specified). However, the surging acceptance of ACC across the globe is further escalating concerns over its energy and safety impacts, due to its ability to regulate the vehicle's longitudinal driving behaviour for extended periods of distance and time.

ACC systems have reached the consumer market for over two decades and given rise to a proliferation of studies focusing on their driving characteristics in real-world conditions, e.g., the response time and the time headway [335, 251]. Moreover, recent advances in onboard measuring and high-performance computing facilitate the investigation of ACC energy impact [336]. For example, the simulation study of an ACC-equipped heavy-duty truck claims to achieve fuel savings of 5.9% and 2.2% during urban and highway driving scenarios, respectively [144]. ACC driving is reported to deliver fuel savings of 22-31% and 12-26% within acceleration and deceleration phases, respectively [337]. ACC systems are also demonstrated to simultaneously improve fuel efficiency and traffic flow [338].

Given that energy consumption is affected by many factors such as the propulsion system, vehicle specifications, and road and traffic conditions [269, 339], the methods to compute or measure energy consumption are vitally important for assessing the energy impact of ACC driving. Four approaches are often observed in the literature.

1) Measured-data-based method: The instantaneous fuel consumption rate is calculated using the mass air flow (MAF) [340], which can be accessed through OBD-II (onboard diagnostics II). However, this method relies on strong assumptions causing deviations from the actual fuel economy [287], for example, the fuel density and the air-fuel ratio are assumed to be constant and equal to 720 g/L and 14.7, respectively.

2) Mathematical-model-based method: The energy consumption is estimated based on detailed mathematical models for vehicle and powertrain dynamics [176, 179, 97]. This method is prevailing in studies on hybrid electric vehicles (HEVs) due to their multiple energy sources. For example, it is employed in a study to integrate cooperative driving

control and energy management strategy (EMS), leading to an energy saving of 17.9% for a multi-agent system (MAS) of HEVs [26].

3) Regression-model-based method: The regression model is fitted to the data from laboratory tests and then used to estimate the vehicle fuel consumption as a function of the speed and the acceleration [341–343].

4) Powertrain-free-based method: The energy indicator only considers the tractive power (positive) propelling the wheels [252, 339], while the powertrain dynamics and the regenerative braking power (negative) are not taken into account.

Most previous studies are carried out in numerical simulations or test-track experiments. To the best of the authors' knowledge, only a limited number of investigations contribute to understanding the energy impact of ACC driving behaviour in real-world applications. A large-scale study with a fleet of 51 test vehicles over 62 days and 199,300 miles (driven by General Motor employees on their daily commutes) was conducted to analyse the GHG emissions benefit of ACC from a statistical perspective [344]. It is important to stress that GHG emissions are directly correlated to fuel consumption. The results showed that ACC driving could significantly reduce GHG emissions at low speeds, which, however, would hardly deliver a meaningful benefit for the whole journey, because ACC utilization rates at low speeds were marginal and low-speed driving only covered a small portion of the total travel distance. Another field experiment with five vehicles was reported [287] to compare the free-flow driving behaviour between cruise control systems and human drivers. The data revealed that cruise control could reduce fuel consumption by 3.3% on average relative to human driving. So far, however, no research has been found that surveyed ACC energy impact in real-world car-following scenarios. The current research sets out to fill this gap.

Two questions have directed much of this work: how to distinguish ACC driving behaviour from that of the human driver and how to identify the ACC energy and safety impacts. As opposed to simulations or test-track experiments as described in previous studies, this work is unique because it was performed in real-world car-following scenarios with a variety of vehicle specifications, propulsion systems, drivers, and road and traffic conditions. Tractive energy consumption serves as the energy performance indicator, ruling out the effect of the propulsion system. Finally, ACC driving behaviour is compared with

that of the human driver from transient and statistical perspectives. Its impact on tractive energy consumption is then evaluated from individual and platoon perspectives.

The rest of this chapter is organized as follows. Section 8.2 describes the methodologies including the modelling of tractive energy demand and the design of the highway driving experiment. In Section 8.3, the results are discussed from the perspectives of driving behaviour and tractive energy consumption. Section 8.4 concludes this work by summarizing the main findings and implications.

8.2 Methodologies

8.2.1 Modelling of tractive energy consumption

When approaching the energy impact of ACC driving behaviour, the aforementioned powertrain-free-based tractive energy consumption is a more suitable assessment indicator from a transport engineering perspective [252]. Although it does not directly reflect the engine fuel consumption or the battery charge depletion, this metric can rule out the energy effect of heterogeneous propulsion systems in the traffic network. In addition, the auxiliary loads are not taken into account in the computation of tractive energy consumption, but all test vehicles were using the same auxiliary functions during the driving campaign in this study. Specifically, the vehicle's tractive energy consumption (E_T, kWh/100 km) is calculated by integrating the tractive power (P_T, kW, acting on the wheels) over time, not considering the negative power components from the regenerative braking, i.e.,

$$P_T(t) = \max\left[0, \left(f_0 \cdot \cos\theta + f_1 \cdot v_n(t) + f_2 \cdot v_n(t)^2 + mg \cdot \sin\theta + \phi m \cdot a_n(t)\right)\frac{v_n(t)}{1000}\right], \quad (8.1)$$

$$E_T = \frac{\int_0^{t_f} P_T(t)dt}{0.036 \cdot \int_0^{t_f} v_n(t)dt}, \quad (8.2)$$

where f_0, f_1, and f_2 are road load coefficients (N, kg/s, and kg/m, respectively); m is the vehicle mass (kg); ϕ is the equivalent inertial mass factor; v_n and a_n are the ego vehicle's speed (m/s) and acceleration (m/s^2), respectively; θ is the road slope (rad); g is the gravitational acceleration (9.81 m/s^2); dt is the time interval (s) between consecutive measurement points; t_f denotes the total duration (s) of the travel period.

8.2.2 Experimental design

Figure 8.1 shows the real-world experiment in highway multiple-car-following scenarios. Field tests were conducted on a section of Autostrada A26 (Italy) between Ispra and Vicolungo, a 124.6 km round trip, to collect driving data under actual traffic conditions. Five vehicles were equipped with global navigation satellite system (GNSS) receivers, able to collect GNSS data with a 10 Hz measurement rate. The receivers were configured to collect signals from both GPS and Galileo (the European GNSS). The average horizontal accuracy reported by the receivers was less than 50 cm. GNSS active antennas were mounted on the roof of the cars, in order to ensure maximum satellite visibility and avoid signal attenuation from the vehicle body. At each time instant, the geographic coordinates (latitude, longitude, and altitude) of the vehicles were recorded. These coordinates were then transformed into a local East, North, and Up (ENU) Cartesian reference frame. Outliers were filtered using typical moving average post-processing. The test section comprises various uphill and downhill segments, providing an appropriate environment to examine different tractive load conditions for human or ACC driving. As shown in Figure 8.1 (a), the altitude profile of the test route was extracted using Google API. The road slope, in Figure 8.1 (b), varies between -8% and 8%, where some rather steep points appear since the highway section is located at the foot of the Alps Mountains.
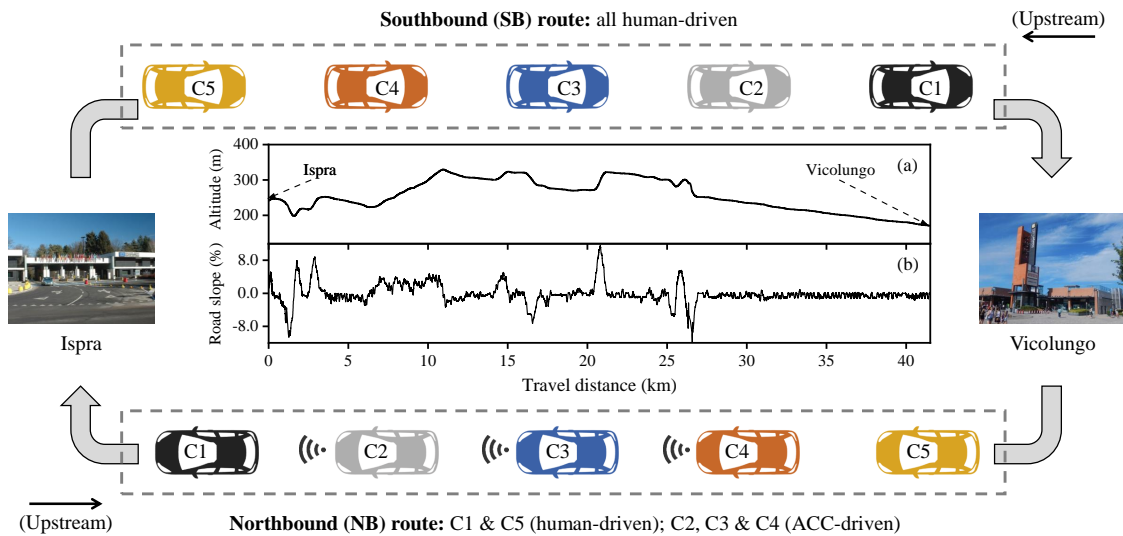
Note: ACC = adaptive cruise control.

Figure 8.1 The real-world driving experiment in highway multiple-car-following scenarios.

Table 8.1 summarizes the main specifications of five passenger cars in the experiment, including the leader (C1) and four followers (C2, C3, C4, and C5). These vehicles were selected to test different manufacturers, types, and years. As explained in Figure 8.1, on the southbound (SB) route (from Ispra to Vicolungo), all vehicles were operated by human drivers. On the northbound (NB) route, however, the followers (C2, C3, and C4) adopted ACC systems to regulate the longitudinal speed and the inter-vehicle spacing. While their leader (C1) and the last one (C5) were human-driven, whose drivers were respectively the same as those on the SB route.

Table 8.1 Main specifications of the test vehicles

Cars	Release year	Car type	Transmission	Mass (kg)	Width (m)	Height (m)	Max. power (kW)
C1	2001	MPV	Automatic	1430	1.715	1.515	72
C2	2018	MPV	Automatic	1838	1.884	1.658	120
C3	2009	MPV	Automatic	1764	1.837	1.639	110
C4	2017	SUV	Automatic	1650	1.805	1.545	104
C5	2011	Coupe	Manual	1315	1.683	1.378	90

Note: MPV = multi-purpose vehicle; SUV = sport utility vehicle.

The multiple-car-following tests were not replicated, owing to the impossibility of replicating the traffic conditions in real-world scenarios, but our driving tests sampled a wide range of variations in highway traffic. It is worth noting that some unexpected issues (e.g., the interference of cut-in vehicles and a brief GPS signal lost when passing through a tunnel) are unavoidable in real-world driving experiments. To deal with these challenges and yield meaningful results, if any of these issues occur, that piece of trajectory is ignored for all test vehicles in the computation of tractive energy consumption. However, these parts only covered a small portion of the total trajectory in our car-following campaign. In addition, the data points included in the analyses of this study have the acceleration ranging from -5 to 3 m/s^2, to rule out data that are generally considered to come from GNSS measurement errors. The outliers beyond this acceleration range appear in each of the real-world driving trajectories but only account for a small proportion (less than 2.5%).

8.3   Results and discussion

This section employs several data analysis techniques to present the results. Firstly, ACC driving behaviour is compared with that of the human driver from transient and statistical

perspectives. In the transient analysis, the time series of speed and tractive power are examined to quantify the string stability and the braking response time, respectively. While the statistical analysis is conducted to explore the joint and marginal distributions of speed, acceleration, and tractive power of each test vehicle in the campaign. Secondly, the impact of ACC on tractive energy consumption is evaluated from individual and platoon perspectives. To isolate the driving behaviour as the only possible contributor to tractive energy differences, the following two techniques are offered to normalize heterogeneous vehicle specifications and road and traffic conditions.

Firstly, it is challenging to assess the ACC tractive energy impact on the individual level, namely, to compare the tractive energy values of the same vehicle (e.g., C2, C3, or C4 in Figure 8.1) driven by the ACC and the human driver (on NB and SB routes, respectively). The main reason for this issue is that the ACC and the human driver experience different road and traffic conditions on different routes. To make meaningful comparisons, the technique called individual normalization introduces the individual normalized tractive energy consumption ($E_{T,Ci}^{in}$), in which each vehicle's tractive energy consumption ($E_{T,Ci}$) is divided by that of the leading one ($E_{T,C1}$) on the same route, i.e.,

$$E_{T,Ci}^{in} = \frac{E_{T,Ci}}{E_{T,C1}}, \text{ where } i \in [1,2,3,4,5], \tag{8.3}$$

In addition, ACC tractive energy impact on the platoon level is evaluated by comparing the tractive energy values of vehicles in the same platoon (e.g., C1-C2-C3-C4-C5 on the NB route). Although vehicles in the same platoon experience nearly the same road and traffic conditions, their specifications are heterogeneous. To tackle this challenge, the technique denoted as platoon normalization assumes that all vehicles on the same route share the same specifications as those of their leader (C1), resulting in the platoon normalized tractive energy consumption ($E_{T,Ci}^{pn}$, kWh/100 km) for each vehicle.

8.3.1 Transient analysis of driving behaviour

To analyse the transient driving behaviours in the highway multiple-car-following scenario, Figure 8.2 provides time series of speed, acceleration, and tractive power of five test vehicles. Specifically, a string of five passenger cars driven by the human driver or the ACC system moves from Ispra to Vicolungo (southbound, SB) and vice versa (northbound,

NB) in a fixed order. As time goes by, the leader (C1) decelerates or accelerates according to traffic conditions. We can then compare the different responses of the rest four followers and compute their corresponding tractive power (P_T) based on Equation (8.1).
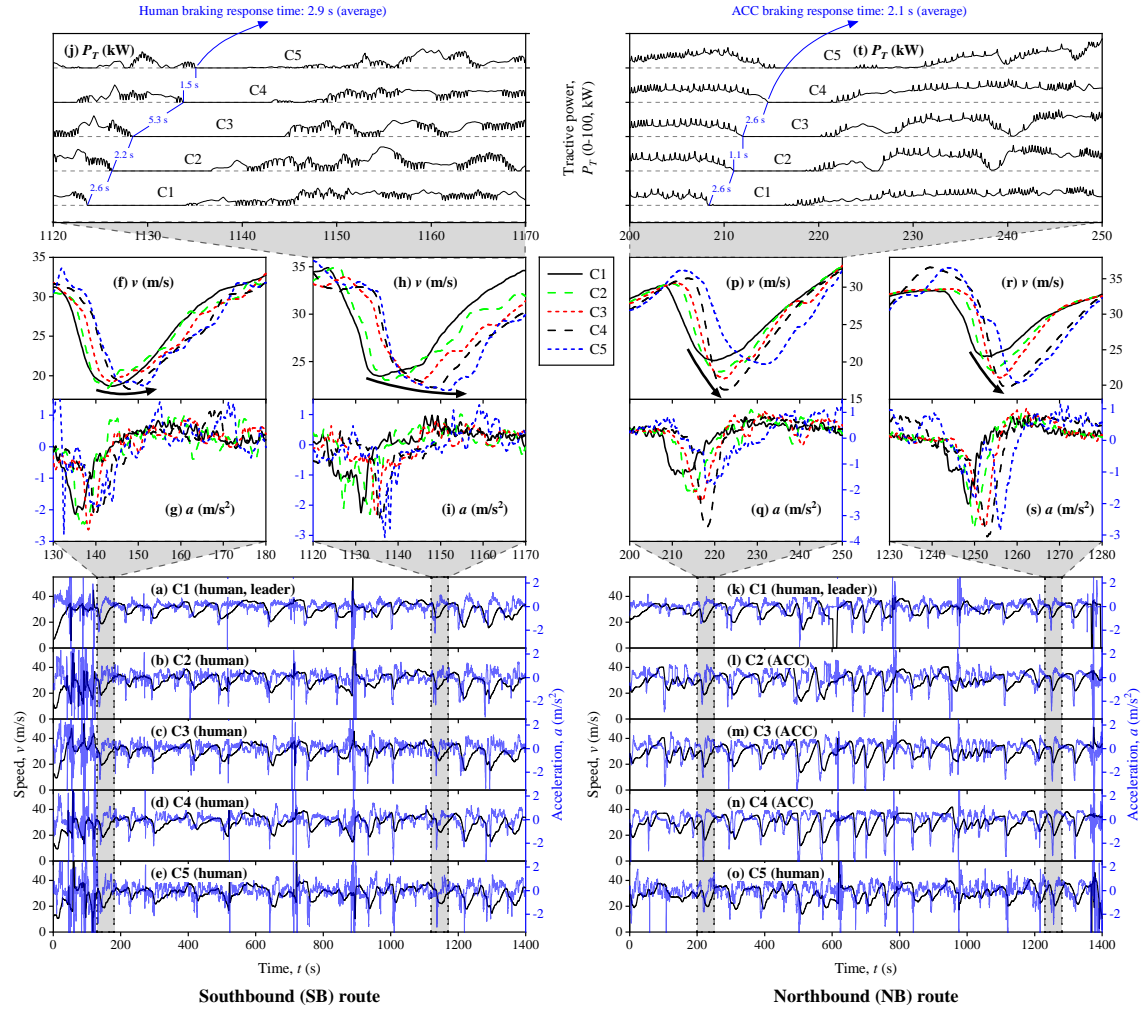
Figure 8.2 Speed, acceleration, and tractive power of test vehicles on the southbound (SB, left) and northbound (NB, right) routes.

In previous studies, string stability is usually defined as the phenomenon where the leader's speed variations are not amplified through the upstream followers [345]. On the SB route, two gray sections (time intervals 130–180 s and 1120-1170 s) in Figure 8.2 (a)-(e) are zoomed in and put into the same time-speed/acceleration coordinates in Figure 8.2 (f)-(i). The black curved arrows in Figure 8.2 (f) and (h) indicate the stable car-following behaviour of human drivers. It is clear that steep speed variations of the leader (C1) are not amplified through the human-driven followers (C2, C3, C4, and C5), whose velocities are not obviously fluctuated. On the NB route, by contrast, two selected time intervals (200–250 s and 1230–1280 s) shown in Figure 8.2 (p)-(s) highlight the

unstable ACC car-following behaviours. More specifically, ACC followers (C2, C3, and C4) significantly enlarge their leader's speed perturbations propagating upstream, causing rear-end collision safety concern. However, the last follower (C5), operated by the human driver, does not exacerbate the instability propagating upstream, and sometimes even can reduce this perturbation.

To quantitatively assess how the leader's speed perturbations are amplified in the car platoon, the percentage overshoot (M_{Ci}) serves as the indicator [346, 347], as described by

$$
\begin{cases}
M_{Ci} = (\Delta v_{Ci} - \Delta v_{C1})/\Delta v_{C1} \times 100\%, \\
\Delta v_{Ci} = \max_{t \in \psi} \left(v_{Ci}(t) \right) - \min_{t \in \psi} \left(v_{Ci}(t) \right), \\
i \in [1, 2, 3, 4, 5],
\end{cases}
\tag{8.4}
$$

where Δv_{Ci} is the speed variation (m/s) of a given vehicle within a specific time interval ψ (s). Figure 8.3 gives M_{Ci} values of test vehicles based on time intervals selected (gray sections) in Figure 8.2. It is apparent that there are no obvious trends for the speed overshoots of human followers on the SB route (blue). Their M_{Ci} values lie around 0%. When we examine ACC followers on the NB route (black), however, strong growth trends in their M_{Ci} values are detected. Their percentage overshoots vary from ∼15% to ∼31% in the 200–250 s interval, and from ∼24% to ∼83% in the 1230-1280 s interval. In contrast, the last follower (C5, human-driven) on the NB route can mitigate these upward trends. The quantitative evidence here is consistent with the above findings in Figure 8.2, namely, consecutive ACC followers can cause string instability, and human followers, however, can react in a way to mitigate speed perturbations propagating upstream.

Figure 8.2 (j) and (t) illustrate the tractive power (P_T) profiles of test vehicles during the SB (1120–1170 s) and the NB (200–250 s) trips, respectively. The vertically stacked tractive power curves are plotted in five horizontal bands, each of which ranges from 0 to 100 kW. In these charts, the tractive power only has positive components and remains zero during braking manoeuvres. By comparing the starting points of the braking phases, we can identify the braking response time of each follower. Figure 8.2 (j) shows that the human drivers' average braking response delay is 2.9 s in the selected time interval. As for ACC tractive power profiles presented in Figure 8.2 (t), the average braking response time is 2.1 s. The results, in this case, report that the responsiveness of ACC is on average higher
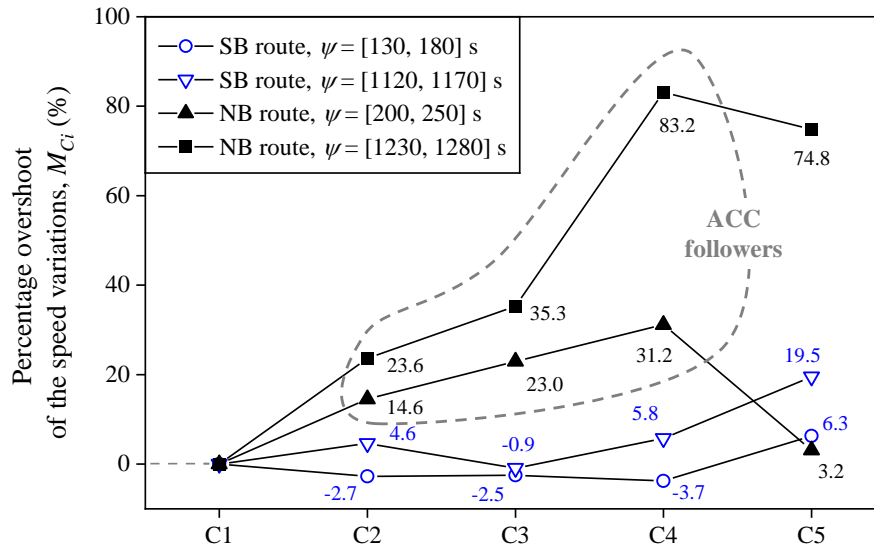
Figure 8.3 Percentage overshoots of speed variations in the platoon.

than that of the human driver. This may partly explain the ACC unstable car-following performance shown above because as stated in previous studies [348, 349], there exists a trade-off between stability and responsiveness in the control system design and calibration. Namely, the faster the control system response, the more unstable the speed tracking (or the more significant the overshoot).

8.3.2 Statistical analysis of driving behaviour

Figure 8.4 uses contour heatmaps to illustrate the speed-acceleration joint probability distributions of the vehicles. The similarity between the distribution heatmaps of two consecutive vehicles is quantified with the 2D correlation coefficient (R) [350]. The similarity coefficients demonstrate that in human-to-human car-following scenarios (on the SB route), the R values lie between 0.86 and 0.88, generally greater than their human-to-ACC, ACC-to-ACC, or ACC-to-human counterparts (on the NB route). The finding reported here might imply that the followers in the automated or mixed traffic flow, relative to those in the manual traffic, generally perform worse in reproducing the driving style of the immediately preceding vehicle. The likely cause for this difference is that the ACC system mainly aims to keep a safe time headway thus shows less flexibility.

Box-and-whisker diagrams in Figure 8.5 show marginal distributions of tractive power, speed, and acceleration. The height of the box is the interquartile range (IQR) between the first (Q1, 25%) and third (Q3, 75%) quartiles, namely, IQR = Q3 – Q1. The median,
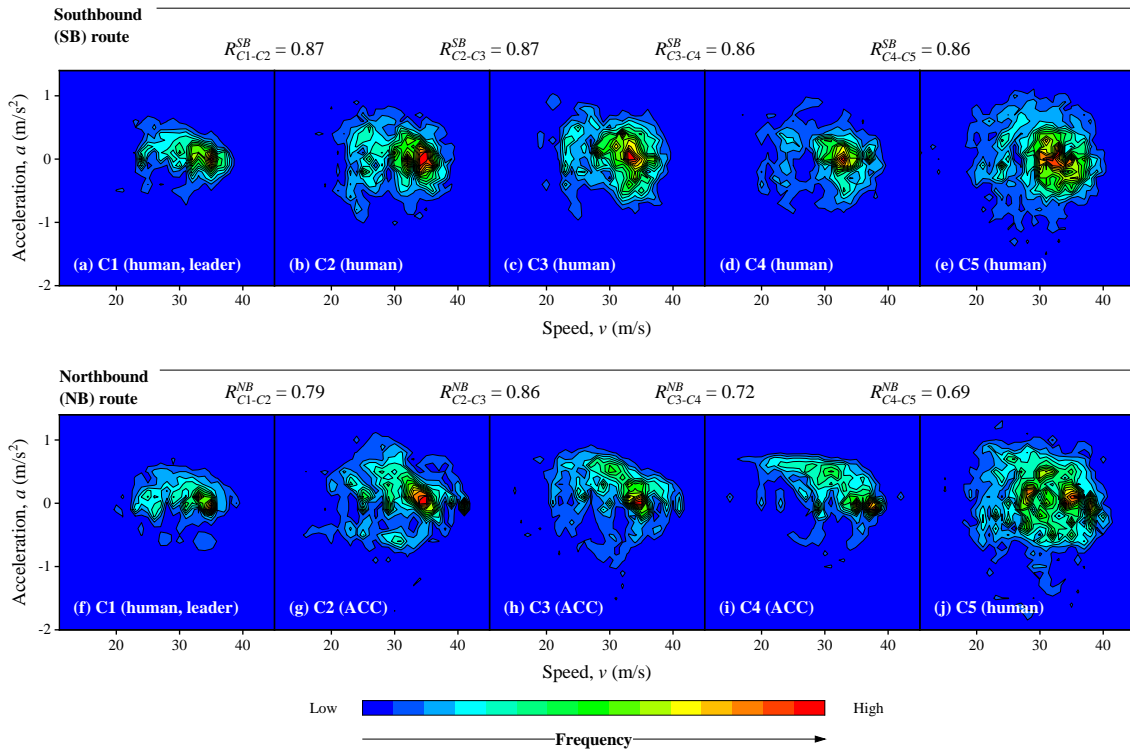
Note: R = similarity measure represented by the correlation coefficient between two joint distributions.

Figure 8.4 Speed-acceleration joint distributions and their correlation coefficients.

the band inside the box, is the second quartile (Q2, 50%). The ends of the whisker (Q1−1.5×IQR and Q3+1.5×IQR) represent the outlier-free interval (OFI). Data points beyond this interval are viewed as being too far from the central value to be reasonable. In Figure 8.5 (a) and (b), the upper boundaries of tractive power OFIs are all compliant with the test vehicles' maximum power in Table 8.1, demonstrating the reliability and validity of test measurements and mathematical modelling in this study. In addition, the distributions in Figure 8.5 (c) and (d) show that the speed values in this highway scenario vary from 13.1 to 45.9 m/s, and their medians lie between 30.0 and 31.1 m/s.

Table 8.2 gives the interquartile range of the speed distribution for each vehicle, denoted as IQR_v. It is worth noting that ACC followers ramp up the driving speed dispersion. However, the human followers, e.g., C3 and C5 in the SB route and C5 in the NB route, can sometimes reduce IQR_v compared with their respective preceding vehicles. This finding is consistent with the above discussions, which demonstrate that human driving may decrease speed perturbations propagating upstream.
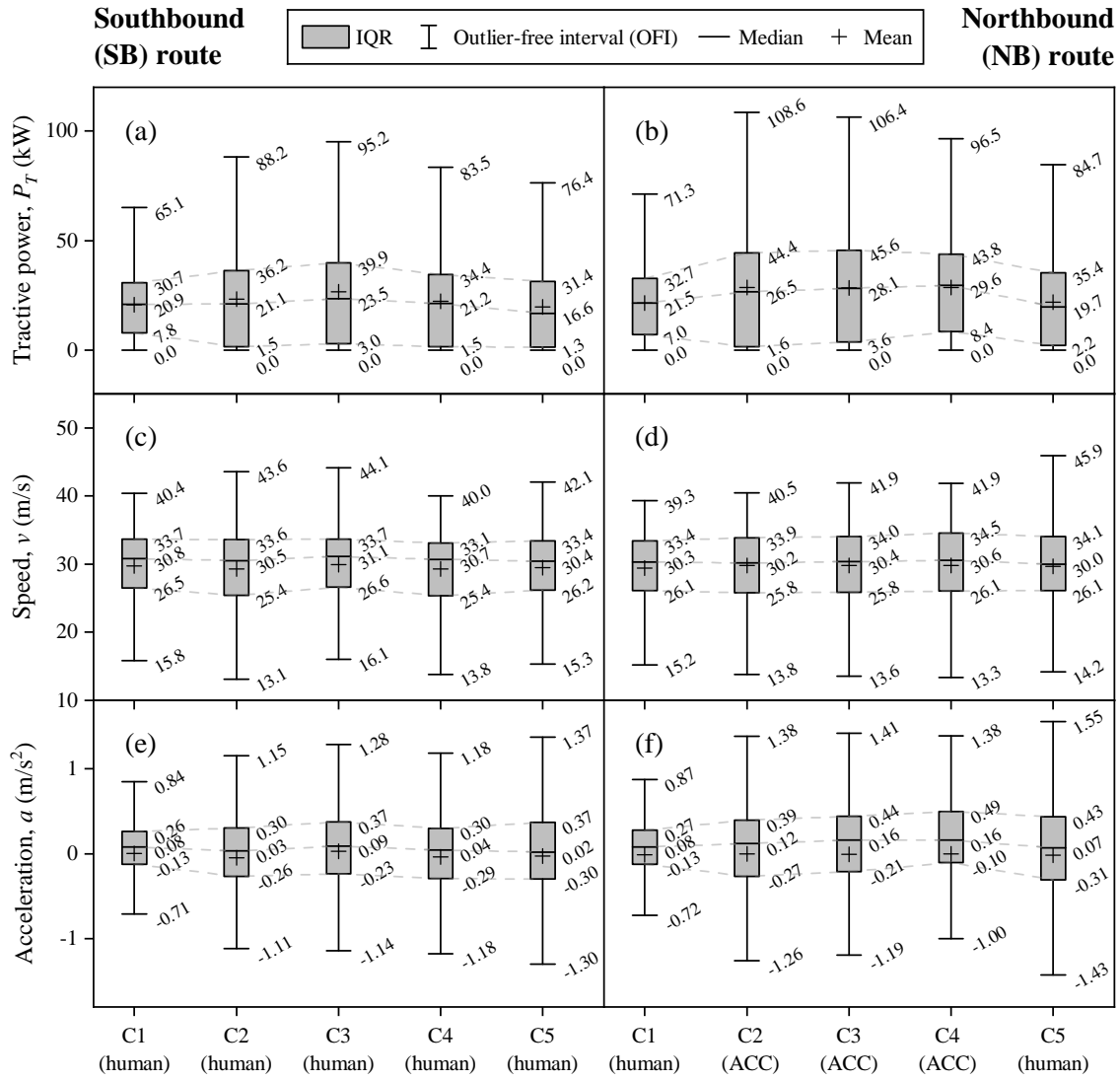
Figure 8.5 Box plots of tractive power, speed, and acceleration.

8.3.3   ACC energy impact on the individual level

As defined in Equation (8.3), the individual normalized tractive energy consumption ($E_{T,Ci}^{in}$) is computed by dividing each vehicle's tractive energy consumption ($E_{T,Ci}$) by that of the leading one ($E_{T,C1}$) on the same route.

Figure 8.6 shows $E_{T,Ci}^{in}$ values of test vehicles on the SB and NB routes, also provides the percentage increase in $E_{T,Ci}^{in}$ caused by ACC driving. The grouped bars of the last follower (C5) operated by the same human driver, suggest that there is an error of about 6% when evaluating ACC energy impact using the proposed individual normalization technique. Results from test vehicles C2, C3 and C4 demonstrate that ACC followers have tractive energy consumption 2.7–20.5% higher than those of human counterparts. This may be attributed to string instability and high responsiveness of ACC systems as

Table 8.2 Interquartile range (IQR) of the speed distribution

	Southbound (SB)		Northbound (NB)	
	Driving	IQR_v	Driving	IQR_v
C1	human	7.2	human	7.3
C2	human	8.2	ACC	8.1
C3	human	7.1	ACC	8.2
C4	human	7.7	ACC	8.4
C5	human	7.2	human	8.0
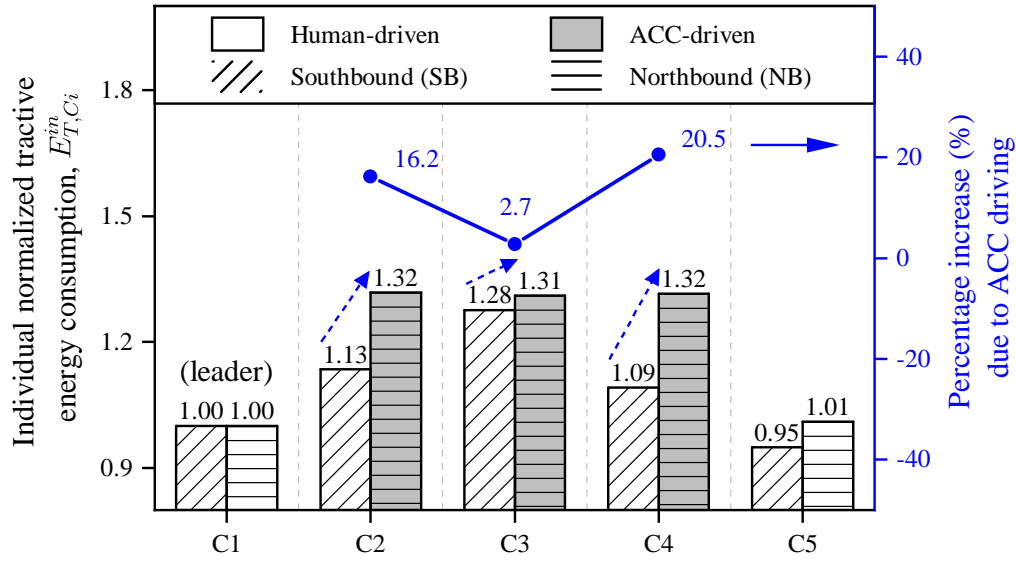
Figure 8.6 ACC energy impact on the individual level.

discussed in Figures 8.2 and 8.3. This outcome is contrary to a recent study by General Motor (GM) [344] that reported a positive total GHG emissions (highly correlated to fuel consumption) benefit of the ACC system. The most likely cause of this controversy is that the GM's analysis also takes into account the fuel-efficient ACC free-flow driving, which can significantly reduce the unnecessary acceleration/braking by human drivers [287].

8.3.4 ACC energy impact on the platoon level

As stated previously, the platoon normalized tractive energy consumption ($E_{T,Ci}^{pn}$) assesses ACC energy impact on the platoon level by assuming that all the vehicles on the same route share the same specifications as those of their leader (C1). The marked lines in Figure 8.7 (a) illustrate the $E_{T,Ci}^{pn}$ values of test vehicles in the homogenized platoon. On the SB route (blue), their values range from 18.8 to 21.6 kWh/100 km. Meanwhile, on the NB route (black), in the platoon mixed with ACC-driven and human-driven vehicles, the $E_{T,Ci}^{pn}$ values
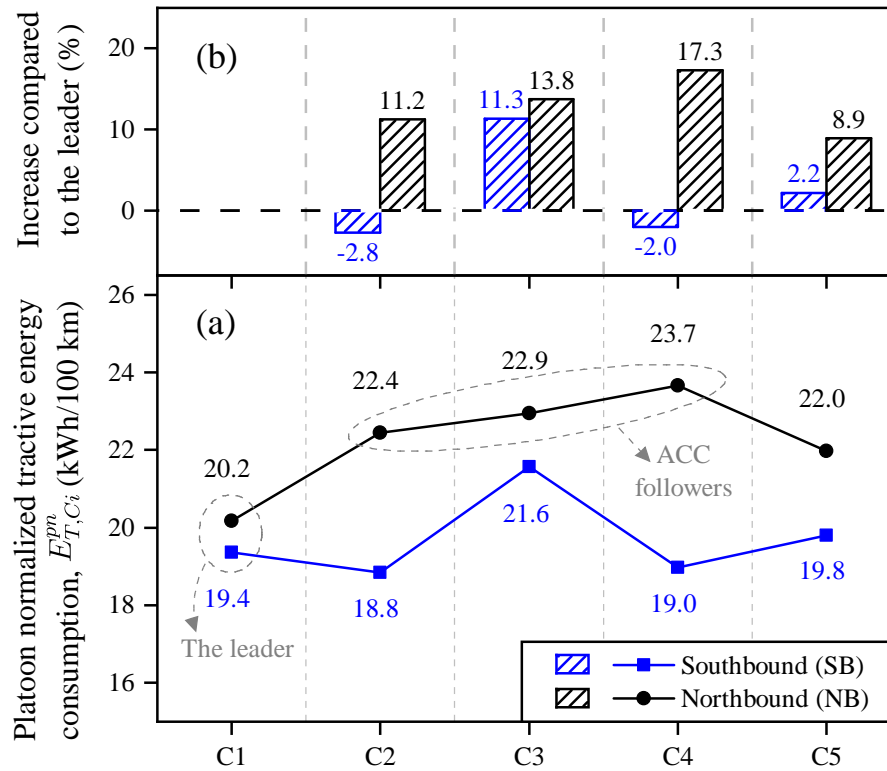
Figure 8.7 ACC energy impact on the platoon level.

lie between 20.2 and 23.7 kWh/100 km. Figure 8.7 (b) shows the followers' percentage increase in $E_{T,Ci}^{pn}$ compared with that of their leader. It is apparent from this chart that the tractive energy values of ACC followers tend to consecutively increase (11.2–17.3%) along with speed perturbations propagating upstream, as emphasized in Figure 8.3. Therefore, the negative effect of ACC on tractive energy efficiency is likely to be related to its string instability characteristic. These findings suggest that functional requirements to guarantee string stability should be introduced for ACC systems in the future.

8.4   Summary

Returning to the questions posed at the beginning of this study, it is now possible to state that the proposed methods can effectively distinguish ACC driving behaviour from that of the human driver and identify the ACC energy and safety impacts, in real-world scenarios with a variety of vehicle specifications, propulsion systems, drivers, and road and traffic conditions. Tractive energy consumption serves as the energy performance indicator that can rule out the effect of the propulsion system. To further isolate the driving behaviour as the only possible contributor to tractive energy differences, the individual and the platoon

normalization techniques are offered to homogenize vehicle specifications and road and traffic conditions. Finally, ACC driving behaviour is compared with that of the human driver from transient and statistical perspectives. Its impact on tractive energy consumption is then evaluated from individual and platoon perspectives. The results from the above methods suggest that:

- ACC followers lead to string instability, i.e., amplifying downstream speed variations. However, human drivers can react in a way to mitigate these speed perturbations.

- The inability of ACC to absorb the speed overshoots may partly be explained by their high responsiveness.

- Statistical results might imply the followers in the automated or mixed traffic flow, relative to those in the manual traffic, generally perform worse in reproducing the driving style of the immediately preceding vehicle.

- On the individual level, ACC followers have tractive energy consumption 2.7–20.5% higher than those of human counterparts.

- On the platoon level, the tractive energy values of ACC followers tend to consecutively increase (11.2–17.3%) as the speed perturbations propagate upstream.

In general, ACC has negative impacts on tractive energy efficiency. This research provides a feasible path for evaluating the energy impact of ACC in real-world applications. Furthermore, the findings have significant implications for ACC safety design, particularly for handling the stability-responsiveness trade-off. A future study carried out on test tracks would be instrumental in our further understanding of ACC energy impacts.

9

Energy impacts of time-gap settings on ACC vehicle platoons on test tracks

Adaptive cruise control (ACC) is one of the most prevailing advanced driver assistance systems (ADAS) and projected to create new opportunities for improving road safety and energy efficiency. However, previous studies warned that these benefits may take much longer than expected to materialize and will largely depend on the control design and calibration during the ACC development. In this context, the present work, for the first time, systematically investigates the energy impacts of time-gap settings of commercial ACC systems in platooning experiments performed on test tracks. To this end, platoons consisting of 5-7 ACC-equipped vehicles are employed to perform both speed perturbation and cruising experiments, on the dynamic platform (DP) and the handling course (HC), respectively, both of which are test tracks of ZalaZone proving ground. ACC platoons adopting short, medium, long, and short/long (mixed) time-gap settings are respectively abbreviated as S-ACC, M-ACC, L-ACC, and SL-ACC platoons. The results suggest that, in six different speed perturbation scenarios, the following vehicles in S-ACC platoons lead to string instability and therefore increased tractive energy consumption, which are on average 18.9-37.1% greater than those of their platoon leaders. On the other hand, the ACC long time-gap setting can contribute to reducing the energy consumption of the whole platoon. Specifically, in different cruising scenarios, SL-ACC platoons can achieve overall fuel savings of 6.1-9.8% compared with S-ACC platoons.

9.1 Introduction

In the European Union (EU), the road transport sector accounts for 24.2% of energy consumption, 16.7% of greenhouse gas (GHG) emissions, and more than 25,000 deaths each year [351, 274]. To tackle these challenges, automated and electrified vehicles (AEVs) and intelligent transportation systems (ITSs) have been in the spotlight for several decades [13]. A major application emerging from these areas is adaptive cruise control (ACC), which is enabled by onboard radar and can regulate the vehicle speed to maintain a safe inter-vehicle spacing or approach a preset speed [29]. ACC has been introduced into the

market primarily for enhancing driving safety and ride comfort by offloading the driver's tasks such as cruising at a constant speed in free-flow traffic or following the preceding vehicle in congested traffic [352]. However, the impacts of ACC on the vehicle- and traffic-level energy consumption in field tests have remained unclear [353], which has hampered efforts towards sustainable mobility and therefore directed much of this work.

Previous studies have reported that increased ACC market penetration may give rise to unstable traffic flow because ACC vehicles can lead to string instability, which amplifies downstream speed perturbations and causes severe traffic oscillations [56, 118, 335]. These phenomenons raise concerns about energy consumption. For example, He et al. [268] demonstrate that ACC-driven vehicles result in tractive energy consumption 2.7–20.5% higher than those of human-driven counterparts in real-world highway car-following scenarios. On the other hand, a large-scale study by General Motor (GM) [344], with a fleet of 51 test vehicles over 199,300 miles (driven by GM's employees on their daily commutes), reports that the ACC system can yield the benefit of reducing greenhouse gas (GHG) emissions (highly correlated to fuel consumption) at low speeds because it can avoid the unnecessary acceleration/braking associated with human drivers [287].

The Joint Research Centre (JRC) of the European Commission carried out four ACC driving campaigns during 2018 and 2019, considering a variety of driving environments (including public roads and test tracks), ACC-equipped vehicles, ACC system settings, ACC platoon configurations, etc. The results have been summarized in several papers. In particular, Makridis et al. [251] derived the distributions of response time and time headway of a commercial ACC system at medium/low speeds (less than 60 km/h) and found that both parameters were close to those commonly reported for human drivers. Another study performed platoon experiments consisting of five ACC-equipped vehicles on the AstaZero proving ground [354]. The results demonstrated that, in all of the testing conditions, ACC leads to string instability, confirming the findings of the other studies [268]. Makridis et al. [288] claimed that ACC driving behaviours are largely affected by vehicle mechanical features, road geometric characteristics, driving speeds, ACC time-gap settings, etc. Moreover, the JRC has made the entire ACC driving database publicly available [288], allowing the scientific community to further work on these data.

In this context, this study, for the first time, systematically investigates the energy impacts of different time-gap settings of commercial ACC systems in platooning

experiments performed on test tracks. The platoons consisting of 5-7 ACC-equipped vehicles are employed to perform both speed perturbation and cruising experiments, on the dynamic platform (DP) and the handling course (HC), respectively, both of which are test tracks of ZalaZone proving ground (located in Zalaegerszeg, Hungary). In the driving campaign, ACC platoons are configured differently, in terms of the ACC time-gap settings of the following vehicles.

The remainder of this chapter is organized as follows. Section 9.2 describes the design of experiments including test tracks of ZalaZone proving ground, ACC vehicle platoons, and data acquisition and processing techniques. Section 9.3 introduces the modelling of tractive energy consumption. In Section 9.4, the results are presented and discussed. Finally, Section 9.5 draws the main conclusions.

9.2   Field platoon data

The open-source trajectory data utilized in this work are collected by the Joint Research Centre (JRC) of the European Commission in platooning experiments performed on two test tracks of the ZalaZone proving ground, with high-end vehicles controlled by commercial ACC systems [288]. The details of the experimental design are provided in the following subsections, including test tracks, configurations of different ACC platoons, and the data acquisition and processing.

9.2.1   Test tracks

The ZalaZone proving ground, in Zalaegerszeg, Hungary, provides a multi-disciplinary facility to investigate future automotive technologies before they go to market [355–357]. In this proving ground, the dynamic platform (DP) is a test track for experiments including high speed (up to 200 km/h) stability, brake, and platooning. Another test track, the handling course (HC), has many alternative routes and diverse types of path, and therefore, can be used for steering, electronic stability program (ESP), and other vehicle dynamic test elements. More detailed information about both test tracks are provided by Ciuffo et al. [289] and Makridis et al. [288].

9.2.2 ACC vehicle platoons

Platooning experiments are performed in speed perturbation scenarios and cruising scenarios on the dynamic platform (DP) and the handling course (HC), respectively. Each platoon consists of 5-7 vehicles with a dedicated leading vehicle that is programmed to follow a specific speed profile. The following vehicles in the platoon are ACC-equipped vehicles available in the European market. The commercial ACC systems usually have several options for the time-gap setting, such as short, medium, and long. Accordingly, platoons in the driving campaign are configured differently as follows.

1) HD platoons: The following vehicles are all human-driven.

2) S-ACC platoons: The following vehicles are all controlled by ACC systems with a short time-gap setting.

3) M-ACC platoons: The following vehicles are all driven by ACC systems with a medium time-gap setting.

4) L-ACC platoons: The following vehicles are all regulated by ACC systems with a long time-gap setting.

5) SL-ACC platoons: Two of the following vehicles are operated by ACC systems with a long time-gap setting, while the others utilize ACC systems with a short time-gap setting. For a better understanding of the arrangement of ACC vehicles, four cases of SL-ACC platoons are provided and compared with S-ACC platoons in Figure 9.5.

9.2.3 Data acquisition and processing

The position and speed of each vehicle were acquired with two measurement systems including the U-Blox M8 device and the Inventure CL-CAN device. Their global navigation satellite system (GNSS) active antennas were mounted on the roof of the vehicle, to ensure maximum satellite visibility and avoid signal attenuation from the vehicle body. Additionally, the distances from the antenna to the front and to the rear bumpers, respectively, were documented for computing the inter-vehicle spacing.

The measurements of different localization devices were synchronized based on coordinated universal time (UTC). The time-series data of position and speed were resampled with B-splines interpolation to a 10 Hz sampling rate. The position has been

transformed from geographic coordinates (latitude, longitude, and altitude) into a local East, North, and Up (ENU) Cartesian reference frame.

9.3 Modelling of tractive energy consumption

As discussed in Section 8.2 of the last chapter, tractive energy consumption is a suitable metric for assessing the energy impact of ACC driving behaviour because it can rule out the energy effect of heterogeneous propulsion systems in the traffic network [268]. Specifically, in a platoon, tractive energy consumption ($E_{T,n}$, kJ) of a vehicle at a specific position (n) can be calculated by integrating tractive power demand ($P_{T,n}$, kW) of this vehicle over time (t, s), not considering negative power components resulting from regenerative braking, i.e.,

$$P_{T,n}(t) = \max \left[0, \left(f_0 \cdot \cos\theta + f_1 \cdot v_n(t) + f_2 \cdot v_n(t)^2 + mg \cdot \sin\theta + \phi m \cdot a_n(t) \right) \frac{v_n(t)}{1000} \right], \quad (9.1)$$

$$E_{T,n} = \int_0^{t_f} P_{T,n}(t) dt, \quad (9.2)$$

where f_0, f_1 and f_2 are road load coefficients (N, kg/s, and kg/m, respectively); m is the vehicle mass (kg); ϕ is the equivalent inertial mass factor; v_n and a_n are speed (m/s) and acceleration (m/s^2) of the vehicle (n), respectively; θ is the road slope (rad); g is the gravitational acceleration (9.81 m/s^2); dt is the time interval (s) between consecutive measurement points; t_f denotes the duration (s) of the trip. The total tractive energy consumption of all vehicles in the platoon can therefore be expressed as

$$\mathbb{E}_T = \sum_{n=1}^{N} E_{T,n}, \quad (9.3)$$

where N is the total number of vehicles in the platoon including the leader and its followers.

It is worth noting that most parameters in Equation (9.1), namely, f_0, f_1, f_2, m, and ϕ, are associated with vehicle specifications, making it difficult to compare tractive energy consumption between different vehicles in heterogeneous platoons. According to previous approaches in the literature [268], it is assumed that vehicles in the platoon share the same specifications so that we can isolate the driving behaviour (represented by v_n and a_n) as the only possible contributor to tractive energy differences.

In addition, our prior studies demonstrate that ACC driving usually causes string instability in field platoon tests [354, 268], in which the leader's speed variations are amplified through the upstream followers [345]. To quantify the energy impact of this characteristic, the percentage increase in tractive energy consumption of the following vehicle at a specific position (n) in the platoon is defined as

$$\delta E_{T,n} = \frac{E_{T,n} - E_{T,1}}{E_{T,1}} \times 100\%, \; n \in [2, 3, ..., N], \tag{9.4}$$

where $E_{T,1}$ and $E_{T,n}$ are tractive energy consumption values (kJ) of the leading and the following vehicles in the same platoon, respectively. Moreover, to assess the impact of string instability on tractive energy consumption of the whole platoon, the average increase in tractive energy consumption of all following vehicles is given by

$$\Delta \overline{E}_T = \frac{1}{N-1} \sum_{n=2}^{N} \delta E_{T,n}, \tag{9.5}$$

9.4 Results and Discussion

To investigate the energy impact of the ACC time-gap setting in different test environments, platoon experiments are performed in speed perturbation scenarios and cruising scenarios on the dynamic platform (DP) and the handling course (HC), respectively. In speed perturbation scenarios, the leading vehicle introduces speed perturbations with different magnitudes (ΔV, km/h, negative) at different desired speeds (V_D, km/h). On the other hand, in cruising scenarios, the leading vehicle attempts to maintain the desired speed (V_D, km/h) but is affected by road geometric characteristics such as slope and curvature, which vary significantly along the path.

9.4.1 ACC energy impact in speed perturbation scenarios

In the platoon, the leading vehicle's speed perturbations may be attenuated or amplified when propagating through upstream followers, causing differences in tractive energy consumption between the leader and its followers. On the dynamic platform (DP), different speed perturbations are performed by the leading vehicle, to examine the energy impacts of different ACC time-gap settings on the platoon.
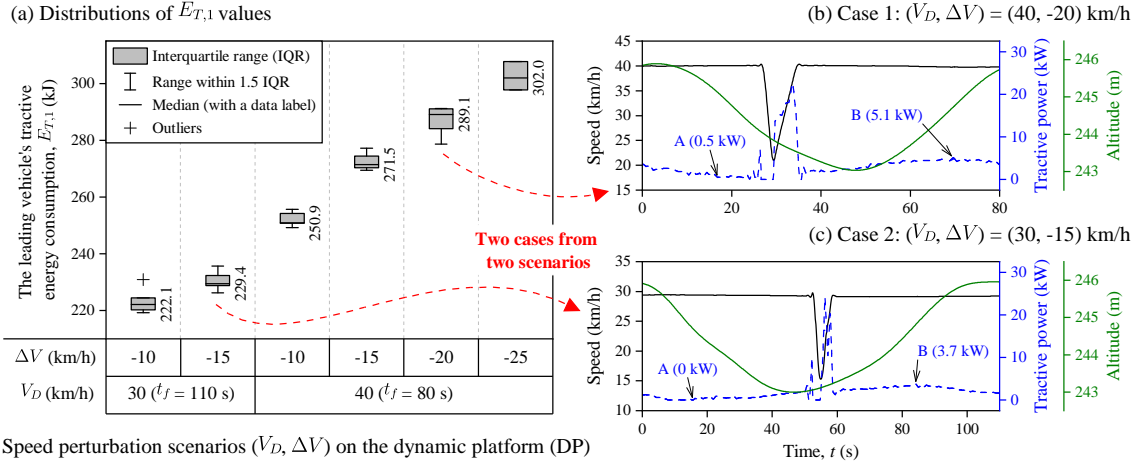
(a) Distributions of $E_{T,1}$ values

(b) Case 1: $(V_D, \Delta V) = (40, -20)$ km/h

(c) Case 2: $(V_D, \Delta V) = (30, -15)$ km/h

Subplots: (a) Distributions of the leading vehicle's tractive energy consumption ($E_{T,1}$) in six different speed perturbation scenarios ($V_D, \Delta V$); and (b) and (c) time-series data of speed, tractive power, and altitude of the leading vehicle in two cases, which are from two different speed perturbation scenarios, namely, ($V_D, \Delta V$) = (40, -20) and (30, -15) km/h, respectively.

Note: V_D = desired speed (km/h); ΔV = speed perturbation magnitude (km/h); t_f = duration (s) of the trip for computing tractive energy consumption; A/B = the point corresponding to the minimum/maximum tractive power during downslope/upslope steady-speed driving.

Figure 9.1 The leading vehicle's tractive energy consumption ($E_{T,1}$, kJ) in six different speed perturbation scenarios on the dynamic platform (DP).

Figure 9.1 (a) shows distributions of the leading vehicle's tractive energy consumption ($E_{T,1}$) in six different speed perturbation scenarios ($V_D, \Delta V$), in which V_D is the desired speed (km/h) and ΔV is the speed perturbation magnitude (km/h, negative). In tick labels of this box plot, t_f denotes the duration (s) of the trip for computing tractive energy consumption, which is set as 110 and 80 s for scenarios with the desired speed (V_D) of 30 and 40 km/h, respectively. In this way, the trips in different scenarios can approximately cover the complete circular test track, which has a diameter of 300 m, and therefore, the energy difference due to the varying road slope can be minimized.

In this graph, the box indicates the interquartile range (IQR) that is derived from 3-7 independent repetitions of platoon tests in each scenario. The whiskers extend to 1.5 times the IQR. The band inside the box is the median (with a data label). While crosses beyond the whiskers represent outliers. The data suggest that the median estimated $E_{T,1}$ values are 222.1 (IQR = 4.2) and 229.4 (IQR = 3.6) kJ for scenarios of ($V_D, \Delta V$) = (30, -10) and (30, -15) km/h, respectively. As to the other four scenarios (V_D = 40 km/h), every increment of -5 km/h in ΔV (ranging from -10 to -25 km/h) leads to an increase of ∼17.0 kJ in the median estimated $E_{T,1}$; while their corresponding IQR values lie between 3.5 to 10.0 kJ. Generally, the median estimated $E_{T,1}$ is found to increase with an increasing magnitude of

speed perturbation. The IQR values across different speed perturbation scenarios are less than 10 kJ, ensuring reproducibility of the results.

Figure 9.1 (b) and (c) provide time-series data of speed, tractive power, and altitude of the leading vehicle in two cases, namely, $(V_D, \Delta V)$ = (40, -20) and (30, -15) km/h, respectively. In both cases, the tractive power reaches a peak ($\sim$23.5 kW) at the vehicle acceleration phase. In addition, the point A (B) annotated in blue is the minimum (maximum) tractive power during downslope (upslope) steady-speed driving. These two points exhibit that the varying road slope of the dynamic platform (DP) can lead to tractive power differences no greater than 4.6 and 3.7 kW in Case 1 and Case 2, respectively.
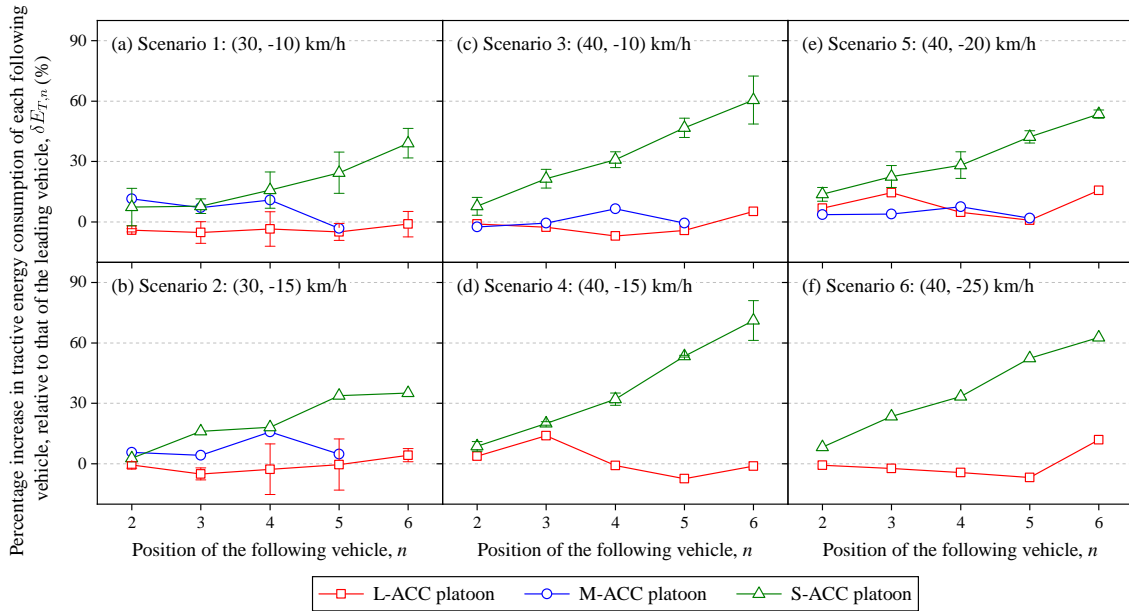
Subplots: (a)-(f) Speed perturbation scenarios 1-6, namely, $(V_D, \Delta V)$ = (30, -10), (30, -15), (40, -10), (40, -15), (40, -20), and (40, -25) km/h, respectively.

Note: V_D = desired speed (km/h); ΔV = speed perturbation magnitude (km/h); L/M/S-ACC platoon = long, medium, or short time-gap adaptive cruise control (ACC) platoon.

Figure 9.2 Percentage increase ($\delta E_{T,n}$, %) in tractive energy consumption of the following vehicle relative to that of the leading vehicle in six different speed perturbation scenarios.

Figure 9.2 (a)-(f) give the percentage increase in tractive energy consumption of each following vehicle (n), relative to that of the leading vehicle, namely, $\delta E_{T,n}$ (%) that is described by Equation (9.4). ACC platoons adopting different time-gap settings (L-ACC, M-ACC, and S-ACC) are color-coded and marked with different symbols (see the legend). Error bars denote the standard deviation of at least three replicates of platoon tests. The results demonstrate that, in six different speed perturbation scenarios, S-ACC platoons show a rapid and continuing growth in $\delta E_{T,n}$ along the upstream direction (of increasing

n). In Scenarios 1 and 2 (V_D = 30 km/h), S-ACC platoons reach similar peak values of $\delta E_{T,n}$ (39.1% and 35.1%, respectively) at the last follower (n = 6). In Scenarios 3-6 (V_D = 40 km/h), the last followers in S-ACC platoons can result in even higher peak values of $\delta E_{T,n}$, ranging from 53.6% to 71.1%.

On the other hand, both L-ACC and M-ACC platoons in each subplot of Figure 9.2 show no clear trend in $\delta E_{T,n}$ values along the upstream direction. These findings provide strong evidence that the leading vehicle's speed perturbations are amplified when propagating upstream in S-ACC platoons, but almost unchanged or even attenuated in M-ACC or L-ACC platoons. Therefore, ACC time-gap settings have a significant influence on the tractive energy consumption of the vehicle platoon in speed perturbation scenarios. More specifically, in the platoon, ACC systems with a short time-gap setting lead to considerable string instability and therefore an increase in energy consumption. In contrast, ACC systems with a medium or long time-gap setting can guarantee a more stable and energy-efficient vehicle behaviour in platoons.

To assess the impact of the ACC time-gap setting on tractive energy consumption of the whole platoon in different speed perturbation scenarios, Table 9.1 lists the average increase in tractive energy consumption of all following vehicles in a platoon, namely, $\Delta \overline{E}_T$ (%), which is defined in Equation (9.5). The results of M-ACC platoons are not given because of insufficient data. The findings in this table suggest that $\Delta \overline{E}_T$ values of L-ACC platoons range from -3.8% to 8.5%, indicating small differences in tractive energy consumption between the leader and its followers in the platoon. S-ACC platoons, however, lead to much larger $\Delta \overline{E}_T$ values that strongly depend on the desired speed (V_D). Specifically, at the V_D of 40 km/h, S-ACC platoons give rise to $\Delta \overline{E}_T$ values lying between 32.1% and 37.1%, nearly doubling those resulting from S-ACC platoons at the V_D of 30 km/h.

Table 9.1 Average increase ($\Delta \overline{E}_T$, %) in tractive energy consumption of all following vehicles relative to that of the leading vehicle in speed perturbation scenarios.

V_D (km/h)	30		40			
ΔV (km/h)	-10	-15	-10	-15	-20	-25
$\Delta \overline{E}_T$ (%) of L-ACC platoons	-3.8	-0.9	-1.9	1.6	8.5	-0.4
$\Delta \overline{E}_T$ (%) of S-ACC platoons	18.9	21.2	33.5	37.1	32.1	36.1

Note: V_D = desired speed (km/h); ΔV = speed perturbation magnitude (km/h); L/S-ACC platoon = long or short time-gap adaptive cruise control (ACC) platoon.

(a) Distributions of E_T^1 values

(b) Case 1: $V_D = 60$ km/h

(c) Case 2: $V_D = 30$ km/h

Subplots: (a) Distributions of the leading vehicle's tractive energy consumption ($E_{T,1}$) in three different cruising scenarios; and (b) and (c) time-series data of speed, tractive power, and altitude of the leading vehicle in two cases, which are from two cruising scenarios, i.e., $V_D = 60$ and 30 km/h, respectively. *Note:* V_D = desired speed (km/h); t_f = duration (s) of the trip for computing tractive energy consumption.

Figure 9.3 The leading vehicle's tractive energy consumption ($E_{T,1}$, kJ) in three different cruising scenarios on the handling course (HC).

9.4.2 ACC energy impact in cruising scenarios

In the cruising experiments carried out on the handling course (HC), the platoon leader attempts to maintain a constant desired speed (V_D) but is significantly affected by external disturbances, namely, the road geometric characteristics including slope and curvature. Figure 9.3 (a) provides the distributions of the leading vehicle's tractive energy consumption ($E_{T,1}$) in three cruising scenarios at desired speeds (V_D) of 30, 50, and 60 km/h, respectively. Corresponding trip durations (t_f) are about 500, 315, and 275 s, respectively. The data in this box plot show that the median estimated $E_{T,1}$ is 1016.7 (IQR = 21.8) kJ at the V_D of 30 km/h, increases to 1318.0 (IQR = 232.3) kJ at the V_D of 50 km/h, and reaches a peak of 1791.4 (IQR = 352.0) kJ at the V_D of 60 km/h. The larger IQR values in high-speed scenarios (V_D = 50 and 60 km/h) indicate relatively poorer reproducibility of the platoon tests. Figure 9.3 (b) and (c) provide time-series data of speed, tractive power, and altitude of the leading vehicle in two cases, belonging to testing scenarios of V_D = 60 and 30 km/h, respectively.

Figure 9.4 (a)-(c) present the following vehicles' percentage increase in tractive energy consumption relative to that of the leading vehicle, namely, $\delta E_{T,n}$ (%) in Equation (9.4). Four types of platoons (HD, L-ACC, S-ACC, and SL-ACC) are compared in three different
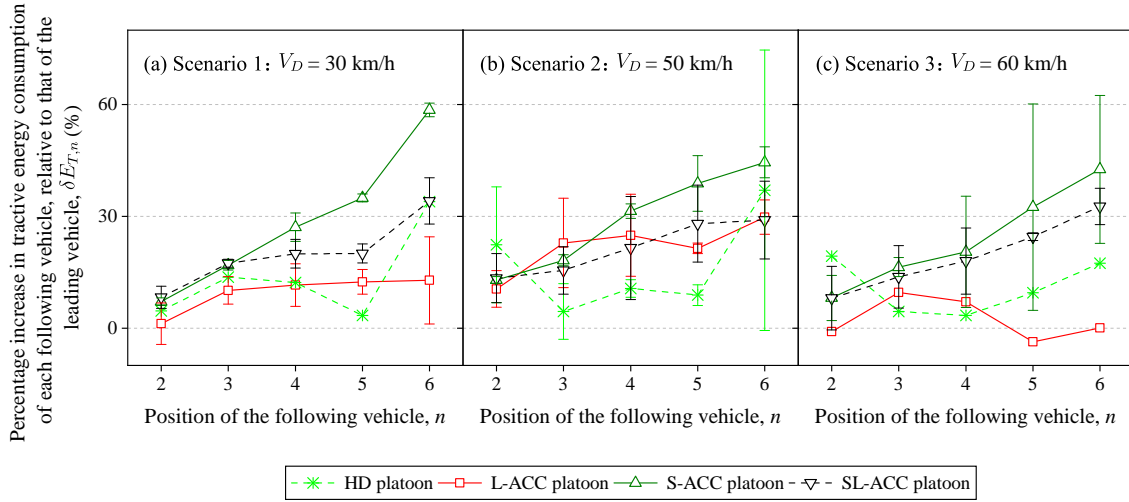
Subplots: (a)-(c) Cruising scenarios 1-3, namely, V_D = 30, 50, and 60 km/h.
Note: V_D = desired speed (km/h); HD platoon = human-driven platoon; L/S/SL-ACC platoon = long, short, or short/long time-gap adaptive cruise control (ACC) platoon.

Figure 9.4 Percentage increase ($\delta E_{T,n}$, %) in tractive energy consumption of the following vehicle relative to that of the leading vehicle in three cruising scenarios on the handling course (HC).

cruising scenarios (V_D = 30, 50, and 60 km/h, respectively). In general, error bars in this graph are much larger than those in Figure 9.2, suggesting greater uncertainties in the energy results of the platooning experiments performed in cruising scenarios. A plausible explanation is that, on the handling course (HC), the road geometry (e.g., slope and curvature) varies more significantly, leading to stronger external disturbances in platooning. Despite the uncertainties, results in this graph extend the validity and generality of previous findings in Figure 9.2 and Table 9.1. Namely, in platoons, ACC systems with a short time-gap setting lead to significant string instability and therefore the increase in energy consumption. Specifically, S-ACC platoons exhibit strong growth trends in $\delta E_{T,n}$ along the upstream direction in each subplot. In these platoons, the last follower (at Position 6) consumes 42.6-58.6% more energy than the leader. On the other hand, ACC systems with a long time-gap setting can mitigate string instability and then reduce energy consumption. For example, in SL-ACC platoons (in which two ACC followers adopt a long time-gap; see Section 9.2.2), the $\delta E_{T,n}$ values of the last follower (at Position 6) are not more than 35%. Furthermore, in L-ACC platoons (in which all ACC followers use a long time-gap), there does not exist a continuous upward trend in $\delta E_{T,n}$.

Table 9.2 summarizes the average increase in tractive energy consumption of all following vehicles relative to that of the platoon leader in the experiments carried out on

Table 9.2 Average increase ($\Delta\overline{E}_T$, %) in tractive energy consumption of all following vehicles relative to that of the leading vehicle in cruising scenarios.

V_D (km/h)	30	50	60
HD platoons	13.6	16.7	10.8
L-ACC platoons	9.6	21.9	2.4
S-ACC platoons	28.9	29.2	24.0
SL-ACC platoons	20.0	21.5	19.4

Note: V_D = desired speed (km/h); HD platoon = human-driven platoon; L/S/SL-ACC platoon = long, short, or short/long time-gap adaptive cruise control (ACC) platoon.

the handling course (HC). The data reveal that HD platoons lead to $\Delta\overline{E}_T$ values ranging from 10.8% to 16.7% at different desired speeds (V_D). It is worth noting that, in three cruising scenarios, S-ACC platoons can always result in the largest $\Delta\overline{E}_T$ values, which are 28.9%, 29.2%, and 24.0% at the V_D of 30, 50, and 60 km/h, respectively. However, SL-ACC platoons, which adopt short and long mixed time-gap settings, can give rise to the $\Delta\overline{E}_T$ value much lower than that of S-ACC platoons in each cruising scenario.

9.4.3 Energy analysis of short/long time-gap ACC platoons

According to Table 9.2, SL-ACC platoons can generally outperform S-ACC platoons in reducing tractive energy consumption. However, more direct comparisons are required to uncover and validate the energy benefit of the short/long (mixed) time-gap settings to SL-ACC platoons. To this end, in Figure 9.5, the marked lines compare tractive energy consumption ($E_{T,n}$) of corresponding vehicles between SL-ACC and S-ACC platoons. Figure 9.5 (a)-(b) and (c)-(d) are four cases belonging to cruising scenarios of $V_D = 30$ and 60 km/h, respectively. The vehicle positions where SL-ACC and S-ACC platoons adopt different ACC time-gap settings are indicated by a green rectangle. In each subplot, the vehicle positions (n) smaller and larger than the ones in the green rectangle are denoted as downstream and upstream positions, respectively. In addition, the blue bars above the marked lines represent the percentage differences (%) in $E_{T,n}$ of corresponding vehicles between two platoons.

The results in this graph demonstrate that, at downstream positions, the differences in $E_{T,n}$ of vehicles between two platoons are negligible, ranging from -0.9% and 4.6%. At positions in green rectangles, however, vehicles of SL-ACC platoons lead to $E_{T,n}$ values much lower than those resulting from corresponding vehicles of S-ACC platoons.

Specifically, the percentage differences lie between -4.2% and -18.4%. Furthermore, at upstream positions, there are also significant differences (from -8.0% to -22.5%) in $E_{T,n}$ between corresponding vehicles in SL-ACC and S-ACC platoons. The findings suggest that the long time-gap ACC vehicles in SL-ACC platoons can mitigate speed perturbations propagating upstream and therefore result in considerable energy savings compared to those of S-ACC platoons.
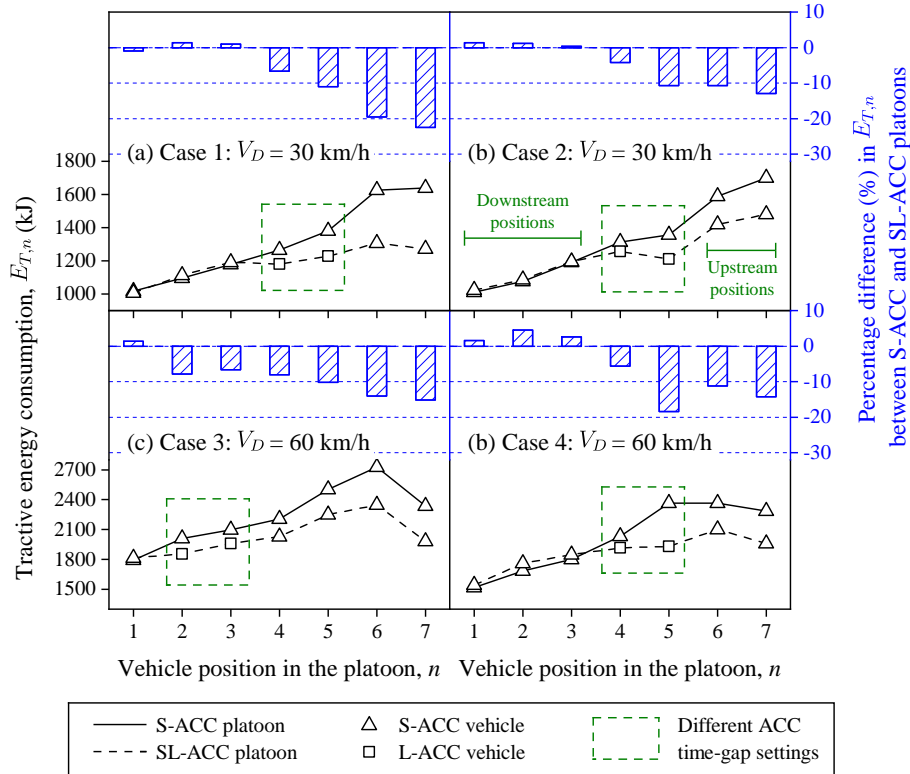
Subplots: (a)-(b) and (c)-(d) are cases from cruising scenarios of V_D = 30 and 60 km/h, respectively.
Note: V_D = desired speed (km/h); S/L/SL = short, long, or short/long time-gap setting; ACC = adaptive cruise control.

Figure 9.5 Differences in tractive energy consumption ($E_{T,n}$, kJ) of vehicles between S-ACC and SL-ACC platoons in cruising scenarios.

Table 9.3 Comparison of total tractive energy consumption ($\mathbb{E}_T$, MJ) between SL-ACC and S-ACC platoons in cruising scenarios.

	V_D = 30 km/h		V_D = 60 km/h	
	Case 1	Case 2	Case 3	Case 4
S-ACC platoon (MJ)	9.20	9.23	15.67	14.05
SL-ACC platoon (MJ)	8.30	8.67	14.23	13.05
Percentage difference (%)	-9.8	-6.1	-9.2	-7.1

Note: V_D = desired speed (km/h); Cases 1-4 correspond to the ones in Figure 9.5 (a)-(d).

To quantify the overall energy differences between SL-ACC and S-ACC platoons, Table 9.3 compares the total tractive energy consumption ($\mathbb{E}_T$) values of these two types of platoons in the four cases presented in Figure 9.5. The data in this table show that, relative to S-ACC platoons, SL-ACC platoons can achieve energy savings between 6.1% and 9.8% in different cruising scenarios.

9.5   Summary

This study investigates the energy impact of the ACC time-gap setting in different test environments. ACC platoon experiments are performed in speed perturbation scenarios and cruising scenarios on the dynamic platform and the handling course, respectively, two test tracks of the ZalaZone proving ground. ACC platoons adopting short, medium, long, and short/long (mixed) time-gap settings are respectively abbreviated as S-ACC, M-ACC, L-ACC, and SL-ACC platoons. The results suggest that, in six different speed perturbation scenarios, the following vehicles in S-ACC platoons lead to string instability and therefore increased tractive energy consumption values, which are on average 18.9-37.1% greater than those of their platoon leaders. On the other hand, the ACC long time-gap setting can contribute to reducing the energy consumption of the whole platoon. Specifically, in different cruising scenarios, SL-ACC platoons can achieve overall fuel savings of 6.1-9.8% compared with S-ACC platoons.

10 Conclusion and outlook

Automated and electrified vehicles (AEVs) have the potential to improve mobility, safety, congestion, emissions, and fuel economy. This thesis, therefore, focuses on the development and assessment of AEVs and brings together insights from multiple disciplines, e.g., vehicle studies to design and control AEVs as well as traffic flow studies to describe and evaluate their driving behaviours. We now conclude the thesis by summarizing the main findings and discussing some future research directions.

10.1 Conclusions

Overall, the main theme of this thesis is to shed light on the development and assessment of AEVs from three aspects: optimizing the driving and powertrain systems of AEVs, modelling the longitudinal driving behaviours of AEVs in microscopic traffic simulation, and evaluating their energy and safety performance in real-world driving conditions.

To optimize the driving and powertrain systems of AEVs

Part I of this thesis focuses on optimizing the driving and powertrain systems of AEVs, including their (mechanical and electrical) components as well as (energy and driving) controllers. **Chapter 3** presents the optimal component sizing of a flex-fuel hybrid powertrain that runs on multiple energy sources including grid electricity, gasoline, and ethanol, aiming to improve the energy efficiency, greenhouse gas (GHG) emissions, and cost-effectiveness of PHEVs. The results indicate that better performances of the PHEV, regarding GHG emissions and energy consumption, are associated with larger battery size and smaller engine displacement but result in a higher cost-to-power ratio. Specifically, for E25-fuelled PHEVs in markets with world average electricity carbon intensity, every 1.0 USD/kW increase in cost-to-power ratio leads to savings of 1.6 MJ energy consumption and 1.7 g CO_2−eq/km WTW GHG emissions. Moreover, a clear benefit of using E25 in the hybrid propulsion system is identified, where the energy consumption and GHG emissions can be reduced by 5.9% and 12.3%, respectively.

In **Chapter 4**, we utilize the Pareto-based approach to investigate the integrated multi-objective optimization of adaptive cruise control (ACC) and energy management strategy (EMS) for AEVs, in which energy efficiency, ride comfort, and tracking safety are selected as objective functions. The results suggest that the energy and the comfort targets are harmonious, but both conflict with the safety target. Validation using real-world driving data shows that the Pareto optimum for ACC and EMS systems, relative to the baseline, can reduce energy consumption (by 7.57%) and tracking error (by 68.94%), while simultaneously satisfying ride comfort needs. In addition, sensitivity analysis proves that the vehicle reaction time impacts significantly on tracking safety, but its effect on energy saving is trivial.

To model driving behaviours of AEVs in traffic simulation

In the second part of this thesis, intensive efforts have been directed at developing microscopic free-flow or car-following models that describe driving behaviours of AEVs in traffic simulation. **Chapter 5** develops the microsimulation free-flow acceleration (MFC) model, attempting to introduce the dynamics of EVs into microscopic modelling. The results suggest that the acceleration and deceleration potential curves underlying the MFC model can accurately represent real dynamics of EVs tested on the chassis dynamometer. Smooth transitions can be guaranteed after implementing the MFC model in microsimulation. When reproducing the on-road driving trajectories, the MFC model can deliver significant reductions in root mean square error (RMSE) of speed (by $\sim$69%) and acceleration (by $\sim$50%) compared with benchmarks. Moreover, the MFC model can accurately predict the vehicle 0-100 km/h acceleration specifications, with RMSE 49.4% and 56.8% lower than those of the Gipps model and the intelligent driver model (IDM), respectively.

Road geometry (e.g., slope and curvature) has significant impacts on driving behaviours of low-level automated vehicles (AVs), but it has been largely ignored in microscopic traffic models. To capture these effects, **Chapter 6** proposes a generic approach to extend any of the microscopic models. The results suggest that two submodels, i.e., the nonlinear vehicle dynamics (NVD) and the radius difference method (RDM), can extend the microscopic model to effectively capture the effects of road slope and road curvature, respectively, on automated driving. Specifically, the NVD is the dominant factor contributing to increasing (by 34.9% on average) model accuracy. In addition, when simulating reckless turning

behaviours (i.e., the vehicle turns at high speeds), the inclusion of the developed RDM is significant for model performance, and the models extended with both the NVD and the RDM can achieve the largest accuracy gains (39.6%).

Motivated by the results in Chapters 5 and 6, **Chapter 7** proposes a general modelling framework, in which ACC models and behaviour car-following (CF) models have been incrementally augmented with physics extensions; namely, perception delay, linear or nonlinear vehicle dynamics, and acceleration constraints. The framework has been applied to the intelligent driver model (IDM), the Gipps model, and to three basic ACC models that are a linear controller coupled with three different spacing policies, i.e., the constant time headway (CTH), the IDM-desired, and the Gipps-equilibrium. The model calibration and validation results demonstrate that when a single extension has been applied, perception delay and linear vehicle dynamics have been the extensions to mostly increase modelling accuracy, whatever the base model considered. Concerning models, Gipps-based ones have outperformed all other CF and ACC models in calibration. Even among ACC models, the linear controllers coupled with the Gipps-equilibrium spacing policy have been the best performing models. On the other hand, IDM-based models have been by far the most robust in validation, showing almost no crash when calibrated parameters have been used to simulate different trajectories.

To evaluate AEVs in real-world driving conditions

In Part III of this thesis, a series of driving experiments are carried out on public roads and test tracks, to compare the energy and safety performances between ACC and human-driven vehicles and to investigate the energy impacts of different ACC time-gap settings. In **Chapter 8**, to examine the difference in driving behaviour between ACC vehicles and human-driven vehicles (HDVs), we perform automated (comprising only ACC vehicles) and mixed (consisting of both ACC vehicles and HDVs) platoon experiments in real-world highway conditions. Results suggest that, unlike human drivers, ACC followers lead to string instability. On the individual level, ACC followers have tractive energy consumption 2.7-20.5% higher than those of human counterparts. On the platoon level, the tractive energy values of ACC followers tend to consecutively increase (11.2-17.3%). In general, therefore, the examined commercial ACC systems have negative impacts on tractive energy efficiency and stability in real-world applications.

Chapter 9 systematically investigates the energy impacts of time-gap settings of commercial ACC systems in platooning experiments performed on test tracks. Platoons consisting of 5-7 ACC vehicles are employed to perform both speed perturbation and cruising experiments. ACC platoons adopting short, medium, long, and short/long (mixed) time-gap settings are respectively abbreviated as S-ACC, M-ACC, L-ACC, and SL-ACC platoons. Results suggest that, in six different speed perturbation scenarios, the following vehicles in S-ACC platoons lead to string instability and therefore increased tractive energy consumption, which are on average 18.9-37.1% greater than those of their platoon leaders. On the other hand, the ACC long time-gap setting can contribute to reducing the energy consumption of the whole platoon. Specifically, in different cruising scenarios, SL-ACC platoons can achieve overall fuel savings of 6.1-9.8% compared with S-ACC platoons.

10.2   Future research directions

This research paves the way to developing and evaluating AEVs from a multi-disciplinary perspective. In this final section, we outline some possible directions for future research related to the work in this thesis.

To optimize the driving and powertrain systems of AEVs

In Chapters 3 and 4, Pareto-based multi-objective optimization (MOO) frameworks are developed to separately address two problems, namely, the sizing of powertrain components and the integrated calibration of control systems. However, both problems share similar system dynamics (e.g., powertrain dynamics and vehicle longitudinal dynamics) and optimization objectives (e.g., energy efficiency, emission, and ride comfort). Therefore, it is worth studying whether an augmented Pareto-based MOO framework, which can simultaneously determine the optimal combination of component specifications and control parameters, can result in more flexible approaches for the development of AEVs.

To prolong the battery life is a critical concern for vehicles with higher degrees of electrification such as plug-in hybrid electric vehicles (PHEVs) and battery electric vehicles (BEVs). Therefore, another interesting topic is to incorporate the battery state-of-health (SoH) model into powertrain simulation and then investigate the methods (e.g., component sizing as well as optimal control design of EMS and ACC) to avoid detrimental effects of over-charging and over-discharging on battery.

To model driving behaviours of AEVs in traffic simulation

Chapters 5-7 are devoted to developing microscopic free-flow or car-following models for describing longitudinal driving behaviours of AEVs in traffic simulation. However, more efforts are required to develop and validate models for predicting the fuel consumption and exhaust emissions of AEVs.

Furthermore, how to accurately model lateral driving behaviours (e.g., lane-changing decision and steering process) of AEVs is a more challenging task due to the complex interaction of vehicles in two dimensions. Another important focus of future work should, therefore, be to develop lane-changing models for AEVs in traffic simulation.

In addition, microscopic traffic models proposed in this project only account for AEVs without connectivity. However, the vehicle-to-vehicle (V2V) communication is forecast to significantly change the vehicle driving characteristics. Consequently, in future works, advanced multi-anticipative microscopic traffic models are required in traffic simulation to describe the acceleration behaviours of vehicles with connectivity features such as cooperative adaptive cruise control (CACC).

To evaluate AEVs in real-world driving conditions

Chapters 8 and 9 focus on evaluating the energy and safety performance of AEVs in a series of vehicle platoon experiments on public roads and test tracks. With the advent of the real driving emissions (RDE) test and the portable emission measurement system (PEMS), future studies are needed to systematically assess the impact of driving automation and powertrain electrification on pollutants, e.g., nitrogen oxides (NO_x), carbon oxides (CO_x), and particulate matter (PM), emitted by AEVs while driven in real-world conditions.

Moreover, human drivers still play an important role in lower levels of driving automation. Therefore, research efforts are needed to better understand drivers' acceptance and experience in terms of usefulness, satisfaction, effort, and risk of different advanced driver assistance systems (ADAS) in various real-world driving scenarios.

References

[1] L. D. Burns, "A vision of our transport future," *Nature*, vol. 497, no. 7448, pp. 181–182, 2013.

[2] M. Noussan, M. Hafner, and S. Tagliapietra, *The Future of Transport Between Digitalization and Decarbonization: Trends, Strategies and Effects on Energy Consumption*. Springer Nature, 2020.

[3] "International Council on Clean Transportation (ICCT) - Global Transportation Roadmap." [Online]. Available: https://theicct.org/transportation-roadmap

[4] ITF, *ITF Transport Outlook 2019*. International Transport Forum (ITF), 2019.

[5] S. Khalili, E. Rantanen, D. Bogdanov, and C. Breyer, "Global transportation demand development with impacts on the energy demand and greenhouse gas emissions in a climate-constrained world," *Energies*, vol. 12, no. 20, p. 3870, 2019.

[6] S. Underwood, S. Marshall, and J. Niles, *Automated, Connected, and Electric Vehicles: An Assessment of Emerging Transportation Technologies and a Policy Roadmap for More Sustainable Transportation*. Ann Arbor, 2014.

[7] IEA, *World Energy Outlook 2012*. International Energy Agency (IEA), 2012.

[8] IPCC, *Climate Change 2014: Synthesis Report*. Intergovernmental Panel on Climate Change (IPCC), 2014.

[9] J. Axsen, P. Plötz, and M. Wolinetz, "Crafting strong, integrated policy mixes for deep CO_2 mitigation in road transport," *Nature Climate Change*, vol. 10, no. 9, pp. 809–818, 2020.

[10] WHO, *Global Status Report on Road Safety 2018: Summary*. World Health Organization (WHO), 2018.

[11] B. Pishue, *US Traffic Hot Spots: Measuring the Impact of Congestion in the United States*. INRIX Research, 2017.

[12] T. Afrin and N. Yodo, "A survey of road traffic congestion measures towards a sustainable and resilient transportation system," *Sustainability*, vol. 12, no. 11, p. 4660, 2020.

[13] M. Alonso Raposo, B. Ciuffo, F. Ardente, J. Aurambout, G. Baldini, R. Braun, and I. Vandecasteele, "The future of road transport: Implications of automated, connected, low-carbon and shared mobility," *European Commission - Joint Research Centre (JRC)*, 2019.

[14] "European Commission - Transport Research and Innovation Monitoring and Information System (TRIMIS) database." [Online]. Available: https://trimis.ec.europa.eu/

[15] T. Möller, A. Padhi, D. Pinner, and A. Tschiesner, "The future of mobility is at our doorstep," *McKinsey Center for Future Mobility*, 2019.

[16] SAE, "Taxonomy and definitions for terms related to driving automation systems for on-road motor vehicles," *SAE International,(J3016)*, 2016.

[17] N. Hawes, "Driving the revolution." [Online]. Available: https://www.birmingham.ac.uk/news/thebirminghambrief/items/2016/11/driving-the-revolution.aspx

[18] T. Avot, *5G on the Highway to V2X*.   Altran, 2018.

[19] Wikipedia, "Vehicle-to-everything." [Online]. Available: https://en.wikipedia.org/wiki/Vehicle-to-everything

[20] IEA, "Global EV Outlook 2020," 2020. [Online]. Available: https://www.iea.org/reports/global-ev-outlook-2020

[21] Wikipedia, "Paris agreement." [Online]. Available: https://en.wikipedia.org/wiki/Paris_Agreement

[22] F. Knobloch, S. V. Hanssen, A. Lam, H. Pollitt, P. Salas, U. Chewpreecha, M. A. Huijbregts, and J.-F. Mercure, "Net emission reductions from electric cars and heat pumps in 59 world regions over time," *Nature Sustainability*, vol. 3, no. 6, pp. 437–447, 2020.

[23] A. Cornet, R. Hensley, C. Hirschberg, P. Schaufuss, A. Tschiesner, A. Venus, and J. Werra, "Reboost: A comprehensive view on the changing powertrain component market and how suppliers can succeed," *online: mckinsey. com*, 2019.

[24] G. Kalghatgi, "Is it really the end of internal combustion engines and petroleum in transport?" *Applied Energy*, vol. 225, pp. 965–974, 2018.

[25] C. Mi and M. A. Masrur, *Hybrid Electric Vehicles: Principles and Applications with Practical Perspectives*.   John Wiley & Sons, 2017.

[26] G. Ma, M. Ghasemi, and X. Song, "Integrated powertrain energy management and vehicle coordination for multiple connected hybrid electric vehicles," *IEEE Transactions on Vehicular Technology*, vol. 67, no. 4, pp. 2893–2899, 2017.

[27] L. Li, X. Wang, R. Xiong, K. He, and X. Li, "AMT downshifting strategy design of HEV during regenerative braking process for energy conservation," *Applied Energy*, vol. 183, pp. 914–925, 2016.

[28] J. Li, Q. Zhou, Y. He, B. Shuai, Z. Li, H. Williams, and H. Xu, "Dual-loop online intelligent programming for driver-oriented predict energy management of plug-in hybrid electric vehicles," *Applied Energy*, vol. 253, p. 113617, 2019.

[29] Y. He, C. Wang, Q. Zhou, J. Li, M. Makridis, H. Williams, G. Lu, and H. Xu, "Multiobjective component sizing of a hybrid ethanol-electric vehicle propulsion system," *Applied Energy*, vol. 266, p. 114843, 2020.

[30] Z. Tian, C. Zhang, and S. Zhang, "Analytical calculation of magnetic field distribution and stator iron losses for surface-mounted permanent magnet synchronous machines," *Energies*, vol. 10, no. 3, p. 320, 2017.

[31] P. Nieuwenhuis, L. Cipcigan, and H. B. Sonder, "The electric vehicle revolution," in *Future Energy*.   Elsevier, 2020, pp. 227–243.

[32] A. Sartbaeva, V. Kuznetsov, S. Wells, and P. Edwards, "Hydrogen nexus in a sustainable energy future," *Energy & Environmental Science*, vol. 1, no. 1, pp. 79–85, 2008.

[33] D. China, "Fueling the future of mobility hydrogen and fuel cell solutions for transportation," *Financ. Advis*, vol. 1, no. 1, 2019.

[34] W. Goodall, T. Dovey, J. Bornstein, and B. Bonthron, "The rise of mobility as a service," *Deloitte Review*, vol. 20, pp. 112–129, 2017.

[35] J. Lazarus, S. Shaheen, S. E. Young, D. Fagnant, T. Voege, W. Baumgardner, J. Fishelson, and J. S. Lott, "Shared automated mobility and public transport," *Road Vehicle Automation 4*, pp. 141–161, 2018.

[36] A. Cohen and S. Shaheen, *Planning for Shared Mobility*. American Planning Association (APA), 2018.

[37] Wikipedia, "Carsharing." [Online]. Available: https://en.wikipedia.org/wiki/Carsharing

[38] Wikipedia, "Ridesharing." [Online]. Available: https://en.wikipedia.org/wiki/Ridesharing

[39] N. D. Chan and S. A. Shaheen, "Ridesharing in North America: Past, present, and future," *Transport Reviews*, vol. 32, no. 1, pp. 93–112, 2012.

[40] H. Wang and H. Yang, "Ridesourcing systems: A framework and review," *Transportation Research Part B: Methodological*, vol. 129, pp. 122–155, 2019.

[41] S. Shaheen and A. Cohen, *Innovative Mobility Carsharing Outlook: Carsharing Market Overview, Analysis, and Trends*. Transportation Sustainability Research Center, University of California, Berkeley, 2016.

[42] J.-P. A. Barthès and P. Bonnifait, "Multi-agent active collaboration between drivers and assistance systems," in *Advances in Artificial Transportation Systems and Simulation*. Elsevier, 2015, pp. 163–180.

[43] S. Choi, F. Thalmayr, D. Wee, and F. Weig, "Advanced driver-assistance systems: Challenges and opportunities ahead," *McKinsey & Company*, pp. 1–11, 2016.

[44] "UN Regulation on Advanced Emergency Braking Systems for cars to significantly reduce crashes." [Online]. Available: https://unece.org/press/un-regulation-advanced-emergency-braking-systems-cars-significantly-reduce-crashes

[45] V. K. Kukkala, J. Tunnell, S. Pasricha, and T. Bradley, "Advanced driver-assistance systems: A path toward autonomous vehicles," *IEEE Consumer Electronics Magazine*, vol. 7, no. 5, pp. 18–25, 2018.

[46] X. Mosquet, M. Andersen, and A. Arora, "A roadmap to safer driving through advanced driver assistance systems," *Auto Tech Review*, vol. 5, no. 7, pp. 20–25, 2016.

[47] S. Lee and Y. Yu, "Study of the night vision system in vehicle," in *2012 IEEE Vehicle Power and Propulsion Conference*. IEEE, 2012, pp. 1312–1316.

[48] Wikipedia, "Backup camera." [Online]. Available: https://en.wikipedia.org/wiki/Backup_camera

[49] Z. Tuo, "Research on adaptive front-lighting system algorithm based on machine vision," in *Proceedings of the 2020 Artificial Intelligence and Complex Systems Conference*, 2020, pp. 21–26.

[50] Y. Gao, C. Lin, Y. Zhao, X. Wang, S. Wei, and Q. Huang, "3D surround view for advanced driver assistance systems," *IEEE Transactions on Intelligent Transportation Systems*, vol. 19, no. 1, pp. 320–328, 2017.

[51] P. Degerman, "Automatic parallel parking: Park assist systems for passenger vehicles," Ph.D. dissertation, Linköpings universitet, 2007.

[52] M. Zhu, X. Wang, and J. Hu, "Impact on car following behavior of a forward collision warning system with headway monitoring," *Transportation Research Part C: Emerging Technologies*, vol. 111, pp. 226–244, 2020.

[53] A. Kamble and S. Potadar, "Lane departure warning system for advanced drivers assistance," in *2018 Second International Conference on Intelligent Computing and Control Systems (ICICCS)*. IEEE, 2018, pp. 1775–1778.

[54] AAA, *Advanced Driver Assistance Technology Names: AAA's Recommendation for Common Naming of Advanced Safety Systems*. American Automobile Association (AAA), 2019.

[55] M. Peplow, "Traffic flow: Cruising through congestion," *Nature*, vol. 429, no. 6993, 2004.

[56] J. Vander Werf, S. E. Shladover, M. A. Miller, and N. Kourjanskaia, "Effects of adaptive cruise control systems on highway traffic flow capacity," *Transportation Research Record*, vol. 1800, no. 1, pp. 78–84, 2002.

[57] J. J. Blum, A. Eskandarian, and S. A. Arhin, "Intelligent speed adaptation (ISA)," in *Handbook of Intelligent Vehicles*. Springer London, 2012, pp. 582–602.

[58] Wikipedia, "Intelligent speed adaptation." [Online]. Available: https://en.wikipedia.org/wiki/Intelligent_speed_adaptation

[59] J. Thalen, "ADAS for the car of the future," B.S. thesis, University of Twente, 2006.

[60] Wikipedia, "Automatic parking." [Online]. Available: https://en.wikipedia.org/wiki/Automatic_parking

[61] P.-M. Hsu, M. H. Li, and K.-C. Chang, "Noise filtering in autonomous emergency braking systems with sensor fusions," SAE Technical Paper, Tech. Rep., 2015.

[62] B. Fildes, M. Keall, N. Bos, A. Lie, Y. Page, C. Pastor, L. Pennisi, M. Rizzi, P. Thomas, and C. Tingvall, "Effectiveness of low speed autonomous emergency braking in real-world rear-end crashes," *Accident Analysis & Prevention*, vol. 81, pp. 24–29, 2015.

[63] A. Bayrak, "Topology considerations in hybrid electric vehicle powertrain architecture design," Ph.D. dissertation, University of Michigan, 2015.

[64] G. Wu, X. Zhang, and Z. Dong, "Powertrain architectures of electrified vehicles: Review, classification and comparison," *Journal of the Franklin Institute*, vol. 352, no. 2, pp. 425–448, 2015.

[65] J. Liu and H. Peng, "Modeling and control of a power-split hybrid vehicle," *IEEE Transactions on Control Systems Technology*, vol. 16, no. 6, pp. 1242–1251, 2008.

[66] S. E. Lucena, "A survey on electric and hybrid electric vehicle technology," *IntechOpen*, pp. 1–21, 2011.

[67] Wikipedia, "Electric motor." [Online]. Available: https://en.wikipedia.org/wiki/Electric_motor

[68] W. Enang and C. Bannister, "Modelling and control of hybrid electric vehicles (a comprehensive review)," *Renewable and Sustainable Energy Reviews*, vol. 74, pp. 1210–1239, 2017.

[69] J. Hu, J. Ni, and Z. Peng, "Transmission architecture and topology design of EVs and HEVs," in *Modeling, Dynamics and Control of Electrified Vehicles*. Elsevier, 2018, pp. 121–157.

[70] A. Z. Sheikh, "Comparative analysis of parallel vs series hybrid electric powertrains," Master's thesis, Rochester Institute of Technology, 2019.

[71] H. Yang, S. Cho, N. Kim, W. Lim, and S. Cha, "Analysis of planetary gear hybrid powertrain system Part 1: Input split system," *International Journal of Automotive Technology*, vol. 8, no. 6, pp. 771–780, 2007.

[72] H. Yang, B. Kim, Y. Park, W. Lim, and S. Cha, "Analysis of planetary gear hybrid powertrain system Part 2: Output split system," *International Journal of Automotive Technology*, vol. 10, no. 3, pp. 381–390, 2009.

[73] Y. He, Q. Zhou, M. Makridis, K. Mattas, J. Li, H. Williams, and H. Xu, "Multiobjective co-optimization of cooperative adaptive cruise control and energy management strategy for PHEVs," *IEEE Transactions on Transportation Electrification*, vol. 6, no. 1, pp. 346–355, 2020.

[74] Y. He, M. Makridis, K. Mattas, G. Fontaras, B. Ciuffo, and H. Xu, "Introducing electrified vehicle dynamics in traffic simulation," *Transportation Research Record*, vol. 2674, no. 9, pp. 776–791, 2020.

[75] Y. Zou, S. E. Li, B. Shao, and B. Wang, "State-space model with non-integer order derivatives for lithium-ion battery," *Applied Energy*, vol. 161, pp. 330–336, 2016.

[76] A. Khaligh and Z. Li, "Battery, ultracapacitor, fuel cell, and hybrid energy storage systems for electric, hybrid electric, fuel cell, and plug-in hybrid electric vehicles: State of the art," *IEEE Transactions on Vehicular Technology*, vol. 59, no. 6, pp. 2806–2814, 2010.

[77] M. Jafari, A. Gauchia, K. Zhang, and L. Gauchia, "Simulation and analysis of the effect of real-world driving styles in an EV battery performance and aging," *IEEE Transactions on Transportation Electrification*, vol. 1, no. 4, pp. 391–401, 2015.

[78] L. Zhang, X. Hu, Z. Wang, F. Sun, and D. G. Dorrell, "Experimental impedance investigation of an ultracapacitor at different conditions for electric vehicle applications," *Journal of Power Sources*, vol. 287, pp. 129–138, 2015.

[79] L. Zhang, X. Hu, Z. Wang, F. Sun, J. Deng, and D. G. Dorrell, "Multiobjective optimal sizing of hybrid energy storage system for electric vehicles," *IEEE Transactions on Vehicular Technology*, vol. 67, no. 2, pp. 1027–1035, 2017.

[80] J. Li, Q. Zhou, Y. He, H. Williams, and H. Xu, "Driver-identified supervisory control system of hybrid electric vehicles based on spectrum-guided fuzzy feature extraction," *IEEE Transactions on Fuzzy Systems*, vol. 28, no. 11, pp. 2691–2701, 2020.

[81] C. Wang, A. Janssen, A. Prakash, R. Cracknell, and H. Xu, "Splash blended ethanol in a spark ignition engine–effect of ron, octane sensitivity and charge cooling," *Fuel*, vol. 196, pp. 21–31, 2017.

[82] C. M. Martinez, X. Hu, D. Cao, E. Velenis, B. Gao, and M. Wellers, "Energy management in plug-in hybrid electric vehicles: Recent progress and a connected vehicles perspective," *IEEE Transactions on Vehicular Technology*, vol. 66, no. 6, pp. 4534–4549, 2016.

[83] P. Pisu and G. Rizzoni, "A comparative study of supervisory control strategies for hybrid electric vehicles," *IEEE Transactions on Control Systems Technology*, vol. 15, no. 3, pp. 506–518, 2007.

[84] S. G. Wirasingha and A. Emadi, "Classification and review of control strategies for plug-in hybrid electric vehicles," *IEEE Transactions on Vehicular Technology*, vol. 60, no. 1, pp. 111–122, 2010.

[85] P. Zhang, F. Yan, and C. Du, "A comprehensive analysis of energy management strategies for hybrid electric vehicles based on bibliometrics," *Renewable and Sustainable Energy Reviews*, vol. 48, pp. 88–104, 2015.

[86] Y. Gao and M. Ehsani, "Design and control methodology of plug-in hybrid electric vehicles," *IEEE Transactions on Industrial Electronics*, vol. 57, no. 2, pp. 633–640, 2009.

[87] L. Tribioli, M. Barbieri, R. Capata, E. Sciubba, E. Jannelli, and G. Bella, "A real time energy management strategy for plug-in hybrid electric vehicles based on optimal control theory," *Energy Procedia*, vol. 45, pp. 949–958, 2014.

[88] H. A. Borhan, A. Vahidi, A. M. Phillips, M. L. Kuang, and I. V. Kolmanovsky, "Predictive energy management of a power-split hybrid electric vehicle," in *2009 American Control Conference*. IEEE, 2009, pp. 3970–3976.

[89] Q. Zhou, "Design optimisation and real-time energy management control of the electrified off-highway vehicle with artificial intelligence," Ph.D. dissertation, University of Birmingham, 2019.

[90] H. Wang, Y. Huang, H. He, C. Lv, W. Liu, and A. Khajepour, "Energy management of hybrid electric vehicles," *Modeling, Dynamics and Control of Electrified Vehicles*, pp. 159–206, 2018.

[91] K. Chau and Y. Wong, "Overview of power management in hybrid electric vehicles," *Energy Conversion and Management*, vol. 43, no. 15, pp. 1953–1968, 2002.

[92] B. Geller, C. Quinn, and T. H. Bradley, "Analysis of design tradeoffs for plug-in hybrid vehicles," *Electric and Hybrid Vehicles: Power Sources, Models, Sustainability, Infrastructure and the Market. Elsevier*, p. 159, 2010.

[93] W. Pedrycz, *Fuzzy Control and Fuzzy Systems*. Research Studies Press Ltd., 1993.

[94] W. Xiong, Y. Zhang, and C. Yin, "Optimal energy management for a series–parallel hybrid electric bus," *Energy Conversion and Management*, vol. 50, no. 7, pp. 1730–1738, 2009.

[95] M. Mohebbi, M. Charkhgard, and M. Farrokhi, "Optimal neuro-fuzzy control of parallel hybrid electric vehicles," in *2005 IEEE Vehicle Power and Propulsion Conference*. IEEE, 2005, pp. 26–30.

[96] Q. Zhou, Y. Zhang, Z. Li, J. Li, H. Xu, and O. Olatunbosun, "Cyber-physical energy-saving control for hybrid aircraft-towing tractor based on online swarm intelligent programming," *IEEE Transactions on Industrial Informatics*, vol. 14, no. 9, pp. 4149–4158, 2017.

[97] S. Xie, X. Hu, T. Liu, S. Qi, K. Lang, and H. Li, "Predictive vehicle-following power management for plug-in hybrid electric vehicles," *Energy*, vol. 166, pp. 701–714, 2019.

[98] L. Serrao, S. Onori, A. Sciarretta, Y. Guezennec, and G. Rizzoni, "Optimal energy management of hybrid electric vehicles including battery aging," in *Proceedings of the 2011 American Control Conference*. IEEE, 2011, pp. 2125–2130.

[99] M. Montazeri-Gh, A. Poursamad, and B. Ghalichi, "Application of genetic algorithm for optimization of control strategy in parallel hybrid electric vehicles," *Journal of the Franklin Institute*, vol. 343, no. 4-5, pp. 420–435, 2006.

[100] A. Sciarretta, L. Serrao, P. Dewangan, P. Tona, E. Bergshoeff, C. Bordons, L. Charmpa, P. Elbert, L. Eriksson, T. Hofman *et al.*, "A control benchmark on the energy management of a plug-in hybrid electric vehicle," *Control Engineering Practice*, vol. 29, pp. 287–298, 2014.

[101] F. R. Salmasi, "Control strategies for hybrid electric vehicles: Evolution, classification, comparison, and future trends," *IEEE Transactions on Vehicular Technology*, vol. 56, no. 5, pp. 2393–2404, 2007.

[102] M. Ansarey, M. S. Panahi, H. Ziarati, and M. Mahjoob, "Optimal energy management in a dual-storage fuel-cell hybrid vehicle using multi-dimensional dynamic programming," *Journal of Power Sources*, vol. 250, pp. 359–371, 2014.

[103] L. V. Pérez, G. R. Bossio, D. Moitre, and G. O. García, "Optimization of power management in an hybrid electric vehicle using dynamic programming," *Mathematics and Computers in Simulation*, vol. 73, no. 1-4, pp. 244–254, 2006.

[104] Y. Zhou, "Predictive energy management for fuel cell hybrid electric vehicle," Ph.D. dissertation, Universite de technologie de Belfort-Montbeliard, 2020.

[105] A. Sciarretta, M. Back, and L. Guzzella, "Optimal control of parallel hybrid electric vehicles," *IEEE Transactions on Control Systems Technology*, vol. 12, no. 3, pp. 352–363, 2004.

[106] S. E. Li, Y. Zheng, K. Li, Y. Wu, J. K. Hedrick, F. Gao, and H. Zhang, "Dynamical modeling and distributed control of connected and automated vehicles: Challenges and opportunities," *IEEE Intelligent Transportation Systems Magazine*, vol. 9, no. 3, pp. 46–58, 2017.

[107] J. Gomes, J. Batra, V. R. Chopda, P. Kathiresan, and A. S. Rathore, "Monitoring and control of bioethanol production from lignocellulosic biomass," in *Waste Biorefinery*. Elsevier, 2018, pp. 727–749.

[108] M. I. Jordan and T. M. Mitchell, "Machine learning: Trends, perspectives, and prospects," *Science*, vol. 349, no. 6245, pp. 255–260, 2015.

[109] X. Hu, T. Liu, X. Qi, and M. Barth, "Reinforcement learning for hybrid and plug-in hybrid electric vehicle energy management: Recent advances and prospects," *IEEE Industrial Electronics Magazine*, vol. 13, no. 3, pp. 16–25, 2019.

[110] Wikipedia, "Artificial neural network." [Online]. Available: https://en.wikipedia.org/wiki/Artificial_neural_network

[111] Z. Chen, C. C. Mi, J. Xu, X. Gong, and C. You, "Energy management for a power-split plug-in hybrid electric vehicle based on dynamic programming and neural networks," *IEEE Transactions on Vehicular Technology*, vol. 63, no. 4, pp. 1567–1580, 2013.

[112] Y. L. Murphey, J. Park, Z. Chen, M. L. Kuang, M. A. Masrur, and A. M. Phillips, "Intelligent hybrid vehicle power control — Part I: Machine learning of optimal vehicle power," *IEEE Transactions on Vehicular Technology*, vol. 61, no. 8, pp. 3519–3530, 2012.

[113] Y. L. Murphey, J. Park, L. Kiliaris, M. L. Kuang, M. A. Masrur, A. M. Phillips, and Q. Wang, "Intelligent hybrid vehicle power control — Part II: Online intelligent energy management," *IEEE Transactions on Vehicular Technology*, vol. 62, no. 1, pp. 69–79, 2012.

[114] Q. Zhou, J. Li, B. Shuai, H. Williams, Y. He, Z. Li, H. Xu, and F. Yan, "Multi-step reinforcement learning for model-free predictive energy management of an electrified off-highway vehicle," *Applied Energy*, vol. 255, p. 113755, 2019.

[115] B. Shuai, Q. Zhou, J. Li, Y. He, Z. Li, H. Williams, H. Xu, and S. Shuai, "Heuristic action execution for energy efficient charge-sustaining control of connected hybrid vehicles with model-free double Q-learning," *Applied Energy*, vol. 267, p. 114900, 2020.

[116] X. Lin, P. Bogdan, N. Chang, and M. Pedram, "Machine learning-based energy management in a hybrid electric vehicle to minimize total operating cost," in *2015 IEEE/ACM International Conference on Computer-Aided Design (ICCAD)*. IEEE, 2015, pp. 627–634.

[117] M. Makridis, K. Mattas, C. Mogno, B. Ciuffo, and G. Fontaras, "The impact of automation and connectivity on traffic flow and CO_2 emissions: A detailed microsimulation study," *Atmospheric Environment*, vol. 226, p. 117399, 2020.

[118] S. E. Shladover, D. Su, and X. Lu, "Impacts of cooperative adaptive cruise control on freeway traffic flow," *Transportation Research Record*, vol. 2324, no. 1, pp. 63–70, 2012.

[119] K. Mattas, M. Makridis, P. Hallac, M. A. Raposo, C. Thiel, T. Toledo, and B. Ciuffo, "Simulating deployment of connectivity and automation on the antwerp ring road," *IET Intelligent Transport Systems*, vol. 12, no. 9, pp. 1036–1044, 2018.

[120] A. Kesting, M. Treiber, M. Schönhof, F. Kranke, and D. Helbing, "Jam-avoiding adaptive cruise control (ACC) and its impact on traffic dynamics," in *Traffic and Granular Flow'05*. Springer, 2007, pp. 633–643.

[121] F. Bu and C.-Y. Chan, "Adaptive and cooperative cruise control," *Handbook of Intelligent Vehicles*, pp. 191–207, 2012.

[122] M. Wang, "Generic model predictive control framework for advanced driver assistance systems," Ph.D. dissertation, Delft University of Technology, 2014.

[123] S. Bernsteiner, "Integration of advanced driver assistance systems on full-vehicle level-parametrization of an adaptive cruise control system based on test drives," Ph.D. dissertation, Technical University Graz, 2016.

[124] C. Wu, Z. Xu, Y. Liu, C. Fu, K. Li, and M. Hu, "Spacing policies for adaptive cruise control: A survey," *IEEE Access*, vol. 8, pp. 50 149–50 162, 2020.

[125] C. Lei, E. Van Eenennaam, W. K. Wolterink, G. Karagiannis, G. Heijenk, and J. Ploeg, "Impact of packet loss on CACC string stability performance," in *2011 11th International Conference on ITS Telecommunications.* IEEE, 2011, pp. 381–386.

[126] S. E. Shladover, "Longitudinal control of automated guideway transit vehicles within platoons," *Journal of Dynamic Systems, Measurement, and Control*, 1978.

[127] H. Chehardoli and M. R. Homaeinezhad, "Third-order leader-following consensus protocol of traffic flow formed by cooperative vehicular platoons by considering time delay: Constant spacing strategy," *Proceedings of the Institution of Mechanical Engineers, Part I: Journal of Systems and Control Engineering*, vol. 232, no. 3, pp. 285–298, 2018.

[128] S. Darbha, K. Rajagopal, and V. Tyagi, "A review of mathematical models for the flow of traffic and some recent results," *Nonlinear Analysis: Theory, Methods & Applications*, vol. 69, no. 3, pp. 950–970, 2008.

[129] A. Farnam and A. Sarlette, "About string stability of a vehicle chain with unidirectional controller," *European Journal of Control*, vol. 50, pp. 138–144, 2019.

[130] D. Swaroop and K. Rajagopal, "A review of constant time headway policy for automatic vehicle following," in *ITSC 2001. 2001 IEEE Intelligent Transportation Systems. Proceedings (Cat. No. 01TH8585).* IEEE, 2001, pp. 65–69.

[131] R. Rajamani and C. Zhu, "Semi-autonomous adaptive cruise control systems," *IEEE Transactions on Vehicular Technology*, vol. 51, no. 5, pp. 1186–1192, 2002.

[132] J. Wang and R. Rajamani, "Should adaptive cruise-control systems be designed to maintain a constant time gap between vehicles?" *IEEE Transactions on Vehicular Technology*, vol. 53, no. 5, pp. 1480–1490, 2004.

[133] J. Zhou and H. Peng, "Range policy of adaptive cruise control vehicles for improved flow stability and string stability," *IEEE Transactions on Intelligent Transportation Systems*, vol. 6, no. 2, pp. 229–237, 2005.

[134] K. Santhanakrishnan and R. Rajamani, "On spacing policies for highway vehicle automation," *IEEE Transactions on Intelligent Transportation Systems*, vol. 4, no. 4, pp. 198–204, 2003.

[135] F. Broqua, "Cooperative driving: Basic concepts and a first assessment of intelligent cruise control strategies," in *DRIVE Conference (1991: Brussels, Belgium). Advanced Telematics in Road Transport. Vol. II*, 1991.

[136] Y. Zhang, B. Kosmatopoulos, P. A. Ioannou, and C. Chien, "Autonomous intelligent cruise control using front and back information for tight vehicle following maneuvers," *IEEE Transactions on Vehicular Technology*, vol. 48, no. 1, pp. 319–328, 1999.

[137] D. N. Godbole, N. Kourjanskaia, R. Sengupta, and M. Zandonadi, "Breaking the highway capacity barrier: Adaptive cruise control-based concept," *Transportation Research Record*, vol. 1679, no. 1, pp. 148–157, 1999.

[138] J. VanderWerf, S. Shladover, N. Kourjanskaia, M. Miller, and H. Krishnan, "Modeling effects of driver control assistance systems on traffic," *Transportation Research Record*, vol. 1748, no. 1, pp. 167–174, 2001.

[139] B. Van Arem, C. J. Van Driel, and R. Visser, "The impact of cooperative adaptive cruise control on traffic-flow characteristics," *IEEE Transactions on Intelligent Transportation Systems*, vol. 7, no. 4, pp. 429–436, 2006.

[140] B. Van Arem, H. Driever, P. Feenstra, J. Ploeg, G. Klunder, I. Wilmink, A. Zoutendijk, Z. Papp, and B. Netten, "Design and evaluation of an integrated full-range speed assistant," TNO, Tech. Rep., 2007.

[141] Y. Zheng, S. E. Li, J. Wang, D. Cao, and K. Li, "Stability and scalability of homogeneous vehicular platoon: Study on the influence of information flow topologies," *IEEE Transactions on Intelligent Transportation Systems*, vol. 17, no. 1, pp. 14–26, 2015.

[142] F. Viti, S. P. Hoogendoorn, T. P. Alkim, and G. Bootsma, "Driving behavior interaction with ACC: Results from a field operational test in the Netherlands," in *2008 IEEE Intelligent Vehicles Symposium*. IEEE, 2008, pp. 745–750.

[143] G. Klunder, M. Li, and M. Minderhoud, "Traffic flow impacts of adaptive cruise control deactivation and (re)activation with cooperative driver behavior," *Transportation Research Record*, vol. 2129, no. 1, pp. 145–151, 2009.

[144] S. Li, K. Li, R. Rajamani, and J. Wang, "Model predictive multi-objective vehicular adaptive cruise control," *IEEE Transactions on Control Systems Technology*, vol. 19, no. 3, pp. 556–566, 2010.

[145] Y. Zheng, S. E. Li, K. Li, F. Borrelli, and J. K. Hedrick, "Distributed model predictive control for heterogeneous vehicle platoons under unidirectional topologies," *IEEE Transactions on Control Systems Technology*, vol. 25, no. 3, pp. 899–910, 2016.

[146] D. Corona, M. Lazar, B. De Schutter, and M. Heemels, "A hybrid MPC approach to the design of a smart adaptive cruise controller," in *IEEE International Conference on Control Applications*. IEEE, 2006, pp. 231–236.

[147] D. Corona and B. De Schutter, "Adaptive cruise control for a smart car: A comparison benchmark for MPC-PWA control methods," *IEEE Transactions on Control Systems Technology*, vol. 16, no. 2, pp. 365–372, 2008.

[148] V. L. Bageshwar, W. L. Garrard, and R. Rajamani, "Model predictive control of transitional maneuvers for adaptive cruise control vehicles," *IEEE Transactions on Vehicular Technology*, vol. 53, no. 5, pp. 1573–1585, 2004.

[149] Wikipedia, "Sliding mode control." [Online]. Available: https://en.wikipedia.org/wiki/Sliding_mode_control

[150] C. M. Martinez and D. Cao, *iHorizon-Enabled Energy Management for Electrified Vehicles*. Butterworth-Heinemann, 2018.

[151] J. Guldner and V. Utkin, "The chattering problem in sliding mode systems," in *Fourteenth International Symposium of Mathematical Theory of Networks and Systems, MTNS2000*, 2000.

[152] A. Ferrara and C. Vecchio, "Second order sliding mode control of vehicles with distributed collision avoidance capabilities," *Mechatronics*, vol. 19, no. 4, pp. 471–477, 2009.

[153] X. Guo, J. Wang, F. Liao, and R. S. H. Teo, "Distributed adaptive integrated-sliding-mode controller synthesis for string stability of vehicle platoons," *IEEE Transactions on Intelligent Transportation Systems*, vol. 17, no. 9, pp. 2419–2429, 2016.

[154] S.-J. Ko and J.-J. Lee, "Fuzzy logic based adaptive cruise control with guaranteed string stability," in *2007 International Conference on Control, Automation and Systems*. IEEE, 2007, pp. 15–20.

[155] J. E. Naranjo, C. González, J. Reviejo, R. García, and T. De Pedro, "Adaptive fuzzy control for inter-vehicle gap keeping," *IEEE Transactions on Intelligent Transportation Systems*, vol. 4, no. 3, pp. 132–142, 2003.

[156] J. E. Naranjo, C. González, R. García, and T. De Pedro, "ACC + Stop&go maneuvers with throttle and brake fuzzy control," *IEEE Transactions on Intelligent Transportation Systems*, vol. 7, no. 2, pp. 213–225, 2006.

[157] K. C. Dey, L. Yan, X. Wang, Y. Wang, H. Shen, M. Chowdhury, L. Yu, C. Qiu, and V. Soundararaj, "A review of communication, driver characteristics, and controls aspects of cooperative adaptive cruise control (CACC)," *IEEE Transactions on Intelligent Transportation Systems*, vol. 17, no. 2, pp. 491–509, 2015.

[158] S. E. Shladover, "Path at 20—history and major milestones," *IEEE Transactions on Intelligent Transportation Systems*, vol. 8, no. 4, pp. 584–592, 2007.

[159] Q. Xu and R. Sengupta, "Simulation, analysis, and comparison of ACC and CACC in highway merging control," in *IEEE IV2003 Intelligent Vehicles Symposium. Proceedings (Cat. No. 03TH8683)*. IEEE, 2003, pp. 237–242.

[160] Z. Wang, G. Wu, and M. J. Barth, "A review on cooperative adaptive cruise control (CACC) systems: Architectures, controls, and applications," in *2018 21st International Conference on Intelligent Transportation Systems (ITSC)*. IEEE, 2018, pp. 2884–2891.

[161] G. Rödönyi, "An adaptive spacing policy guaranteeing string stability in multi-brand ad hoc platoons," *IEEE Transactions on Intelligent Transportation Systems*, vol. 19, no. 6, pp. 1902–1912, 2017.

[162] C. Flores and V. Milanés, "Fractional-order-based ACC/CACC algorithm for improving string stability," *Transportation Research Part C: Emerging Technologies*, vol. 95, pp. 381–393, 2018.

[163] J. Ploeg, N. Van De Wouw, and H. Nijmeijer, "Lp string stability of cascaded systems: Application to vehicle platooning," *IEEE Transactions on Control Systems Technology*, vol. 22, no. 2, pp. 786–793, 2013.

[164] M. Wang, "Infrastructure assisted adaptive driving to stabilise heterogeneous vehicle strings," *Transportation Research Part C: Emerging Technologies*, vol. 91, pp. 276–295, 2018.

[165] Y. Bian, Y. Zheng, W. Ren, S. E. Li, J. Wang, and K. Li, "Reducing time headway for platooning of connected vehicles via V2V communication," *Transportation Research Part C: Emerging Technologies*, vol. 102, pp. 87–105, 2019.

[166] I. G. Jin and G. Orosz, "Optimal control of connected vehicle systems with communication delay and driver reaction time," *IEEE Transactions on Intelligent Transportation Systems*, vol. 18, no. 8, pp. 2056–2070, 2016.

[167] L. Zhang and G. Orosz, "Motif-based design for connected vehicle systems in presence of heterogeneous connectivity structures and time delays," *IEEE Transactions on Intelligent Transportation Systems*, vol. 17, no. 6, pp. 1638–1651, 2016.

[168] J.-W. Kwon and D. Chwa, "Adaptive bidirectional platoon control using a coupled sliding mode control method," *IEEE Transactions on Intelligent Transportation Systems*, vol. 15, no. 5, pp. 2040–2048, 2014.

[169] B. Sakhdari, "Real-time autonomous cruise control of connected plug-in hybrid electric vehicles under uncertainty," Ph.D. dissertation, University of Waterloo, 2018.

[170] S. Park, H. A. Rakha, K. Ahn, K. Moran, B. Saerens, and E. Van den Bulck, "Predictive ecocruise control system: Model logic and preliminary testing," *Transportation Research Record*, vol. 2270, no. 1, pp. 113–123, 2012.

[171] S. E. Li, Q. Guo, S. Xu, J. Duan, S. Li, C. Li, and K. Su, "Performance enhanced predictive control for adaptive cruise control system considering road elevation information," *IEEE Transactions on Intelligent Vehicles*, vol. 2, no. 3, pp. 150–160, 2017.

[172] S. Xu, S. E. Li, B. Cheng, and K. Li, "Instantaneous feedback control for a fuel-prioritized vehicle cruising system on highways with a varying slope," *IEEE Transactions on Intelligent Transportation Systems*, vol. 18, no. 5, pp. 1210–1220, 2016.

[173] Y. Luo, T. Chen, and K. Li, "Multi-objective decoupling algorithm for active distance control of intelligent hybrid electric vehicle," *Mechanical Systems and Signal Processing*, vol. 64, pp. 29–45, 2015.

[174] B. Sakhdari, M. Vajedi, and N. L. Azad, "Ecological adaptive cruise control of a plug-in hybrid electric vehicle for urban driving," in *2016 IEEE 19th International Conference on Intelligent Transportation Systems (ITSC)*. IEEE, 2016, pp. 1739–1744.

[175] G. Li and D. Görges, "Ecological adaptive cruise control and energy management strategy for hybrid electric vehicles based on heuristic dynamic programming," *IEEE Transactions on Intelligent Transportation Systems*, vol. 20, no. 9, pp. 3526–3535, 2018.

[176] L. Li, X. Wang, and J. Song, "Fuel consumption optimization for smart hybrid electric vehicle during a car-following process," *Mechanical Systems and Signal Processing*, vol. 87, pp. 17–29, 2017.

[177] X. Hu, J. Jiang, B. Egardt, and D. Cao, "Advanced power-source integration in hybrid electric vehicles: Multicriteria optimization approach," *IEEE Transactions on Industrial Electronics*, vol. 62, no. 12, pp. 7847–7858, 2015.

[178] Q. Zhou, W. Zhang, S. Cash, O. Olatunbosun, H. Xu, and G. Lu, "Intelligent sizing of a series hybrid electric power-train system based on chaos-enhanced accelerated particle swarm optimization," *Applied Energy*, vol. 189, pp. 588–601, 2017.

[179] M. Vajedi and N. L. Azad, "Ecological adaptive cruise controller for plug-in hybrid electric vehicles using nonlinear model predictive control," *IEEE Transactions on Intelligent Transportation Systems*, vol. 17, no. 1, pp. 113–122, 2015.

[180] M. Awad and R. Khanna, "Multiobjective optimization," in *Efficient Learning Machines*. Springer, 2015, pp. 185–208.

[181] Y. Luo, T. Chen, S. Zhang, and K. Li, "Intelligent hybrid electric vehicle ACC with coordinated control of tracking ability, fuel economy, and ride comfort," *IEEE Transactions on Intelligent Transportation Systems*, vol. 16, no. 4, pp. 2303–2308, 2015.

[182] W. H. van Willigen, E. Haasdijk, and L. J. Kester, "Evolving intelligent vehicle control using multi-objective neat," in *2013 IEEE Symposium on Computational Intelligence in Vehicles and Transportation Systems (CIVTS)*. IEEE, 2013, pp. 9–15.

[183] W. Jakob and C. Blume, "Pareto optimization or cascaded weighted sum: A comparison of concepts," *Algorithms*, vol. 7, no. 1, pp. 166–185, 2014.

[184] H. Yu, R. Jiang, Z. He, Z. Zheng, L. Li, R. Liu, and X. Chen, "Automated vehicle-involved traffic flow studies: A survey of assumptions, models, speculations, and perspectives," *Transportation Research Part C: Emerging Technologies*, vol. 127, p. 103101, 2021.

[185] L. Elefteriadou *et al.*, *An Introduction to Traffic Flow Theory*. Springer, 2014, vol. 84.

[186] Wikipedia, "Equations of motion." [Online]. Available: https://en.wikipedia.org/wiki/Equations_of_motion

[187] M. Makridis, G. Fontaras, B. Ciuffo, and K. Mattas, "MFC free-flow model: Introducing vehicle dynamics in microsimulation," *Transportation Research Record*, vol. 2673, no. 4, pp. 762–777, 2019.

[188] M. Brackstone and M. McDonald, "Car-following: A historical review," *Transportation Research Part F: Traffic Psychology and Behaviour*, vol. 2, no. 4, pp. 181–196, 1999.

[189] A. Reuschel, "Fahrzeugbewegungen in der kolonne," *Osterreichisches Ingenieur Archiv*, vol. 4, pp. 193–215, 1950.

[190] L. A. Pipes, "An operational analysis of traffic dynamics," *Journal of Applied Physics*, vol. 24, no. 3, pp. 274–281, 1953.

[191] D. C. Gazis, R. Herman, and R. W. Rothery, "Nonlinear follow-the-leader models of traffic flow," *Operations Research*, vol. 9, no. 4, pp. 545–567, 1961.

[192] G. F. Newell, "Nonlinear effects in the dynamics of car following," *Operations Research*, vol. 9, no. 2, pp. 209–229, 1961.

[193] R. L. Bierley, "Investigation of an intervehicle spacing display," *Highway Research Record*, no. 25, 1963.

[194] P. G. Gipps, "A behavioural car-following model for computer simulation," *Transportation Research Part B: Methodological*, vol. 15, no. 2, pp. 105–111, 1981.

[195] W. Leutzbach and R. Wiedemann, "Development and applications of traffic simulation models at the karlsruhe institut für verkehrswesen," *Traffic Engineering & Control*, vol. 27, no. 5, pp. 270–278, 1986.

References

[196] B. Sultan, M. Brackstone, and M. McDonald, "Drivers' use of deceleration and acceleration information in car-following process," *Transportation Research Record*, vol. 1883, no. 1, pp. 31–39, 2004.

[197] M. Bando, K. Hasebe, A. Nakayama, A. Shibata, and Y. Sugiyama, "Dynamical model of traffic congestion and numerical simulation," *Physical Review E*, vol. 51, no. 2, p. 1035, 1995.

[198] D. Helbing and B. Tilch, "Generalized force model of traffic dynamics," *Physical Review E*, vol. 58, no. 1, p. 133, 1998.

[199] M. Treiber, A. Hennecke, and D. Helbing, "Congested traffic states in empirical observations and microscopic simulations," *Physical Review E*, vol. 62, no. 2, p. 1805, 2000.

[200] R. Jiang, Q. Wu, and Z. Zhu, "Full velocity difference model for a car-following theory," *Physical Review E*, vol. 64, no. 1, p. 017101, 2001.

[201] X. Chen, "Modeling traffic flow dynamic and stochastic evolution," Ph.D. dissertation, Tsinghua University, 2012.

[202] X. Chen, L. Li, Q. Shi *et al.*, *Stochastic Evolutions of Dynamic Traffic Flow*. Springer, 2015.

[203] Y. Zhang, P. Ni, M. Li, H. Liu, and B. Yin, "A new car-following model considering driving characteristics and preceding vehicle's acceleration," *Journal of Advanced Transportation*, vol. 2017, 2017.

[204] S. Siuhi and M. S. Kaseko, "Parametric study of stimulus-response behavior for car-following models," in *Proceedings of the Transportation Research Board 89th Annual Meeting, USA*, 2010. [Online]. Available: https://trid.trb.org/view/910163

[205] S. Siuhi, "Parametric study of stimulus-response behavior incorporating vehicle heterogeneity in car-following models," Ph.D. dissertation, University of Nevada, Las Vegas, 2009.

[206] M. Saifuzzaman, "Incorporating risk taking and driver errors in car-following models," Ph.D. dissertation, Queensland University of Technology, 2016.

[207] B. Ciuffo, V. Punzo, and M. Montanino, "Thirty years of Gipps' car-following model: Applications, developments, and new features," *Transportation Research Record*, vol. 2315, no. 1, pp. 89–99, 2012.

[208] V. Punzo and F. Simonelli, "Analysis and comparison of microscopic traffic flow models with real traffic microscopic data," *Transportation Research Record*, vol. 1934, no. 1, pp. 53–63, 2005.

[209] V. Punzo and A. Tripodi, "Steady-state solutions and multiclass calibration of Gipps microscopic traffic flow model," *Transportation Research Record*, vol. 1999, no. 1, pp. 104–114, 2007.

[210] H. Zhao, R. He, and C. Ma, "An extended car-following model at signalised intersections," *Journal of Advanced Transportation*, vol. 2018, 2018.

[211] A. Kesting, M. Treiber, and D. Helbing, "Enhanced intelligent driver model to access the impact of driving strategies on traffic capacity," *Philosophical Transactions of the Royal Society A: Mathematical, Physical and Engineering Sciences*, vol. 368, no. 1928, pp. 4585–4605, 2010.

[212] J. Searle, "Equations for speed, time and distance for vehicles under maximum acceleration," *SAE Technical Paper*, Tech. Rep., 1999.

[213] H. Rakha, I. Lucic, S. H. Demarchi, J. R. Setti, and M. V. Aerde, "Vehicle dynamics model for predicting maximum truck acceleration levels," *Journal of Transportation Engineering*, vol. 127, no. 5, pp. 418–425, 2001.

[214] H. Rakha and I. Lucic, "Variable power vehicle dynamics model for estimating truck accelerations," *Journal of Transportation Engineering*, vol. 128, no. 5, pp. 412–419, 2002.

[215] H. Rakha, M. Snare, and F. Dion, "Vehicle dynamics model for estimating maximum light-duty vehicle acceleration levels," *Transportation Research Record*, vol. 1883, no. 1, pp. 40–49, 2004.

[216] H. Rakha, "Validation of Van Aerde's simplified steadystate car-following and traffic stream model," *Transportation Letters*, vol. 1, no. 3, pp. 227–244, 2009.

[217] H. A. Rakha, K. Ahn, W. Faris, and K. S. Moran, "Simple vehicle powertrain model for modeling intelligent vehicle applications," *IEEE Transactions on Intelligent Transportation Systems*, vol. 13, no. 2, pp. 770–780, 2012.

[218] K. Fadhloun, H. Rakha, A. Loulizi, and A. Abdelkefi, "Vehicle dynamics model for estimating typical vehicle accelerations," *Transportation Research Record*, vol. 2491, no. 1, pp. 61–71, 2015.

[219] K. Fadhloun and H. Rakha, "A novel vehicle dynamics and human behavior car-following model: Model development and preliminary testing," *International Journal of Transportation Science and Technology*, vol. 9, no. 1, pp. 14–28, 2020.

[220] M. Tran, D. Banister, J. D. Bishop, and M. D. McCulloch, "Realizing the electric-vehicle revolution," *Nature Climate Change*, vol. 2, no. 5, pp. 328–333, 2012.

[221] J. E. Campbell, D. B. Lobell, and C. B. Field, "Greater transportation energy and GHG offsets from bioelectricity than ethanol," *Science*, vol. 324, no. 5930, pp. 1055–1057, 2009.

[222] L. Kumar and S. Jain, "Electric propulsion system for electric vehicular technology: A review," *Renewable and Sustainable Energy Reviews*, vol. 29, pp. 924–940, 2014.

[223] E. Sadeghinezhad, S. Kazi, F. Sadeghinejad, A. Badarudin, M. Mehrali, R. Sadri, and M. R. Safaei, "A comprehensive literature review of bio-fuel performance in internal combustion engine and relevant costs involvement," *Renewable and Sustainable Energy Reviews*, vol. 30, pp. 29–44, 2014.

[224] A. Ostadi and M. Kazerani, "A comparative analysis of optimal sizing of battery-only, ultracapacitor-only, and battery–ultracapacitor hybrid energy storage systems for a city bus," *IEEE Transactions on Vehicular Technology*, vol. 64, no. 10, pp. 4449–4460, 2014.

[225] L. Xu, C. D. Mueller, J. Li, M. Ouyang, and Z. Hu, "Multi-objective component sizing based on optimal energy management strategy of fuel cell electric vehicles," *Applied Energy*, vol. 157, pp. 664–674, 2015.

[226] X. Hu, S. J. Moura, N. Murgovski, B. Egardt, and D. Cao, "Integrated optimization of battery sizing, charging, and power management in plug-in hybrid electric vehicles," *IEEE Transactions on Control Systems Technology*, vol. 24, no. 3, pp. 1036–1043, 2015.

[227] X. Wu, B. Cao, X. Li, J. Xu, and X. Ren, "Component sizing optimization of plug-in hybrid electric vehicles," *Applied Energy*, vol. 88, no. 3, pp. 799–804, 2011.

[228] P. Iodice, A. Senatore, G. Langella, and A. Amoresano, "Effect of ethanol–gasoline blends on CO and HC emissions in last generation si engines within the cold-start transient: An experimental investigation," *Applied Energy*, vol. 179, pp. 182–190, 2016.

[229] C. Wang, J. M. Herreros, C. Jiang, A. Sahu, and H. Xu, "Engine thermal efficiency gain and well-to-wheel greenhouse gas savings when using bioethanol as a gasoline-blending component in future spark-ignition engines: A China case study," *Energy & Fuels*, vol. 32, no. 2, pp. 1724–1732, 2018.

[230] C. Wang, S. Zeraati-Rezaei, L. Xiang, and H. Xu, "Ethanol blends in spark ignition engines: RON, octane-added value, cooling effect, compression ratio, and potential engine efficiency gain," *Applied Energy*, vol. 191, pp. 603–619, 2017.

[231] C. Samaras and K. Meisterling, "Life cycle assessment of greenhouse gas emissions from plug-in hybrid vehicles: Implications for policy," *Environmental Science & Technology*, vol. 42, no. 9, pp. 3170–3176, 2008.

[232] T. H. Bradley and A. A. Frank, "Design, demonstrations and sustainability impact assessments for plug-in hybrid electric vehicles," *Renewable and Sustainable Energy Reviews*, vol. 13, no. 1, pp. 115–128, 2009.

[233] C. H. Stephan and J. Sullivan, "Environmental and energy implications of plug-in hybrid-electric vehicles," *Environmental Science & Technology*, vol. 42, no. 4, pp. 1185–1190, 2008.

[234] Wikipedia, "Common ethanol fuel mixtures." [Online]. Available: https://en.wikipedia.org/wiki/Common_ethanol_fuel_mixtures

[235] G. Fontaras, N.-G. Zacharof, and B. Ciuffo, "Fuel consumption and CO_2 emissions from passenger cars in Europe–laboratory versus real-world emissions," *Progress in Energy and Combustion Science*, vol. 60, pp. 97–131, 2017.

[236] K. Yu, H. Yang, X. Tan, T. Kawabe, Y. Guo, Q. Liang, Z. Fu, and Z. Zheng, "Model predictive control for hybrid electric vehicle platooning using slope information," *IEEE Transactions on Intelligent Transportation Systems*, vol. 17, no. 7, pp. 1894–1909, 2016.

[237] J. M. Luján, C. Guardiola, B. Pla, and A. Reig, "Cost of ownership-efficient hybrid electric vehicle powertrain sizing for multi-scenario driving cycles," *Proceedings of the Institution of Mechanical Engineers, Part D: Journal of Automobile Engineering*, vol. 230, no. 3, pp. 382–394, 2016.

[238] M. Chen and G. A. Rincon-Mora, "Accurate electrical battery model capable of predicting runtime and I-V performance," *IEEE Transactions on Energy Conversion*, vol. 21, no. 2, pp. 504–511, 2006.

[239] T. Liu, X. Hu, S. E. Li, and D. Cao, "Reinforcement learning optimized look-ahead energy management of a parallel hybrid electric vehicle," *IEEE/ASME Transactions on Mechatronics*, vol. 22, no. 4, pp. 1497–1507, 2017.

[240] S. M. Ahmeda and M. Abo-Zahhad, "A new hybrid algorithm for ECG signal compression based on the wavelet transformation of the linearly predicted error," *Medical Engineering & Physics*, vol. 23, no. 2, pp. 117–126, 2001.

[241] H. L. MacLean and L. B. Lave, "Life cycle assessment of automobile/fuel options," *Environmental Science & Technology*, vol. 37, no. 23, pp. 5445–5452, 2003.

[242] IEA, *CO$_2$ Emissions from Fuel Combustion 2018*. International Energy Agency (IEA), 2018. [Online]. Available: https://www.oecd-ilibrary.org/content/publication/co2_fuel-2018-en

[243] K. Deb and H. Jain, "An evolutionary many-objective optimization algorithm using reference-point-based nondominated sorting approach, Part I: Solving problems with box constraints," *IEEE Transactions on Evolutionary Computation*, vol. 18, no. 4, pp. 577–601, 2013.

[244] H. Jain and K. Deb, "An evolutionary many-objective optimization algorithm using reference-point based nondominated sorting approach, Part II: Handling constraints and extending to an adaptive approach," *IEEE Transactions on Evolutionary Computation*, vol. 18, no. 4, pp. 602–622, 2013.

[245] Q. Zhu, Q. Lin, Z. Du, Z. Liang, W. Wang, Z. Zhu, J. Chen, P. Huang, and Z. Ming, "A novel adaptive hybrid crossover operator for multiobjective evolutionary algorithm," *Information Sciences*, vol. 345, pp. 177–198, 2016.

[246] S. H. R. Pasandideh and S. T. A. Niaki, "Multi-response simulation optimization using genetic algorithm within desirability function framework," *Applied Mathematics and Computation*, vol. 175, no. 1, pp. 366–382, 2006.

[247] G. J. Offer, "Automated vehicles and electrification of transport," *Energy & Environmental Science*, vol. 8, no. 1, pp. 26–30, 2015.

[248] L. Zhang, Y. Wang, and Z. Wang, "Robust lateral motion control for in-wheel-motor-drive electric vehicles with network induced delays," *IEEE Transactions on Vehicular Technology*, vol. 68, no. 11, pp. 10 585–10 593, 2019.

[249] Y. Wang, Z. Wang, L. Zhang, M. Liu, and J. Zhu, "Lateral stability enhancement based on a novel sliding mode prediction control for a four-wheel-independently actuated electric vehicle," *IET Intelligent Transport Systems*, vol. 13, no. 1, pp. 124–133, 2018.

[250] J. Li, Q. Zhou, H. Williams, and H. Xu, "Back-to-back competitive learning mechanism for fuzzy logic based supervisory control system of hybrid electric vehicles," *IEEE Transactions on Industrial Electronics*, vol. 67, no. 10, pp. 8900–8909, 2019.

[251] M. Makridis, K. Mattas, and B. Ciuffo, "Response time and time headway of an adaptive cruise control. An empirical characterization and potential impacts on road capacity," *IEEE Transactions on Intelligent Transportation Systems*, vol. 21, no. 4, pp. 1677–1686, 2019.

[252] B. Ciuffo, M. Makridis, T. Toledo, and G. Fontaras, "Capability of current car-following models to reproduce vehicle free-flow acceleration dynamics," *IEEE Transactions on Intelligent Transportation Systems*, vol. 19, no. 11, pp. 3594–3603, 2018.

[253] V. Milanés and S. E. Shladover, "Modeling cooperative and autonomous adaptive cruise control dynamic responses using experimental data," *Transportation Research Part C: Emerging Technologies*, vol. 48, pp. 285–300, 2014.

[254] L. Guo, H. Chen, Q. Liu, and B. Gao, "A computationally efficient and hierarchical control strategy for velocity optimization of on-road vehicles," *IEEE Transactions on Systems, Man, and Cybernetics: Systems*, vol. 49, no. 1, pp. 31–41, 2018.

[255] F. Zhang, X. Hu, R. Langari, and D. Cao, "Energy management strategies of connected HEVs and PHEVs: Recent progress and outlook," *Progress in Energy and Combustion Science*, vol. 73, pp. 235–256, 2019.

[256] S. Qiu, L. Qiu, L. Qian, and P. Pisu, "Hierarchical energy management control strategies for connected hybrid electric vehicles considering efficiencies feedback," *Simulation Modelling Practice and Theory*, vol. 90, pp. 1–15, 2019.

[257] M. Ghasemi and X. Song, "Powertrain energy management for autonomous hybrid electric vehicles with flexible driveline power demand," *IEEE Transactions on Control Systems Technology*, vol. 27, no. 5, pp. 2229–2236, 2018.

[258] M. Hovgard, O. Jonsson, N. Murgovski, M. Sanfridson, and J. Fredriksson, "Cooperative energy management of electrified vehicles on hilly roads," *Control Engineering Practice*, vol. 73, pp. 66–78, 2018.

[259] H. S. Mahmassani, "50th anniversary invited article - autonomous vehicles and connected vehicle systems: Flow and operations considerations," *Transportation Science*, vol. 50, no. 4, pp. 1140–1162, 2016.

[260] D. Ngoduy, "Linear stability of a generalized multi-anticipative car following model with time delays," *Communications in Nonlinear Science and Numerical Simulation*, vol. 22, no. 1-3, pp. 420–426, 2015.

[261] M. Wang, S. P. Hoogendoorn, W. Daamen, B. van Arem, B. Shyrokau, and R. Happee, "Delay-compensating strategy to enhance string stability of adaptive cruise controlled vehicles," *Transportmetrica B: Transport Dynamics*, vol. 6, no. 3, pp. 211–229, 2018.

[262] K. Wu, M. Kuang, M. Milacic, X. Zhang, and J. Sun, "Analysis of effects of fuel cell system dynamics on optimal energy management," in *Dynamic Systems and Control Conference*, vol. 58295. American Society of Mechanical Engineers, 2017, p. V003T43A001.

[263] X. Hu, C. M. Martinez, and Y. Yang, "Charging, power management, and battery degradation mitigation in plug-in hybrid electric vehicles: A unified cost-optimal approach," *Mechanical Systems and Signal Processing*, vol. 87, pp. 4–16, 2017.

[264] Z. Chen, R. Xiong, C. Wang, and J. Cao, "An on-line predictive energy management strategy for plug-in hybrid electric vehicles to counter the uncertain prediction of the driving cycle," *Applied Energy*, vol. 185, pp. 1663–1672, 2017.

[265] Z. Chen and S. Andresen, "A multiobjective optimization model of production-sourcing for sustainable supply chain with consideration of social, environmental, and economic factors," *Mathematical Problems in Engineering*, vol. 2014, 2014.

[266] J. Pavlovic, B. Ciuffo, G. Fontaras, V. Valverde, and A. Marotta, "How much difference in type-approval CO_2 emissions from passenger cars in Europe can be expected from changing to the new test procedure (NEDC vs. WLTP)?" *Transportation Research Part A: Policy and Practice*, vol. 111, pp. 136–147, 2018.

[267] G. Fontaras, B. Ciuffo, N. Zacharof, S. Tsiakmakis, A. Marotta, J. Pavlovic, and K. Anagnostopoulos, "The difference between reported and real-world CO_2 emissions: How much improvement can be expected by WLTP introduction," *Transportation Research Procedia*, vol. 25, pp. 3933–3943, 2017.

[268] Y. He, M. Makridis, G. Fontaras, K. Mattas, H. Xu, and B. Ciuffo, "The energy impact of adaptive cruise control in real-world highway multiple-car-following scenarios," *European Transport Research Review*, vol. 12, pp. 1–11, 2020.

[269] C. Fiori, V. Arcidiacono, G. Fontaras, M. Makridis, K. Mattas, V. Marzano, C. Thiel, and B. Ciuffo, "The effect of electrified mobility on the relationship between traffic conditions and energy consumption," *Transportation Research Part D: Transport and Environment*, vol. 67, pp. 275–290, 2019.

[270] W. J. Schakel and B. Van Arem, "Improving traffic flow efficiency by in-car advice on lane, speed, and headway," *IEEE Transactions on Intelligent Transportation Systems*, vol. 15, no. 4, pp. 1597–1606, 2014.

[271] D. Helbing, "Traffic and related self-driven many-particle systems," *Reviews of Modern Physics*, vol. 73, no. 4, p. 1067, 2001.

[272] B. Cao and Z. Yang, "Car-following models study progress," in *2009 Second International Symposium on Knowledge Acquisition and Modeling*, vol. 3. IEEE, 2009, pp. 190–193.

[273] G. F. Newell, "A simplified car-following theory: A lower order model," *Transportation Research Part B: Methodological*, vol. 36, no. 3, pp. 195–205, 2002.

[274] EC, *A European Strategy for Low-Emission Mobility*. European Commission (EC), 2016.

[275] S. Tsiakmakis, G. Fontaras, B. Ciuffo, and Z. Samaras, "A simulation-based methodology for quantifying European passenger car fleet CO_2 emissions," *Applied Energy*, vol. 199, pp. 447–465, 2017.

[276] A. K. Maurya and P. S. Bokare, "Study of deceleration behaviour of different vehicle types." *International Journal for Traffic & Transport Engineering*, vol. 2, no. 3, 2012.

[277] M. Treiber and A. Kesting, "Microscopic calibration and validation of car-following models–a systematic approach," *Procedia-Social and Behavioral Sciences*, vol. 80, pp. 922–939, 2013.

[278] W. J. Schakel, B. Van Arem, and B. D. Netten, "Effects of cooperative adaptive cruise control on traffic flow stability," in *13th International IEEE Conference on Intelligent Transportation Systems*. IEEE, 2010, pp. 759–764.

[279] J. Wang, H. A. Rakha, and K. Fadhloun, "Validation of the Rakha-Pasumarthy-Adjerid car-following model for vehicle fuel consumption and emission estimation applications," *Transportation Research Part D: Transport and Environment*, vol. 55, pp. 246–261, 2017.

[280] L. Yue and H. Wang, "An optimization design method of combination of steep slope and sharp curve sections for mountain highways," *Mathematical Problems in Engineering*, vol. 2019, 2019.

[281] B. G. Ros, V. L. Knoop, T. Takahashi, I. Sakata, B. van Arem, and S. P. Hoogendoorn, "Optimization of traffic flow at freeway sags by controlling the acceleration of vehicles equipped with in-car systems," *Transportation Research Part C: Emerging Technologies*, vol. 71, pp. 1–18, 2016.

[282] B. G. Ros, W. J. Schakel, A. E. Papacharalampous, M. Wang, V. L. Knoop, I. Sakata, B. van Arem, and S. P. Hoogendoorn, "Using advanced adaptive cruise control systems to reduce congestion at sags: An evaluation based on microscopic traffic simulation," *Transportation Research Part C: Emerging Technologies*, vol. 102, pp. 411–426, 2019.

[283] K. Chung, J. Rudjanakanoknad, and M. J. Cassidy, "Relation between traffic density and capacity drop at three freeway bottlenecks," *Transportation Research Part B: Methodological*, vol. 41, no. 1, pp. 82–95, 2007.

[284] R. P. Bhattacharyya, "Modeling human driving from demonstrations," Ph.D. dissertation, Stanford University, 2021.

[285] M. Treiber, A. Kesting, and D. Helbing, "Delays, inaccuracies and anticipation in microscopic traffic models," *Physica A: Statistical Mechanics and its Applications*, vol. 360, no. 1, pp. 71–88, 2006.

[286] M. Saifuzzaman and Z. Zheng, "Incorporating human-factors in car-following models: A review of recent developments and research needs," *Transportation Research Part C: Emerging Technologies*, vol. 48, pp. 379–403, 2014.

[287] S. Park, H. Rakha, K. Ahn, and K. Moran, "Fuel economy impacts of manual, conventional cruise control, and predictive eco-cruise control driving," *International Journal of Transportation Science and Technology*, vol. 2, no. 3, pp. 227–242, 2013.

[288] M. Makridis, K. Mattas, A. Anesiadou, and B. Ciuffo, "OpenACC: An open database of car-following experiments to study the properties of commercial ACC systems," *Transportation Research Part C: Emerging Technologies*, vol. 125, p. 103047, 2021.

[289] B. Ciuffo, K. Mattas, M. Makridis, G. Albano, A. Anesiadou, Y. He, S. Josvai, D. Komnos, M. Pataki, S. Vass *et al.*, "Requiem on the positive effects of commercial adaptive cruise control on motorway traffic and recommendations for future automated driving systems," *Transportation Research Part C: Emerging Technologies*, vol. 130, p. 103305, 2021.

[290] X. D. Kan, L. Xiao, H. Liu, M. Wang, W. J. Schakel, X. Lu, B. van Arem, S. E. Shladover, and R. A. Ferlis, "Cross-comparison and calibration of two microscopic traffic simulation models for complex freeway corridors with dedicated lanes," *Journal of Advanced Transportation*, vol. 2019, 2019.

[291] X. Li, T. Song, H. Kuang, and S. Dai, "Phase transition on speed limit traffic with slope," *Chinese Physics B*, vol. 17, no. 8, p. 3014, 2008.

[292] K. Komada, S. Masukura, and T. Nagatani, "Effect of gravitational force upon traffic flow with gradients," *Physica A: Statistical Mechanics and its Applications*, vol. 388, no. 14, pp. 2880–2894, 2009.

[293] J. Zhou, Z. Shi, and J. Cao, "An extended traffic flow model on a gradient highway with the consideration of the relative velocity," *Nonlinear Dynamics*, vol. 78, no. 3, pp. 1765–1779, 2014.

[294] Y. Li, H. Zhao, L. Zhang, and C. Zhang, "An extended car-following model incorporating the effects of lateral gap and gradient," *Physica A: Statistical Mechanics and its Applications*, vol. 503, pp. 177–189, 2018.

[295] B. G. Ros, "Traffic flow at sags: Theory, modeling and control," Ph.D. dissertation, Delft University of Technology, 2016.

[296] B. G. Ros, V. L. Knoop, Y. Shiomi, T. Takahashi, B. van Arem, and S. P. Hoogendoorn, "Modeling traffic at sags," *International Journal of Intelligent Transportation Systems Research*, vol. 14, no. 1, pp. 64–74, 2016.

[297] M. Kasai and J. Xing, "Use of particle filtering to establish a time-varying car-following model," *International Journal of Intelligent Transportation Systems Research*, vol. 17, no. 1, pp. 49–60, 2019.

[298] Y. Liang and A. Su, "Study on traffic flow affected by the ultra-high of road turning," in *Proceedings of 2011 International Conference on Electronic & Mechanical Engineering and Information Technology*, vol. 8. IEEE, 2011, pp. 3986–3990.

[299] W. Zhu and L. Zhang, "Friction coefficient and radius of curvature effects upon traffic flow on a curved road," *Physica A: Statistical Mechanics and its Applications*, vol. 391, no. 20, pp. 4597–4605, 2012.

[300] Y. Zheng, R. Cheng, and H. Ge, "The feedback control research on straight and curved road with car-following model," *Physics Letters A*, vol. 381, no. 27, pp. 2137–2143, 2017.

[301] Z. Jin, R. Cheng, and H. Ge, "Nonlinear density wave and energy consumption investigation of traffic flow on a curved road," *Chinese Physics B*, vol. 26, no. 11, p. 110504, 2017.

[302] Z. Liu, H. Ge, and R. Cheng, "Kdv–burgers equation in the modified continuum model considering the effect of friction and radius on a curved road," *Physica A: Statistical Mechanics and its Applications*, vol. 503, pp. 1218–1227, 2018.

[303] Y. Sun, H. Ge, and R. Cheng, "An extended car-following model considering driver's desire for smooth driving on the curved road," *Physica A: Statistical Mechanics and its Applications*, vol. 527, p. 121426, 2019.

[304] W. Zhu and R. Yu, "A new car-following model considering the related factors of a gyroidal road," *Physica A: Statistical Mechanics and its Applications*, vol. 393, pp. 101–111, 2014.

[305] X. Meng and L. Yan, "Stability analysis in a curved road traffic flow model based on control theory," *Asian Journal of Control*, vol. 19, no. 5, pp. 1844–1853, 2017.

[306] M. Rout, D. Sain, S. Swain, and S. Mishra, "PID controller design for cruise control system using genetic algorithm," in *2016 International Conference on Electrical, Electronics, and Optimization Techniques (ICEEOT)*. IEEE, 2016, pp. 4170–4174.

[307] S. Cheng, L. Li, M. Mei, Y. Nie, and L. Zhao, "Multiple-objective adaptive cruise control system integrated with DYC," *IEEE Transactions on Vehicular Technology*, vol. 68, no. 5, pp. 4550–4559, 2019.

[308] R. Rajamani, *Vehicle Dynamics and Control*. Springer Science & Business Media, 2011.

[309] AASHTO, *A Policy on Geometric Design of Highways and Streets*. American Association of State Highway and Transportation Officials (AASHTO), 2011.

[310] F. L. Mannering and S. S. Washburn, *Principles of Highway Engineering and Traffic Analysis*. John Wiley & Sons, 2020.

[311] D. Jia and D. Ngoduy, "Platoon based cooperative driving model with consideration of realistic inter-vehicle communication," *Transportation Research Part C: Emerging Technologies*, vol. 68, pp. 245–264, 2016.

[312] L. Xiao, M. Wang, and B. van Arem, "Realistic car-following models for microscopic simulation of adaptive and cooperative adaptive cruise control vehicles," *Transportation Research Record*, vol. 2623, no. 1, pp. 1–9, 2017.

[313] J. Johansson, "Specify the curve speed adaption parameters within the adaptive cruise control system," Master's thesis, Chalmers University of Technology, 2020.

[314] V. Punzo, Z. Zheng, and M. Montanino, "About calibration of car-following dynamics of automated and human-driven vehicles: Methodology, guidelines and codes," *Transportation Research Part C: Emerging Technologies*, 2021.

[315] M. Ab Malek and M. Ali, "Evolutionary tuning method for PID controller parameters of a cruise control system using metamodeling," *Modelling and Simulation in Engineering*, vol. 2009, 2009.

[316] F. Gao, D. Dang, and S. E. Li, "Control of a heterogeneous vehicular platoon with uniform communication delay," in *2015 IEEE International Conference on Information and Automation*. IEEE, 2015, pp. 2419–2424.

[317] V. Punzo and M. Montanino, "A two-level probabilistic approach for validation of stochastic traffic simulations: Impact of drivers' heterogeneity models," *Transportation research part C: emerging technologies*, vol. 121, p. 102843, 2020.

[318] D. Swaroop, J. K. Hedrick, C. Chien, and P. Ioannou, "A comparision of spacing and headway control laws for automatically controlled vehicles," *Vehicle System Dynamics*, vol. 23, no. 1, pp. 597–625, 1994.

[319] G. Gunter, R. Stern, and D. B. Work, "Modeling adaptive cruise control vehicles from experimental data: Model comparison," in *2019 IEEE Intelligent Transportation Systems Conference (ITSC)*. IEEE, 2019, pp. 3049–3054.

[320] Y. Wang, G. Gunter, M. Nice, M. L. Delle Monache, and D. Work, "Online parameter estimation methods for adaptive cruise control systems," *IEEE Transactions on Intelligent Vehicles*, 2020.

[321] Y. He, B. Ciuffo, Q. Zhou, M. Makridis, K. Mattas, J. Li, Z. Li, F. Yan, and H. Xu, "Adaptive cruise control strategies implemented on experimental vehicles: A review," *IFAC-PapersOnLine*, vol. 52, no. 5, pp. 21–27, 2019.

[322] C. Flores, J. Muñoz, C. A. Monje, V. Milanés, and X. Lu, "Iso-damping fractional-order control for robust automated car-following," *Journal of Advanced Research*, 2020.

[323] M. Treiber and A. Kesting, "Evidence of convective instability in congested traffic flow: A systematic empirical and theoretical investigation," *Procedia-Social and Behavioral Sciences*, vol. 17, pp. 683–701, 2011.

[324] M. Montanino and V. Punzo, "Trajectory data reconstruction and simulation-based validation against macroscopic traffic patterns," *Transportation Research Part B: Methodological*, vol. 80, pp. 82–106, 2015.

[325] M. Montanino, J. Monteil, and V. Punzo, "From homogeneous to heterogeneous traffic flows: Lp string stability under uncertain model parameters," *Transportation Research Part B: Methodological*, vol. 146, pp. 136–154, 2021.

[326] M. Montanino and V. Punzo, "On string stability of a mixed and heterogeneous traffic flow: A unifying modelling framework," *Transportation Research Part B: Methodological*, vol. 144, pp. 133–154, 2021.

[327] A. Eskandarian, *Handbook of Intelligent Vehicles*. Springer, 2012, vol. 2.

[328] X. Zhang, Y. Huang, K. Guo, T. Peng, S. Sun, and W. Li, "Integrated spacing policy considering micro-and macroscopic characteristics," *Automotive Innovation*, vol. 2, no. 2, pp. 102–109, 2019.

[329] L. Xiao and F. Gao, "Practical string stability of platoon of adaptive cruise control vehicles," *IEEE Transactions on Intelligent Transportation Systems*, vol. 12, no. 4, pp. 1184–1194, 2011.

[330] G. Gunter, D. Gloudemans, R. E. Stern, S. McQuade, R. Bhadani, M. Bunting, M. L. Delle Monache, R. Lysecky, B. Seibold, J. Sprinkle *et al.*, "Are commercially implemented adaptive cruise control systems string stable?" *IEEE Transactions on Intelligent Transportation Systems*, pp. 1–12, 2020.

[331] G. Kesteven, "The coefficient of variation," *Nature*, vol. 158, no. 4015, pp. 520–521, 1946.

[332] M. Zhu, X. Wang, A. Tarko *et al.*, "Modeling car-following behavior on urban expressways in shanghai: A naturalistic driving study," *Transportation Research Part C: Emerging Technologies*, vol. 93, pp. 425–445, 2018.

[333] V. Punzo and M. Montanino, "Speed or spacing? Cumulative variables, and convolution of model errors and time in traffic flow models validation and calibration," *Transportation Research Part B: Methodological*, vol. 91, pp. 21–33, 2016.

[334] D. Jia, K. Lu, J. Wang, X. Zhang, and X. Shen, "A survey on platoon-based vehicular cyber-physical systems," *IEEE Communications Surveys & Tutorials*, vol. 18, no. 1, pp. 263–284, 2015.

[335] M. Makridis, K. Mattas, D. Borio, R. Giuliani, and B. Ciuffo, "Estimating reaction time in adaptive cruise control system," in *2018 IEEE Intelligent Vehicles Symposium (IV)*. IEEE, 2018, pp. 1312–1317.

[336] M. Aloso Raposo, B. Ciuffo, M. Makridis, and C. Thiel, "The r-evolution of driving: from connected vehicles to coordinated automated road transport (C-ART): Part I, framework for a safe & efficient coordinated automated road transport (C-ART) system study," *European Commission - Joint Research Centre (JRC)*, 2018.

[337] C. Wu, G. Zhao, and B. Ou, "A fuel economy optimization system with applications in vehicles with human drivers and autonomous vehicles," *Transportation Research Part D: Transport and Environment*, vol. 16, no. 7, pp. 515–524, 2011.

[338] M. Mamouei, I. Kaparias, and G. Halikias, "A framework for user-and system-oriented optimisation of fuel efficiency and traffic flow in adaptive cruise control," *Transportation Research Part C: Emerging Technologies*, vol. 92, pp. 27–41, 2018.

[339] Y. D. Ko, B. D. Song, and Y. Oh, "Mathematical analysis of environmental effects of forming a platoon of smart vehicles," *Sustainability*, vol. 11, no. 3, p. 571, 2019.

[340] G. S. Larue, H. Malik, A. Rakotonirainy, and S. Demmel, "Fuel consumption and gas emissions of an automatic transmission vehicle following simple eco-driving instructions on urban roads," *IET Intelligent Transport Systems*, vol. 8, no. 7, pp. 590–597, 2014.

[341] K. Ahn, "Microscopic fuel consumption and emission modeling," Ph.D. dissertation, Virginia Polytechnic Institute and State University, 1998.

[342] W. F. Faris, H. A. Rakha, R. I. Kafafy, M. Idres, and S. Elmoselhy, "Vehicle fuel consumption and emission modelling: An in-depth literature review," *International Journal of Vehicle Systems Modelling and Testing*, vol. 6, no. 3-4, pp. 318–395, 2011.

[343] M. Zhou, H. Jin, and W. Wang, "A review of vehicle fuel consumption models to evaluate eco-driving and eco-routing," *Transportation Research Part D: Transport and Environment*, vol. 49, pp. 203–218, 2016.

[344] W. Dvorkin, J. King, M. Gray, and S. Jao, "Determining the greenhouse gas emissions benefit of an adaptive cruise control system using real-world driving data," SAE Technical Paper, Tech. Rep., 2019.

[345] C. Lei, E. M. van Eenennaam, W. K. Wolterink, J. Ploeg, G. Karagiannis, and G. Heijenk, "Evaluation of CACC string stability using SUMO, Simulink, and OMNeT++," *EURASIP Journal on Wireless Communications and Networking*, vol. 2012, no. 1, pp. 1–12, 2012.

[346] O. Munyaneza, B. B. Munyazikwiye, and H. R. Karimi, "Speed control design for a vehicle system using fuzzy logic and PID controller," in *2015 International Conference on Fuzzy Theory and Its Applications (iFUZZY)*. IEEE, 2015, pp. 56–61.

[347] K. Osman, M. F. Rahmat, and M. A. Ahmad, "Modelling and controller design for a cruise control system," in *2009 5th International Colloquium on Signal Processing & Its Applications*. IEEE, 2009, pp. 254–258.

[348] E. Bedner, D. Fulk, and A. Hac, "Exploring the trade-off of handling stability and responsiveness with advanced control systems," SAE Technical Paper, Tech. Rep., 2007.

[349] K. H. Ang, G. Chong, and Y. Li, "PID control system analysis, design, and technology," *IEEE Transactions on Control Systems Technology*, vol. 13, no. 4, pp. 559–576, 2005.

[350] MathWorks, "2D correlation coefficient." [Online]. Available: https://uk.mathworks.com/help/images/ref/corr2.html

[351] W. Zhao, D. Ngoduy, S. Shepherd, R. Liu, and M. Papageorgiou, "A platoon based cooperative eco-driving model for mixed automated and human-driven vehicles at a signalised intersection," *Transportation Research Part C: Emerging Technologies*, vol. 95, pp. 802–821, 2018.

[352] S. E. Shladover, C. Nowakowski, X. Lu, and R. Ferlis, "Cooperative adaptive cruise control: Definitions and operating concepts," *Transportation Research Record*, vol. 2489, no. 1, pp. 145–152, 2015.

[353] I. Mahdinia, R. Arvin, A. Khattak, and A. Ghiasi, "Safety, energy, and emissions impacts of adaptive cruise control and cooperative adaptive cruise control," *Transportation Research Record*, vol. 2674, no. 6, pp. 253–267, 2020.

[354] M. Makridis, K. Mattas, B. Ciuffo, F. Re, A. Kriston, F. Minarini, and G. Rognelund, "Empirical study on the properties of adaptive cruise control systems and their impact on traffic flow and string stability," *Transportation Research Record*, vol. 2674, no. 4, pp. 471–484, 2020.

[355] Z. Szalay, Z. Hamar, and P. Simon, "A multi-layer autonomous vehicle and simulation validation ecosystem axis: Zalazone," in *International Conference on Intelligent Autonomous Systems*.   Springer, 2018, pp. 954–963.

[356] Z. Szalay, "Structure and architecture problems of autonomous road vehicle testing and validation," in *15th Mini Conference on Vehicle System Dynamics, Identification and Anomalies-VSDIA*, 2016.

[357] Z. Szalay, Z. Hamar, and Á. Nyerges, "Novel design concept for an automotive proving ground supporting multilevel CAV development," *International Journal of Vehicle Design*, vol. 80, no. 1, pp. 1–22, 2019.